

PRECAMBRIAN CRUSTAL EVOLUTION IN THE GREAT FALLS TECTONIC ZONE

By

JENNIFER N. GIFFORD

A DISSERTATION PRESENTED TO THE GRADUATE SCHOOL
OF THE UNIVERSITY OF FLORIDA IN PARTIAL FULFILLMENT
OF THE REQUIREMENTS FOR THE DEGREE OF
DOCTOR OF PHILOSOPHY

UNIVERSITY OF FLORIDA
2013

© 2013 Jennifer N. Gifford

To my family and friends, without your support I never would have made it this far.

ACKNOWLEDGMENTS

I wish to thank the National Science Foundation for funding my project through grants EAR0545715, EAR0538133, EAR0546751 and EAR0609952. I wish to thank my advisors Dr. Paul Mueller and Dr. David Foster for their guidance and patience. I also wish to thank my committee; Dr. Karen Bjorndal, Dr. Kyle Min, Dr. Michael Perfit, and Dr. Ray Russo, for their guidance and helpful reviews of my dissertation material. I wish to thank my family for their un-ending love and support. And finally, I wish to thank Dr. Shawn Malone for his support and assistance.

TABLE OF CONTENTS

	<u>page</u>
ACKNOWLEDGMENTS.....	4
LIST OF TABLES.....	7
LIST OF FIGURES.....	9
LIST OF OBJECTS.....	15
LIST OF ABBREVIATIONS.....	16
ABSTRACT.....	17
CHAPTER	
1 INTRODUCTION.....	19
2 GRASSRANGE XENOLITHS.....	25
Introduction.....	25
Geologic Background.....	26
Results.....	27
Whole-Rock Geochemistry.....	28
U-Pb Geochronology In Zircon.....	30
Hf Isotopes In Zircon.....	31
Sm-Nd Whole-Rock Isotopes.....	33
Discussion.....	34
Origins Of The Granitic Xenoliths.....	34
Origins Of The Schistose and Quartzite Xenoliths.....	36
Implications For Great Falls Tectonic Zone Evolution.....	38
Conclusions.....	41
3 MISSOURI BREAKS XENOLITHS.....	70
Introduction.....	70
Geologic Background.....	72
Sample Descriptions.....	74
Big Slide Diatreme.....	74
Robinson Ranch Diatreme.....	74
Little Sand Creek Diatreme.....	75
Bearpaw Mountains At Lloyd Divide.....	76
Highwood Mountains.....	77
Results.....	77
Whole-Rock Geochemistry.....	77
U-Pb Geochronology Of Zircon.....	78

Hf Isotopes In Zircon	84
Sm-Nd Whole-Rock Isotopes	88
Discussion	90
Origins Of The Meta-Igneous Xenoliths	90
Implications For Great Falls Tectonic Zone Evolution	93
Conclusions	97
4 LITTLE ROCKY MOUNTAINS	130
Introduction	130
Geologic Background.....	131
Stratigraphy	132
Previous Geochronology And Geochemistry.....	134
Sample Descriptions	134
Amphibolite.....	134
Quartzofeldspathic Schists	135
Gneisses	136
Other Samples	137
Results.....	138
Whole-Rock Geochemistry.....	138
U-Pb Geochronology Of Zircon	140
Hf Isotopes In Zircon	144
Sm-Nd Whole-Rock Isotopes	147
Discussion	148
Geochemical Insight Into Sample Origins.....	148
Little Rocky Mountains as Exposed Medicine Hat Block Crust.....	149
Correlation of igneous ages	149
Insights into meta-sediment provenance	150
Other regional considerations	153
Conclusions	155
5 SUMMARY/CONCLUSIONS	187
APPENDIX	
A METHODS.....	195
U-Pb And Hf Isotopic Analysis Of Zircon	195
Whole-Rock Geochemistry	196
B SUPPLEMENTARY DATA TABLES	198
LIST OF REFERENCES	199
BIOGRAPHICAL SKETCH.....	212

LIST OF TABLES

<u>Table</u>	<u>page</u>
2-1 Major, trace and rare earth element data of granitoid xenoliths from the Grassrange. Major elements in wt. %, trace and rare earth elements in ppm ...	43
2-2 Major, trace and rare earth element data of schist and quartzite xenoliths from the Grassrange. Major elements in wt. %, trace and rare earth elements in ppm	45
2-3 Granitoid xenoliths, Grassrange, zircon LA-ICP-MS U-Pb data ²⁰⁷ Pb/ ²⁰⁶ Pb ages and Hf-isotope data reported (Ma)	47
2-4 Schist and quartzite xenoliths, Grassrange, zircon LA-ICP-MS U-Pb data ²⁰⁷ Pb/ ²⁰⁶ Pb ages and Hf-isotope data reported (Ma)	48
2-5 LA-ICP-MS Nd-isotope data reported (Ma)	49
3-1 Major, trace and rare earth element data of igneous protolith xenoliths from the Big Slide and Little Sand Creek diatremes. Major elements in wt. %, trace and rare earth elements in ppm	99
3-2 Major, trace and rare earth element data of xenoliths from Robinson Ranch Diatreme, the Bearpaw Mountains, and the Highwood Mountains. Major elements in wt. %, trace and rare earth elements in ppm	101
3-3 Igneous protolith xenoliths, Missouri Breaks, zircon LA-ICP-MS U-Pb data, ²⁰⁷ Pb/ ²⁰⁶ Pb ages and Hf-isotope data reported (Ma)	103
3-4 LA-ICP-MS Nd-isotope data reported (Ma)	104
4-1 Major, trace and rare earth element data of orthogneiss samples from the Little Rocky Mountains. Major elements in wt. %, trace and rare earth elements in ppm	157
4-2 Major, trace and rare earth element data of amphibolite samples from the Little Rocky Mountains. Major elements in wt. %, trace and rare earth elements in ppm	159
4-3 Major, trace and rare earth element data of schist samples from the Little Rocky Mountains. Major elements in wt. %, trace and rare earth elements in ppm	161
4-4 Major, trace and rare earth element data of paragneiss samples from the Little Rocky Mountains. Major elements in wt. %, trace and rare earth elements in ppm	163

4-5	Orthogneiss and amphibolite samples, Little Rocky Mountains, zircon LA-ICP-MS U-Pb data $^{207}\text{Pb}/^{206}\text{Pb}$ ages and Hf-isotope data reported (Ma).....	165
4-6	Schist and paragneiss samples, LRM, zircon LA-ICP-MS U-Pb data $^{207}\text{Pb}/^{206}\text{Pb}$ ages and Hf-isotope data reported (Ma)	166
4-7	Whole rock LA-ICP-MS Nd isotope data reported (Ma).....	167

LIST OF FIGURES

<u>Figure</u>	<u>page</u>
1-1 (A) Paleoproterozoic Laurentia (after Hoffman, 1988; Foster et al., 2006; Davidson, 2008) and a location map showing study area. (B) Generalized map of Precambrian basement provinces of southwestern Laurentia	23
1-2 Generalized depiction of Cenozoic alkaline rock occurrences in the Montana alkali province (after Hearn et al., 1989). The limits of the Great Falls tectonic zone (shown in pink) are not well defined and are based on.....	24
2-1 Generalized map of Precambrian basement provinces of southwestern Laurentia. Exposures of basement in Laramide-style uplifts are shown in the dark grey shaded areas.....	50
2-2 Generalized depiction of Cenozoic alkaline rock occurrences in the Montana alkali province (after Hearn et al., 1989). The limits of the Great Falls tectonic zone (shown in pink) are not well defined	51
2-3 Representative examples of photomicrographs of (A) granitic sample MX-08 in plain polarized light (PPL); (B) granitic sample MX-08 in cross polarized light (XPL); (C) schist sample HAL-1 in PPL; (D) schist sample HAL-1	52
2-4 Granitoid samples plotted on an alumina saturation index (Shand, 1943; modified by Frost et al., 2001). ~2.5 Ga granitoids (diamonds), ~1.7 Ga granitoids (squares).....	53
2-5 Plot of P_2O_5/TiO_2 vs. MgO/CaO (after Werner, 1987) proposed to discriminate magmatic vs. sedimentary protoliths for all meta-igneous granitoids and schistose samples.....	54
2-6 Compositional discriminant diagram showing the discriminant function 3 (DF3) vs. SiO_2 for all granitoid and schistose samples (after Shaw, 1972). Rocks with positive DF3 values are interpreted to be of igneous origin.....	55
2-7 Primitive-mantle normalized “spider” diagrams (McDonough and Sun, 1995) for (A) granitoid samples and (B) schistose samples, using data in Table 2-1 and 2-2. Relative enrichment of large ion lithophile elements	56
2-8 Chondrite normalized rare earth element diagram (McDonough and Sun, 1995) for granitoid samples using data in Table 2-1.....	57
2-9 Concordia diagrams showing U-Pb data for granitoid samples MX-08 (A) and MX-18 (B). Each ellipse represents a single spot analysis and its 2σ standard error	58

2-10	(A) Concordia diagrams plotting composite U-Pb data for granitoid sample MX-06. Each ellipse represents a single spot analysis and its 2 σ standard error. (B) Expanded view of lower end of concordia showing samples.....	59
2-11	(A) Concordia diagrams plotting composite U-Pb data for granitoid sample MX-09. Each ellipse represents a single spot analysis and its 2 σ standard error. (B) Expanded view of lower end of concordia showing samples.....	60
2-12	(A) Concordia diagrams plotting composite U-Pb data for granitoid sample MX-10. Each ellipse represents a single spot analysis and its 2 σ standard error. (B) Expanded view of lower end of concordia showing samples.....	61
2-13	(A) Concordia diagrams plotting composite U-Pb data for granitoid sample MX-11. Each ellipse represents a single spot analysis and its 2 σ standard error. (B) Expanded view of lower end of concordia showing samples.....	62
2-14	Probability density plots comparing the cumulative <10% discordant zircon analyses of (A) the 6 granitoid samples, 155 grains; (B) The 5 schist samples, 59 grains; (C) The 3 quartzite samples, 95 grains.....	63
2-15	Sm-Nd evolution diagram showing the range for the ~1.7 granitoids (gray stars), ~2.5 granitoids (white stars), Little Belt mountains (white bar), and the generalized evolution of northern Wyoming province crust	64
2-16	Histogram showing Sm-Nd depleted mantle model ages (Ga) of granitoid, schist, and quartzite whole rocks. Depleted Mantle model ages calculated using the model of DePaolo, 1981.....	65
2-17	Hf evolution diagram showing the range for the ~1.7 granitoids (circles), ~2.5 granitoids (diamonds), schistose (square), quartzite (triangle), and LBMs (black dashes) from ages 1.70 Ga to 1.89 Ga	66
2-18	Published Archean to earliest Proterozoic U-Pb ages of zircon from the northern Wyoming craton compared to published, ages for the MHB. OC – Owl Creek Mountains, BM - Bighorn Mountains	67
2-19	Trace element discrimination diagrams (after Pearce et al., 1984) for granitoid samples: (A) Heavy rare earth element Y ppm vs. high field strength element Nb ppm, (B) Heavy rare earth element Yb ppm.....	68
2-20	Comparison of published U-Pb ages from the southern Trans-Hudson Orogen against the northern Trans Hudson Orogen, Great Falls tectonic zone (this study), and Yavapai-Central Plains	69
3-1	Generalized map of Precambrian basement provinces of southwestern Laurentia (after Ross et al., 1991; Condie, 1992; Doughty et al., 1998; Vogl et al., 2004; Foster et al., 2006, 2012). Exposures of basement	105

3-2	Generalized depiction of Cenozoic alkaline rock occurrences in the Montana alkali province (after Hearn et al., 1989). The limits of the Great Falls tectonic zone (shown in pink) are not well defined	106
3-3	Photomicrographs of selected meta-igneous samples, with Plane Polarized light (PPL) images on the left, and Cross Polarized Light (XPL) images on the right. Scale bar is 1 mm. (A) Sample LD10-01, a garnet	107
3-4	Photomicrographs of selected meta-igneous samples, with Plane Polarized light (PPL) images on the left, and Cross Polarized Light (XPL) images on the right. Scale bar is 1 mm. (A) BSD10-05 is a mafic meta-granitoid.....	108
3-5	Xenolith samples plotted on an alumina saturation index (Shand, 1943; modified by Frost et al., 2001). Meta-igneous - blue diamonds	109
3-6	(A) Primitive-mantle normalized “spider” diagrams (McDonough and Sun, 1995) for meta-igneous samples. (B) Chondrite normalized REE diagram (McDonough and Sun, 1995) for meta-igneous samples	110
3-7	(A) Concordia diagram plotting composite U-Pb data for meta-granitoid sample BSD10-04. Each ellipse represents a single spot analysis and its 2 σ error. (B) Expanded view of lower end of concordia	111
3-8	Concordia diagram plotting composite U-Pb data for mafic meta-granitoid sample BSD10-05. Each ellipse represents a single spot analysis and its 2 σ error	112
3-9	Concordia diagram showing U-Pb upper intercept regression for amphibolite samples LSC10-03 (A) and LSC10-10 (B) as well as mafic granulitic gneiss LSC10-13 (C). Each ellipse represents a single spot analysis	113
3-10	(A) Concordia diagram plotting discordance \leq 10% U-Pb data for mafic gneiss sample LSC10-11. Each ellipse represents a single spot analysis and its 2 σ error. (B) Expanded view of concordia excluding xenocrystic.....	114
3-11	Concordia diagram showing U-Pb upper intercept regression for granitoid samples RRD10-05 (A) and RRD10-09 (B). Each ellipse represents a single spot analysis and its 2 σ error	115
3-12	(A) Concordia diagram plotting composite U-Pb data for garnet granulite sample RRD10-13. Each ellipse represents a single spot analysis and its 2 σ error. (B) Expanded view of upper end of concordia showing calculated	116
3-13	Concordia diagram plotting composite U-Pb discordia regression for orthogneiss sample LD10-07. Each ellipse represents a single spot analysis and its 2 σ error	117

3-14	(A) Concordia diagram plotting composite U-Pb data for orthogneiss sample LD10-08. Each ellipse represents a single spot analysis and its 2σ error. (B) Expanded view of lower end of concordia showing spread of samples	118
3-15	(A) Concordia diagram plotting composite U-Pb data for orthogneiss sample LD10-01. Each ellipse represents a single spot analysis and its 2σ error. (B) Expanded view of lower end of concordia showing spread of samples	119
3-16	Concordia diagram showing U-Pb upper intercept regression for quartz pegmatite sample LD10-11. Each ellipse represents a single spot analysis and its 2σ error	120
3-17	(A) Concordia diagrams plotting composite U-Pb data for orthogneiss sample HX-1. Each ellipse represents a single spot analysis and its 2σ error. (B) Expanded view of upper end of concordia showing samples	121
3-18	(A) Concordia diagram plotting composite U-Pb data for dioritic granulite sample RRD10-20. (B) Concordia diagram plotting composite U-Pb data for meta-granitoid sample LSC10-12. Each ellipse represents a single.....	122
3-19	Hf evolution diagram showing the granitoid and meta-igneous samples (blue diamonds) against the granitoid samples from the Grassrange (Chapter 2) (orange squares) and data from the Little Belt Mountains	123
3-20	(A) Probability density plot showing initial ϵ_{Hf} values for sample LD10-07. (B) Probability density plot showing Hf T_{DM} values for sample LD10-07. Met. – metamorphic zircons; Mag. – magmatic zircons.....	124
3-21	Sm-Nd evolution diagram showing the meta-igneous samples (blue diamonds), Little Belt Mountains (green bar), and four different northern Wyoming province crustal outcrops (all citations are in the text)	125
3-22	Histogram showing Sm-Nd depleted mantle model ages (Ga) of meta-igneous whole rocks. T_{DM} calculated using the model of DePaolo, 1981	126
3-23	Trace element discrimination diagrams (after Pearce et al., 1984) for meta-igneous samples (blue diamonds): (A) Heavy rare earth element Y (ppm) vs. high field strength element Nb (ppm), (B) Heavy rare earth element Yb	127
3-24	Published Archean to earliest Paleoproterozoic U-Pb ages of zircon from the northern Wyoming craton (red bars) compared to published ages for the MHB (blue bars) (all citations are in the text). OC – Owl Creek Mountains	128
3-25	Comparison of published U-Pb ages from the southern Trans-Hudson Orogen (all citations are in the text) against the northern Trans Hudson Orogen, Great Falls tectonic zone (Chapter 2 and this study), and.....	129

4-1	Generalized map of Precambrian basement provinces of southwestern Laurentia (after Ross et al., 1991; Condie, 1992; Doughty et al., 1998; Vogl et al., 2004; Foster et al., 2006, 2012). Exposures of basement	168
4-2	Location of the Little Rocky Mountains relative to a generalized depiction of Cenozoic alkaline rock occurrences in the Montana alkali province (after Hearn et al., 1989). The limits of the Great Falls tectonic zone	169
4-3	Map of the Little Rocky Mountains (after Hearn et al., 1989). Sample locations are shown as yellow stars	170
4-4	Photomicrographs of selected meta-plutonic samples from the Little Rocky Mountains. Mineral abbreviations are after Whitney and Evans (2010). Plane light (PPL) micrographs are on the left	171
4-5	Photomicrographs of selected meta-supracrustal samples from the Little Rocky Mountains. Mineral abbreviations are after Whitney and Evans (2010). PPL micrographs are on the left, and XPL micrographs	172
4-6	Schist, orthogneiss and paragneiss samples plotted on an alumina saturation index (Shand, 1943; modified by Frost et al., 2001). Schists (green triangles), orthogneisses (blue diamonds), and paragneisses.....	173
4-7	Ternary CaO-MgO-Al ₂ O ₃ variation diagram showing the expected fields of meta-igneous and meta-sedimentary rocks for all schists (circles) and paragneisses (squares) (after Leyreloup et al., 1977)	174
4-8	Primitive-mantle normalized “spider” diagrams (McDonough and Sun, 1995) for (A) orthogneiss and amphibolite samples and (B) detrital schistose and paragneiss samples. Relative enrichment of large ion lithophile	175
4-9	Chondrite normalized diagram (McDonough and Sun, 1995) for orthogneiss and amphibolite samples using data from Tables 4-1 and 4-2. Orthogneiss samples show elevated concentrations of light versus	176
4-10	Concordia diagrams showing U-Pb data showing spread of zircons and weighted mean age for orthogneiss samples MLR-01 (A) and MLR-06 (B). Each ellipse represents a single spot analysis and its 2 σ error	177
4-11	Concordia diagrams showing U-Pb data for orthogneiss samples MLR-15 (A) and MLR-19 (B). Each ellipse represents a single spot analysis and its 2 σ error.....	178
4-12	(A) Concordia diagrams plotting composite U-Pb data for orthogneiss sample LRM-3. Each ellipse represents a single spot analysis and its 2 σ error. (B) Expanded view of upper end of concordia showing the oldest, most	179

4-13	Concordia diagram showing U-Pb data for orthogneiss sample LRM-5. Each ellipse represents a single spot analysis and its 2σ error	180
4-14	Concordia diagram showing U-Pb data for orthogneiss sample LRM-7. Each ellipse represents a single spot analysis and its 2σ error	181
4-15	(A) Concordia diagrams plotting composite U-Pb data for orthogneiss sample MLR-09. Red dashed lines indicate trends within the analyses. (B) Expanded view of upper end of concordia showing the oldest	182
4-16	(A) Concordia diagrams plotting composite U-Pb data for amphibolite sample MLR-03. Red dashed lines indicate trends within the analyses. (B) Expanded view of upper end of concordia showing the oldest	183
4-17	Probability density plots comparing the $\leq 10\%$ discordant detrital zircon analyses of the schist and paragneiss samples. Orthogneiss ages are included for comparison	184
4-18	(A) Lu-Hf evolution diagram showing the range for the orthogneiss (blue diamond), amphibolites (orange circle), schistose (green triangle), and paragneisses (red square). (B) Sm-Nd evolution diagram.....	185
4-19	Published Archean to earliest Proterozoic U-Pb ages of zircon from the northern Wyoming craton (citations in the text) compared to published, ages for the MHB (citations in text). Wyoming – yellow bars.....	186
5-1	Schematic evolution of the Great Falls tectonic zone based on geologic constraints and chronology. (A) map-view: ocean subduction between the Wyoming province (WP) and the Medicine Hat Block (MHB)	194

LIST OF OBJECTS

<u>Object</u>	<u>page</u>
B-1 External supplemental data tables.....	198

LIST OF ABBREVIATIONS

BDL	Below detection limit
BSE	Bulk silicate earth
BTM	Beartooth Mountains
CCBULK	Bulk continental crust
CHUR	Chondritic uniform reservoir
DM	Depleted mantle
GFTZ	Great Falls tectonic zone
HFSE	High field strength element
HREE	Heavy rare earth element
LBM	Little Belt Mountains
LIL	Large ion lithophile
LOI	Loss on ignition
LRM	Little Rocky Mountains
MHB	Medicine-Hat Block
MR	Madison Range
MSWD	Mean standard weighted deviates
N/A	Not applicable
PM	Primitive mantle
PPM	Parts per million
REE	Rare earth elements
THO	Trans-Hudson Orogeny
TR	Teton Range
TRM	Tobacco Root Mountains
WT. %	Weight percent

Abstract of Dissertation Presented to the Graduate School
of the University of Florida in Partial Fulfillment of the
Requirements for the Degree of Doctor of Philosophy

PRECAMBRIAN CRUSTAL EVOLUTION IN THE GREAT FALLS TECTONIC ZONE

By

Jennifer N. Gifford

May 2013

Chair: David A. Foster
Cochair: Paul A. Mueller
Major: Geological Sciences

The Great Falls Tectonic Zone (GFTZ) is a zone of northeast trending geological structures in central Montana that parallel structures in the underlying basement. U-Pb zircon and Nd isotopic data from the Little Belt Mountains (LBM) suggest that the GFTZ formed at ~1.86 to 1.80 Ga due to ocean subduction followed by collision between the Archean Wyoming Province (WP) and Medicine Hat Block (MHB). This study characterizes the GFTZ basement by geochronological and geochemical analysis of crustal xenoliths collected from Montana Alkali Province volcanics and exposed basement rock in the Little Rocky Mountains (LRM).

Xenoliths collected from the Grassrange and Missouri Breaks diatremes and volcanics in the Bearpaw and Highwood Mountains have igneous crystallization ages from ~1.7 Ga to 1.9 Ga and 2.4 Ga to 2.7 Ga, and metamorphic ages from ~1.65 Ga to 1.84 Ga. Zircon Lu-Hf and whole-rock Sm-Nd data indicate that the xenoliths originated from reworked older continental crust mixed with mantle-derived components in all cases. Trace element patterns show fluid mobile element enrichments and fluid immobile element depletions suggestive of a subduction origin. Igneous ages in the

LRM range older, from ~2.4 Ga to 3.2 Ga. Geochemical evidence suggests that the LRM meta-igneous units also formed in a subduction setting. Detrital zircon ages span the early Paleoproterozoic to Mesoarchean, with abundant 2.8 Ga ages.

Zircon U-Pb igneous crystallization age data from xenoliths and the LRM are consistent with U-Pb zircon igneous crystallization ages from the MHB, suggesting that this segment of the GFTZ shares an affinity with concealed MHB crust. Published detrital zircon ages from the northern Wyoming Province reveal more abundant >3.0 Ga ages than the MHB or GFTZ samples. These geochronologic and geochemical data from the xenoliths and LRM samples allow for a refined model for crustal evolution in the GFTZ. Subduction under the Neoarchean to Paleoproterozoic crust of the MHB formed an igneous arc followed by metamorphism during the MHB-WP collision. Later Paleoproterozoic tectonothermal activity represents post-orogenic collapse after the terminal collision. Tectonic activity in the Cenozoic led to basement uplift and the formation of xenolith bearing volcanic units sampled for this study.

CHAPTER 1 INTRODUCTION

Archean North America is formed by the amalgamation of the Slave, Rae, Hearne, Nain, Superior, Wyoming, and Medicine Hat Block provinces. These areas of old, stable lithosphere are termed cratons, which represent proto-continents which assembled over Earth history into the continents. Ancestral North America, known as Laurentia, includes numerous crustal blocks with independent histories prior to this assembly. These blocks include the Slave, Rae and Hearne provinces of north-central Canada, the Superior province, the Nain province of eastern Canada, and the Wyoming province in Wyoming and Montana. In addition to the large variably exposed cratons, are smaller Archean tectonic elements. Many of these elements, such as the Sask Craton and Medicine Hat Block are concealed beneath younger sedimentary sequences. Laurentia also includes a series of Paleoproterozoic orogenic belts that represent the collisions between these cratons during continental assembly. The various provinces contain Early Proterozoic reactivation which appears to be related in trend and intensity to the orogenic belts and suture zones that frame them (Hoffman, 1988). The orogenic belts and suture zones range in age from ~2.0 Ga (Thelon orogeny suturing the Slave and Rae cratons) (van Breemen et al., 1987; Tirrul and Grotzinger, 2010) to ~1.6 Ga (accretion of the Mazatzal terrane onto the Wyoming Province) (Karlstrom and Bowring, 1987). Hoffman (1988) concluded that Laurentia essentially accreted within the span of only 150 million years.

The Wyoming Province is one of the oldest cratons in Laurentia (e.g., Wooden and Mueller, 1988; Baird et al., 1996; Frost et al., 1998; Henstock et al., 1998; Foster et al., 2006; Mueller and Frost, 2006). The craton is surrounded on all sides by

Proterozoic suture zones and orogenic belts resulting from continental margin accretion and collisions with other Archean cratons (e.g., Superior-Wyoming collision at 1.71–1.77 Ga; Nelson et al., 1993; Dahl et al., 1999), or with Proterozoic terranes (e.g., Colorado province at 1.78 Ga; Karlstrom and Houston, 1984; Chamberlain, 1998) (Figure 1-1). Northwest of the Wyoming craton are the Great Falls tectonic zone (GFTZ) and the Medicine Hat block (MHB), which are largely defined by aeromagnetic, xenolith, and borehole data (Figure 1-1) (Ross et al., 1991; Pilkington et al., 1992; Villeneuve et al., 1993; Baird et al., 1996; Gorman et al., 2002; Sims et al., 2004). The Great Falls tectonic zone strikes northeast to southwest between the Archean Wyoming Province to the south, and the Archean Medicine Hat Block to the north (Figure 1-1). Because the GFTZ is primarily covered by Phanerozoic sedimentary rocks, interpretations of the origin and evolution of this zone vary widely. O'Neill and Lopez (1985) first described the GFTZ as a Paleoproterozoic suture, which has since been supported by geochronologic and geochemical data from Mueller et al. (2002) from gneisses of the Little Belt Mountains that revealed a subduction-generated igneous arc signature in rocks formed during the time interval of 1.9 Ga to 1.8 Ga. Roberts et al. (2002) also supported the ocean-subduction hypothesis based on $^{40}\text{Ar}/^{39}\text{Ar}$ analyses on biotite and $^{207}\text{Pb}/^{206}\text{Pb}$ step-leach analyses on garnet from the Montana Metasedimentary Province (MMP). Garnets revealed a metamorphic event between 1.82 and 1.79 Ga, followed by post-tectonic cooling between 1.78 to 1.74 Ga (biotite) (Roberts et al., 2002), which was related to continental collision between Wyoming and the MHB along the GFTZ. Alternatively, Boerner et al. (1998) suggested that the GFTZ is an intra-continental shear zone and that the MHB and Wyoming cratons are contiguous units. They

propose that the subsurface Vulcan Structure represents the Hearne-Wyoming suture and that based on potential field maps (Ross, 1991), the Deep Probe seismic experiment, Southern Alberta Refraction Experiment (SAREX) (Henstock et al, 1998), and electromagnetic studies (Boerner et al., 1998) the lithosphere is continuous throughout the GFTZ. This continuity would then link the geologic histories of the northern Wyoming Province and the MHB (e.g., Buhlman et al., 2000; Boerner et al., 1998).

This dissertation addresses the nature of the Great Falls Tectonic zone crust, as well as characterizing GFTZ crust to evaluate possible links to the Wyoming Craton and/or Medicine Hat Block. Several specific objectives to address these issues include: 1) establish the age of crustal units, 2) identify the origins of the sampled crust in terms of plate tectonic settings, 3) examination of the relationships between timing and nature of crustal generation of GFTZ crust to test tectonic models of the zone's origin. This will be accomplished over three chapters, focused on the GFTZ segment in north-central Montana.

Chapters Two and Three utilize crustal xenoliths entrained in magmas and ejected to the surface by Cenozoic magmatism throughout the Montana Alkali Province. These afford a unique opportunity to characterize the age and chemistry of the concealed crust of the GFTZ. Xenoliths are some of the only direct samples of the crystalline basement in central Montana. Chapter Two examines a crustal xenolith suite collected from the Grassrange diatremes (Figure 1-2) of central Montana. Data generated by this study reveals major tectonic events at c. 2.5 Ga and c. 1.75 Ga, related to subduction zone processes. Chapter Three focuses on a sample suite

collected further north, from the Missouri Breaks diatremes and lavas in the Bearpaw and Highwood Mountains (Figure 1-2). Abundant evidence of c. 2.5 - 2.6 Ga tectonic activity is preserved, as well as events at c. 1.75 - 1.89 Ga. Chapter Four examines the Precambrian rock exposed in the Little Rocky Mountains (Figure 1-2). This domal uplift exposes some of the only crystalline basement of the MHB and provides a unique sampling opportunity. The rocks are dominantly Neoproterozoic, with both igneous ages and detrital zircon ages consistent with a Medicine Hat Block affinity.

Through the study of basement exposures from the Little Belt and Little Rocky Mountains, as well as through crustal xenoliths from seven locations across the Great Falls tectonic zone, this dissertation seeks to further define evolution of the GFTZ and the timing of ocean closure and collision between the Wyoming Province and the MHB as well as further characterize the age and composition of the crust beneath central Montana. Further, this study provides evidence on the extent of Archean basement in north-central Montana, and suggests that the Archean basement therein is related to the MHB.

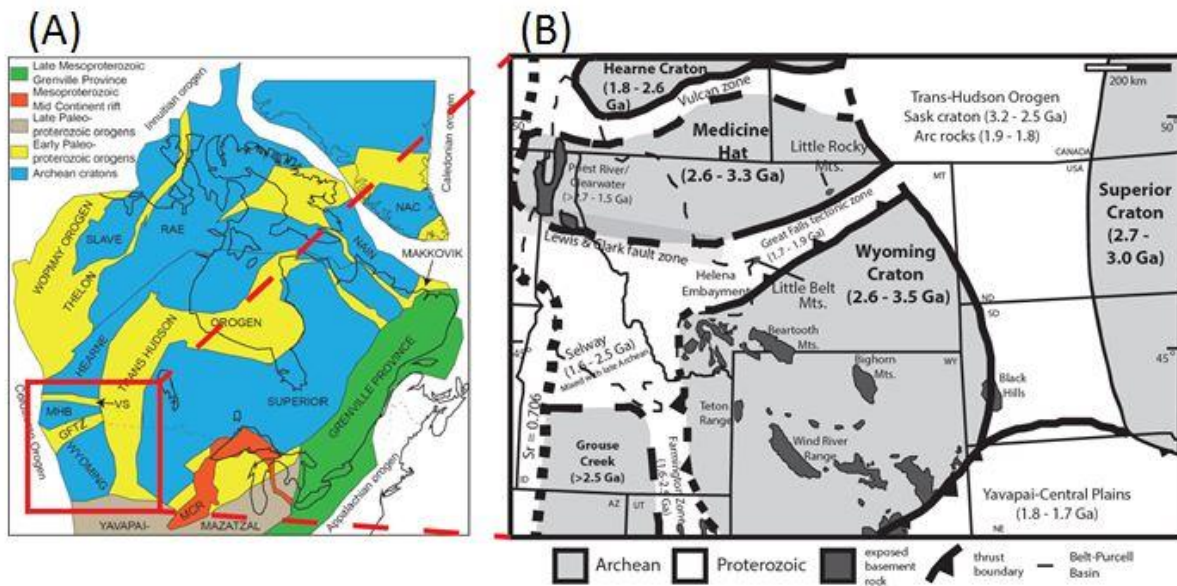


Figure 1-1. (A) Paleoproterozoic Laurentia (after Hoffman, 1988; Foster et al., 2006; Davidson, 2008) and a location map showing study area. (B) Generalized map of Precambrian basement provinces of southwestern Laurentia (after Ross et al., 1991; Condie, 1992; Doughty et al., 1998; Vogl et al., 2004; Foster et al., 2006, 2012). Exposures of basement in Laramide-style uplifts are shown in the dark grey shaded areas.

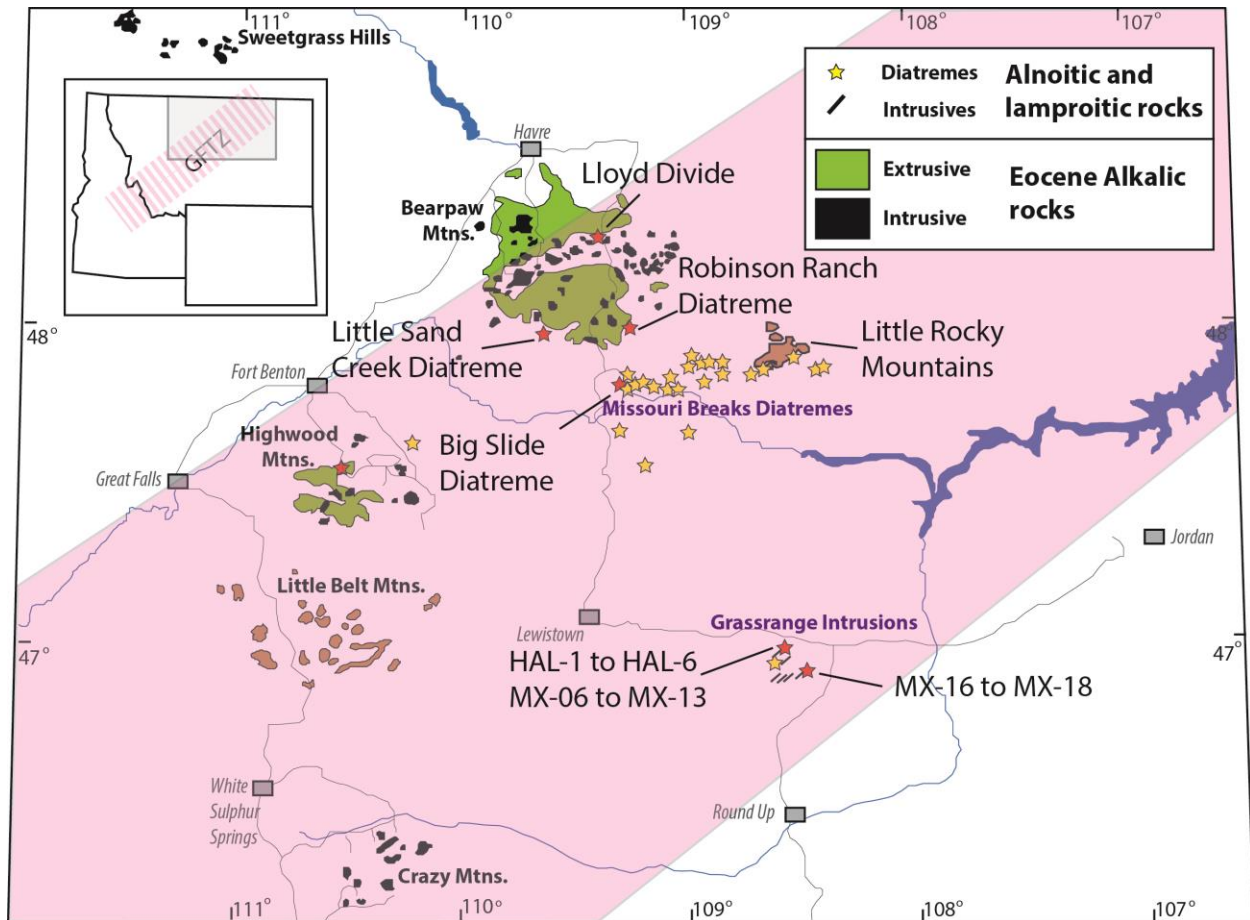


Figure 1-2. Generalized depiction of Cenozoic alkaline rock occurrences in the Montana alkali province (after Hearn et al., 1989). The limits of the Great Falls tectonic zone (shown in pink) are not well defined and are based on aeromagnetic data from Sims et al., 2004.

CHAPTER 2 GRASSRANGE XENOLITHS

Introduction

The Archean Wyoming Province is a geophysically and geochemically distinct entity within the North American continent surrounded by Paleoproterozoic orogenic belts (e.g., Wooden and Mueller, 1988; Baird et al., 1996; Frost et al., 1998; Henstock et al., 1998; Mueller and Frost, 2006). The surrounding Proterozoic orogenic zones resulted from collisions with Paleoproterozoic terranes (e.g., Colorado province at 1.78 Ga; Karlstrom and Houston, 1984; Chamberlain, 1998) or other Archean cratons (e.g., Superior-Wyoming collision at 1.71 to 1.77 Ga; Nelson et al., 1993; Dahl et al., 1999) (Figure 2-1). There is significant uncertainty regarding the 700 km wide zone of Archean and Paleoproterozoic tectonic elements that separate the Wyoming Craton from the Hearne Province. This zone includes features identified from geophysical surveys, borehole data (Villeneuve et al., 1993), and limited xenoliths (Davis et al., 1995; Gorman et al., 2002). These are from north to south in Figure 2-1: the E-W trending Vulcan structure (Eaton et al., 1999), the Archean Medicine Hat Block (e.g., Lemieux et al., 2000), and the c. 1.7 to 1.9 Ga Great Falls Tectonic Zone (O'Neill and Lopez, 1985; Mueller et al., 2002; Mueller et al., 2005; Foster et al., 2006).

The Great Falls Tectonic Zone (GFTZ) strikes southwest to northeast between the Archean Wyoming Craton to the south and the Archean Medicine Hat block to the north and is largely covered by Phanerozoic sedimentary rocks. Consequently, interpretations of the origin and evolution of this zone vary widely. O'Neill and Lopez (1985) identified the GFTZ and suggested that it formed a Paleoproterozoic suture zone between the Archean Medicine Hat and Wyoming cratons. Geochronologic and

geochemical data (Mueller et al., 2002) provide additional support for this hypothesis, revealing a subduction-generated igneous arc signature in rocks formed during the time interval of 1.9 Ga to 1.8 Ga in the Little Belt Mountains. An alternative hypothesis views the Medicine Hat and Wyoming cratons as contiguous units separated by an intra-continental shear zone (GFTZ) reactivated by involvement with the Paleoproterozoic Trans-Hudson Orogeny (THO), with the Hearne-Wyoming suture proposed to be the subsurface Vulcan Structure (Ross, 1991; Henstock et al. 1998; Boerner et al., 1998). These geophysically based models propose a continuity of lithosphere across the GFTZ, thereby linking the histories of the northern Wyoming Province and the Medicine Hat block (MHB) (e.g., Buhlman et al., 2000; Boerner et al., 1998).

Crustal xenoliths were ejected to the surface by Cenozoic magmatism in the Montana Alkali Province within the GFTZ from the Bearpaw Mountains, Missouri Breaks diatremes, and Grassrange diatremes (Figure 2-2). These xenoliths provide samples that can be used to obtain both age and compositional information for the crystalline basement in the GFTZ. We report U/Pb ages and Hf isotopic data from zircon, as well as whole-rock geochemical and isotopic data, from a suite of crustal xenoliths from the Eocene Grassrange intrusions (~50 Ma) of central Montana. These data give insight into the range of rock compositions and ages in the Great Falls tectonic zone and provide strong evidence that the GFTZ is a suture zone between the MHB and Wyoming craton.

Geologic Background

Extensive Phanerozoic sedimentary cover conceals much of the Precambrian geology of the GFTZ. The Little Belt Mountains (LBM) of Central Montana are a basement-cored foreland structure of the Rocky Mountains intruded by Tertiary stocks

(Kleinkopf et al., 1972; Marvin et al., 1973) and contain the most extensive outcrops of Proterozoic rocks in the GFTZ (Figure 2-2). The Little Belt Mountain exposures include Paleoproterozoic dioritic orthogneisses and minor magmatic paragneisses (Pirsson, 1900; Weed, 1900; Vogl et al., 2003). The gneissic fabric predominantly strikes east-west and dips variably from north to south (Holm and Schneider, 2002; Vogl et al., 2003). The dioritic gneisses and migmatites are intruded by amphibolite dikes, pegmatites, and post-tectonic leucogranite (Vogl et al., 2003). Mueller et al. (2002) obtained an U-Pb zircon age on the Pinto diorite of 1.86 Ga; other gneissic units yield U-Pb zircon ages ranging from 1.88-1.86 Ga (Mueller et al., 2002). Vogl et al. (2003) and Foster et al. (2006) give U-Pb zircon ages of other 1.79-1.86 Ga dioritic gneisses, amphibolites and granitoids from the LBM exposures. Dahl et al. (2000) present U-Pb data for monazite from a metapelite in the LBM, which yielded an age of 1.86 Ga. Holm and Schneider (2002) presented nine $^{40}\text{Ar}/^{39}\text{Ar}$ ages from the LBM; six biotite separates yielded ages ranging from 1.81 Ga to 1.77 Ga, and three hornblende samples yielded a range of 1.80 Ga to 1.78 Ga. These $^{40}\text{Ar}/^{39}\text{Ar}$ ages record cooling after the last tectonothermal activity in the LBM part of the GFTZ.

Results

U-Pb and Lu-Hf data from igneous and detrital zircons in addition to whole-rock geochemical and isotopic data from xenoliths collected from two Eocene diatremes in the Grassrange, Montana are presented below. Sample locations are shown in Figure 2-2. Geochemical and isotopic data and the latitude and longitude of the two sample locations are summarized in Tables B-1 through B-4 (Appendix B).

Whole-Rock Geochemistry

Xenoliths were divided into three categories on the basis of hand-sample and thin section petrography, and major element geochemistry: granitic orthogneiss, quartzite/sandstone, and schist (Table 2-1 and 2-2). Representative photomicrographs for each group are shown in Figure 2-3. Granitic gneisses range in texture from hypidiomorphic granular to moderately foliated. They all contain blocky grains of microcline (>4mm), quartz, and minor biotite. Plagioclase is often sericitized (Figure 2-3A, B); rare titanite and zircon grains are also present. The granitoid samples have silica contents ranging from 73 to 77 wt. %. Sample MX-11 has a silica content of 80 wt. % suggesting silicification, because its trace element ratios are consistent with those of the lower silica samples (see below). Collectively, the granitic samples cluster along the metaluminous – peraluminous boundary (Figure 2-4) when plotted according to the alumina saturation index of Shand (1943).

The second and third groups consist of five biotite schists and three quartzites/sandstones respectively. Schists are characterized by equigranular quartz, plagioclase, and K-feldspars in all of the samples (ranging from 25 – 30% each) with clots of muscovite inter-grown with sillimanite. Biotite defines a foliation along with accessory muscovite (Figure 2-3C, D). The protolith(s) of these schists may be sedimentary, volcanoclastic, and/or volcanic based on major element compositions (60 to 82% SiO₂). Abundances of Al₂O₃ are relatively low (9.1 to 13.6 wt. %), but alkali contents are sufficiently high that their normative mineralogy contains 2 to 9% corundum. The third group consists of three un-foliated biotite quartzites or sandstones. Quartz grains range from sub- to well-rounded, and some show clear euhedral authogenic overgrowths (Figure 2-3E, F). Visual estimates of other phases found within

the quartzites/sandstones include plentiful biotite, oxides, and trace amounts of muscovite and feldspars. The metamorphic grade of the quartzites is therefore lower than the schists.

Petrographic discrimination between sedimentary, volcanoclastic, and/or volcanic origins for the schists is difficult; however, variations of Ca, Mg, and Al concentrations provide some insight into their origins. Using the P_2O_5/TiO_2 versus MgO/CaO plot of Werner (1987) to distinguish magmatic from sedimentary rocks indicates a likely sedimentary origin for most samples (Figure 2-5). Shaw (1972) used a discriminant function with the equation: $DF3 = 10.44 - 0.21SiO_2 - 0.32Fe_2O_3t - 0.98MgO + 0.55CaO + 1.46Na_2O + 0.54K_2O$ to distinguish igneous versus sedimentary protoliths; igneous rocks have a positive DF3 value, and sedimentary rocks have a negative value (Figure 2-6). Among the schistose samples, one lies within the igneous field, while the remaining four are within the sedimentary field of Werner (1987) (Figure 2-5). In the Shaw (1972) diagram (Figure 2-6), one sample also plots within the igneous field and the remaining four within the sedimentary field. Although most of the schistose samples have compositional characteristics that indicate a sedimentary protolith, these discriminants are not sufficiently accurate to exclude a volcanoclastic component.

Trace element geochemistry (Table 2-1) of the granitoid orthogneiss xenoliths is summarized in Figure 2-7A, normalized relative to primitive mantle values of McDonough and Sun (1995). The trace element patterns of the granitoid samples are compared to the 5 schist samples in Figure 2-7B. The plots show general enrichments in fluid mobile incompatible elements, such as Rb, Ba, and Pb, up to 600 times the primitive mantle values. This relative enrichment is paired with minimal enrichment in

fluid immobile trace elements, including heavy REE (Figure 2-8). The majority of samples show lower values of Eu, Sr, and Ti relative to elements of similar compatibility. One sample, MX-18, lacks a Eu anomaly; however, it shares the Sr and Ti anomalies of the other samples. Nb and Ta are depleted relative to the observed values for neighboring elements in all of the granitic samples when normalized to primitive mantle

U-Pb Geochronology In Zircon

Meta-granitoid samples MX-06, MX-08, MX-09, MX-10, MX-11, and MX-18 were large enough for whole rock geochemistry and zircon separation (~10 to 20 cm diameter). Individual zircon $^{207}\text{Pb}/^{206}\text{Pb}$ ages from 153 grains (<10% discordance) from these samples reveal a wide spread, from 1.72 Ga to 2.55 Ga, despite their relatively uniform elemental compositions (Table 2-2). Two samples, MX-08 and MX-18, give Paleoproterozoic crystallization ages of 1.73 ± 0.01 Ga (Figure 2-9A) and 1.74 ± 0.01 Ga (Figure 2-9B) respectively, without inherited zircons. Zircons from the remaining four granitic samples reveal two distinct populations of $^{207}\text{Pb}/^{206}\text{Pb}$ ages, which are separated by > 500 Ma and do not overlap at the 2σ level, but do lie along a discordia. Younger ages (lower intercepts) range from 1.76 ± 0.02 Ga to 1.87 ± 0.02 Ga (Table 2-2) and represent 30% of all grains <10% discordant. Ages in the older population (upper intercepts) range from 2.46 ± 0.16 Ga to 2.53 ± 0.01 Ga and represent 17% of the <10% discordant grains. The remaining data yield intermediate ages that lie along a mixing line (discordia) between the older and younger ages, and constitute more than half of the analyses for each sample (Figure 2-10 to 2-13).

Two groups of metasedimentary samples were processed for detrital zircon analysis. The biotite schist samples MX-13, HAL-1, HAL-2, HAL-5, and HAL-6 yielded zircons ranging from sub-rounded to well-rounded. In aggregate, $^{207}\text{Pb}/^{206}\text{Pb}$ ages from

59 zircons <10% discordant range from ~1.75 Ga to ~3.06 Ga (Table 2-3), with prominent age peaks at ~1.86 Ga (42% of the grains, from 1.82 to 1.90 Ga) and ~2.69 Ga (15% of the grains, from 2.63 to 2.71 Ga) (Figure 2-14). The three quartzite/sandstone samples (MX-12, MX-16, MX-17) yielded ninety-five zircons <10% discordant with ages ranging from ~1.02 Ga to ~2.85 Ga (Table 2-3). The most prominent age peaks are illustrated in Figure 2-14, and lie at ~1.87 Ga (51% of the total, from 1.81-1.92 Ga), ~2.60 Ga (7% of the total, from 2.57 to 2.61 Ga), and ~2.68 Ga (8% of the total, from 2.67 to 2.72 Ga). Figure 2-14 shows a probability distribution function comparing detrital zircon age spectra from the schists and the quartzites/sandstones; data from the granitic samples are provided for comparison.

Hf Isotopes In Zircon

Zircons were chosen for Lu-Hf analysis based on their U-Pb age (and discordance), zonation patterns, and grain size. Granitoid xenoliths MX-06, MX-09, MX-10, and MX-11 yielded upper intercept crystallization U-Pb ages of 2.46 Ga to 2.53 Ga. For these samples, ϵHf at the estimated time of protolith crystallization ($\epsilon\text{Hf}_{(T)}$, ~2.5 Ga) was calculated for each zircon regardless of their apparent age in order to evaluate the extent to which “new” Hf was added to the grains defining the discordia and lower intercept. Zircon $\epsilon\text{Hf}_{(2.5 \text{ Ga})}$ for these samples ranged from 3.0 to -6.7 (Table 2-2). When the initial ϵHf is calculated for the individual age (IA) of each analyzed grain (1.8 to 2.5 Ga) within each ~2.5 Ga granitoid, the initial ϵHf values ranged from 2.3 to -20.2 (Table 2-2). These differences likely reflect variable input of juvenile versus evolved materials in the genesis of the parental magma over the course of zircon crystallization. As suggested by the reduced ranges of $\epsilon\text{Hf}_{2.5}$, averages for each sample ranged from -1.1 to -4.3, with standard deviations of 1.8 to 0.8. The more coherent Hf isotopic

compositions calculated at ~2.5 Ga suggest that the younger ages reflect Pb-loss and that the Lu-Hf system remained largely closed during metamorphism. These samples give a limited range of depleted mantle model ages (T_{DM}) from 2.85 Ga to 2.93 Ga (Table 2-2). For the Paleoproterozoic samples (MX-08 and MX-18) the measured Hf isotopic compositions for all zircons were recalculated to the U-Pb crystallization ages of 1.73 Ga and 1.74 Ga respectively. The $\epsilon Hf_{(1.7 Ga)}$ for <10% discordant zircons from the samples range from -4.7 to -12.0 for MX-08 with an average of -10.0 and a standard deviation of 1.4. MX-18 ranges from -7.4 to -15.0 with an average of -11.6 and a standard deviation of 2.1 (Table 2-2). Average Hf $T_{(DM)}$ model ages for samples MX-08 and MX-18 were calculated to be 2.51 Ga and 2.58 Ga respectively. As with the older grains, calculating the initial Hf compositions using the upper intercept ages ($\epsilon Hf_{(T)}$) yields more coherent estimates of initial Hf compositions than using the $^{207}Pb/^{206}Pb$ age of each zircon ($\epsilon Hf_{(IA)}$), i.e., the discordant ages represent Pb-loss rather than extraneous grains. The Hf T_{DM} ages represent minimum mantle separation ages because Lu/Hf in zircon is invariably lower than in whole-rocks (e.g., Griffin et al., 2002). Calculation of secondary or crustal residence ages, however, require knowledge of the Lu/Hf of source(s) and were not calculated because the data ultimately suggest a mixing of crustal and mantle sources at ~1.7 Ga.

Only 3 of the 5 schist samples yielded zircons large enough for U-Pb and Lu-Hf isotopic analysis. Initial Hf isotopic compositions were calculated using the $^{207}Pb/^{206}Pb$ of each individual zircon. MX-13, HAL-2, and HAL-5 have initial ϵHf values for the <10% discordant grains that ranged from 2.8 to -9.9, 6.8 to -11.4 and 9.9 to -11.1, respectively (Table 2-3). MX-13 has Hf $T_{(DM)}$ model ages ranging from 2.13 Ga to 2.80

Ga while HAL-2 and HAL-5 have Hf $T_{(DM)}$ model ages ranging from 1.98 Ga to 2.87 Ga and 1.85 Ga to 3.15 Ga, respectively (Table 2-3). Hf isotopes were also measured in zircons from quartzite/sandstone samples MX-12, MX-16, and MX-17, which yielded a range of initial ϵ_{Hf} values from 5.8 to -14.4, 3.7 to -11.7, and 6.8 to -9.5, respectively (Table 2-3). The calculated Hf $T_{(DM)}$ model ages range from 1.61 Ga to 3.03 Ga for MX-12, 2.13 Ga to 2.99 Ga for MX-16, and 1.95 Ga to 2.99 Ga for MX-17 (Table 2-3).

Sm-Nd Whole-Rock Isotopes

As a group, the granitic xenoliths show a range in $\epsilon_{Nd(0)}$ from -26.5 to -34.4. Initial ratios were calculated using the best estimates of the individual crystallization ages ($^{207}Pb/^{206}Pb$ ages 2.46 Ga to 2.53 Ga) shown in Figures 2-10 to 2-13, and values for samples MX-08 and MX-18 were calculated using the $^{207}Pb/^{206}Pb$ ages shown in Figure 2-9 (i.e., 1.73 Ga and 1.74 Ga)). This yielded $\epsilon_{Nd(2.5 Ga)}$ of 3.2 to -1.2 (Table 2-4, Figure 2-15), and $\epsilon_{Nd(1.7 Ga)}$ of -6.0 and -6.5 (Table 2-4, Figure 2-15). Depleted mantle model ages for granitoid samples MX-06, MX-09, MX-10, and MX-11 were calculated using the model of DePaolo (1981) and ranged from 2.50 Ga to 2.79 Ga (Figure 2-16). Granitic samples MX-08 and MX-18 yielded depleted mantle model ages (calculated at ~1.7 Ga; DePaolo, 1981) of 2.47 Ga and 2.51 Ga (Table 2-4) respectively, overlapping with the ~2.5 Ga granitoids. The initial ϵ_{Nd} values are shown with initial ϵ_{Nd} values for orthogneisses from the Little Belt Mountains (Mueller et al., 2002) and with an estimated evolution path of ϵ_{Nd} for northern Wyoming province crust (Wooden and Mueller, 1988; Mueller et al., 1993; Frost, 1993; Mueller et al., 2010). Isotopically, the granitic $\epsilon_{Nd(2.5 Ga)}$ values are intermediate between 2.5 Ga depleted mantle and typical northern Wyoming province crust, suggesting involvement of both crustal and mantle sources. The five schist samples show a range in $\epsilon_{Nd(0)}$ values from -24.1 to -24.8, and depleted

mantle model ages ranging from 2.35 Ga to 2.57 Ga (Table 2-4). The three quartzite samples show a range in $\epsilon\text{Nd}_{(0)}$ values from -13.7 to -23.8, and depleted mantle model ages ranging from 1.84 Ga to 2.42 Ga (Table 2-4).

Discussion

Origins Of The Granitic Xenoliths

Zircon U-Pb age-data show that the granitic xenoliths fall into two distinct ranges in terms of their crystallization ages, 2.46 Ga to 2.53 Ga for four of the six meta-granitoids, and younger ages of 1.73 Ga and 1.74 Ga for the other two. The coherence of initial Hf isotopic data calculated at the proposed crystallization ages suggest these ages are robust and that the younger ages in each sample reflect loss of radiogenic Pb much more so than formation of new zircon with Hf from a higher Lu/Hf source (e.g., whole rock). The spread of sample data through the metaluminous and peraluminous fields (Figure 2-4) is not particularly diagnostic, but is similar to granitic suites from continental arc and continental collision granitoids (e.g. Mainar and Piccoli, 1989; Rogers and Hawkesworth, 1989; Chappell and White, 2001; Villaseca et al., 2012). These xenoliths share relatively similar normalized trace element patterns that are consistent with those found in typical modern convergent margin igneous rocks (Figure 2-7A, Pearce, 1983). The ~2.5 Ga granitoid orthogneiss samples have negative Eu and Sr anomalies (Figure 2-8), which typically represent fractional crystallization of plagioclase during their petrogenesis or residual plagioclase in the source. Figure 2-8 shows REE plots of the granitic samples normalized to chondritic values (McDonough and Sun, 1995). Depletion in the HREE is evident, indicating equilibrium with garnet and/or amphibole-pyroxene-bearing residue. Lastly, there are enrichments in fluid mobile elements such as Pb and Ba, which are commonly related to fluxing water from

subducted materials in arc settings (Pearce, 1983; Thompson et al., 1984). Samples MX-08 and MX-18 yielded Paleoproterozoic ages of 1.73 Ga and 1.74 Ga and represent magmas formed and crystallized at that time. Elemental abundances follow the same general trace element pattern observed in the older granitoid samples; however, the overall abundance of these elements is lower (Figs. 2-7 and 2-8).

The evolved Nd and Hf isotopic signatures of the granitoids suggest two different histories for the ~1.7 Ga and ~2.5 Ga granitoids. Figure 2-15 illustrates the variation of initial ϵ_{Hf} versus age for all xenoliths using the apparent $^{207}\text{Pb}/^{206}\text{Pb}$ age of each individual zircon for the detrital samples (<10% discordant), and the values for $\epsilon_{\text{Hf}}(2.5)$ and $\epsilon_{\text{Hf}}(1.7)$ for the granitic samples. The older samples (MX-06, MX-09, MX-10, MX-11) crystallized at ~2.5 Ga, but have mean Hf T_{DM} for their zircons from 2.85 Ga to 2.93 Ga and $\epsilon_{\text{Hf}}(2.5)$ values from -6.7 to 3.0 (Figure 2-17). The range of initial Hf isotopic compositions is largely mirrored in the $\epsilon_{\text{Nd}}(2.5)$ values and collectively suggest involvement of the depleted mantle and an older enriched component such as the northern Wyoming craton lithosphere (Figure 2-15, Mueller et al., 2010; Mirnejad and Bell, 2006; Mirnejad and Bell, 2008). The mechanism of interaction with the older reservoir may have occurred by direct contact with ~2.8 Ga crust, or by incorporation of ~2.8 Ga detritus from the Wyoming craton that was being subducted (e.g., Mueller et al., 2010) and mixed into the sub-lithospheric mantle wedge.

The Paleoproterozoic samples (~1.7 Ga, MX-08 and MX-18) give mean Hf T_{DM} ages for their zircons of 2.53 Ga and 2.58 Ga respectively (Table 2-2), which constitute greater discrepancies between crystallization and model ages than observed for the older rocks, suggesting a stronger influence of older crust in their genesis. Shown on

Figure 2-17, a line with a slope approximating the bulk continental crust evolution ($^{176}\text{Lu}/^{177}\text{Hf} = 0.0115$; Rudnick and Gao, 2003) is plotted to coincide with the lower part of the range of the ~2.5 Ga granitic samples, it is clear that the $\epsilon\text{Hf}_{(1.7)}$ values for the c. 1.7 Ga samples cluster above the evolution line. Using the average of the Lu/Hf of the four xenoliths ($^{176}\text{Lu}/^{177}\text{Hf} = 0.016$) does not make an appreciable difference over this span of time. This relationship suggests that the ~1.7 Ga granitic samples were not derived solely from partial melts of the ~2.5 Ga granites. The older component in these samples may be related to pre-1.8 Ga lithosphere, e.g., new lithosphere formed during the ~2.5 Ga event, or the older lithosphere that influenced the ~2.5 Ga magmas. The $\epsilon\text{Hf}_{(1.7)}$ values for zircons from the ~1.7 Ga granites range from -4.7 to -15.0, suggesting mixing between a DM (depleted mantle)-like component and an evolved crustal component(s), which likely include the ~2.5 Ga granitoids. The $\epsilon\text{Nd}_{(1.7)}$ values calculated are -6.0 and -6.5, and plot below data for the Little Belt Mountains (Figure 2-15), and seem to indicate a mixture between a DM-like source and an older crustal component. However, it is important to note that these Paleoproterozoic samples are not the product of wholesale melting of the ~2.5 Ga granitic material based on their bulk compositions as well as Sm-Nd and Lu-Hf systematics (Figure 2-17). They clearly contain portions of new crust likely formed during the ~1.8-1.9 Ga Little Belt subduction event (Mueller et al., 2002; Vogl et al., 2003; Foster et al., 2006, 2012).

Origins Of The Schistose and Quartzite Xenoliths

The biotite schist xenoliths are difficult to constrain in terms of origin because only a maximum age of deposition can be determined. The Al_2O_3 to alkali ratio is sufficiently high in these rocks to produce normative corundum, which may be attributed to clays within the protolith, i.e., a possible indicator of a sedimentary component and

consistent with the large amount of intergrown sillimanite and muscovite. These schistose xenoliths share relatively similar trace element patterns (Figure 2-7B) with the granitoid xenoliths (Figure 2-7A) and are consistent with those found in typical modern convergent margins (Pearce, 1984; Rogers and Hawkesworth, 1989; Taylor and McLennan, 1995; Chappell and White, 2001). As discussed below, the dominant zircon age-peak within the schists (1.81 Ga to 1.90 Ga) corresponds to the time of Little Belt igneous activity, which suggests that the samples may contain re-worked volcanoclastic material from the Little Belt arc. Zircon $^{207}\text{Pb}/^{206}\text{Pb}$ ages from the quartzite and schist zircons that cluster between 1.81 Ga and 1.90 Ga (Figure 2-14) show initial ϵHf values ranging from 9.9 to -14.4 (Table 2-3). The 1.81 Ga to 1.90 Ga range of values for the detrital grains also overlaps with initial ϵHf data from orthogneisses from the Little Belt Mountains, which range from -6.6 to 9.9 (Weiss et al., 2009). The range of initial ϵHf values suggests that both juvenile (mantle like), and evolved sources contributed to the petrogenesis of their parent rocks. The range of $\epsilon\text{Nd}_{(0)}$ for the schist samples is very small, from -24.8 to -24.1, and the Nd depleted mantle model ages range only from 2.34 Ga to 2.57 Ga (Table 2-4). Both the Hf in zircon and Nd in whole-rock systematics indicate a mixture of sources in the provenance of these samples.

The quartzites/sandstones share a similar Paleoproterozoic and Archean detrital zircon age-distribution to the schistose samples (Figure 2-14). They are not identical, however, because the minimum age of the youngest observed grains are Mesoproterozoic. Sample MX-16, contains detrital zircons with ages of ~1.0 Ga (3 grains) and MX-12 contains one ~1.3 Ga detrital zircon, while the youngest detrital grains in the schists are c. 1.75 Ga or older. The lack of a metamorphic overprint on

these samples and presence of a small population of Mesoproterozoic zircon suggests that they are from part of the Phanerozoic cover sequence. The zircon population is consistent with that in the Cambrian Flathead sandstone (Sears and Link, 2007; Mueller et al., 2008b).

Implications For Great Falls Tectonic Zone Evolution

The geochemistry and geochronology of the Grassrange xenolith suite and similar data from the Little Belt Mountains (Mueller et al., 2002; Vogl et al., 2003; Weiss et al., 2009) illustrate the heterogeneous nature of the central part of the GFTZ and its relationship to surrounding terranes. These relationships are shown in Figure 2-18, in which published Archean to earliest Proterozoic U-Pb ages of zircon from the GFTZ are compared to ages from the northern Wyoming craton and the limited ages reported for the MHB. Ages were limited to those older than 2.4 Ga in order to make the most direct comparisons of pre-GFTZ data. Crystallization ages of the granitic samples (indicated by a star) as well as the detrital suites of zircons from the schist and quartzite samples are also plotted in Figure 2-18. Among the quartzite/sandstone and schist samples, those samples that contain a prominent age peak are indicated by a darker bar within the gray bar showing the range of zircon ages. The dominance of ~2.5 - 2.6 Ga ages suggests that they share a closer affinity to the MHB, which is characterized by Neoproterozoic ages, than to the northern Wyoming Province, which is dominantly Mesoproterozoic (Figure 2-18). The older (~2.7 to 2.8 Ga and ~3.0 Ga) Archean ages in the detrital samples are not distinctive, i.e., comparable to published data from both the MHB (Villeneuve et al., 1993; Davis et al., 1995) and the northern Wyoming Province (e.g., Mueller et al. 2010). The two granitic samples interpreted to have formed 1.73 Ga to 1.74 Ga ago (MX-08 and MX-18) were most likely melts that crystallized during the

final stage of the continent-continent collision between the MHB and northern Wyoming craton, or post-collision extension and underplating, based on their negative initial Hf and Nd compositions, i.e., considerably more negative than the values for samples of comparable age from the Little Belt Mountains (Weiss et al., 2009). Consequently, the ages of the main Archean detrital zircon age peaks for the schists (2.63 Ga to 2.71 Ga) and the quartzites (2.57 Ga to 2.61 Ga) appear to be derived from Medicine Hat Block or southern Hearne Province.

Although limited in geographic distribution and age, the immobile trace element abundances for both Archean and Proterozoic meta-granitoids support the proposition that the protoliths of both formed in a volcanic arc or syn-collisional setting or represent reworking of material initially formed in a subduction setting (Figure 2-19; Pearce et al (1984)). In particular, these samples preserve the relative depletion in HFSEs (Figure 2-7A) characteristic of subduction zone magmatism (e.g., Thompson et al., 1984; Pearce et al., 1984) and reported for the Little Belt gneisses (Mueller et al., 2002). Trace element data from the Paleoproterozoic samples are easier to interpret because of the similarity in age to the Paleoproterozoic gneisses in the Little Belt Mountains. These data are consistent with models proposed by Mueller et al. (2002, 2005) that the GFTZ represented a closing ocean basin and terminal continent-continent collision between the Wyoming Craton and Medicine Hat block. The primarily subchondritic $\epsilon\text{Hf}_{(1.7)}$ (zircons) and $\epsilon\text{Nd}_{(1.7)}$ (whole-rock) values for the granitic Paleoproterozoic samples (Figure 2-17; Figure 2-15) both indicate substantial mixing between a DM-like component and an evolved Archean crustal component to a greater extent than evident in the slightly older (~1.86 Ga) igneous rocks in the Little Belt Mountains. This suggests

that the ~1.7 Ga granitoids interacted with a significant amount of evolved material during their petrogenesis, a process consistent with formation in a continental collision zone in which older crust was thickened and melted. The origin of the ~2.5 Ga gneisses is more difficult to constrain because they have no counterparts in either the Little Belt Mountains or in the Archean gneisses exposed in the Beartooth Mountains or in southwestern Montana (see below).

The U-Pb ages from the schist and quartzite/sandstone samples are predominantly from 1.81 to 1.90 Ga, and show a range of initial ϵ_{Hf} for their zircons that overlaps with the range for the Little Belt Mountains (Figure 2-17). In this plot of zircon $^{207}\text{Pb}/^{206}\text{Pb}$ ages against their initial ϵ_{Hf} , the 1.81 to 1.90 Ga zircons from schist and quartzite samples appear to reflect a mixture of depleted mantle (defined by the upper dotted line) and crustal sources (defined by the lower dashed line) in their parent rocks. Extrapolating from the lower limit of initial ϵ_{Hf} values for the ~2.5 Ga granitic rocks using a crustal evolution line with a Lu/Hf ratio of 0.08 (Rudnick and Gao, 2003) indicates more input from juvenile material and less from a more evolved (older) source for these Paleoproterozoic zircons. Mueller and Wooden (2012), for example, showed initial ϵ_{Hf} values as low as -9 at 3.4 Ga for the northern Wyoming Province. In contrast, the ~1.7 Ga granites show more negative ϵ_{Hf} values at their time of crystallization, which suggests more intimate interaction with older reservoirs. Together, the initial ϵ_{Hf} data from both igneous and metasedimentary rocks may be best viewed as a continuum recording the transition from magma generation in a subduction setting where relatively primitive oceanic lithosphere was being subducted to a final continent-continent

collisional setting in which magmas received more input from older sources (e.g., Mueller et al., 2011).

To better understand the role of the GFTZ in the overall collisional history of Laurentia, it is important to note that collision of MHB and Wyoming coincided with other circum-Wyoming province collisions (Mueller et al., 2011; Figure 2-20). For example, the Wyoming-Colorado collision occurred between ~1.66-1.80 Ga (Bickford and Boardman, 1984; Sims and Peterman, 1986; Karlstrom and Bowring, 1988; Premo and Van Schmus, 1989; Van Schmus et al., 1993; Chamberlain, 1998; Selverstone et al., 2000; Hill and Bickford, 2001; Hill, 2004), and the Wyoming-Superior collision to form the southern part of the Trans-Hudson orogen occurred at 1.71-1.77 Ga (Karlstrom and Houston, 1984; Nelson et al., 1993; Resor et al., 1996; Dahl et al., 1999). The data presented here support the suggestion of Mueller et al. (2005) that the amalgamation of the Wyoming craton to the Superior craton and the Medicine Hat Craton was in part simultaneous, which places significant limits on plate tectonic relations during this very rapid period of continental growth (e.g., Hoffman, 1989; Mueller et al., 2005).

Conclusions

Geochronology and geochemistry of crustal xenoliths from the Grassrange provide new insight into the complex history of the crust in the GFTZ, including: 1) Both Archean and Proterozoic granitic xenoliths show HFSE depletions and LIL enrichments characteristic of formation in a subduction modified environment. The limited enrichment of HREE relative to primitive mantle values reflects the source mineralogy, likely lower crustal materials where garnet is residual after melt extraction. 2) U-Pb data (<10% discordant) show distinct intervals (~1.7 and ~2.5 Ga) that are coincident with documented tectonothermal events in the MHB, suggesting that the buried crust

sampled by the Grassrange diatremes represents reworked MHB material in addition to juvenile Paleoproterozoic arc material similar to that in the Little Belt Mountains. 3) Zircon Hf and whole-rock Nd isotopic data for the ~2.5 Ga granitic samples indicate that juvenile and reworked crustal material mixed to varying degrees during crustal formation at ~2.5 Ga. These data, along with initial Hf isotope ratios for Archean detrital zircons, provide no evidence for crust as old as that which characterizes the northern Wyoming Province (2.8-3.5 Ga). 4) The Hf and Nd isotopic data for the ~1.7 Ga granitic samples indicate a mixture of older crust (e.g., the ~2.5 Ga crust in the older xenoliths) and a more juvenile source. This is in contrast to exposures of 1.8-1.9 Ga igneous material in the LBM, which involve far higher proportions of juvenile material, hypothesized to represent the arc formed during closure of the Little Belt ocean (Mueller et al., 2002). 5) The Great Falls tectonic zone was initiated prior to ~1.9 Ga as a convergent boundary related to the closing of an ocean basin between the Wyoming craton and the MHB that also produced the igneous suite of the Little Belt arc. The Great Falls tectonic zone then evolved into a more transpressional boundary by ca. 1.77 as Wyoming moved east towards final collision with the Superior and Hearne provinces as well as the MHB (Dahl et al., 1999; Mueller et al., 2000; Mueller et al., 2002; Mueller et al., 2005).

The compositions and ages of these xenoliths provide additional evidence for the evolution of the Great Falls tectonic zone via the closure of a Paleoproterozoic ocean and the addition of a significant volume of juvenile crust prior to continent-continent collision. These data also suggest that the arc was built on crust of the MHB rather than that of the Wyoming Province and that the arc evolved during the period of rapid coalescence of cratons that formed Laurentia in the Paleoproterozoic.

Table 2-1. Major, trace and rare earth element data of granitoid xenoliths from the Grassrange. Major elements in wt. %, trace and rare earth elements in ppm.

Sample wt. %	MX-06 Granitoids	MX-08	MX-09	MX-10	MX-11	MX-18
SiO ₂	75	74	75	74	80	77
TiO ₂	0.14	0.06	0.24	0.17	0.14	0.05
Al ₂ O ₃	13	14	14	13	11	13
Fe ₂ O ₃	0.33	0.47	1.04	0.94	0.51	0.70
MnO	0.01	0.01	0.01	0.01	0.01	0.01
MgO	0.05	0.13	0.24	0.25	0.30	0.06
CaO	0.71	0.62	0.92	0.63	0.23	0.97
Na ₂ O	2.9	3.8	3.7	3.0	2.3	3.9
K ₂ O	6.4	4.4	5.0	6.5	6.1	4.7
P ₂ O ₅	0.07	0.05	0.09	0.06	0.10	0.04
LOI	0.84	1.3	0.61	0.73	0.31	0.56
Total	99.20	99.40	100.25	99.54	100.43	100.92
ppm						
Li	5.1	6.9	5.9	4.2	7.9	4.2
Sc	1.5	2.1	1.6	1.4	1.6	1.2
Ti	841	47	1748	1073	913	51
V	14	12	16	18	14	12
Cr	4.1	4.3	7.5	6.7	4.6	6.0
Co	35	20	2.8	3.0	1.1	2.6
Ni	3.4	3.0	3.8	4.1	3.6	3.5
Cu	4.3	24	6.2	3.5	2.9	4.3
Zn	20	25	29	23	24	24
Ga	15	23	14	14	13	16
Rb	170	164	130	161	207	129
Sr	103	67	138	91	70	105
Y	16	4.6	19	9.2	9.3	3.3
Zr	34	39	29	33	13	57
Nb	22	16	30	21	25	8.8
Cs	0.47	1.7	0.40	1.0	1.9	2.6
Ba	900	430	902	804	736	636
La	73	23	104	67	57	23
Ce	146	42	203	130	106	41
Pr	15	4.3	21	13	11	4.3
Nd	48	14	65	41	36	14
Sm	8.3	2.4	10	6.2	5.8	2.4
Eu	0.83	0.41	1.1	0.85	0.79	0.68
Gd	5.8	1.5	7.0	4.1	4.1	1.6
Tb	0.77	0.18	0.88	0.49	0.51	0.20
Dy	3.6	0.85	4.0	2.2	2.3	0.86
Ho	0.57	0.15	0.67	0.34	0.34	0.14
Er	1.5	0.45	1.6	0.84	0.81	0.35
Tm	0.21	0.07	0.18	0.10	0.09	0.05
Yb	1.4	0.55	0.92	0.60	0.44	0.34
Lu	0.19	0.09	0.10	0.08	0.05	0.06

Table 2-1. Continued.

Sample ppm	MX-06 Granitoids	MX-08	MX-09	MX-10	MX-11	MX-18
Hf	1.2	1.8	0.95	1.1	0.45	2.4
Ta	3.0	2.9	1.0	0.91	1.5	0.68
Pb	36	33	49	29	29	42
Th	42	6.6	77	40	34	19
U	2.0	1.7	6.8	2.5	1.7	2.9

Table 2-2. Major, trace and rare earth element data of schist and quartzite xenoliths from the Grassrange. Major elements in wt. %, trace and rare earth elements in ppm.

Sample wt. %	MX-13 Schists	HAL-1	HAL-2	HAL-5	HAL-6	MX-12 Quartzites	MX-16	MX-17
SiO ₂	78	80	76	82	65	84	83	80
TiO ₂	0.51	0.51	0.38	0.40	0.69	0.40	0.14	0.37
Al ₂ O ₃	11	10	13	9.2	17	9.1	2.3	9.9
Fe ₂ O ₃	3.2	3.4	2.8	2.4	4.8	0.76	2.3	2.6
MnO	0.03	0.03	0.02	0.02	0.05	0.01	0.07	0.02
MgO	0.97	1.0	0.91	0.68	1.7	0.32	0.46	0.86
CaO	0.46	0.35	0.29	0.66	0.76	0.47	4.7	0.61
Na ₂ O	1.5	0.76	0.96	1.9	2.16	1.06	0.04	2.0
K ₂ O	3.9	2.7	4.0	2.7	6.22	1.98	0.36	2.9
P ₂ O ₅	0.12	0.15	0.14	0.13	0.15	0.13	0.28	0.14
LOI	0.87	1.0	1.2	1.2	1.9	1.6	5.1	0.74
Total	100.26	100.23	99.77	100.94	100.27	100.10	99.10	100.37
ppm								
Li	25	42	39	19	42	16	24	21
Sc	7.4	8.6	7.5	6.6	14.69	4.93	1.54	5.73
Ti	4236	2841	2185	2285	4586	2970	518	2851
V	48	51	47	42	90	37	48	40
Cr	46	47	41	37	76	36	21	34
Co	6.4	6.9	5.7	4.8	11	38	8.1	12
Ni	18	18	15	12	35	5.1	13	15
Cu	7.3	5.7	11	14	6.8	8.7	16	7.8
Zn	57	58	50	40	92	24	33	57
Ga	12	13	15	9.6	22	11	2.6	10
Rb	148	136	115	108	230	74	12	120
Sr	119	56	80	100	171	66	84	99
Y	8.7	15	12	12	13	9.8	8.3	10
Zr	167	263	153	281	216	135	36	107
Nb	16	12	11	13	24	14	9.1	11
Cs	7.7	7.0	5.4	4.9	13	1.8	0.45	5.8
Ba	694	430	818	503	1193	330	1207	568

Table 2-2. Continued.

Sample ppm	MX-13 Schists	HAL-1	HAL-2	HAL-5	HAL-6	MX-12 Quartzites	MX-16	MX-17
La	37	41	36	39	47	31	10	31
Ce	77	84	79	79	96	64	19	64
Pr	8.6	9.5	8.6	8.5	10	7.0	2.4	7.2
Nd	30	33	31	30	36	24	9.0	25
Sm	5.4	6.3	5.7	5.3	6.5	4.3	1.8	4.7
Eu	1.1	0.94	1.1	0.96	1.4	0.73	0.45	0.93
Gd	3.9	5.1	4.6	4.3	4.9	3.1	1.7	3.8
Tb	0.50	0.67	0.59	0.55	0.63	0.42	0.24	0.51
Dy	2.2	3.3	2.8	2.7	2.9	2.1	1.3	2.4
Ho	0.34	0.56	0.46	0.46	0.49	0.37	0.26	0.38
Er	0.82	1.5	1.2	1.2	1.2	0.99	0.74	0.92
Tm	0.10	0.19	0.15	0.16	0.16	0.14	0.10	0.12
Yb	0.66	1.3	0.95	1.1	1.1	0.94	0.68	0.75
Lu	0.10	0.20	0.15	0.17	0.17	0.14	0.10	0.11
Hf	4.9	7.5	4.4	7.9	6.2	4.0	1.0	3.2
Ta	0.88	0.82	0.67	0.88	1.6	2.9	0.25	0.96
Pb	22	14	26	20	32	8.2	4.4	21
Th	17	17	17	14	17	10	2.3	13
U	4.2	4.1	3.8	3.5	3.8	2.9	2.4	3.2

Table 2-3. Granitoid xenoliths, Grassrange, zircon LA-ICP-MS U-Pb data $^{207}\text{Pb}/^{206}\text{Pb}$ ages and Hf-isotope data reported (Ma).

Sample Number	Young U-Pb Age	Error 2 σ	Old U-Pb Age	Error 2 σ	$\epsilon\text{Hf}_{(\text{IA})}$ Highest	$\epsilon\text{Hf}_{(\text{IA})}$ Lowest	$\epsilon\text{Hf}_{(\text{T})}^*$ Highest	$\epsilon\text{Hf}_{(\text{T})}^*$ Lowest	$\epsilon\text{Hf}_{(\text{T})}^*$ Average	Std. Dev.	Hf Model Age (DM) ^{a*}	Std. Dev.
MX-06	1842	110	2524	25	2.3	-19.9	3.0	-3.6	-1.1	1.8	2849	70
MX-08	1731	5	N/A	N/A	-0.5	-11.8	-4.7	-12.0	-10.0	1.4	2506	54
MX-09	1765	37	2519	15	-0.6	-19.3	0.4	-5.5	-2.0	1.8	2878	73
MX-10	1828	16	2528	8	-3.0	-19.5	-1.4	-3.8	-2.9	0.8	2923	36
MX-11	1818	21	2456	160	-4.6	-20.2	-0.6	-6.7	-4.3	1.7	2932	74
MX-18	1736	9	N/A	N/A	-7.5	-15.0	-7.6	-15.0	-11.6	2.1	2581	94

^(IA)Zircons reduced to individual U-Pb age.

*zircons reduced to old U-Pb age, if "Old U-Pb Age" column is "N/A", sample reduced to Young U-Pb Age.

^aDepleted mantle model ages were calculated using the model of Mueller et al. (2008).

Table 2-4. Schist and quartzite xenoliths, Grassrange, zircon LA-ICP-MS U-Pb data
²⁰⁷Pb/²⁰⁶Pb ages and Hf-isotope data reported (Ma).

Sample Number	Age Range	Age Population	Age Population	$\epsilon\text{Hf}_{(IA)}$ Highest	$\epsilon\text{Hf}_{(IA)}$ Lowest	Hf T _(DM) ^a Highest	Hf T _(DM) ^a Lowest
Schist							
MX-13	1848 - 2409	1897	N/A	2.8	-9.9	2804	2129
HAL-1	1809 - 2531	1864	N/A	N/A	N/A	N/A	N/A
HAL-2	1818 - 2666	1899	2628	6.8	-11.4	2874	1982
HAL-5	1839 - 3054	1866	2679	9.9	-11.1	3148	1850
HAL-6	1751 - 1871	1781	N/A	N/A	N/A	N/A	N/A
Quartzite							
MX-12	1282 - 2684	1871	N/A	5.8	-14.4	3027	1610
MX-16	1018 - 2851	1847	N/A	3.7	-11.7	2985	2126
MX-17	1813 - 2690	1864	2680	6.8	-9.5	2889	1950

^(IA)Zircons reduced to individual U-Pb age.

^aDepleted Mantle model ages were calculated using the model of Mueller et al. (2008).

Table 2-5. LA-ICP-MS Nd-isotope data reported (Ma).

Sample Number	Sm (ppm)	Nd (ppm)	$^{143}\text{Nd}/^{144}\text{Nd}$	$\epsilon\text{Nd}_{(0)}$	$\epsilon\text{Nd}_{(T)}$ *	Nd Model Age (DM) ^a
Granitoids						
MX-06	8.27	47.83	0.51120	-28.0	1.9	2592
MX-08	2.41	14.00	0.51128	-26.5	-6.0	2465
MX-09	10.20	65.44	0.51088	-34.4	-1.2	2791
MX-10	6.18	41.24	0.51104	-31.2	3.2	2501
MX-11	5.82	36.28	0.51108	-30.4	1.0	2584
MX-18	2.37	13.61	0.51126	-26.8	-6.5	2513
Schists						
MX-13	5.36	29.79	0.51139	-24.4	N/A	2422
HAL-1	6.28	33.44	0.51141	-24.1	N/A	2511
HAL-2	6.28	33.44	0.51137	-24.8	N/A	2574
HAL-5	5.71	31.16	0.51138	-24.6	N/A	2484
HAL-6	5.27	30.12	0.51139	-24.3	N/A	2345
Quartzites						
MX-12	4.25	23.98	0.51142	-23.8	N/A	2341
MX-16	1.82	9.00	0.51194	-13.7	N/A	1840
MX-17	4.74	25.46	0.51144	-23.3	N/A	2421

*Granitic sample reduced to old age peak U-Pb age (Table 2-3), if "Old U-Pb Age" column is empty, sample reduced to "Young U-Pb Age" column.

^aDepleted Mantle model ages were calculated using the model of DePaolo (1981).

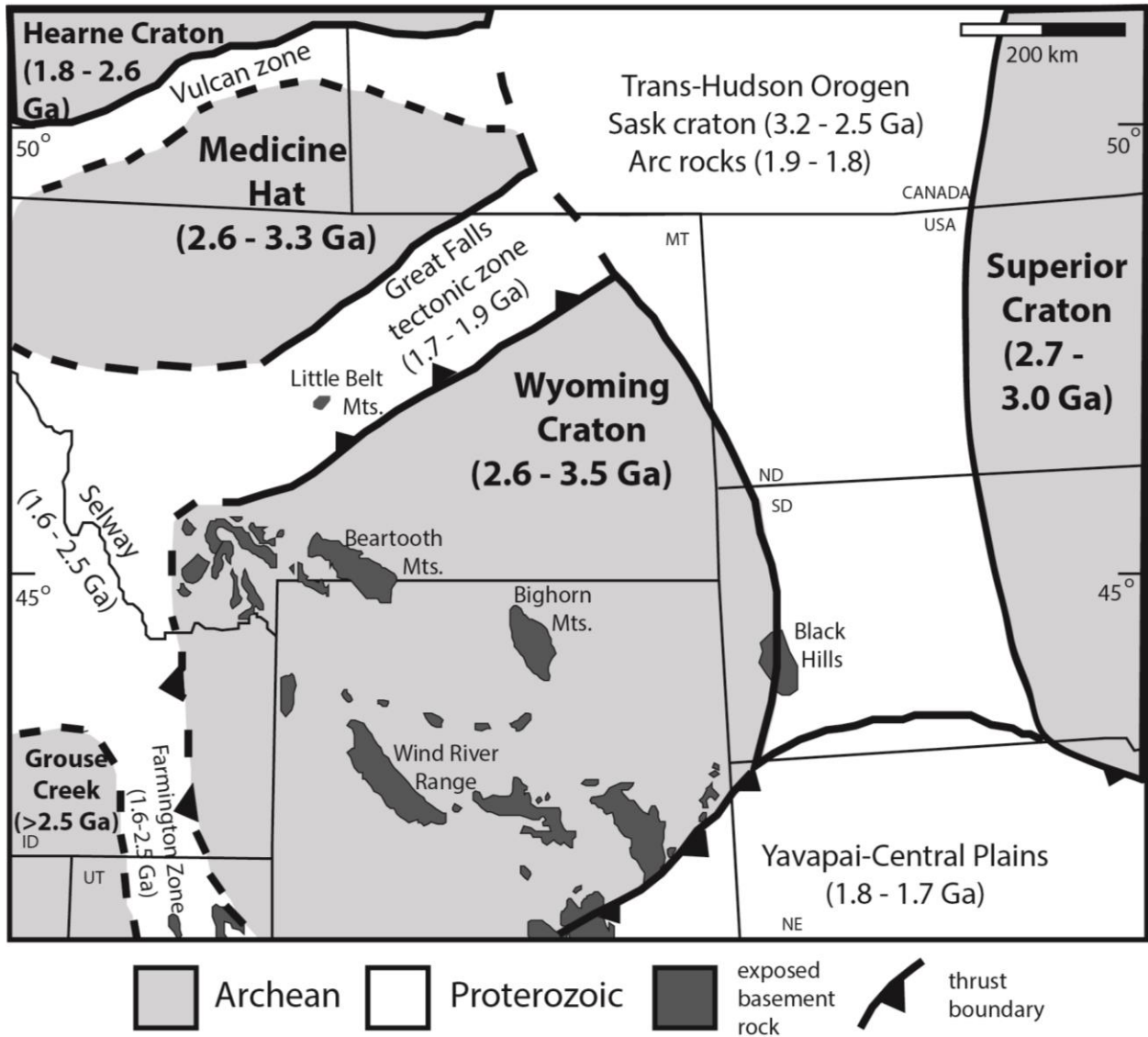


Figure 2-1. Generalized map of Precambrian basement provinces of southwestern Laurentia (after Ross et al., 1991; Condie, 1992; Vogl et al., 2004; Foster et al., 2006). Exposures of basement in Laramide-style uplifts are shown in the dark grey shaded areas.

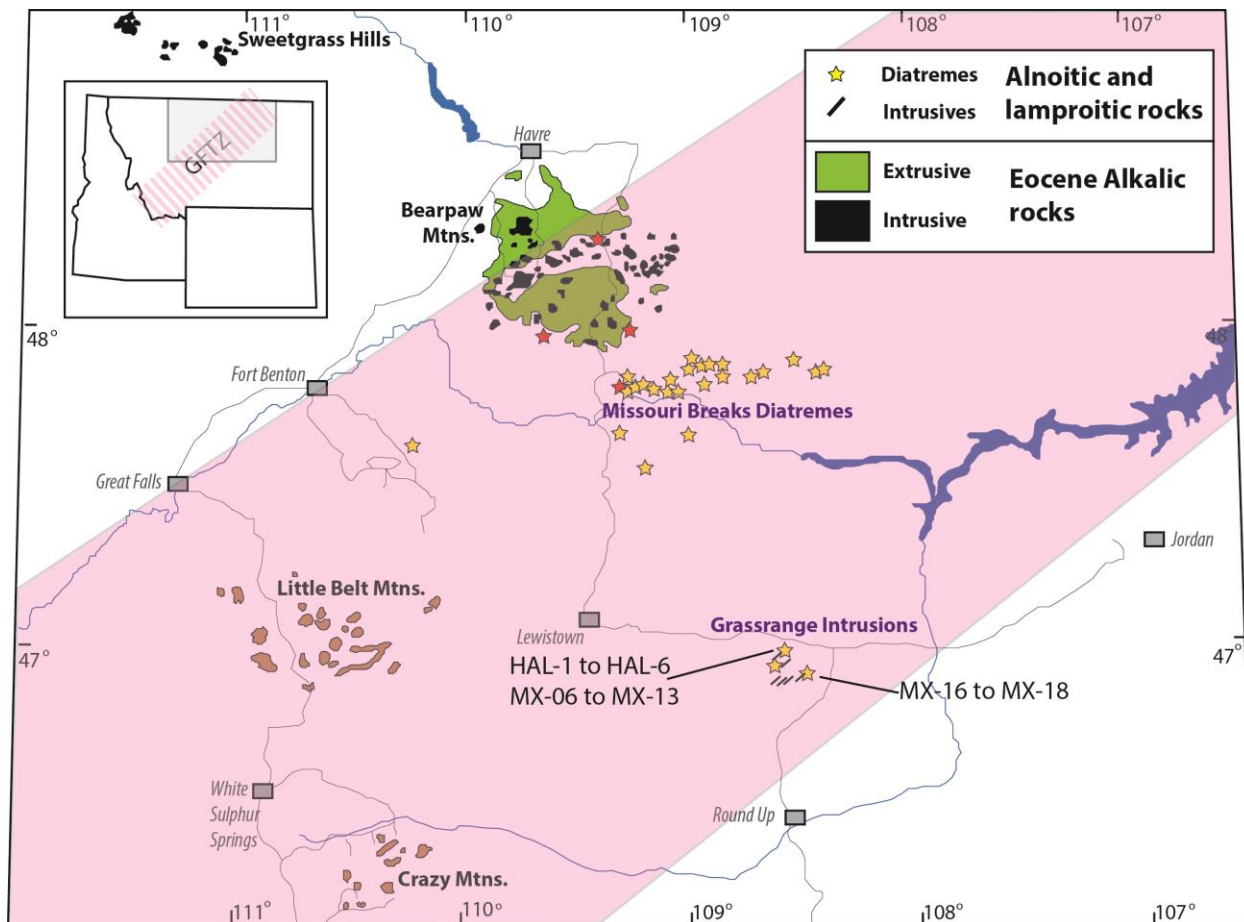
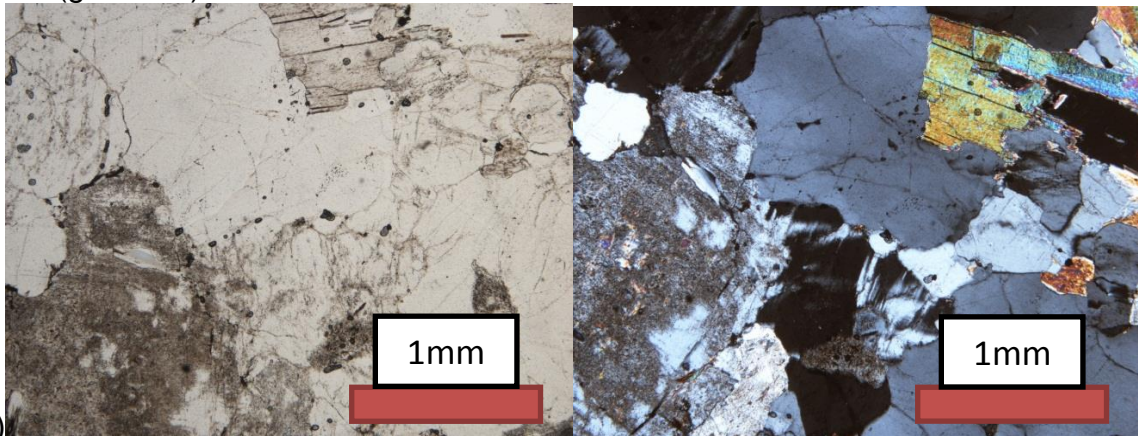


Figure 2-2. Generalized depiction of Cenozoic alkaline rock occurrences in the Montana alkali province (after Hearn et al., 1989). The limits of the Great Falls tectonic zone (shown in pink) are not well defined and are based on aeromagnetic data from Sims et al., 2004.

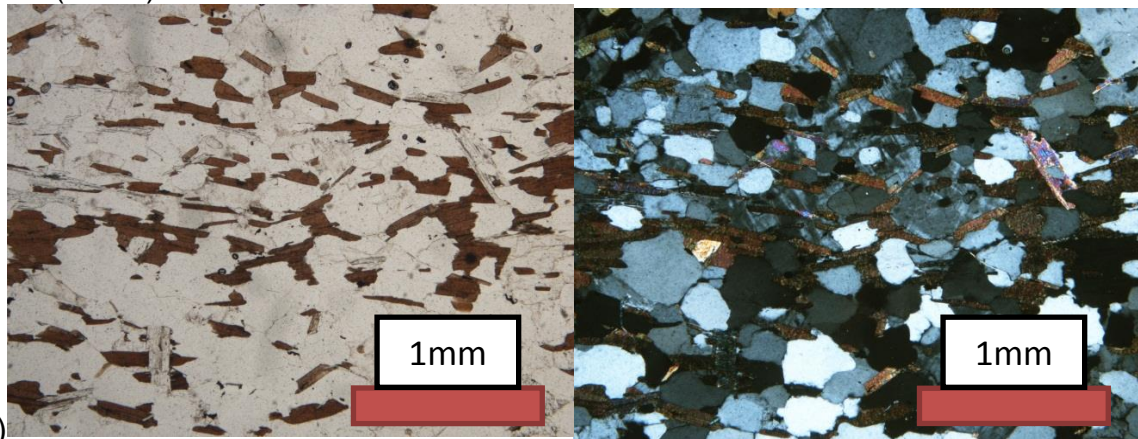
MX-08 (granitoid)



(A)

(B)

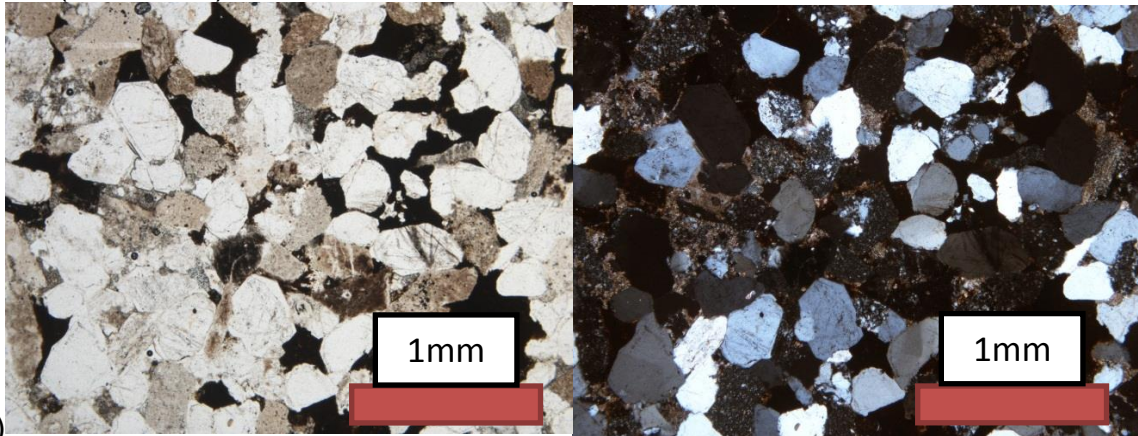
HAL-1 (schist)



(C)

(D)

MX-16 (sandstone)



(E)

(F)

Figure 2-3. Representative examples of photomicrographs of (A) granitic sample MX-08 in plain polarized light (PPL); (B) granitic sample MX-08 in cross polarized light (XPL); (C) schist sample HAL-1 in PPL; (D) schist sample HAL-1 in XPL; (E) quartzite sample MX-16 in PPL; (F) quartzite sample MX-16 in XPL. Scale bars are 1mm in size.

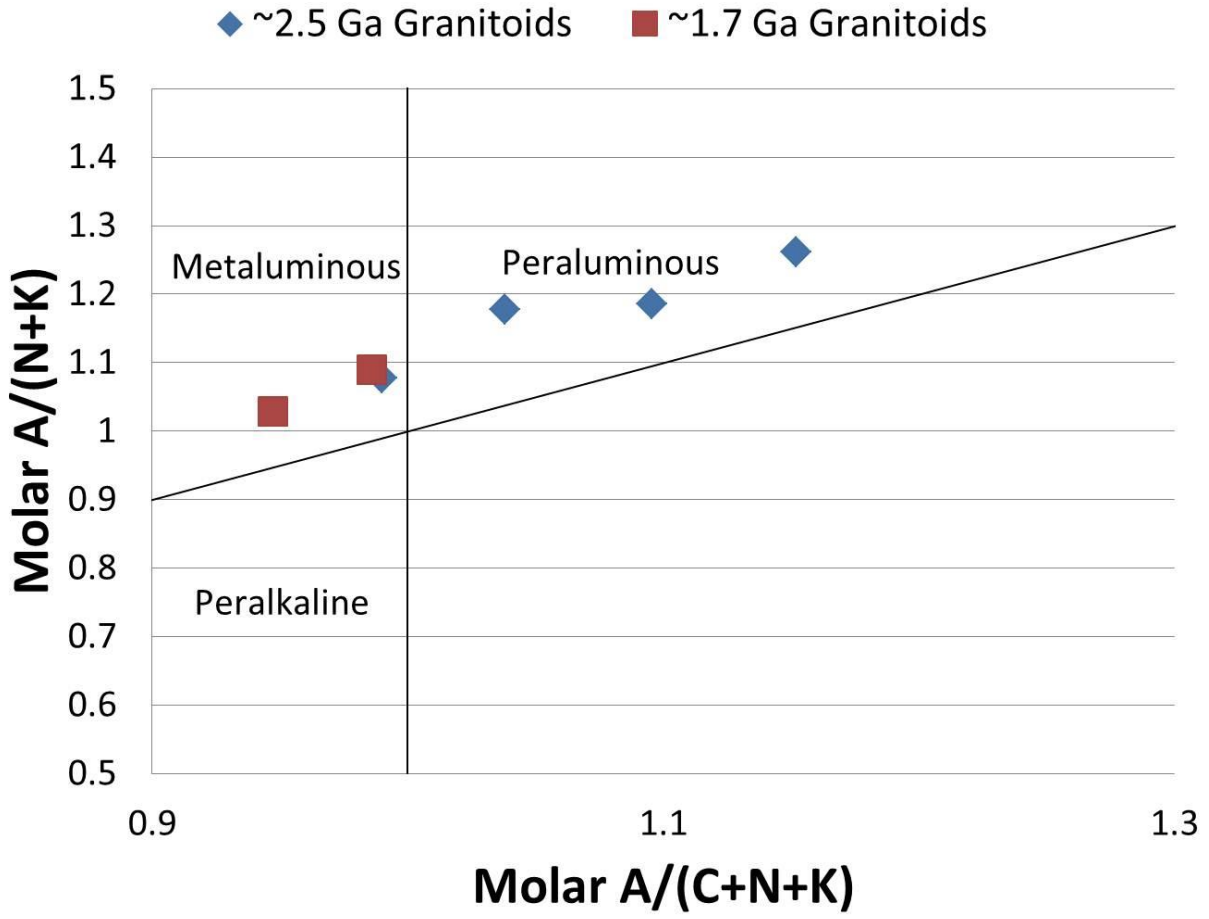


Figure 2-4. Granitoid samples plotted on an alumina saturation index (Shand, 1943; modified by Frost et al., 2001). ~2.5 Ga granitoids (diamonds), ~1.7 Ga granitoids (squares).

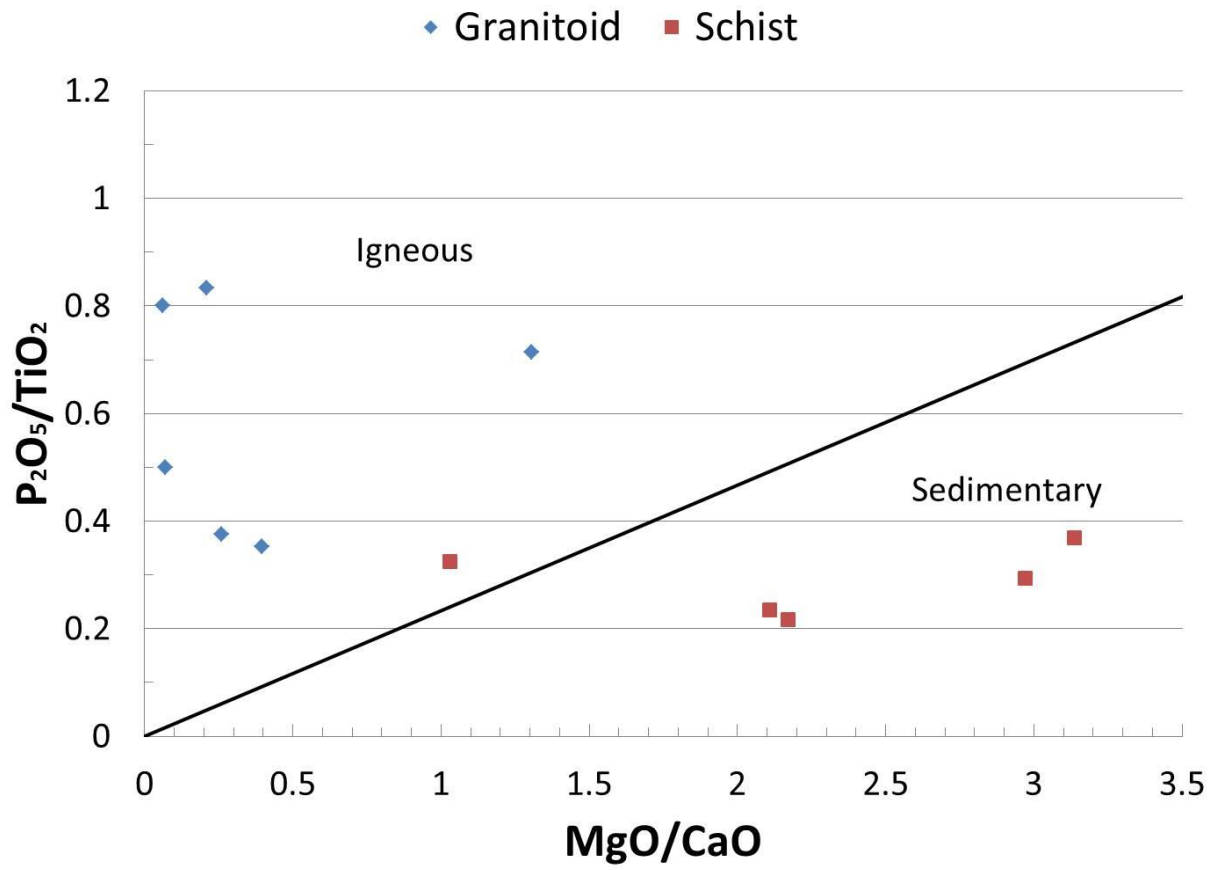


Figure 2-5. Plot of P_2O_5/TiO_2 vs. MgO/CaO (after Werner, 1987) proposed to discriminate magmatic vs. sedimentary protoliths for all meta-igneous granitoids and schistose samples.

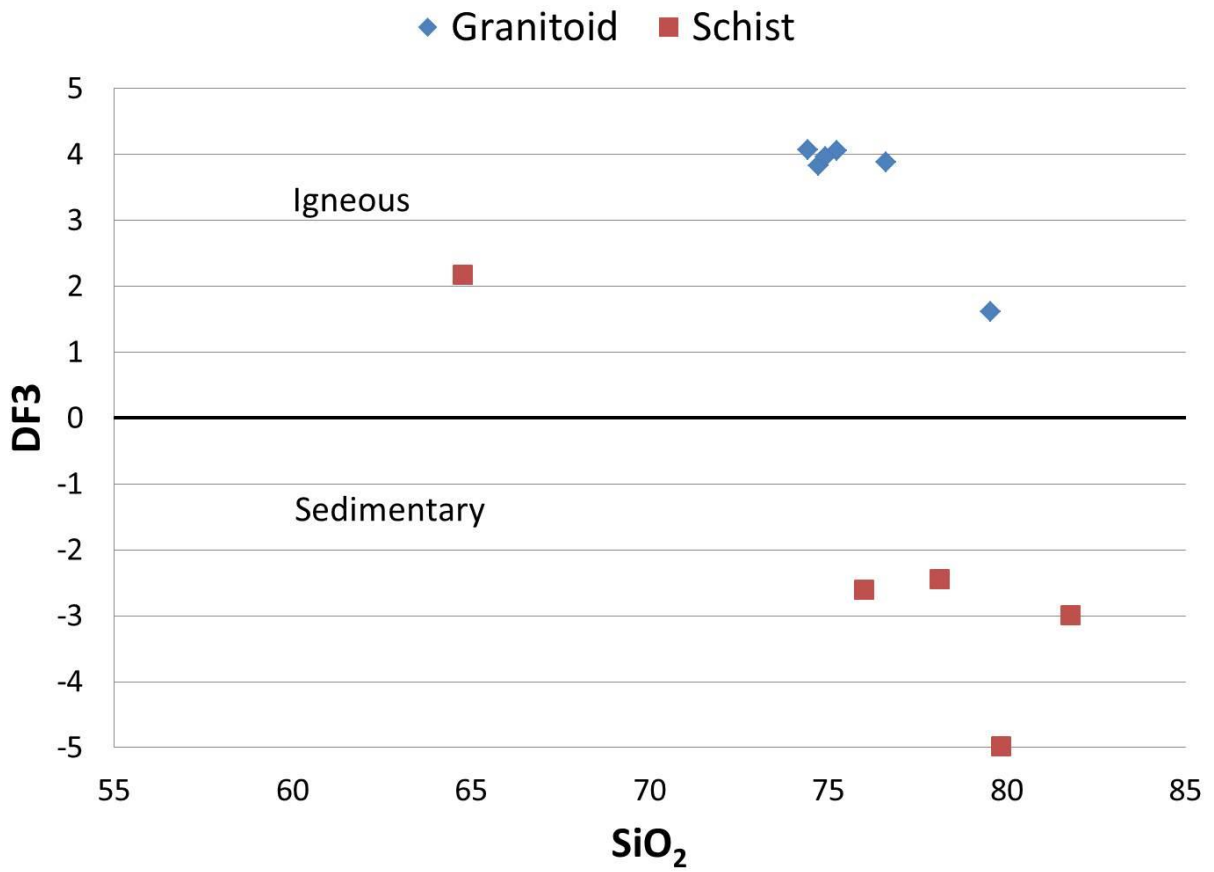


Figure 2-6. Compositional discriminant diagram showing the discriminant function 3 (DF3) vs. SiO₂ for all granitoid and schistose samples (after Shaw, 1972). Rocks with positive DF3 values are interpreted to be of igneous origin, and rocks with a negative value are interpreted to have a sedimentary origin.

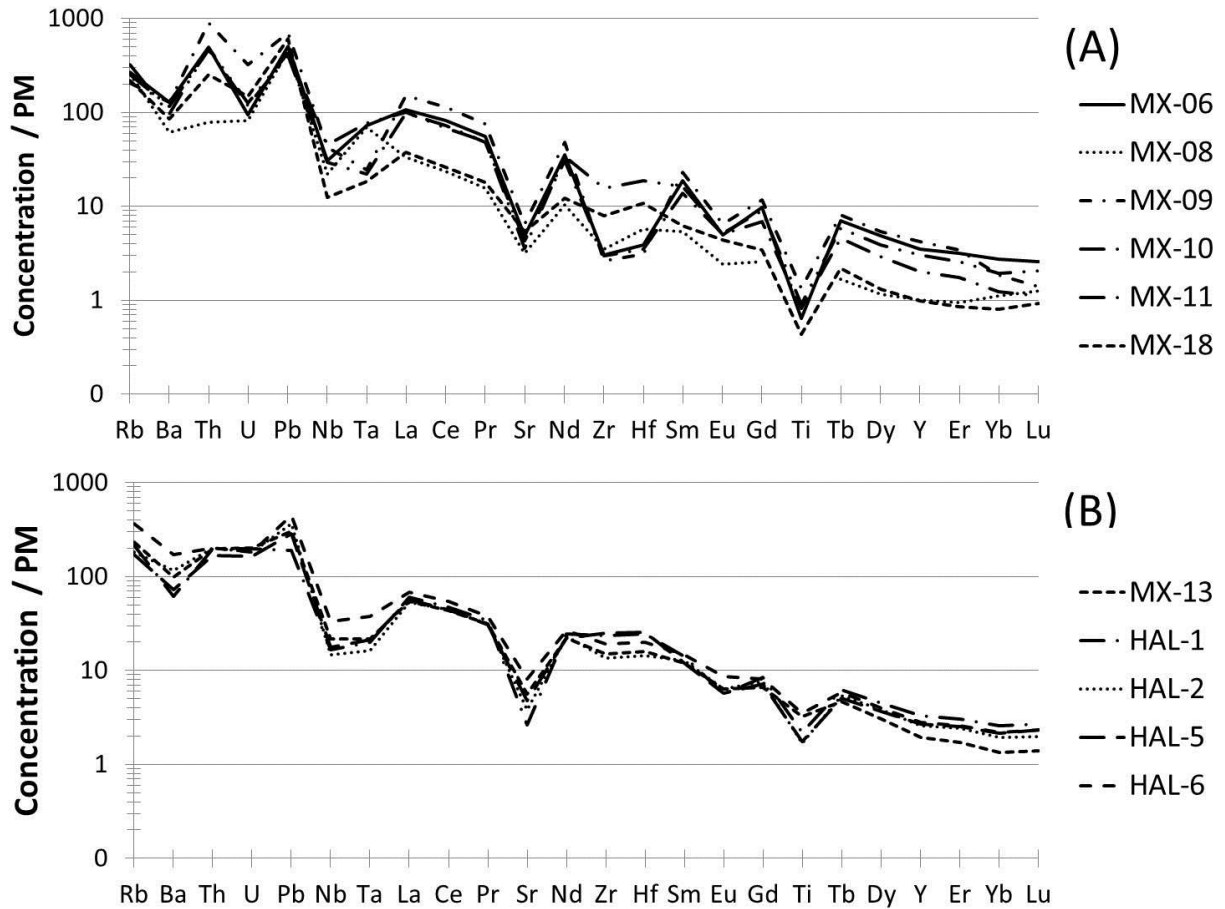


Figure 2-7. Primitive-mantle normalized “spider” diagrams (McDonough and Sun, 1995) for (A) granitoid samples and (B) schistose samples, using data in Table 2-1 and 2-2. Relative enrichment of large ion lithophile elements (LILEs) to high field strength elements (HFSE) suggests formation in an arc environment.

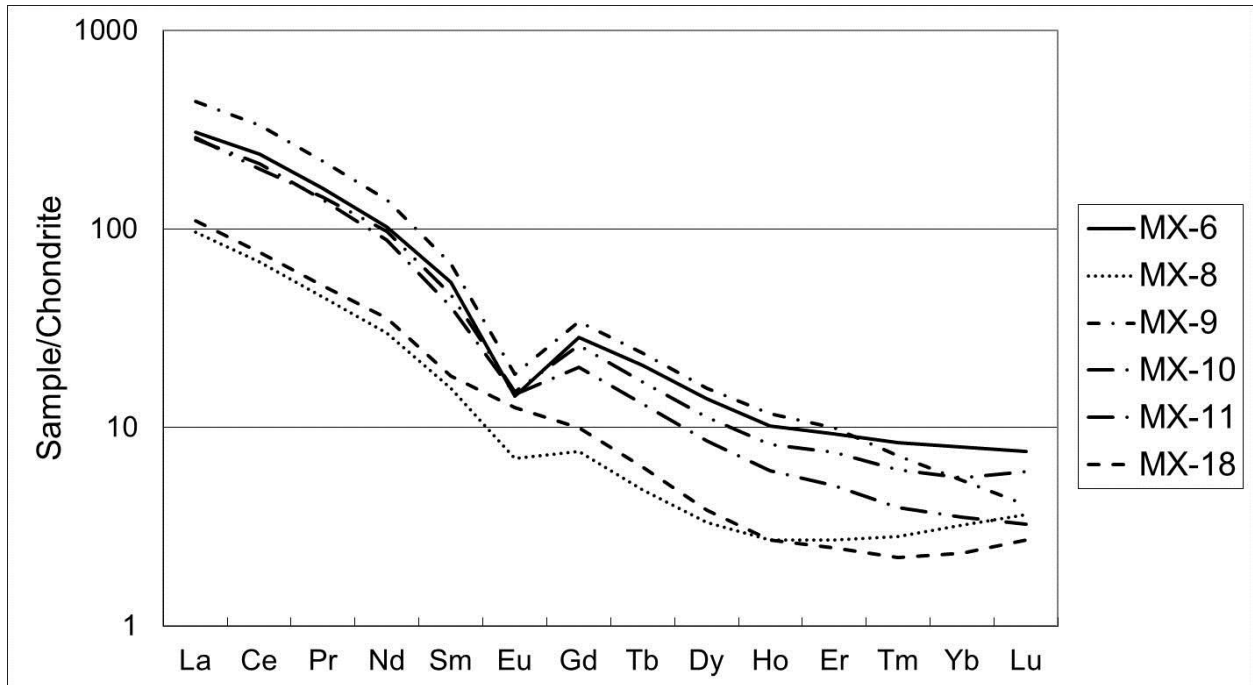


Figure 2-8. Chondrite normalized rare earth element diagram (McDonough and Sun, 1995) for granitoid samples using data in Table 2-1.

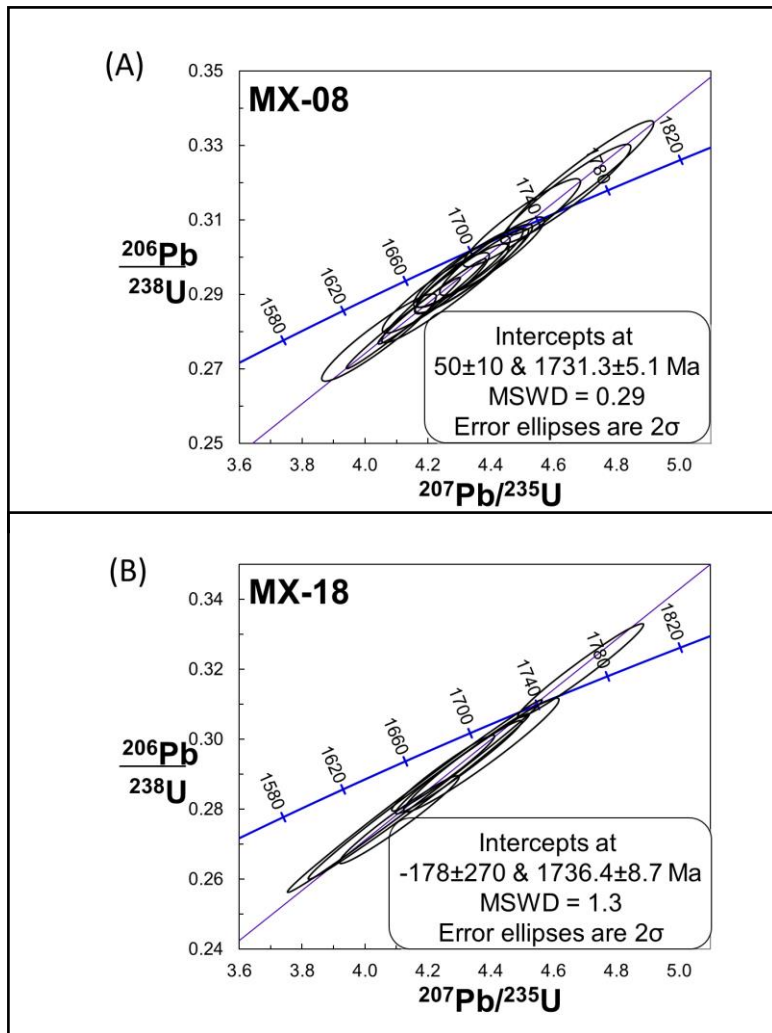


Figure 2-9. Concordia diagrams showing U-Pb data for granitoid samples MX-08 (A) and MX-18 (B). Each ellipse represents a single spot analysis and its 2σ standard error.

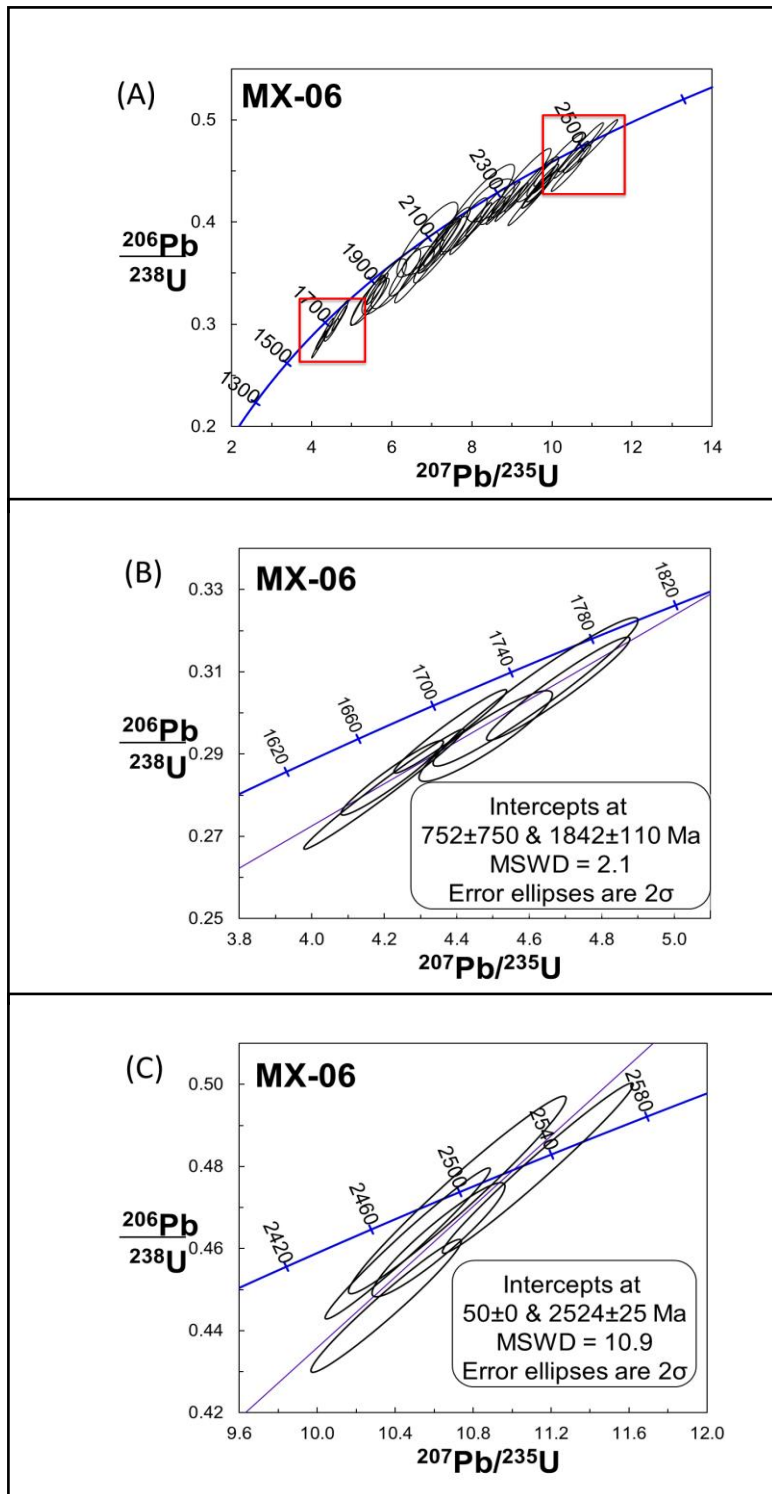


Figure 2-10. (A) Concordia diagrams plotting composite U-Pb data for granitoid sample MX-06. Each ellipse represents a single spot analysis and its 2σ standard error. (B) Expanded view of lower end of concordia showing samples selected for regression. (C) Expanded view of upper end of concordia showing samples selected for regression.

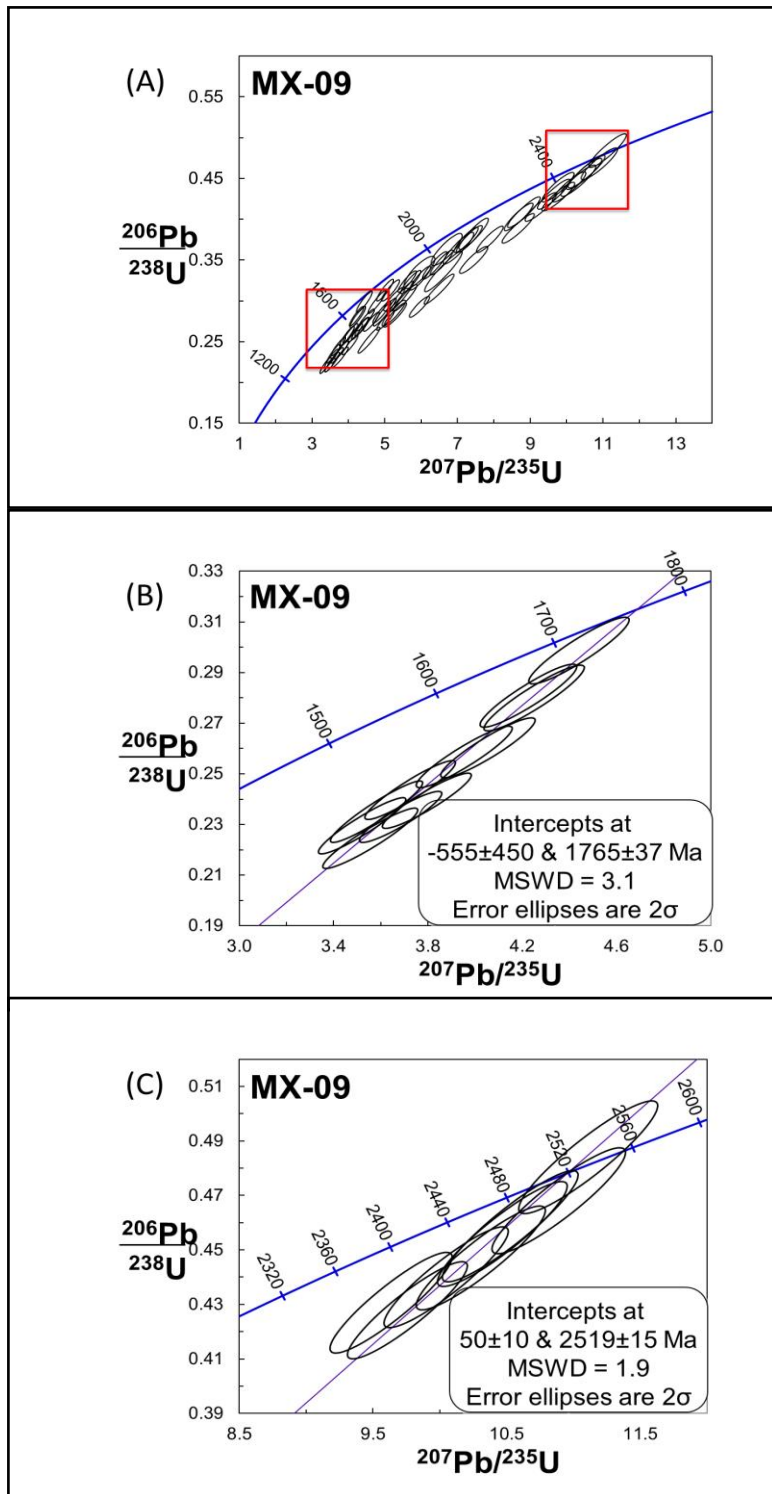


Figure 2-11. (A) Concordia diagrams plotting composite U-Pb data for granitoid sample MX-09. Each ellipse represents a single spot analysis and its 2σ standard error. (B) Expanded view of lower end of concordia showing samples selected for regression. (C) Expanded view of upper end of concordia showing samples selected for regression.

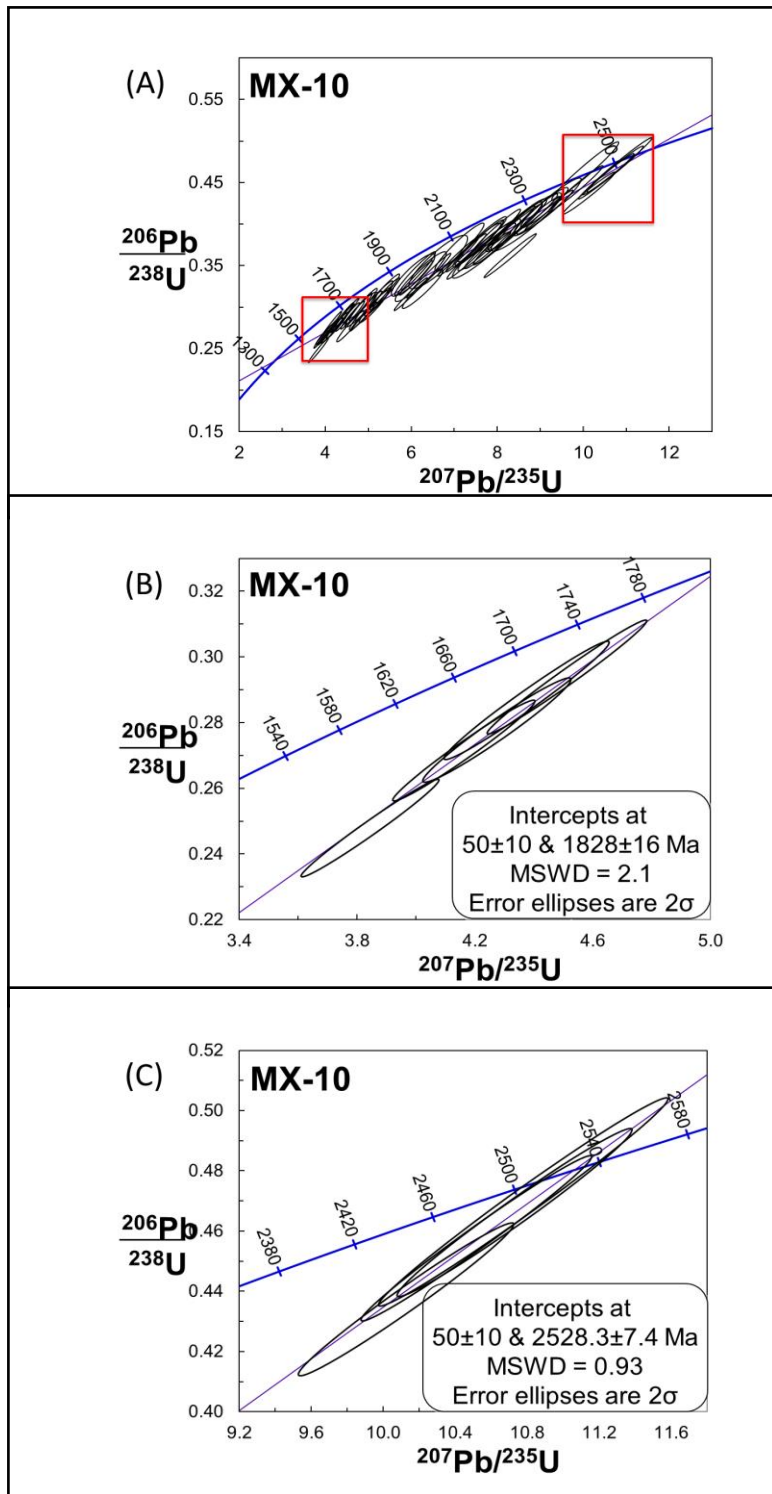


Figure 2-12. (A) Concordia diagrams plotting composite U-Pb data for granitoid sample MX-10. Each ellipse represents a single spot analysis and its 2σ standard error. (B) Expanded view of lower end of concordia showing samples selected for regression. (C) Expanded view of upper end of concordia showing samples selected for regression.

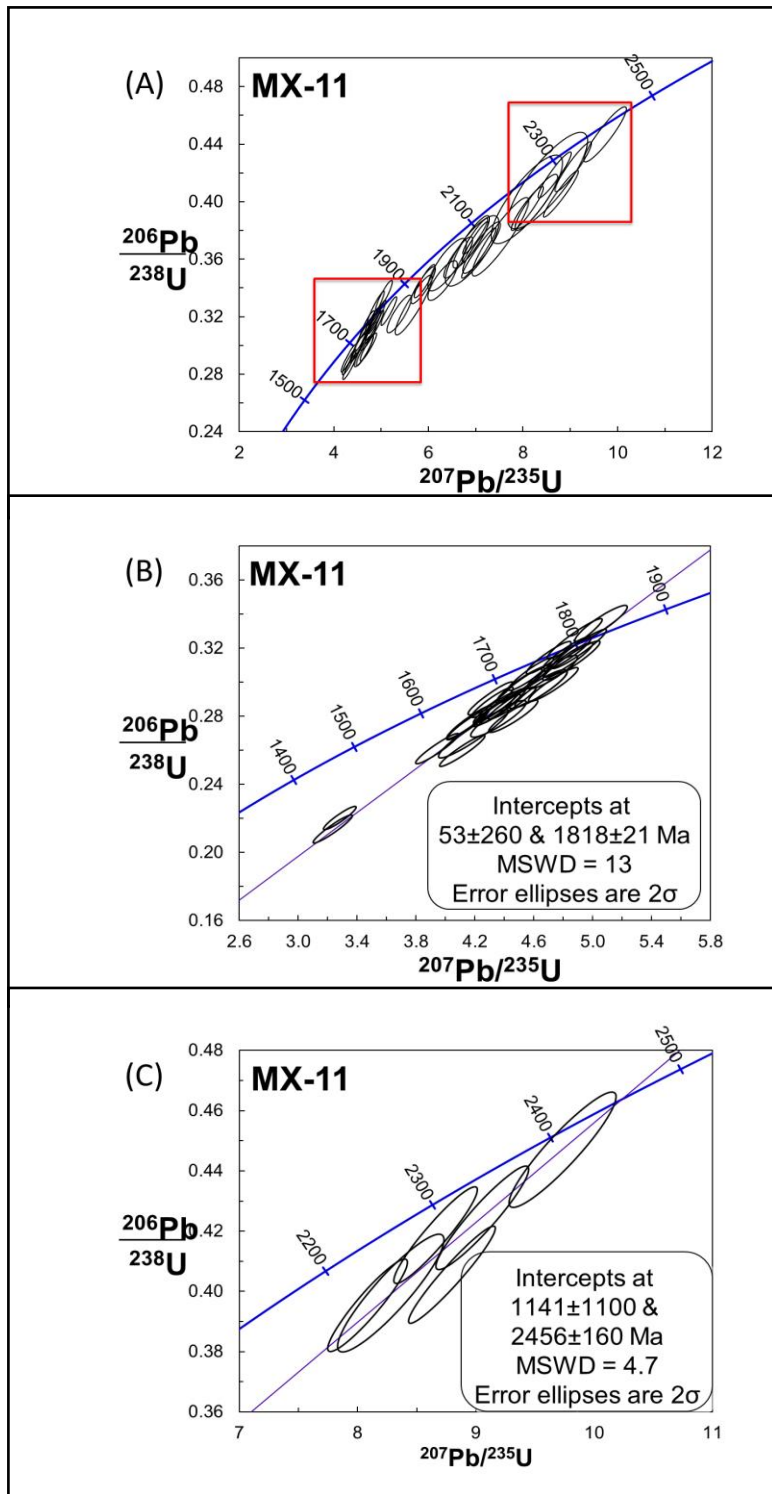


Figure 2-13. (A) Concordia diagrams plotting composite U-Pb data for granitoid sample MX-11. Each ellipse represents a single spot analysis and its 2σ standard error. (B) Expanded view of lower end of concordia showing samples selected for regression. (C) Expanded view of upper end of concordia showing samples selected for regression.

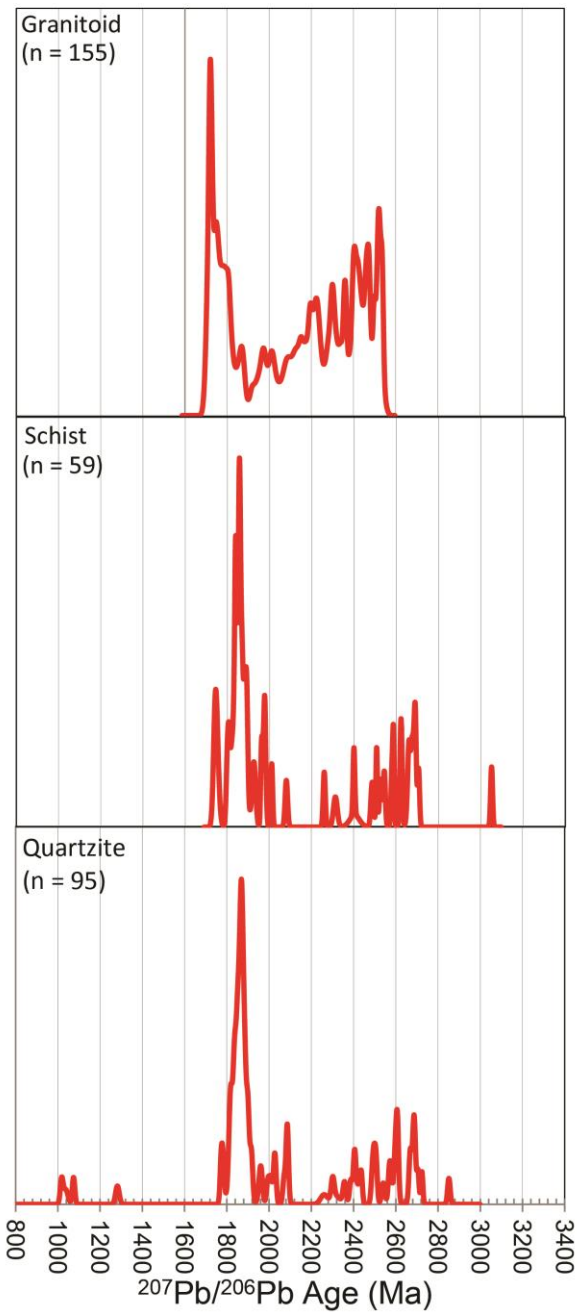


Figure 2-14. Probability density plots comparing the cumulative <10% discordant zircon analyses of (A) the 6 granitoid samples, 155 grains; (B) The 5 schist samples, 59 grains; (C) The 3 quartzite samples, 95 grains.

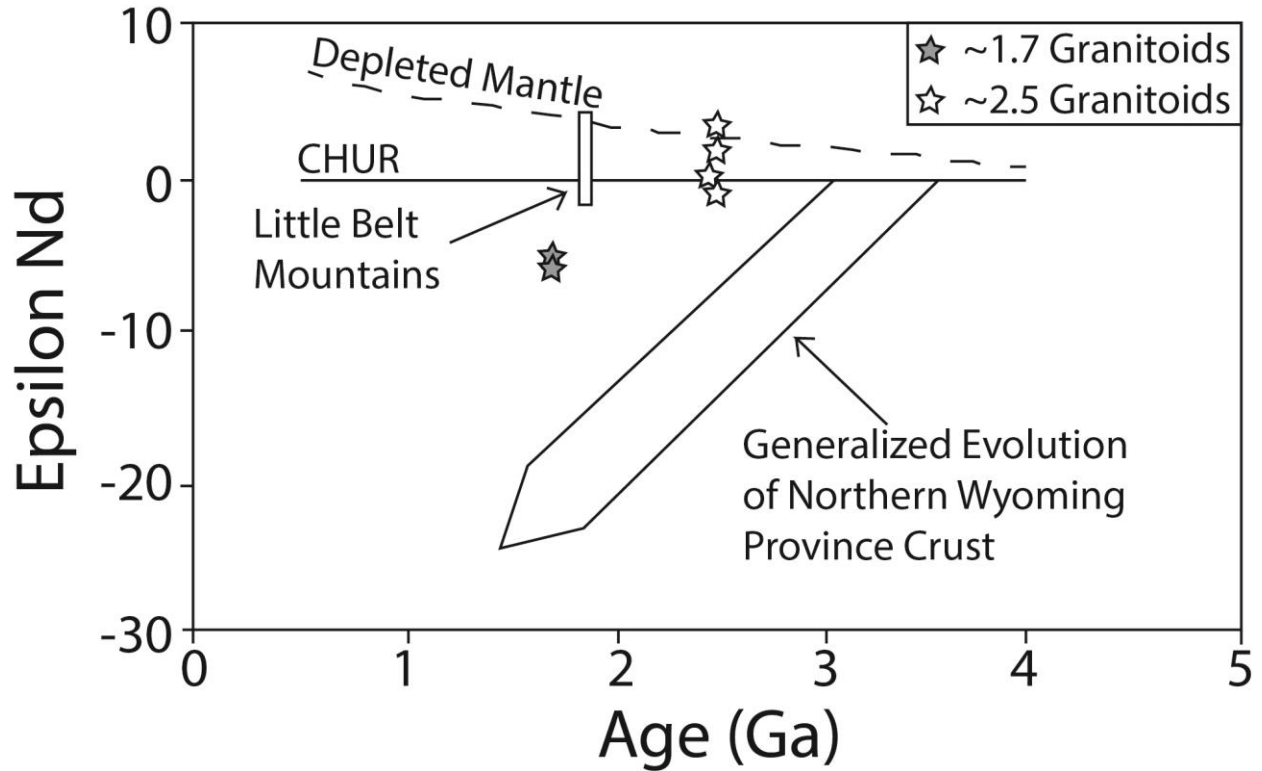


Figure 2-15. Sm-Nd evolution diagram showing the range for the ~1.7 granitoids (gray stars), ~2.5 granitoids (white stars), Little Belt mountains (white bar), and the generalized evolution of northern Wyoming province crust (Wooden and Mueller, 1988; Mueller et al., 1993; Frost, 1993). CHUR – chondritic uniform reservoir (Faure and Mensing, 2005).

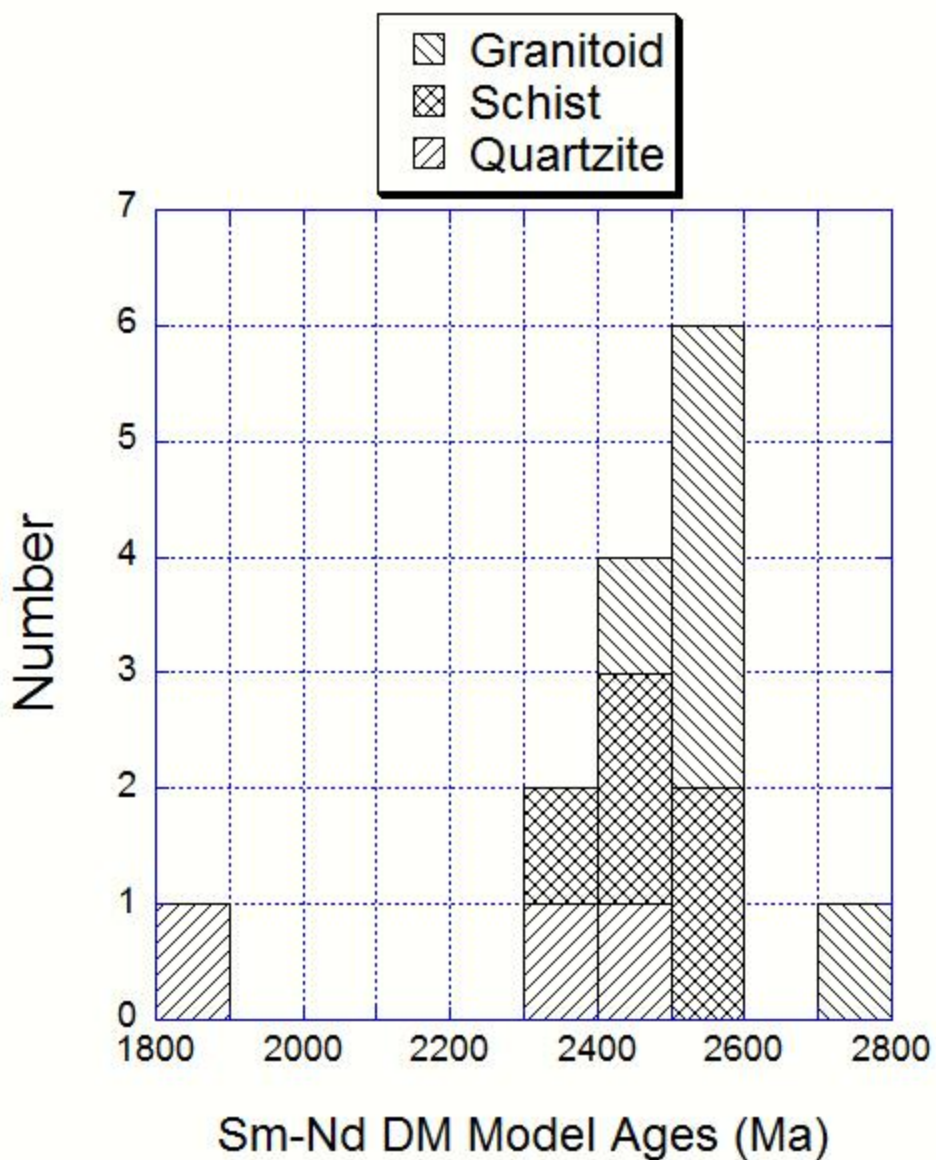


Figure 2-16. Histogram showing Sm-Nd depleted mantle model ages (Ga) of granitoid, schist, and quartzite whole rocks. Depleted Mantle model ages calculated using the model of DePaolo, 1981.

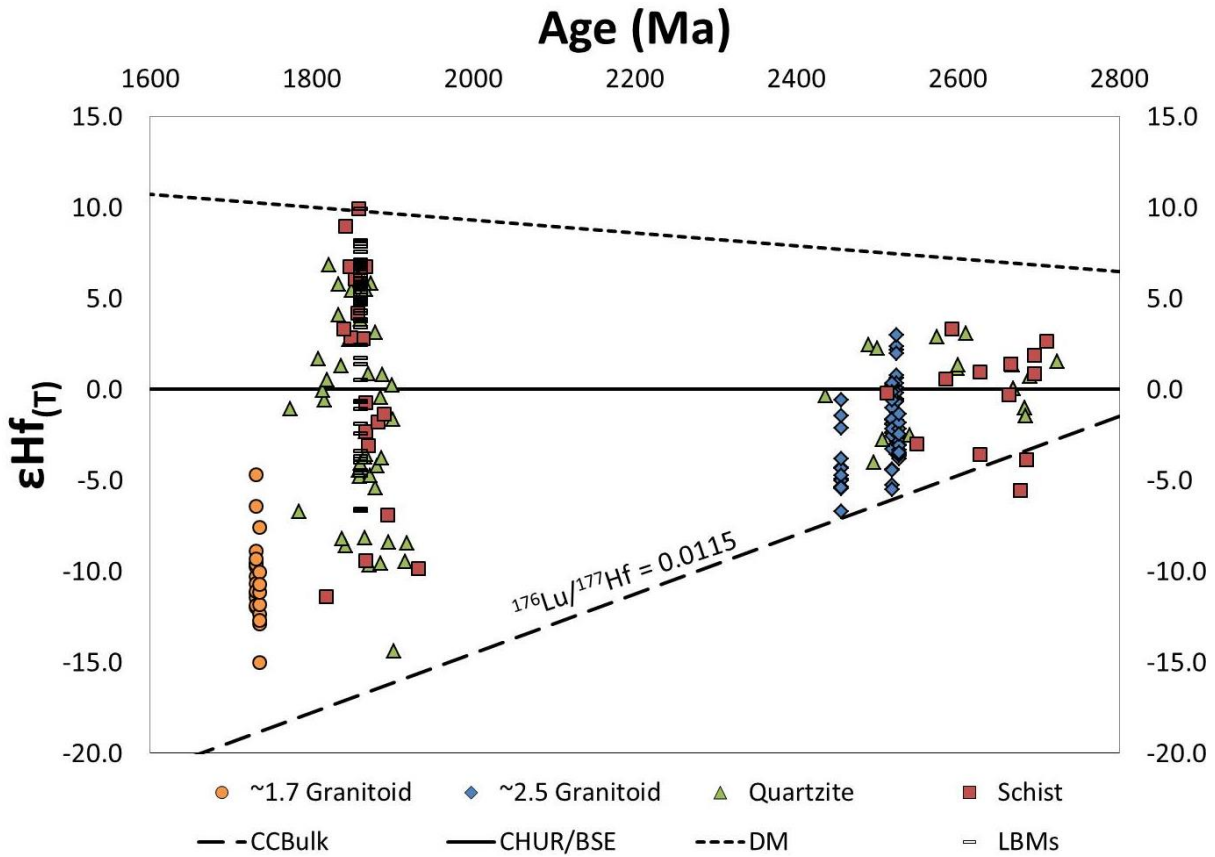


Figure 2-17. Hf evolution diagram showing the range for the ~1.7 granitoids (circles), ~2.5 granitoids (diamonds), schistose (square), quartzite (triangle), and LBMs (black dashes) from ages 1.70 Ga to 1.89 Ga and from 2.40 Ga to 2.75 Ga. CCBulk – bulk continental crust calculated using Rudnick and Gao (2003) (dashed line), CHUR – chondritic uniform reservoir, BSE – bulk silicate earth (Faure and Mensing, 2005) (solid line), DM – depleted mantle (Chauvel and Blichert-Toft, 2001)(dotted line).

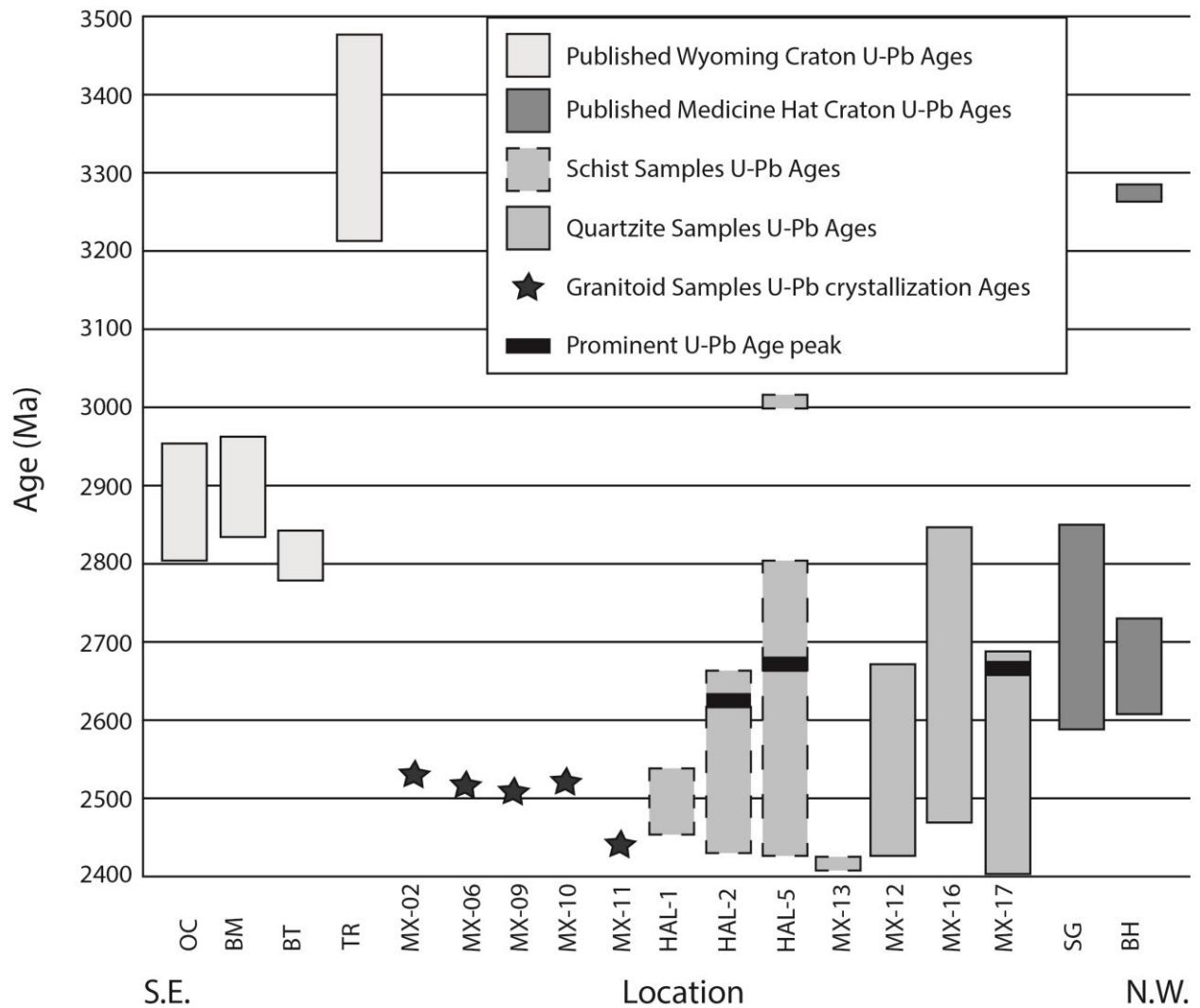


Figure 2-18. Published Archean to earliest Proterozoic U-Pb ages of zircon from the northern Wyoming craton (Heimlich and Banks, 1968; Mueller et al., 1995; Kirkwood, 2000; Mogk et al., 2004; Frost and Fanning, 2006; Mueller et al., 2010, Krogh et al., 2011) compared to published, ages for the MHB (Villeneuve et al., 1993; Davis et al., 1995). OC – Owl Creek Mountains, BM - Bighorn Mountains, BT – Beartooth Mountains, TR – Tobacco Root Mountains, SG – Sweetgrass Hills, BH – borehole. Wyoming – light gray, Medicine Hat – dark gray. Crystallization ages of granitoids from this study – stars, from schists (detrital) – medium gray with dashed lines, and quartzite (detrital) – medium gray with solid lines. Prominent age peaks from Figure 2-14 – black bars.

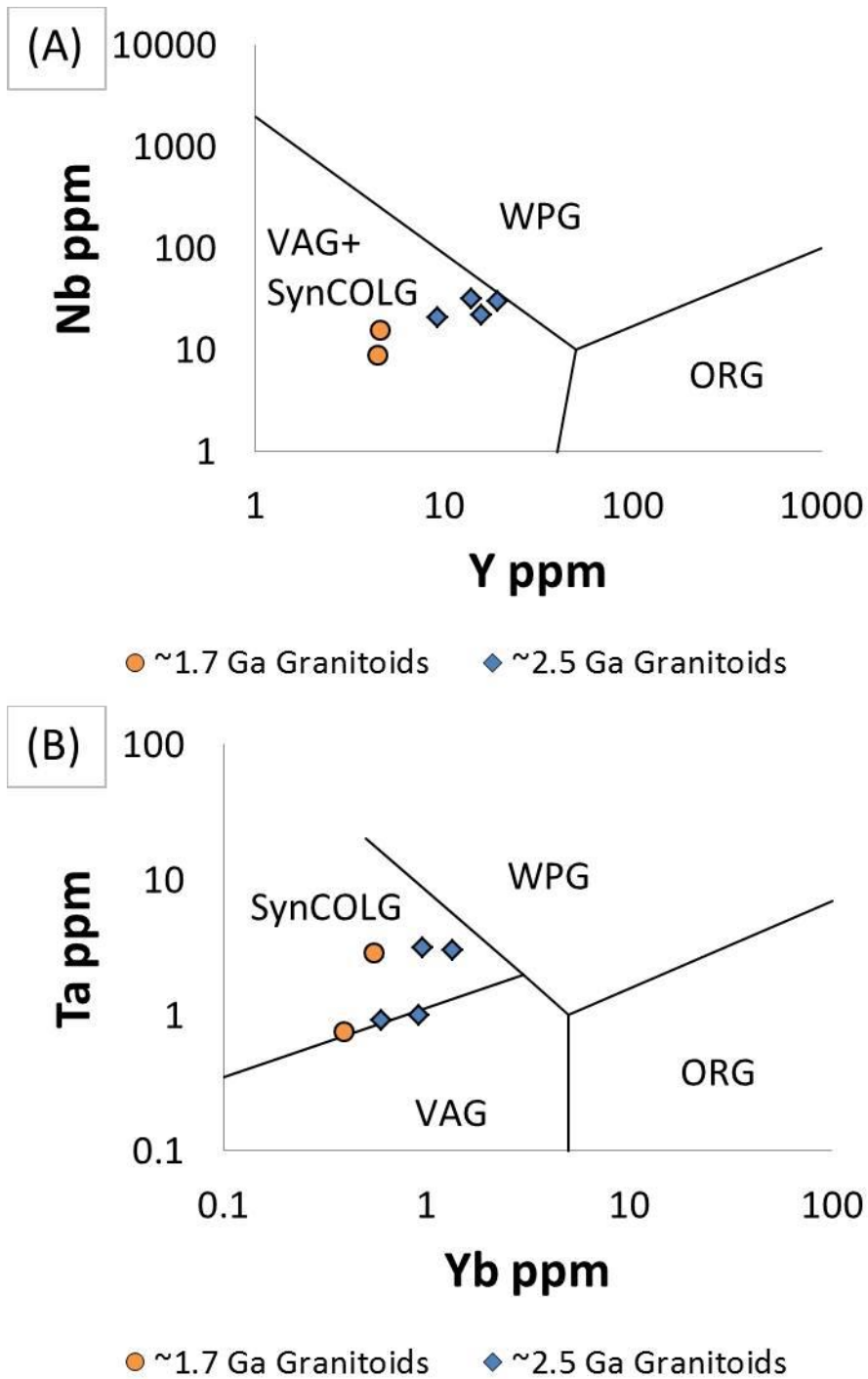


Figure 2-19. Trace element discrimination diagrams (after Pearce et al., 1984) for granitoid samples: (A) Heavy rare earth element Y ppm vs. high field strength element Nb ppm, (B) Heavy rare earth element Yb ppm vs. high field strength element Ta ppm. ~1.7 granitoids are shown in orange circles and ~2.5 granitoids are shown in blue diamonds.

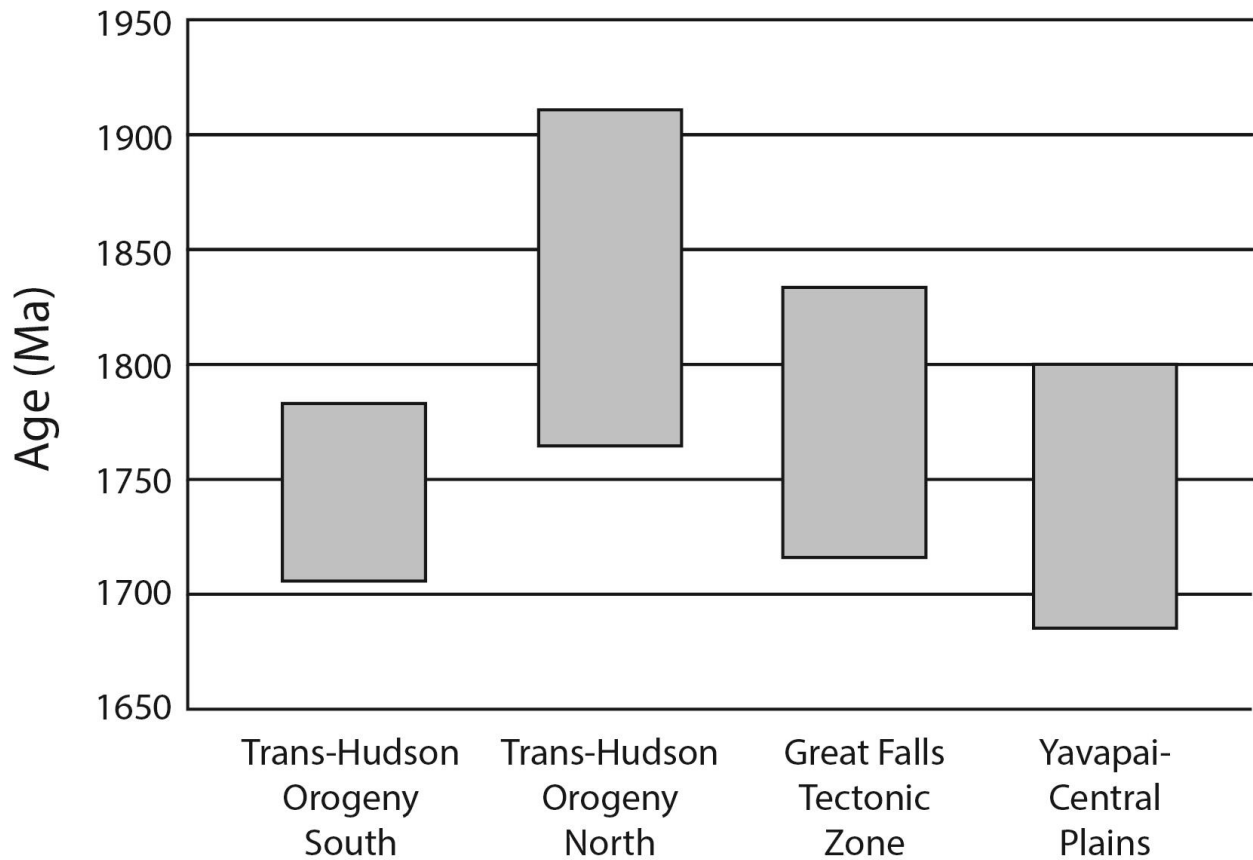


Figure 2-20. Comparison of published U-Pb ages from the southern Trans-Hudson Orogen (Karlstrom and Houston, 1984; Nelson et al., 1993; Resor et al., 1996; Dahl et al., 1999) against the northern Trans Hudson Orogen (Lewry et al., 1987; Hoffman, 1988; Bickford et al., 1990; Gordon et al., 1990; Machado, 1990; Lewry et al., 1994; Lucas et al., 1996; Sun et al., 1996; Machado et al., 1999; Mueller et al., 2002), Great Falls tectonic zone (this study), and Yavapai-Central Plains (Bickford and Boardman, 1984; Sims and Peterman, 1986; Karlstrom and Bowring, 1988; Premo and Van Schmus, 1989; Van Schmus et al., 1993; Chamberlain, 1998; Selverstone et al., 2000; Hill and Bickford, 2001; Hill, 2004).

CHAPTER 3 MISSOURI BREAKS XENOLITHS

Introduction

Laurentia is composed of a number of Archean cratons sutured together across several Proterozoic mobile belts. The Archean Wyoming Province is one of the oldest Laurentian cratons, and is surrounded on all sides by Paleoproterozoic orogenic belts and suture zones (e.g., Wooden and Mueller, 1988; Baird et al., 1996; Frost et al., 1998; Henstock et al., 1998; Foster et al., 2006; Mueller and Frost, 2006). The Proterozoic mobile belts resulted from continental margin accretion and collisions with other Archean cratons (e.g., Superior-Wyoming collision at 1.71–1.77 Ga; Nelson et al., 1993; Dahl et al., 1999), or with Proterozoic terranes (e.g., Colorado province at 1.78 Ga; Karlstrom and Houston, 1984; Chamberlain, 1998) (Figure 3-1). The Great Falls tectonic zone (GFTZ) is one such zone, proposed to have formed by convergence and collision between the Wyoming Craton and the Medicine Hat Block (MHB) to the north (Figure 3-1) (Ross et al., 1991; Pilkington et al., 1992; Baird et al., 1996; Mueller et al., 2002; Gorman et al., 2002; Sims et al., 2004).

The Great Falls tectonic zone was first described as a Paleoproterozoic suture zone between the Hearne Craton and the Wyoming Province by O'Neill and Lopez (1985). Geochronologic and geochemical data by Mueller et al. (2002), taken from meta-igneous gneisses in the Little Belt Mountains (LBM), reveal a subduction-generated igneous arc signature in rocks formed during the interval of 1.9 Ga to 1.8 Ga. Further support came from Roberts et al. (2002) who obtained biotite $^{40}\text{Ar}/^{39}\text{Ar}$ and $^{207}\text{Pb}/^{206}\text{Pb}$ step-leached garnet ages from the Montana meta-sedimentary terrane (MMT, Figure 3-1) and interpreted them to reflect a metamorphic event between 1.82

and 1.79 Ga, followed by post-tectonic cooling between 1.78 and 1.74 Ga. Pressure-temperature-time paths (Harms et al., 2004) from three metamorphic suites from the Tobacco Root Mountains and metamorphosed mafic dikes and sills revealed crustal thickening, metamorphism, and partial melting occurring between 1.78 and 1.76 Ga. An alternative origin for the GFTZ was suggested by Boerner et al. (1998), who hypothesized that the GFTZ is an intra-continental shear zone, and that the MHB and Wyoming cratons are contiguous units. They proposed that the Hearne-Wyoming suture is associated with the Vulcan magnetic structure (Ross, 1991; Henstock et al. 1998; Boerner et al., 1998; Figure 3-1) and that, based on geophysical models, there is a continuity of lithosphere throughout the GFTZ and northern Wyoming Province. This interpretation would then link the histories of the northern Wyoming Province and the MHB (e.g., Buhlman et al., 2000; Boerner et al., 1998).

Crustal xenoliths entrained in Cenozoic magmas erupted in the Montana Alkali Province afford a unique opportunity to characterize the age and chemistry of the subsurface of the GFTZ. This paper expands on crustal xenolith data from the Grassrange diatremes, Montana presented by Gifford et al. (in review) (Chapter 2). Whole-rock major and trace element geochemistry, whole-rock Sm-Nd isotopes, and zircon U-Pb geochronology and Hf-isotopic compositions were obtained from 17 crustal xenoliths from 5 additional locations within the Montana Alkali Province (Figure 3-2). Three xenoliths from the Big Slide diatreme (Missouri Breaks), 5 xenoliths from the Little Sand Creek diatreme (Bearpaw Mtns.), 4 xenoliths from the Robinson Ranch diatreme (Bearpaw Mtns.), 4 xenoliths from a location within the Bearpaw Mountain volcanics called Lloyd Divide, and 1 xenolith from the Highwood Mountains were included in this

study (Figure 3-2), which seeks to further define the timing of ocean closure and collision between the MHB and the Wyoming Province, as well as test models for the Paleoproterozoic evolution of the Great Falls tectonic zone.

Geologic Background

The Wyoming Craton and the largely concealed Medicine Hat block (Figure 3-1) are separated by the Great Falls tectonic zone (GFTZ), a region of Paleoproterozoic tectonic activity (c. 1.86 to 1.71 Ga) that likely records the closure of an ocean basin (Giletti, 1966; O'Neill and Lopez, 1985; Mueller et al., 2002; Harms et al., 2004). The timing of tectonic activity in the GFTZ is of particular interest due to its overlap with the Laurentia-forming collisions in the Trans-Hudson orogen (c. 1.83–1.72 Ga; Bickford et al., 1990; Dahl et al., 1999).

Documentation of the MHB is largely from aeromagnetic and seismic data, supplemented by samples from a few deep boreholes (e.g., Ross, 2002). Geochronology of crystalline basement collected from cores penetrating MHB crust reveals a range of ages from 3.27 Ga to 2.65 Ga (Villeneuve et al., 1993). The northern boundary of the block is the aeromagnetically defined Vulcan low, interpreted by Ross (2002) to mark a Proterozoic collision between the Medicine Hat Block and the Hearne Craton. Basement rocks are exposed in three main areas of the northwestern Wyoming craton (Bighorn and Beartooth ranges of the Bighorn-Beartooth magmatic zone, and the Madison, Tobacco Root, etc. of the Montana Meta-sedimentary Terrane), uplifted by Laramide thick-skinned thrusting. These uplifts are identified as sharing a common heritage primarily due to their similar Pb-isotopic data (Wooden et al., 1988; Mogk et al., 1992; Chamberlain et al., 2003; Frost, 1993; Mueller and Frost, 2006). Meta-igneous rocks of the Montana meta-sedimentary province record ages from 3.3 Ga to 3.1 Ga

(Mueller et al., 1996). The Beartooth and Bighorn mountains contain abundant metamorphosed tonalite-trondhjemite-granodiorite (TTG) suites with protolith ages between 2.9 to 2.8 Ga (Frost et al., 2006a; Mueller et al., 2010). The southern Wyoming Craton contains igneous arc terranes formed and accreted at 2.68 Ga to 2.5 Ga (Frost et al., 2006b). Dike emplacement at ~2.1 Ga is recorded across the Wyoming craton, possibly related to a period of Paleoproterozoic rifting (Premo and Van Schmus, 1989; Cox et al., 2000; Mueller et al., 2004).

The Great Falls tectonic zone of North-Central Montana hosts numerous occurrences of Cenozoic alkalic magmatism and diatreme emplacement. These include localities in the Bearpaw Mountains, Highwood Mountains, Sweetgrass Hills, Crazy Mountains, and the Grassrange and Missouri Breaks diatreme swarms (Figure 3-2). Many of these localities contain crustal and upper mantle xenoliths (Collerson et al., 1989; Hearn, 1989; Hearn et al., 1989; Joswiak, 1992; Carlson and Irving, 1994; Downes et al., 2004; Bolhar et al., 2007; Facer et al., 2009; Blackburn et al., 2010, 2011). Crustal xenoliths described in this study are from the Highwood Mountains, Big Slide Diatreme, Robinson Ranch diatreme, Little Sand Creek diatreme, and Lloyd Divide locality; xenoliths are carried by Eocene minettes (54–50 Ma) of the Bearpaw Mountain volcanic field (Marvin et al., 1980; Hearn, 1989; MacDonald et al., 1992). U-Pb ages of zircons from xenoliths collected in the Little Sand Creek locality are from ca. 3.0 to 1.8 Ga (Bolhar et al., 2007). Mafic granulite xenoliths from the Grassrange Hills yield ages at c. 1.8 Ga, and Sm-Nd isochrons (garnet, clinopyroxene, and whole rock) ranging from 1.7 to 1.5 Ga (Davis et al., 1995), which may represent either metamorphosed Archean crust or an addition to the lower crust ca. 1.8 Ga. Barnhart et

al. (2012) analyzed 5 granulite xenoliths from the Robinson Ranch diatreme ranging from mafic to felsic in nature, and dating was done on monazite grains using the U-Th-total Pb procedure and yielded three age populations: c. 1.3 Ga to c. 1.5 Ga; c. 1.7 Ga to c. 1.8 Ga; and c. 2.0 Ga to c. 2.1 Ga. Barnhart et al. (2012) interpreted these populations as representing an incremental assembly of the high velocity lower crustal layer suggested by Gorman et al. (2002) during the formation of the GFTZ.

Sample Descriptions

Big Slide Diatreme

BSD10-04 is a medium to fine grained quartzofeldspathic meta-leuco-granitoid. Plagioclase occurs as annealed, rounded, and sutured grains 0.5 – 2 mm in diameter, and comprising ~40% of the sample. Quartz grains are anhedral, lobate, and up to 2 mm in diameter. Undulose extinction is present in many quartz grains. Trace occurrences of perthitic K-feldspar, biotite, muscovite, and opaque phases are also present. BSD10-05 is a mafic meta-granitoid (Figure 3-4A). Biotite is the dominant phase, occurring both as large clots that appear pseudomorphic after pyroxene or amphibole, and finer grains scattered throughout the matrix. The matrix is dominated by fine-grained plagioclase (>1 mm), although a few large (≥ 4 mm) grains of plagioclase are present as well. BSD10-06 is a medium-grained garnet granulite with abundant clinopyroxene. It exhibits granoblastic texture with individual grains ranging up to 2 mm in diameter.

Robinson Ranch Diatreme

RRD10-05 is an amphibole biotite meta-granitoid (Figure 3-3B). Amphibole occurs as (≥ 2 mm), anhedral grains with biotite reaction rims, and are not oriented. The biotite is unaltered and generally in contact with the amphibole grains. Plagioclase

and microcline are subhedral and blocky, with a wide range of grain sizes (<1 – 3 mm in diameter). Quartz is abundant, generally anhedral to subhedral, and shows a similar range of sizes to the feldspar grains. The sample shows fractures. Sample RRD10-09 is similar, but displays a finer grained texture and more extensive alteration in the form of larger biotite reaction rims around amphibole and sericitized feldspars. RRD10-13 is a garnet granulite with 2-3 mm subhedral poikilitic garnets, which contain abundant fractures and rounded quartz and feldspar inclusions. There are domains rich in fine-grained blocky sericitized plagioclase and anhedral quartz. Annealing textures on some of the quartz is common as well. Trace amounts of muscovite and biotite are scattered throughout the matrix. The sample shows abundant fractures as well as high temperature hornblende and pyroxene veins. Evidence suggests that the sample underwent retrogressive metamorphism at amphibolite facies. RRD10-20 is a highly altered and highly retrogressively metamorphosed dioritic granulite. The sample contains large amounts of hornblende and biotite. There are sections which appear to have been recrystallized, and clots of biotite contain cores which might have been pyroxene. Fine-grained recrystallized, elongate quartz grains and ribbons range throughout the sample.

Little Sand Creek Diatreme

LSC10-03 is a fine to medium grained, lineated, biotite and amphibole rich rock (Figure 3-3C). Amphibole is approximately 1 – 2 mm long and subhedral, with some grains showing poikilitic texture and containing inclusions and/or alteration minerals. Plagioclase grains are up to 3 mm in diameter, blocky, and generally subhedral. Quartz occurs as finer subhedral grains, up to 0.3 mm in diameter and many grains display undulose extinction. Preferred orientation of amphibole grains defines a lineation, with

a weak compositional layering between amphibole-rich and quartzofeldspathic-rich domains defining a fabric. There are large amounts of opaque minerals. LSC10-10 is a fine to medium grained amphibolite. Amphibole is subhedral and generally ≤ 0.5 mm in length, although the grain size varies in compositional bands through the sample. There is fracturing and alteration throughout different zones of the sample. Plagioclase occurs as subhedral and blocky grains up to 0.5 mm in diameter, with grain size varying depending on the layer. LSC10-13 is a mafic granulite gneiss. Biotite is present, but does not form a foliation within the sample. Minor amounts of anhedral plagioclase are scattered around the sample. Euhedral grains of amphibole and clinopyroxene are up to 2 mm, blocky, and prevalent throughout the sample. LSC10-11 is a highly altered mafic gneiss (Figure 3-4B). The sample contains foliated clots of intergrown high temperature mafic minerals as well as highly altered amphibole and plagioclase. Chlorite and biotite are present throughout the sample along with abundant opaques. LSC10-12 is a highly altered and silicified meta-granitoid (Figure 3-4C). Potassium-feldspar grains display tartan-twinning, and twinned plagioclase and quartz are present. There is highly chloritized biotite as well as trace amounts of muscovite. The plagioclase grains are pervasively sericitized and clay-altered. Within the plagioclase grains, there is evidence of myrmekitic texture.

Bearpaw Mountains At Lloyd Divide

Samples LD10-01 (Figure 3-3A), LD10-07, and LD10-08 are garnet quartzofeldspathic gneisses. Compositional banding is defined by garnet rich and quartzofeldspathic layers. Garnet grains are up to 1 mm and are anhedral. Quartz and plagioclase is finer and anhedral, although some plagioclase grains are blocky. LD10-

11 appears to be 98% coarse quartz (>1 cm in diameter), with trace amounts of amphibole and pyroxene.

Highwood Mountains

Sample HX-1 is a biotite quartzofeldspathic gneiss. The sample contains biotite-rich and K-feldspar-rich bands, which are several mm thick. The sample fabric is defined by several elements: a biotite foliation; recrystallized, elongate quartz grains and ribbons; and plagioclase feldspar augen.

Results

U-Pb and Lu-Hf data from igneous and metamorphic zircons in addition to whole-rock geochemical and isotopic data from xenoliths collected from three Eocene diatremes in the Missouri Breaks, as well as one from the Bearpaw Mountain extrusives, and one xenolith from the Highwood Mountains are presented below. Sample locations are shown in Figure 3-2. Methods are described in Appendix A. Geochemical and isotopic data and the latitude and longitude of the sample locations are summarized in Tables B-4 through B-6 (Appendix B).

Whole-Rock Geochemistry

All of the samples from this study (except LD10-11) are meta-igneous. Representative photomicrographs are shown in Figure 3-3 and 3-4. The samples have silica contents ranging from 48 to 74 wt. %. Sample LD10-11 is a silica-rich (98% silica) igneous rock. As a result, this sample is not considered further for geochemical results. The xenoliths represented by blue diamonds in Figure 3-5 (molar Al/(Na+K) vs. molar Al/(Ca+Na+K) cluster along the metaluminous – peraluminous boundary. Trace element geochemistry (Table 3-1 and 3-2) of the meta-igneous xenoliths is summarized in Figure 3-6A (contents normalized to primitive mantle values of McDonough and Sun,

1995). The plots show enrichments in some fluid mobile incompatible elements, such as Rb, Ba, and Pb, up to 750 times the primitive mantle values. This relative enrichment is paired with minimal enrichment in fluid immobile trace elements, including heavy REE. This is a typical pattern in modern convergent margin rocks (e.g., Thompson et al., 1984). Figure 3-6B shows rare earth element data from the meta-igneous xenoliths normalized to the chondritic values of McDonough and Sun (1995). The samples show variability in the values of Eu and Sr relative to elements of similar compatibility. These include both negative and positive anomalies in Eu and Sr. Nb and Ta are depleted relative to the observed values for neighboring elements in all of the samples when normalized to primitive mantle, with the exception of orthogneiss HX-1.

U-Pb Geochronology Of Zircon

Zircon analyses used for age calculations were limited to those with discordance $\leq 10\%$. This is an arbitrary, but commonly adopted, standard filter used to screen out disturbed analyses. For each sample, zircon analyses with ages that do not overlap within error of the main population's mean and standard deviation are considered "outliers" and are excluded from further age calculations. In some cases, ages define discordia which trend to Proterozoic metamorphic events, Cambrian exhumation and exposure, or recent Pb-loss. In those samples where there appears to be a metamorphic age, the U concentration in the sample can be examined to discriminate between metamorphic and igneous zircon growth. During metamorphism, fluids can oxidize the U in a rock to the +6 valence state, increasing its solubility (e.g., Rubatto 2002). Because the U is fluid mobile, this leads to any zircons that crystallized under

those conditions to have higher U values. Metamorphic zircons can potentially have higher ^{238}U cps relative to the mean of the main populations of zircons within a sample.

Big Slide diatreme yielded 3 meta-igneous samples large enough for whole rock geochemistry and zircon separation (~10-20 cm diameter). BSD10-06 is a garnet granulite and yielded only 2 zircon grains, both of which had discordance $\leq 10\%$. One grain was 1.74 ± 0.02 Ga and the other was 1.83 ± 0.01 Ga (Table 3-3). BSD10-04 yielded 60 zircons, 55 of which show discordance $\leq 10\%$ (Figure 3-7A). The younger zircons range from 1.59 ± 0.01 to 1.84 ± 0.02 Ga. The concordia plot of grains $\leq 10\%$ discordant, and with $< 3\%$ $^{206}\text{Pb}/^{238}\text{U}$ error, reveals scatter suggestive of disturbance to the zircon U-Pb system (Figure 3-7B). To assist with determining a metamorphic age of the sample, the U intensity in each analysis was examined. Those grains with ^{238}U cps significantly higher than the mean of the main population (i.e., grain: 1,360,220 cps vs. mean of population: 546,312 cps) may represent metamorphic zircons. Statistically, the mean $^{207}\text{Pb}/^{206}\text{Pb}$ crystallization ages of the high U grains cannot be distinguished from the mean $^{207}\text{Pb}/^{206}\text{Pb}$ crystallization ages of the low U grain, so U intensities are not a useful discriminator in this case. A weighted mean calculated from all of the $\leq 10\%$ discordant grains, including those with high U intensities, yields a metamorphic age of 1.72 ± 0.01 Ga. When Hf was analyzed in these zircons, it was observed that there was a very large disconnect between the U-Pb ages and the Hf model ages (discussed below), leading to the conclusion that the age of BSD10-04 should be older than the 1.72 Ga mentioned above. Because of this, a single Archean-aged grain (2.68 ± 0.4 Ga) with anomalously high error (i.e., 3.9% on $^{206}\text{Pb}/^{238}\text{U}$) contained in BSD10-04 is believed to be an approximation of the minimum igneous crystallization age for this

sample. Data are summarized in Table 3-3. BSD10-05 yielded 46 zircons with discordance $\leq 10\%$ which yielded an upper intercept minimum metamorphic crystallization age of 1.74 ± 0.01 Ga (Figure 3-8).

Little Sand Creek diatreme yielded 5 meta-igneous samples large enough for whole rock geochemistry and zircon separation (~10-20 cm diameter). LSC10-03 and LSC10-10 are amphibolites, LSC10-11 is a mafic gneiss, LSC10-12 is a meta-granitoid, and LSC10-13 is a mafic granulite. Data are summarized in Table 3-3. Four of these samples are discussed in the following paragraph, but LSC10-12 did not yield a crystallization age and is discussed later. LSC10-03 yielded 49 grains with discordance $\leq 10\%$, which yielded an upper intercept interpreted as a minimum igneous crystallization age of 1.81 ± 0.01 Ga (Figure 3-9A). LSC10-10 yielded 26 grains with discordance $\leq 10\%$, which yielded an upper intercept minimum igneous crystallization age of 1.79 ± 0.1 Ga (Figure 3-9B). LSC10-13 yielded 48 grains with discordance $\leq 10\%$, 1 was excluded because of high error (i.e., 185 Ma on $^{206}\text{Pb}/^{238}\text{U}$ and 97 Ma on $^{207}\text{Pb}/^{235}\text{U}$), and 4 outliers were excluded. Forty-four grains yielded an upper intercept on concordia of 1.78 ± 0.03 Ga, which approximates a minimum age for LSC10-13 (Figure 3-9C). LSC10-11 yielded 50 zircons with discordance $\leq 10\%$ (Figure 3-10A), including a group of older zircons (~2.75 to 3.14 Ga) which were determined to be xenocrystic based on their Hf values, and have been excluded from age calculations. When all of the grains (excluding those interpreted as xenocrysts) are plotted on concordia, the upper intercept of the discordia line is 2.61 ± 0.07 Ga, which is interpreted as an approximate igneous crystallization age for the sample (Figure 3-10B).

The lower intercept of the discordia line, interpreted as an approximate metamorphic age is 1.65 ± 0.1 Ga. These data are summarized in Table 3-3.

Robinson Ranch diatreme yielded 4 meta-igneous samples large enough for whole rock geochemistry and zircon separation (~10-20 cm diameter). Data are summarized in Table 3-3. Three of these samples are discussed in the following paragraph, but RRD10-20 did not yield a crystallization age and is discussed later. RRD10-05 (meta-granitoid) yielded 32 zircons ($\leq 10\%$ discordance), and 2 outliers were excluded. Thirty grains ($\leq 10\%$ discordance) yielded a minimum igneous crystallization age of 1.89 ± 0.01 Ga (Figure 3-11A). RRD10-09 (meta-granitoid) yielded 52 zircons with discordance $\leq 10\%$, 2 of which were excluded as outliers. Fifty grains yielded a minimum igneous crystallization age of 1.88 ± 0.01 Ga (Figure 3-11B). RRD10-13 (garnet granulite) yielded 37 zircons with discordance $\leq 10\%$ which lie in 2 clusters along concordia with a single younger grain separated (Figure 3-12A). The five grains in the older cluster yield an upper intercept age of 1.87 ± 0.01 Ga (Figure 3-12B), which is interpreted as a minimum igneous crystallization age for the sample.

The Lloyd Divide location in the Bearpaw Mountains yielded 1 igneous and 3 meta-igneous xenoliths large enough for whole rock geochemistry and zircon separation (~10-20 cm diameter). LD10-01, LD10-07, and LD10-08 are orthogneisses, and LD10-11 is a silica-rich igneous rock. Zircons from LD10-07 and LD10-08 reveal two distinct populations of $^{207}\text{Pb}/^{206}\text{Pb}$ ages, which are separated by > 500 Ma and do not overlap at the 2σ level, but do lie along a discordia (Figure 3-11, 3-12). LD10-07 yielded 55 zircons, only 4 of which had discordance $\leq 10\%$, and one that was excluded because of large measurement error (i.e., $> 3\%$ on $^{206}\text{Pb}/^{238}\text{U}$ and $^{207}\text{Pb}/^{235}\text{U}$). When all of the

grains are plotted on concordia, the upper intercept of the discordia line is 2.62 ± 0.05 Ga, which is interpreted as an approximate igneous crystallization age for the sample (Figure 3-13). Data are summarized in Table 3-3. To assist with determining a metamorphic age, ^{238}U cps were examined. Both of the low discordance analyses contained high ^{238}U cps relative to the mean of the main population (i.e., grain: 3,455,340 and 6,304,710 cps vs. mean of population: 956,443 cps). A weighted mean of the 2 low discordance analyses yields an age of 1.75 ± 0.19 Ga, which corresponds to documented tectonothermal events in the region and is interpreted as a poorly defined minimum metamorphic age for this sample. LD10-08 yielded 60 grains, 32 of which had discordance between 0 and 10% (Figure 3-14A). This yielded a discordia with an upper intercept of 2.44 ± 0.07 Ga, interpreted to be a minimum igneous crystallization age. When the 30 youngest zircons within the sample, (~ 1.60 to 1.84 Ga) are plotted on concordia, (Figure 3-14B), it is clear that there is a complex Pb-loss pattern within the sample. Seven grains show high ^{238}U cps relative to the mean of the main population (i.e., grains: 16,126,100 to 10,220,000 cps vs. mean of population: 3,030,927 cps). Statistically, the mean $^{207}\text{Pb}/^{206}\text{Pb}$ crystallization ages of the high U cps grains cannot be distinguished from the mean $^{207}\text{Pb}/^{206}\text{Pb}$ crystallization ages of the low U cps grains, so U intensities are not a useful discriminant in this case. When a weighted mean was taken on all of the $\leq 10\%$ discordant grains, an age of 1.71 ± 0.03 Ga was calculated. This is interpreted to be a minimum metamorphic age for this sample. LD10-01 yielded 50 grains, only 43 with discordance $\leq 10\%$. Figure 3-15A shows a concordia diagram with all 50 analyses. A discordia calculation (Figure 3-15A) yielded an upper intercept age of 2.52 ± 0.08 Ga, which is interpreted as a minimum

igneous crystallization age for this sample. Figure 3-15B shows the cluster of Paleoproterozoic-age zircons with discordance $\leq 10\%$. The ages range from 1.57 to 1.85 Ga. Because of the scatter, ^{238}U cps were examined. Four grains show high ^{238}U cps (i.e., grains: 21,978,800 to 7,620,440 cps vs. mean of population: 1,723,033 cps). Statistically, the high U grains cannot be distinguished from the low U grains, so U intensities are not a useful discriminant in this case. A weighted mean of all of the grains that show discordance $\leq 10\%$ yields an age of 1.74 ± 0.02 Ga, interpreted as a minimum metamorphic age (Table 3-3). LD10-11 yielded 63 grains, 43 of which showed discordance $\leq 10\%$, and 6 grains that are outliers and were excluded. 37 grains were used to calculate a minimum igneous crystallization age for the sample of 1.78 ± 0.03 Ga (Table 3-3, Figure 3-16).

One orthogneiss xenolith (HX-1) was found within the Highwood Mountains. Data are summarized in Table 3-3. Out of 22 grains, only 19 had discordance $\leq 10\%$, one of which was an outlier and was excluded. In a pattern similar to the orthogneisses from the Grassrange (MX-06, MX-09, MX-10, and MX-11) (Chapter 2), HX-1 yielded an igneous crystallization age as well as an age of metamorphism (Figure 3-17A). The youngest four grains with discordance $\leq 10\%$ yielded an upper intercept of 1.85 ± 0.01 Ga, interpreted as a minimum metamorphic age (Figure 3-17B). The oldest 4 grains similarly yielded an upper intercept of 2.65 ± 0.01 Ga, interpreted as a minimum igneous crystallization age for HX-1 (Figure 3-17C). The remaining zircon grains yield intermediate ages that lie along a mixing line (discordia) between the older and younger ages.

Samples RRD10-20 (dioritic granulite) and LSC10-12 (meta-granitoid) show signs of retrograde metamorphism disturbing the U-Pb isotopic system, and complicating any interpretations. Both samples show a common age of zircons from ~1.7 to 1.8 Ga, which can be attributed to possible metamorphism within the GFTZ. The age-data are complex and show indeterminate age relationships (Table B-5). Sample RRD10-20 (Figure 3-18A) yielded a dominant population ranging from ~2.21 to 2.59 Ga, which is likely an igneous population, but Pb-loss has affected the sample to the extent that an igneous crystallization age determination would be speculative at best. There are grains ranging in age from ~2.73 to 3.24 Ga that appear to be from a variety of sources based on their Hf isotopes (discussed below). The older grains appear to lie along a discordia, but do not display Hf systematics indicating they came from the same (or similar) sources, so a discordia regression is not viable. LSC10-12 (Figure 3-18B) yielded a dominant population of zircons at ~2.8 Ga. There is a scattering of older grains (~3.0 to 3.3 Ga) which appear to be from a variety of sources based on their Hf isotopes (discussed below). LSC10-12 also yielded a population of 14 grains that range in age from 1.92 to 1.68 Ga, which is an indication that the sample was affected by the wide-scale metamorphism within the GFTZ.

Hf Isotopes In Zircon

Zircons were selected for Lu-Hf analysis based on different factors. Samples were arranged by $^{207}\text{Pb}/^{206}\text{Pb}$ age to choose a representative population of ages for Hf analysis. Zircons were preferentially chosen for low discordance (as discussed above) to increase the likelihood of an accurate U-Pb age with which to reduce the Hf isotopic data. Zircons were further chosen based on zonation and grain size. If a zircon showed zonation and a U-Pb analysis was undertaken in a particular domain, ideally,

the Hf spot would also be within the same domain. The Hf spot-size is 40 μ m, and the zircon (or zonation) needed to be large enough to accommodate the spot. $\epsilon\text{Hf}_{(\text{initial})}$ calculations used the calculated igneous crystallization ages for the individual meta-igneous samples (Table 3-3). Hf T_{DM} ages are minimum mantle separation ages due to uncertainties in source initial Hf isotopic composition (e.g., Griffin et al., 2002). Two methods of $\epsilon\text{Hf}_{(\text{initial})}$ calculations are discussed: Calculations using the concordia igneous crystallization age of a given sample, and calculations based on the individual $^{207}\text{Pb}/^{206}\text{Pb}$ ages (IA) from each zircon. Both sets of $\epsilon\text{Hf}_{(\text{initial})}$ values are recorded in Table 3-3. These values were averaged and a standard deviation and median taken to estimate the variance of isotopic values about the mean (Table 3-3). If the median and average are within measurement error of each other, then standard deviation is likely to be a good estimate of the dispersion of the data. The meta-igneous samples are plotted on Figure 3-19, ($^{207}\text{Pb}/^{206}\text{Pb}$ age vs. initial ϵHf) portrayed by blue diamonds.

Xenoliths LD10-01, LD10-08, and LSC10-11 yielded zircon ages that followed the pattern seen in orthogneiss xenoliths MX-06, MX-09, MX-10, and MX-11 from the Grassrange (Chapter 2). The samples yielded upper intercept (igneous crystallization) U-Pb ages ranging from 2.44 Ga to 2.61 Ga. Zircon $\epsilon\text{Hf}_{(\text{IA})}$ values for the samples range from -1.8 to -27.7 (Table 3-3), while $\epsilon\text{Hf}_{(2.4-2.6 \text{ Ga})}$ values for the samples range from 6.9 to -16.9 (Table 3-3). The more negative $\epsilon\text{Hf}_{(2.4-2.6 \text{ Ga})}$ values are likely the result of source compositions ranging from DM-like material to evolved (crustal-like) material. Averages of the $\epsilon\text{Hf}_{(2.4-2.6 \text{ Ga})}$ values for each sample range from -0.4 to -11.5, with standard deviations of 3.0 to 3.7 (Table 3-3). ϵHf values for analyses of younger zircon (i.e., Paleoproterozoic) are similar to those of Archean concordant grains when

calculated to the igneous crystallization age of the sample. This suggests that the Paleoproterozoic analyses reflect Pb loss along discordia, and not younger zircon growth, and further suggests that the Hf isotopic system remained primarily closed during metamorphism. These samples give a range of depleted mantle model ages (T_{DM}) from 2.77 Ga to 3.32 Ga (Table 3-3).

Sample LD10-07 also yielded ages that followed the pattern seen in orthogneiss xenoliths MX-06, MX-09, MX-10, and MX-11 from the Grassrange (Chapter 2). However, when Hf data were reduced using the upper intercept concordia ages calculated for LD10-07 (~2.62 Ga), certain grains yielded $\epsilon Hf_{(2.6 \text{ Ga})}$ that plot above DM values. When the measured $\epsilon Hf_{(observed)}$ values are plotted on a probability density plot (Figure 3-20A,B), it becomes evident that the Hf data yields a bimodal distribution. This is a clear indication that during the ~1.75 Ga metamorphic event new zircon growth integrated Hf with higher ϵ values. $\epsilon Hf_{(observed)}$ values for these metamorphic (labeled as “Met.” on Figure 3-20A) grains range from -48 to -54 (Figure 3-20A) as opposed to the magmatic grains (labeled as “Mag.” on Figure 3-20A) that do not appear to have incorporated new Hf which range from -56 to -62 (Figure 3-20A). Similarly, the Hf depleted mantle model ages (Hf T_{DM}) also appear to be bimodal (Figure 3-20B) with averages of 2.62 and 2.88 Ga and standard deviations of 0.06 and 0.04 for the metamorphic and magmatic respectively for LD10-07.

BSD10-04 primarily yielded Paleoproterozoic-age zircons. When $\epsilon Hf_{(1.8)}$ was calculated, the values were suspiciously low, ($\epsilon Hf_{(1.8)} = \sim -30$; Table 3-3), and Hf $T_{(DM)}$ ages were calculated and yielded ages of ~3.4 Ga, indicating a much older crustal source was involved in the sample petrogenesis. However, when $\epsilon Hf_{(2.7)}$ was calculated

for the sample based on the single U-Pb analysis mentioned above, the calculated values shifted from ~ -30 to -12 which fits the evolution model of the Archean-age xenoliths better than the values calculated at ~1.8 Ga. When plotted on Figure 3-19, the sample lies along a reasonable Lu-Hf crustal evolution curve indicating the sample was primarily a crustal melt. Zircon $\epsilon\text{Hf}_{(2.7 \text{ Ga})}$ ranged from -9.4 to -14.0 (Table 3-3), $\epsilon\text{Hf}_{(\text{IA})}$ values ranged from -30.9 to -37.7 (Table 3-3), and BSD10-04 average zircon Hf $T_{(\text{DM})}$ calculated to 3362 Ma.

For the Paleoproterozoic samples (LSC10-03, LSC10-10, LSC10-13, RRD10-05, RRD10-09, RRD10-13 and LD10-11) the measured Hf isotopic compositions for all zircons were recalculated to the U-Pb igneous crystallization ages ($\epsilon\text{Hf}_{(\text{T})}$), which can be seen in Table 3-3 (~1.77 to 1.89 Ga). The $\epsilon\text{Hf}_{(1.8-1.9 \text{ Ga})}$ for $\leq 10\%$ discordant zircons from the Paleoproterozoic samples range from -13.8 to 8.0 with averages between -9.4 to 6.3 and standard deviations between 0.8 to 3.0 (Table 3-3). BSD10-06 only yielded 2 grains eligible for Hf analysis, and each grain was reduced to its individual $^{207}\text{Pb}/^{206}\text{Pb}$ age (IA), yielding $\epsilon\text{Hf}_{(\text{IA})}$ of 10.1 and 7.0. Average Hf $T_{(\text{DM})}$ model ages for the Paleoproterozoic samples (BSD10-06, LD10-11, LSC10-03, LSC10-10, LSC10-13, RRD10-05, and RRD10-09, RRD10-13) range from ~1.84 Ga in BSD10-06 to ~2.59 Ga in RRD10-13 (Table 3-3). The Hf T_{DM} ages represent minimum mantle separation ages because Lu/Hf in zircon is invariably lower than in whole-rocks (e.g., Griffin et al., 2002). Calculation of secondary or crustal residence ages requires knowledge of the Lu/Hf of the source(s) and were not calculated because the data ultimately suggest a mixing of crustal and mantle sources at ~1.8 to 1.9 Ga.

RRD10-20 yielded an older population of zircons (~2.7 to 3.2 Ga) which appear to lie along a discordia which yields an upper intercept age of ~3.4 Ga. However, when ~3.4 Ga is used for calculating $\epsilon\text{Hf}_{(3.4)}$, the isotope values for the older population of zircons lie above values for DM. This indicates that these older grains likely do not come from the same source and should not be regressed as a group, and that the oldest component within RRD10-20 is not ~3.4 Ga. The ~2.7 to 3.2 Ga grains may have been acquired from multiple sedimentary sources. Similar to RRD10-20, LSC10-12 yielded an older population of zircons (~3.0 to 3.3 Ga) which appear to lie along a discordia that yields an upper intercept age of ~3.4 Ga. However, when ~3.4 Ga is used for calculating $\epsilon\text{Hf}_{(3.4)}$ for LSC10-12, the isotope values for the older population of zircons lie above values for DM. This indicates that these older grains likely do not come from the same source and should not be regressed as a group, and that the oldest component within LSC10-12 is not ~3.4 Ga.

Sm-Nd Whole-Rock Isotopes

As a group, the meta-igneous xenoliths show a range in $\epsilon\text{Nd}_{(0)}$ from -5.6 to -45.9. Initial ratios were calculated using the best estimates of the individual rock crystallization ages ($^{207}\text{Pb}/^{206}\text{Pb}$ ages 1.79 Ga to 2.68 Ga) shown in Table 3-4. This yielded $\epsilon\text{Nd}_{(2.4-2.7)}$ of -0.3 to -5.0 (Table 3-4, Figure 3-21), and $\epsilon\text{Nd}_{(1.7-1.9)}$ of -0.9 to -10.0 (Table 3-4, Figure 3-21). Depleted mantle model ages for the Archean meta-igneous samples were calculated using the model of DePaolo (1981) and ranged from 2.78 Ga to 3.33 Ga (Figure 3-22) (excluding LSC10-11). The Paleoproterozoic meta-igneous samples (excluding LD10-11) yielded depleted mantle model ages (DePaolo, 1981) between 2.46 Ga and 2.55 Ga (Table 3-4), overlapping with the igneous crystallization age of the ~2.4 to 2.6 Ga meta-igneous samples. RRD10-13 yielded an igneous

crystallization age of 1.87 Ga, and a Nd $T_{(DM)}$ of 3.06 Ga, which is far older than the other Paleoproterozoic samples. This indicates that the source melt for RRD10-13 was likely from a much older crustal source, or interacted with such a source. The initial ϵNd values of all of the meta-igneous samples (excluding LD10-11) are shown (Figure 3-21) with initial ϵNd values for orthogneisses (green bar) from the Little Belt Mountains (Mueller et al., 2002) and with initial ϵNd values for four different regions within the northern Wyoming province (Miller et al., 1986; Wooden and Mueller, 1988; Frost, 1993; Mueller et al., 1996; Mueller et al., 2004; Frost et al., 2006; Mueller et al., 2010). Shown on Figure 3-21, two evolution lines approximating lower continental crustal evolution using $^{147}Sm/^{144}Nd = 0.1532$ (Rudnick and Gao, 2003) are plotted. These lines begin at DM and CHUR/BSE values at 3.5 Ga, based on the oldest Sm-Nd T_{DM} ages derived from the xenoliths. Isotopically, the Archean meta-igneous $\epsilon Nd_{(2.4-2.7 Ga)}$ values range between 2.5 Ga depleted mantle and 2.5 Ga lower crustal ϵNd ($^{147}Sm/^{144}Nd = 0.1532$; Rudnick and Gao, 2003, yields $\epsilon Nd_{(2.5 Ga)} = -10 \pm 2$), suggesting differing levels of involvement of both crustal and mantle sources (Figure 3-21). The Proterozoic meta-igneous samples yielded $\epsilon Nd_{(1.7-1.9 Ga)}$ values that also range between DM and lower crustal values, indicating different degrees of mixing between juvenile and evolved sources (Figure 3-21). Sample LSC10-11 yielded a Sm-Nd $T_{(DM)}$ of 4.96, and LD10-11 yielded a Sm-Nd $T_{(DM)}$ of ~ 1.59 Ga, which is younger than the calculated igneous crystallization age of ~ 1.83 Ga for the sample. These values are not geologically realistic, and are most likely attributable to difficulties in measuring such low concentrations of Sm and Nd.

Discussion

Origins Of The Meta-Igneous Xenoliths

The xenoliths from the Missouri Breaks Diatremes, the Bearpaw Mountains, and the Highwood Mountains show similarities in trace elements, U-Pb ages, and Hf and Sm-Nd isotopic systems to those from further south in the GFTZ in the Grassrange area (Chapter 2). Zircon U/Pb ages from plutonic and meta-igneous xenoliths yield two suites of igneous crystallization ages: an older range between 2.43 Ga and 2.68 Ga (six samples), and younger ages between 1.74 Ga and 1.89 Ga (eight samples). When Hf isotopic data within each sample are reduced to the sample igneous crystallization age, each suite of zircons shows a relatively small spread of ϵ_{Hf} values with overlapping error envelopes (excluding LD10-07). This suggests that the younger zircons within the samples experienced a Pb loss event(s) that effected their U-Pb ages, but did not affect their Hf isotopes. This indicates that the grains affected by Pb loss formed from magmas with the same Hf isotopes as the concordant grains. The range of initial Hf isotopic compositions for the Paleoproterozoic samples scatter from DM to slightly below CHUR/BSE, which are values typical of an arc-type environment (e.g., Dhuime et al., 2011). Trace element patterns are also suggestive of a subduction zone origin or recycling of subduction-generated crust. This includes the relatively elevated LIL and suppressed HFSE contents commonly observed in arc related rocks. Enrichment in fluid mobile elements (e.g., Pb and Ba) relative to immobile elements is a common effect of fluid fluxing in subduction environments (Pearce, 1983; Thompson et al., 1984). Tectonic discrimination diagrams (Figure 3-23; Pearce, 1983) also support a volcanic arc origin for the protoliths of the samples. Some of the older meta-igneous samples have positive Eu and Sr anomalies indicating accumulation of plagioclase, but others

show negative Eu and Sr anomalies (Figure 3-6B), which indicates the removal of plagioclase during petrogenesis by fractional crystallization or retention of plagioclase in the source. Very minor depletion in the HREE is evident in some samples (Fig 3-6A), which is likely due to residual garnet in the source. These data suggest that the Paleoproterozoic meta-igneous xenoliths represent magmas formed and crystallized during the ocean-subduction and subsequent continent-continent collision that formed the GFTZ. Trace element patterns for the Paleoproterozoic samples are very similar to the pattern observed in the older meta-igneous samples (Figure 3-6), suggesting both may have originated in a subduction-zone environment, or recycled such crust.

Whole-rock Nd and zircon Hf isotopic data reveal different mixes of mantle and crustal material. Figure 3-19 illustrates the variation of initial ϵHf versus age for zircons from all xenoliths using the apparent $^{207}\text{Pb}/^{206}\text{Pb}$ age of each individual zircon for the detrital samples, and the values for $\epsilon\text{Hf}_{(2.4-2.6\text{ Ga})}$ and $\epsilon\text{Hf}_{(1.7-1.9\text{ Ga})}$ for the meta-igneous samples. The older samples can be split into two groups. The first, LD10-01, LD10-07, and LD10-08, crystallized between ~ 2.44 Ga and ~ 2.62 Ga, but have mean Hf T_{DM} for their zircons from 2.77 Ga to 2.88 Ga and $\epsilon\text{Hf}_{(2.4-2.6\text{ Ga})}$ values from -9.8 to 6.9 (Figure 3-19). The $\epsilon\text{Hf}_{(2.4-2.6\text{ Ga})}$ values for the samples are suggestive of depleted mantle playing an important role in their petrogenesis with ϵHf values close to or at the value of DM at ~ 2.4 to 2.6 Ga (Figure 3-19). However, $\epsilon\text{Nd}_{(2.4-2.6\text{ Ga})}$ values lie below CHUR/BSE which suggests mixing between depleted mantle and an old enriched crustal component occurred in the late Archean and/or early Paleoproterozoic (Figure 3-21, Mueller et al., 2010; Mirnejad and Bell, 2006; Mirnejad and Bell, 2008). The evolved source may have been involved via direct assimilation of c. 2.8 Ga or older Wyoming craton materials, or

that subducted sediments contributed this evolved component (Mueller et al., 2010). The second group includes Archean xenoliths BSD10-04 and LSC10-11, which exhibit much lower $\epsilon\text{Hf}_{(2.6-2.7 \text{ Ga})}$, ranging from -5.7 to -16.9. This indicates that the samples crystallized from a primarily evolved (crustal) melt with only minor input from a more juvenile source (DM). While LSC10-11 did not yield an ϵNd value, the ϵNd value for BSD10-04 is -5.0 which lies below CHUR/BSE and is another indication of a greater input of evolved (crustal) material, such as older MHB crust.

The Paleoproterozoic samples (~1.74 Ga to ~1.89 Ga, BSD10-05, LSC10-03, LSC10-10, LSC10-13, RRD10-05, RRD10-09, RRD10-13, and LD10-11) have average Hf T_{DM} ages of their zircons of ~1.95 Ga to ~2.59 Ga (Table 3-3), which suggests differing influences of older crust and depleted mantle in their genesis. Shown on Figure 3-19, two evolution lines approximating lower continental crustal evolution using $^{176}\text{Lu}/^{177}\text{Hf} = 0.0187$ (Rudnick and Gao, 2003) are plotted. These lines begin at DM and CHUR/BSE values at 3.5 Ga, based on the oldest Hf T_{DM} ages derived from the xenoliths. It is clear that the $\epsilon\text{Hf}_{(1.7-1.9 \text{ Ga})}$ values for the Paleoproterozoic samples cluster well above the evolution line. The $\epsilon\text{Hf}_{(1.7-1.9 \text{ Ga})}$ range close to DM values at ~1.7 to 1.9 Ga, which suggests that depleted mantle played an important part of their petrogenesis (Figure 3-19). These ϵHf values (7.9 to -9.6) are similar to those of similar age from the Little Belt Mountains (Weiss et al., 2009) (Figure 3-19). While some of the $\epsilon\text{Hf}_{(1.8-1.9 \text{ Ga})}$ values are more negative than those from the Little Belt Mountains, both data sets seem to indicate a mixture between a DM-like source and an older crustal component to different degrees, likely formed in an arc-like environment. The single exception to this pattern is BSD10-05 which has an igneous crystallization age of 1.74

Ga, similar to the ages of the granitoid samples from the Grassrange (Chapter 2). The range of $\epsilon\text{Hf}_{(1.7)}$ values for the sample is from -6.3 to -11.0, which overlaps with the values from the Grassrange, indicating that BSD10-05 has a larger influence of crustal sources in its petrogenesis. ϵNd values for the Paleoproterozoic samples range from -0.9 to -7.4 (Figure 3-21). The two most positive ϵNd values (samples LSC10-03 and LSC10-10) are similar to ϵNd data from the Little Belt Mountains (Mueller et al., 2002) and reinforce the suggestion that the samples might have formed in an ocean-continent subduction environment. The five more negative ϵNd values (samples BSD10-05, LSC10-13, RRD10-05, RRD10-09, and RRD10-13) are very similar to the ~1.7 Ga granitoid samples (MX-08, MX-18) from the Grassrange (Chapter 2) and seem to indicate slightly more mixing of an older crustal component within these samples, possibly indicating primary formation after oceanic subduction was completed and during the ensuing continental collision.

Implications For Great Falls Tectonic Zone Evolution

The dataset presented in this study is best interpreted in conjunction with the existing data from the Grassrange area to the south (Chapter 2) and the Little Belt Mountains to the southwest (Mueller et al., 2002). When taken together, these studies provide an enhanced characterization of the poorly exposed GFTZ crust in central Montana. Evidence from seven of the eight meta-igneous Paleoproterozoic samples (LSC10-03, LSC10-10, LSC10-13, RRD10-05, RRD10-09, RRD10-13, and LD10-11) suggest that these rocks formed 1.79-1.89 Ga ago, and that similar to the Little Belt Mountains (Mueller et al., 2002; Weiss et al., 2009), the depleted mantle was an important part of their petrogenesis. The relatively juvenile initial Hf and Nd compositions (Figure 3-19; Figure 3-21) indicate that the samples were most likely

formed during the consumption of oceanic crust between the Medicine Hat block and the northern Wyoming craton. These data support models proposed by Mueller et al. (2002, 2005) that the GFTZ resulted from ocean basin closure between the Wyoming Craton and Medicine Hat block (see also Harms et al., 2004). The primarily subchondritic $\epsilon\text{Hf}_{(1.7)}$ (zircons) and $\epsilon\text{Nd}_{(1.7)}$ (whole-rock) values for Paleoproterozoic sample BSD10-05 (Figure 3-19; Figure 3-21) both indicate substantial mixing between a DM-like component and an evolved Archean crustal component to a greater extent than evident in the slightly older (~1.79 – 1.89 Ga) Missouri Breaks xenoliths and igneous rocks in the Little Belt Mountains. This suggests that the ~1.74 Ga BSD10-05 interacted with a significant amount of evolved material during its petrogenesis, a process consistent with formation in a continental collision zone in which older crust was thickened and melted. The trace element patterns (Figure 3-6) from the Archean and Paleoproterozoic orthogneisses (i.e., relative depletion of HFSE) are also consistent with patterns in rocks from modern continental arcs (e.g., Thompson et al., 1984; Pearce et al., 1984); however, this does not discriminate between volcanic arc, syn-collisional, or post-collisional origins. Isotopic data from the Little Belt Mountains (Mueller et al., 2002) and from this study indicate that the igneous arc was built upon continental crust. $\epsilon\text{Hf}_{(1.7-1.9 \text{ Ga})}$ (zircons) and $\epsilon\text{Nd}_{(1.7-1.9 \text{ Ga})}$ (whole-rock) values for the Paleoproterozoic meta-igneous samples (Figure 3-19; Figure 3-21) suggest that mixing between a DM-like component and an evolved Archean crustal component occurred to a slightly greater extent than is observed in the (~1.86 Ga) Little Belt Mountain sample suite (Mueller et al., 2002; Weiss et al., 2009).

Geochronologic data provide insight into the cratonic affinity of the igneous arc basement. Figure 3-24, illustrates the ranges of ages observed in this study compared to published data from the Wyoming craton (Heimlich and Banks, 1968; Mueller et al., 1995; Kirkwood, 2000; Mogk et al., 2004; Frost and Fanning, 2006; Mueller et al., 2010, Krogh et al., 2011) and Medicine Hat block (Villeneuve et al., 1993; Davis et al., 1995; Gorman et al., 2002). Ages were limited to those older than 2.4 Ga in order to make the most direct comparisons of pre-GFTZ data. Igneous crystallization ages of the meta-igneous samples (indicated by a star) are plotted in Figure 3-24. The dominance of ~2.4 - 2.7 Ga igneous crystallization ages suggests that the meta-igneous samples share a closer affinity to the MHB, which is characterized by Neoarchean ages, than to the northern Wyoming Province, which is dominantly Mesoarchean (Figure 3-24). Based on the affinity of the older meta-igneous samples from this study the Paleoproterozoic magmatic arc was built on MHB crust. This implies the polarity of ocean subduction was beneath the MHB, which is supported by the Deep Probe velocity model of Gorman et al. (2002). These authors cited an upper mantle floating reflector, interpreted to be a subducted slab, dipping beneath the MHB. During subduction, the Wyoming craton would be attached to the down-going slab, likely leading to MHB crust over-riding Wyoming crust. Further evidence of this can be seen in SW Montana within the Tobacco Root Mountains, which preserves evidence of Wyoming province material being buried to depths great enough for anatectic melts to have been created at 1.77 Ga (Mueller et al., 2004, 2005).

Harms et al. (2004) calculated pressure-temperature-time paths from three metamorphic suites and metamorphosed mafic dikes and sills from the Tobacco Root

Mountains which revealed crustal thickening, metamorphism, and partial melting of rock occurring between 1.78 and 1.76 Ga. Similarly, Mueller et al. (2005) showed evidence from zircons from the Tobacco Root Mountains and monazite from the Highland Mountains that the northwestern Wyoming province experienced an episode of high-grade metamorphism at ~1.77 Ga. Further, Roberts et al. (2002) examined rocks from the Montana meta-sedimentary terrane (MMT, which includes the Tobacco Root Mountains and the Highlands), which yielded $430 \text{ }^{40}\text{Ar}/^{39}\text{Ar}$ biotite ages as well as $4 \text{ }^{207}\text{Pb}/^{206}\text{Pb}$ step-leached garnet ages. Roberts et al. (2002) suggested that metamorphic events in the MMT took place between 1.82 and 1.79 (garnet growth ages), and that between 1.78 to 1.74 Ga the MMT was rapidly cooling (biotite cooling ages). We suggest that the 1.78 to 1.77 Ga metamorphic ages are representative of terminal collision between the MHB and Wyoming province, and that this led to thickening and crustally derived granitoid magmatism represented by the ~1.73 and 1.74 Ga granitoids from the Grassrange diatremes (Chapter 2), as well as metamorphism of the MHB country rock represented by the 1.75 Ga metamorphic ages of the orthogneiss samples from the Bearpaw Mountains (this study).

The timing of arc magmatism and continental collision in the GFTZ broadly coincides with the overall amalgamation of the constituent Laurentian cratons (Mueller et al., 2011; Figure 3-25). These include collisions between the Wyoming-Superior and Hearn-Superior, which formed the Trans-Hudson orogen at 1.7 - 1.9 Ga (Karlstrom and Houston, 1984; Lewry et al., 1987; Hoffman, 1988; Bickford et al., 1990; Gordon et al., 1990; Machado, 1990; Nelson et al., 1993; Lewry et al., 1994; Lucas et al., 1996; Resor et al., 1996; Sun et al., 1996; Dahl et al., 1999; Machado et al., 1999; Mueller et al.,

2002), and the Wyoming-Colorado collision at ~1.66 - 1.80 Ga (Bickford and Boardman, 1984; Sims and Peterman, 1986; Karlstrom and Bowring, 1988; Premo and Van Schmus, 1989; Van Schmus et al., 1993; Chamberlain, 1998; Selverstone et al., 2000; Hill and Bickford, 2001; Hill, 2004). Data from this study reinforce the generally synchronous nature of the amalgamation event and places significant limits on plate geometries during Laurentian growth (e.g., Hoffman, 1989; Mueller et al., 2005).

Conclusions

Zircons in the meta-igneous samples fall into two categories. The first category shows two distinct age populations. The older population is represented by magmatic zircons with upper intercept concordia ages of ~2.43 Ga to ~2.65 Ga. These same samples contain a younger population of metamorphic zircons with minimum ages of ~1.72 Ga to ~1.85 Ga. The Archean igneous crystallization ages documented in the xenoliths is consistent with younger ages observed in the MHB. These ages are younger than those expected from the northern Wyoming Craton, indicating that the Paleoproterozoic arc was built upon MHB Archean crust. The second category of meta-igneous samples shows a single age population represented by magmatic zircons with upper intercept concordia ages of ~1.74 Ga to ~1.89 Ga. Geochemistry and geochronology of the metamorphic ages of zircons in the Archean samples and the igneous crystallization ages of the Paleoproterozoic samples correlate with the ~1.86 Ga magmatism in the Little Belt Mountains and the tectonic events associated with the collision of the Medicine Hat block with the Wyoming craton that terminated formation the Great Falls tectonic zone. The geochemistry of the crustal xenoliths from this study support the proposal that the GFTZ experienced ocean subduction and arc magmatism from 1.89 to 1.78 Ga. These data also suggest that the volcanic arc created during

ocean-continent subduction was built on MHB crust, rather than that of the Wyoming Province, and that the polarity of subduction was beneath the MHB. Evidence from the southwestern GFTZ suggests that the system transitioned to continent-continent collision around 1.78 Ga to 1.77 Ga when there was a period of crustal thickening and metamorphism within the GFTZ related to terminal collision. After terminal collision was completed, there was then post-orogenic collapse and extension which likely resulted in upwelling mantle heating and partially melting the lower crust leading to crustally derived granitoid magmatism. This can be seen in the ~1.73 and 1.74 Ga granitoid xenoliths from the Grassrange (Chapter 2) as well as ~1.74 Ga mafic meta-granitoid sample BSD10-05 from the Missouri Breaks. The Great Falls tectonic zone, therefore, is constrained to the same general 150 Ma time period during which other blocks were sutured to form Paleoproterozoic Laurentia (Hoffman, 1988, 1989).

Table 3-1. Major, trace and rare earth element data of igneous protolith xenoliths from the Big Slide and Little Sand Creek diatremes. Major elements in wt. %, trace and rare earth elements in ppm.

Sample wt. %	BSD10-04*	BSD10-05*	BSD10-06	LSC10-03	LSC10-10*	LSC10-11*	LSC10-12*	LSC10-13*
SiO ₂	73	48	60	50	48	57	69	48
TiO ₂	0.09	4.7	0.60	0.55	0.90	0.16	BDL	0.57
Al ₂ O ₃	15	14	16	18	21	15	16	8.0
Fe ₂ O ₃	0.69	18	8.1	7.8	6.1	1.1	0.47	5.2
MnO	0.04	0.05	0.15	0.13	0.09	0.02	0.02	0.18
MgO	0.21	12.8	3.7	6.2	3.1	2.2	0.08	14
CaO	2.2	1.8	4.6	6.9	13	0.96	4.4	14
Na ₂ O	5.7	1.5	3.9	3.9	1.7	0.54	2.3	1.4
K ₂ O	2.9	6.8	0.81	2.9	0.75	10	9.7	2.2
P ₂ O ₅	0.04	0.39	0.12	0.27	0.12	0.01	0.06	0.32
LOI	0.88	0.93	1.4	3.1	1.5	2.0	2.2	1.7
Total	101.31	108.87	99.71	99.76	96.07	88.45	104.18	95.66
ppm								
Li	N/A	43	N/A	7.8	4.5	N/A	N/A	13
Sc	N/A	4.8	N/A	26	15	N/A	N/A	39
Ti	N/A	23187	N/A	3418	5922	N/A	N/A	3814
V	N/A	284	N/A	114	192	N/A	N/A	115
Cr	N/A	50	N/A	209	49	N/A	N/A	16
Co	N/A	37	N/A	32	20	N/A	N/A	12
Ni	N/A	85	N/A	120	37	N/A	N/A	11
Cu	N/A	4.4	N/A	16	45	N/A	N/A	11
Zn	N/A	249	N/A	85	38	N/A	N/A	283
Ga	N/A	39	N/A	16	30	N/A	N/A	14
Rb	N/A	323	N/A	103	34	N/A	N/A	110
Sr	N/A	278	N/A	1644	1547	N/A	N/A	410
Y	N/A	2.2	N/A	37	12	N/A	N/A	28
Zr	N/A	38	N/A	25	31	N/A	N/A	49
Nb	N/A	9.8	N/A	5.0	7.0	N/A	N/A	11
Cs	N/A	1.6	N/A	4.3	0.31	N/A	N/A	2.8
Ba	N/A	6863	N/A	5724	829	N/A	N/A	1365

Table 3-1. Continued.

Sample ppm	BSD10-04*	BSD10-05*	BSD10-06	LSC10-03	LSC10-10*	LSC10-11*	LSC10-12*	LSC10-13*
La	N/A	28	N/A	21	7.3	N/A	N/A	11
Ce	N/A	55	N/A	55	17	N/A	N/A	32
Pr	N/A	6.2	N/A	7.9	2.2	N/A	N/A	5.1
Nd	N/A	23	N/A	35	9.0	N/A	N/A	26
Sm	N/A	3.0	N/A	8.1	2.4	N/A	N/A	8.7
Eu	N/A	1.4	N/A	1.9	1.1	N/A	N/A	1.3
Gd	N/A	2.0	N/A	7.2	2.3	N/A	N/A	8.1
Tb	N/A	0.16	N/A	1.0	0.35	N/A	N/A	1.2
Dy	N/A	0.49	N/A	6.2	2.1	N/A	N/A	6.0
Ho	N/A	0.06	N/A	1.2	0.41	N/A	N/A	0.96
Er	N/A	0.19	N/A	3.3	1.0	N/A	N/A	2.3
Tm	N/A	0.01	N/A	0.49	0.18	N/A	N/A	0.30
Yb	N/A	0.06	N/A	3.0	1.1	N/A	N/A	1.6
Lu	N/A	0.01	N/A	0.40	0.16	N/A	N/A	0.20
Hf	N/A	0.30	N/A	0.46	1.1	N/A	N/A	1.3
Ta	N/A	0.23	N/A	0.16	0.47	N/A	N/A	0.94
Pb	N/A	7.0	N/A	11	3.4	N/A	N/A	9.7
Th	N/A	0.28	N/A	0.37	1.9	N/A	N/A	6.6
U	N/A	0.17	N/A	0.90	0.49	N/A	N/A	1.7

BDL – below detection limit, N/A – not applicable.

*Major elements were analyzed with an incorrect calibration, thus values may be off by 10%.

Table 3-2. Major, trace and rare earth element data of xenoliths from Robinson Ranch Diatreme, the Bearpaw Mountains, and the Highwood Mountains. Major elements in wt. %, trace and rare earth elements in ppm.

Sample	RRD10-05*	RRD10-09*	RRD10-13*	RRD10-20*	LD10-01	LD10-07*	LD10-08	LD10-11	HX-1
wt. %									
SiO ₂	58	58	56	64	74	70	68	98	67
TiO ₂	0.65	0.65	0.80	0.01	0.15	0.32	0.42	0.05	0.69
Al ₂ O ₃	11	13	20	22	14	16	14	0.77	14
Fe ₂ O ₃	6.2	6.1	9.2	0.49	2.5	6.6	5.2	1.1	7.2
MnO	0.09	0.09	0.08	0.02	0.04	0.08	0.06	0.01	0.10
MgO	8.5	8.6	6.3	1.2	0.81	1.9	1.9	0.03	1.6
CaO	2.8	4.9	0.97	2.1	2.1	2.5	2.1	0.06	4.5
Na ₂ O	1.9	2.2	1.2	4.4	3.5	3.8	3.0	0.40	3.0
K ₂ O	3.5	3.6	7.8	7.9	2.6	3.6	3.3	0.06	4.1
P ₂ O ₅	0.19	0.27	0.03	0.04	0.02	0.06	0.02	0.03	0.30
LOI	0.46	0.59	0.59	0.51	0.23	0.37	1.3	0.27	0.23
Total	93.67	98.48	103.59	103.00	99.93	105.17	99.67	100.38	102.76
ppm									
Li	29	24	7.2	4.9	4.7	5.7	4.7	1.5	5.9
Sc	13	13	23	0.29	5.2	11	11	0.27	12
Ti	3220	3346	5284	661	872	2665	2717	452	3644
V	91	98	215	5.5	32	73	74	8.7	34
Cr	158	217	285	3.7	35	94	102	6.3	25
Co	19	20	20	0.83	5.1	14	11	0.57	6.0
Ni	81	92	46	5.1	13	42	14	3.6	36
Cu	18	6.4	37	1.1	10	32	7.6	24	22
Zn	61	60	83	4.6	26	60	40	4.9	141
Ga	17	17	24	17	15	18	17	BDL	23
Rb	106	95	308	198	42	60	59	0.67	89
Sr	685	781	366	1554	447	304	281	63	386
Y	14	14	26	1.5	9.5	21	22	0.68	40
Zr	10	35	56	16	5.4	16	35	1.4	100
Nb	5.2	4.3	10	BDL	0.63	4.0	6.8	BDL	17
Cs	1.4	0.82	3.3	0.19	0.46	0.39	0.75	0.14	0.34
Ba	3507	5239	5086	15074	1577	1709	1363	BDL	3462

Table 3-2. Continued.

Sample ppm	RRD10-05*	RRD10-09*	RRD10-13*	RRD10-20*	LD10-01	LD10-07*	LD10-08	LD10-11	HX-1
La	47	40	35	6.9	23	49	18	0.74	53
Ce	90	77	59	12	36	83	28	1.4	110
Pr	9.8	9.1	6.2	1.2	3.3	8.3	2.7	0.18	12
Nd	38	35	22	4.0	9.1	30	9.3	0.72	49
Sm	6.1	6.0	4.4	0.67	1.3	4.8	2.1	0.13	8.9
Eu	1.9	2.0	2.2	2.3	1.1	1.4	0.89	0.04	2.7
Gd	4.4	4.7	4.3	0.81	1.5	4.4	2.8	0.12	8.1
Tb	0.53	0.53	0.68	0.05	0.24	0.65	0.56	0.01	1.2
Dy	2.6	2.5	4.1	0.21	1.6	3.7	3.5	0.09	6.8
Ho	0.47	0.45	0.81	0.03	0.34	0.72	0.68	0.02	1.3
Er	1.2	1.3	2.4	0.09	0.95	2.0	1.8	0.05	3.8
Tm	0.20	0.17	0.36	0.01	0.19	0.32	0.27	0.01	0.52
Yb	1.1	1.0	2.3	0.06	1.1	2.0	1.6	0.04	3.3
Lu	0.17	0.15	0.34	0.01	0.17	0.30	0.23	0.01	0.48
Hf	0.49	0.61	1.2	BDL	0.21	0.51	0.77	BDL	2.3
Ta	0.13	0.11	0.67	0.03	0.02	0.05	0.10	BDL	0.79
Pb	19	18	28	11	26	28	29	3.81	23
Th	1.3	0.05	7.2	1.4	0.42	6.5	1.1	BDL	5.7
U	0.15	0.18	1.3	0.45	0.08	0.13	0.33	0.22	0.30

BDL – below detection limit.

*Major elements were analyzed with an incorrect calibration, thus values may be off by 10%.

Table 3-3. Igneous protolith xenoliths, Missouri Breaks, zircon LA-ICP-MS U-Pb data, $^{207}\text{Pb}/^{206}\text{Pb}$ ages and Hf-isotope data reported (Ma).

Sample Number	$^{207}\text{Pb}/^{206}\text{Pb}$ Age	Error 2 σ	$^{207}\text{Pb}/^{206}\text{Pb}$ Age	Error 2 σ	$\epsilon\text{Hf}_{(\text{IA})}$ Highest	$\epsilon\text{Hf}_{(\text{IA})}$ Lowest	$\epsilon\text{Hf}_{(\text{T})}^*$ Highest	$\epsilon\text{Hf}_{(\text{T})}^*$ Lowest	$\epsilon\text{Hf}_{(\text{T})}^*$ Mean	$\epsilon\text{Hf}_{(\text{T})}^*$ S.D.**	$\epsilon\text{Hf}_{(\text{T})}^*$ Median	Hf $T_{(\text{DM})}^{\text{a}*}$	Std. Dev.
Big Slide Diatreme													
BSD10-04	2684	39	1718	12	-30.9	-37.7	-9.4	-14.0	-11.3	1.2	-11.2	3362	46
BSD10-05	N/A	N/A	1738	12	-6.5	-11.7	-6.3	-11.0	-9.2	1.2	-9.2	2466	45
BSD10-06	1742	24	1831	10	10.1	7.0	N/A	N/A	N/A	N/A	N/A	1844	19
Little Sand Creek Diatreme													
LSC10-03	N/A	N/A	1805	4	8.0	4.1	8.0	4.1	6.3	0.8	6.4	1945	31
LSC10-10	N/A	N/A	1790	13	2.8	-3.9	2.3	-3.9	-1.5	1.6	-1.5	2237	64
LSC10-11	2606	65	1647	100	-2.6	-24.1	-5.7	-16.9	-11.5	3.0	-11.1	3319	119
LSC10-13	N/A	N/A	1783	25	-3.7	-9.5	-4.4	-9.1	-6.2	1.2	-6.1	2396	43
Robinson Ranch Diatreme													
RRD10-05	N/A	N/A	1894	11	-3.2	-8.9	-3.1	-8.7	-6.1	1.3	-6.2	2492	49
RRD10-09	N/A	N/A	1875	8	-3.1	-9.9	-3.5	-9.6	-5.6	1.4	-5.4	2453	53
RRD10-13	N/A	N/A	1872	10	-3.3	-19.0	-3.4	-13.8	-9.4	3.0	-9.5	2589	110
Lloyd Divide, Bearpaw Mountains													
LD10-01	2517	76	1738	22	-7.5	-24.3	6.9	-4.1	-0.4	3.5	-1.3	2810	132
LD10-07	2622	54	1746	190	-4.2	-19.1	1.2	-1.6	0.3	1.0	0.8	2878	36
					***Metamorphic zircons		-10.0	-15.43	-13.0	1.7	-13.1	2616	64
LD10-08	2438	70	1718	28	-1.8	-24.7	4.6	-9.8	-1.1	3.7	-1.6	2773	141
LD10-11	N/A	N/A	1777	33	6.3	-4.8	6.2	-2.2	2.0	2.5	2.1	2085	95
Highwood Mountains													
HX-1	2649	8	1846	50	N/A	N/A	N/A	N/A	N/A	N/A	N/A	N/A	N/A

(IA)Zircons reduced to individual U-Pb age.

*zircons reduced to $^{207}\text{Pb}/^{206}\text{Pb}$ age, excluding inherited grains.

^aDM model ages were calculated using the model of Mueller et al. (2008).

**Standard deviation.

***Metamorphic zircons from sample LD10-07, reduced to 1.75 Ga.

Table 3-4. LA-ICP-MS Nd-isotope data reported (Ma).

Sample Number	Age (Ma)	Sm (ppm)	Nd (ppm)	$^{143}\text{Nd}/^{144}\text{Nd}$	$\epsilon\text{Nd}_{(0)}$	$\epsilon\text{Nd}_{(T)}$ [*]	Nd T _(DM) ^a
Big Slide Diatreme							
BSD10-04	2684	1.1	8.6	0.510276	-45.9	-5.0	3129
BSD10-05	1738	3.0	22.7	0.510896	-33.8	-8.2	2470
Little Sand Creek Diatreme							
LSC10-03	1803	8.1	34.8	0.511883	-14.6	-1.9	2459
LSC10-10	1790	2.4	9.0	0.512158	-9.2	-0.9	2540
LSC10-11	2606	0.3	1.6	0.510508	-41.4	N/A	N/A
LSC10-12	N/A	0.6	2.3	0.511122	-29.4	N/A	N/A
LSC10-13	1783	8.7	25.7	0.512343	-5.6	-7.4	N/A
Robinson Ranch Diatreme							
RRD10-05	1890	6.1	38.0	0.511126	-29.3	-5.3	2508
RRD10-09	1875	6.0	35.3	0.511188	-28.1	-5.6	2550
RRD10-13	1872	4.4	22.3	0.511176	-28.4	-10.0	3059
RRD10-20	N/A	0.7	4.0	0.510820	-35.3	N/A	3075
Lloyd Divide, Bearpaw Mountains							
LD10-01	2517	1.3	9.1	0.510762	-36.4	-1.4	2783
LD10-07	2430	4.8	29.6	0.510920	-33.4	-3.1	2848
LD10-08	2551	2.1	9.3	0.511319	-25.6	-4.9	3332
LD10-11	1832	0.1	0.7	0.511955	-13.2	N/A	1589
Highwood Mountains							
HX-1	2649	7.6	40.2	0.511106	-33.2	-0.3	3265

*Orthogneiss and amphibolite samples reduced to $^{207}\text{Pb}/^{206}\text{Pb}$ age (Table 3-3).

^aDM model ages were calculated using the model of DePaolo (1981).

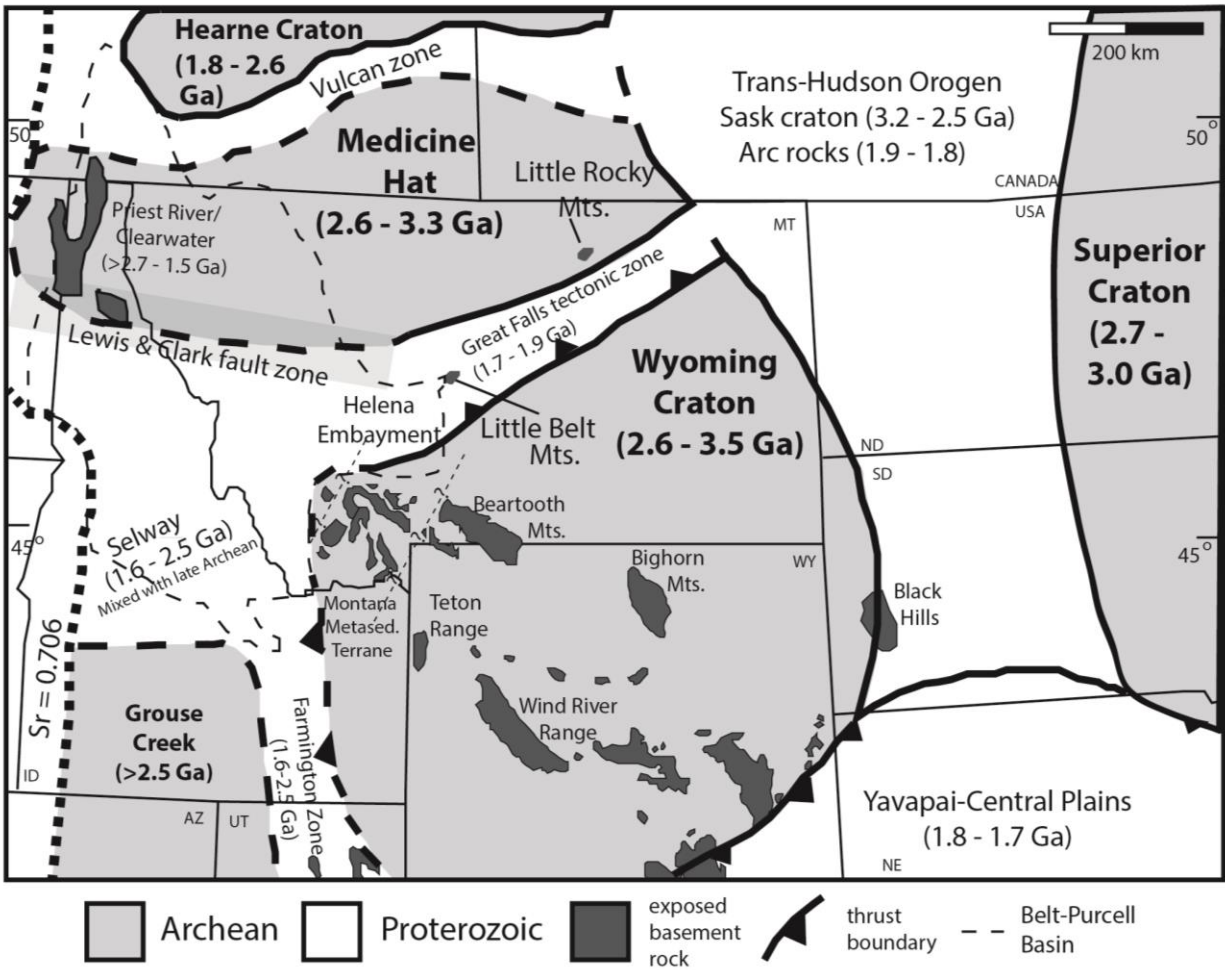


Figure 3-1. Generalized map of Precambrian basement provinces of southwestern Laurentia (after Ross et al., 1991; Condie, 1992; Doughty et al., 1998; Vogl et al., 2004; Foster et al., 2006, 2012). Exposures of basement in Laramide-style uplifts are shown in the dark grey shaded areas.

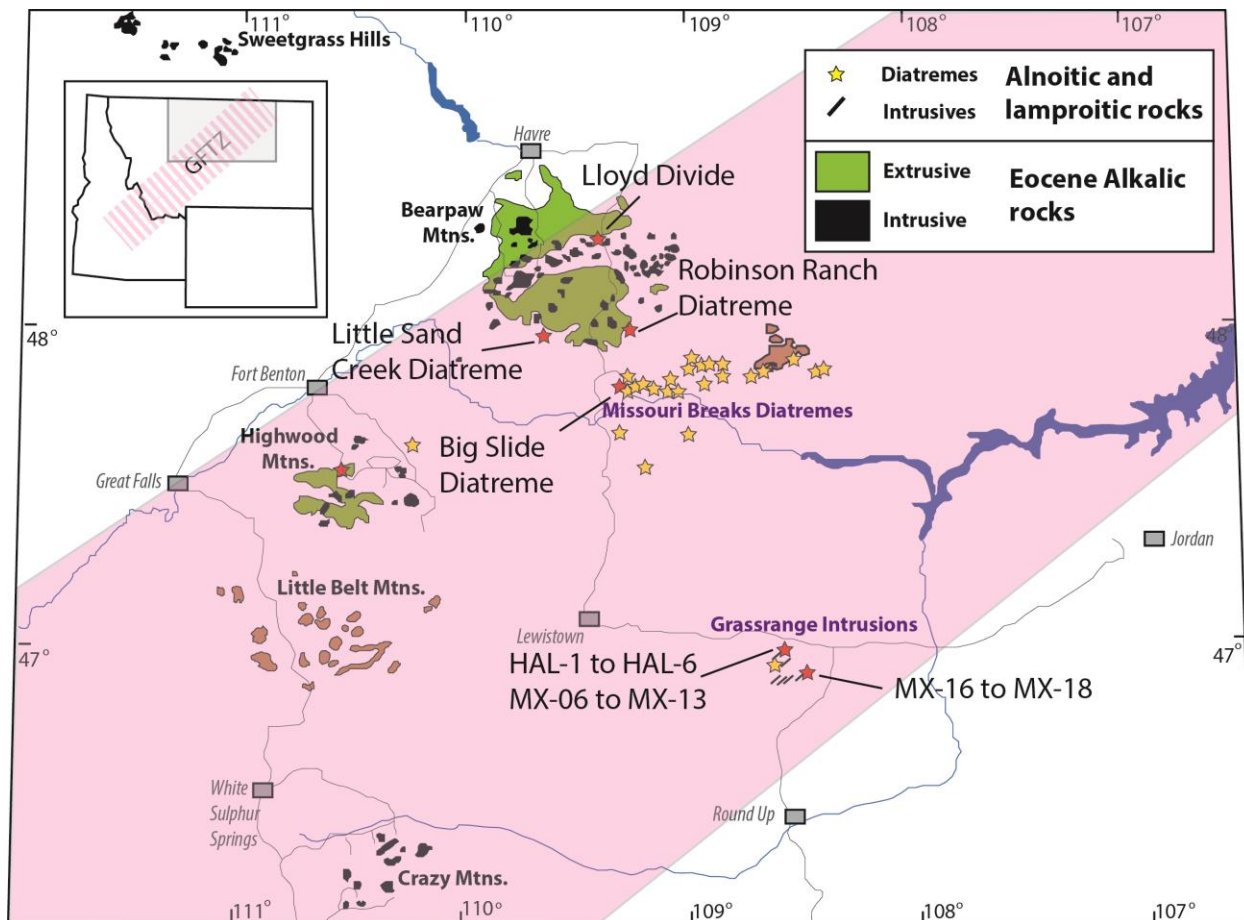


Figure 3-2. Generalized depiction of Cenozoic alkaline rock occurrences in the Montana alkali province (after Hearn et al., 1989). The limits of the Great Falls tectonic zone (shown in pink) are not well defined and are based on aeromagnetic data from Sims et al. (2004). Sample locations shown as red stars.

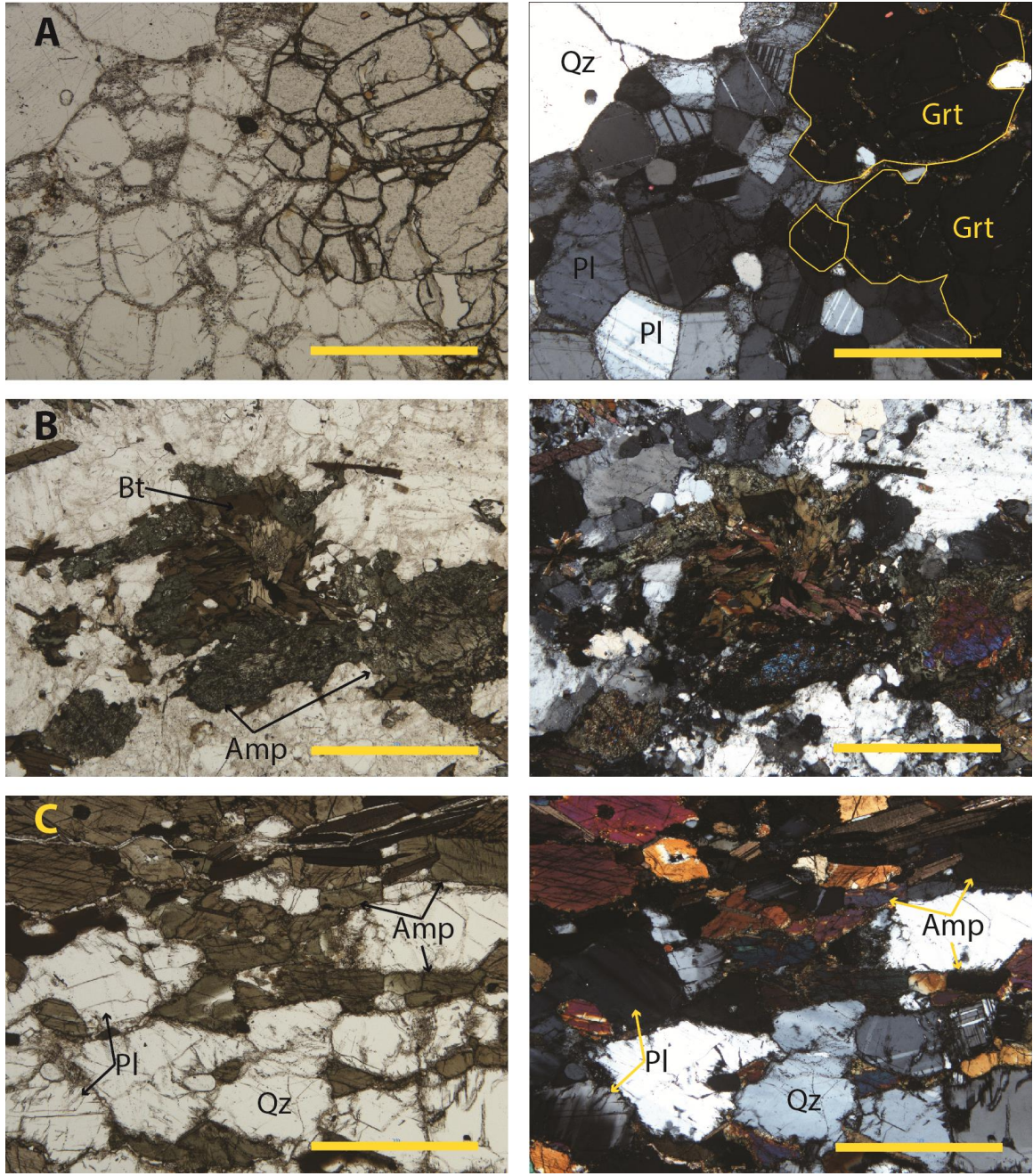


Figure 3-3. Photomicrographs of selected meta-igneous samples, with Plane Polarized light (PPL) images on the left, and Cross Polarized Light (XPL) images on the right. Scale bar is 1 mm. (A) Sample LD10-01, a garnet quartzofeldspathic gneiss. Compositional banding is defined by garnet rich and quartzofeldspathic layers. Note that both garnet and plagioclase are sub- to euhedral and fresh. (B) Sample RRD10-05, an amphibole biotite meta-granitoid. Amphibole occurs as, anhedral, altered grains with biotite reacting with the amphibole. (C) Sample LSC10-03 is a fine to medium grained linedated biotite amphibolite, where amphibole grain preferred orientation defines the rock fabric.

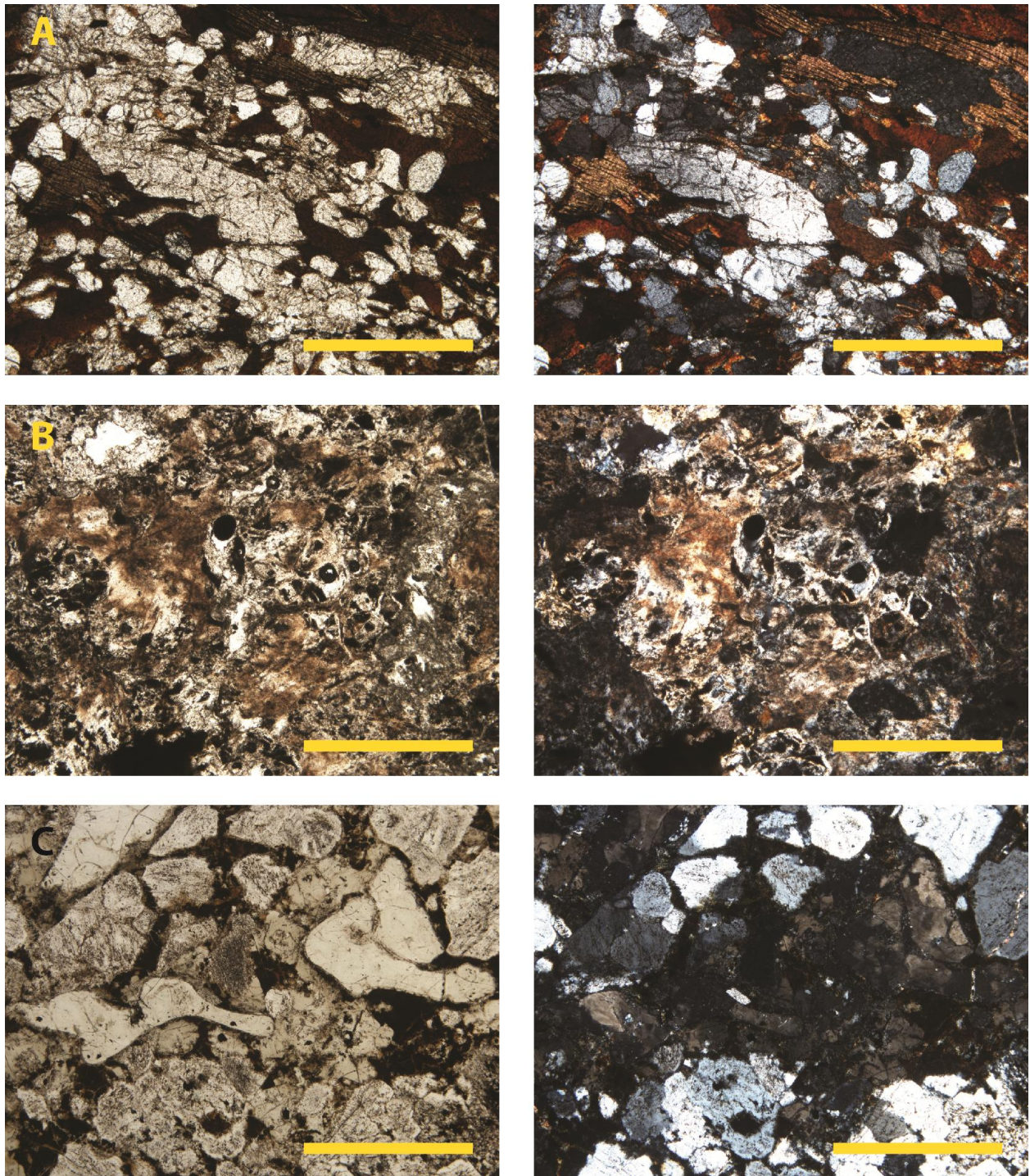


Figure 3-4. Photomicrographs of selected meta-igneous samples, with Plane Polarized light (PPL) images on the left, and Cross Polarized Light (XPL) images on the right. Scale bar is 1 mm. (A) BSD10-05 is a mafic meta-granitoid. Biotite is the dominant phase, with plagioclase, orthoclase and quartz common as well. (B) LSC10-11 and (C) LSC10-12 are presumed highly altered and retrogressed meta-igneous samples. See text for details.

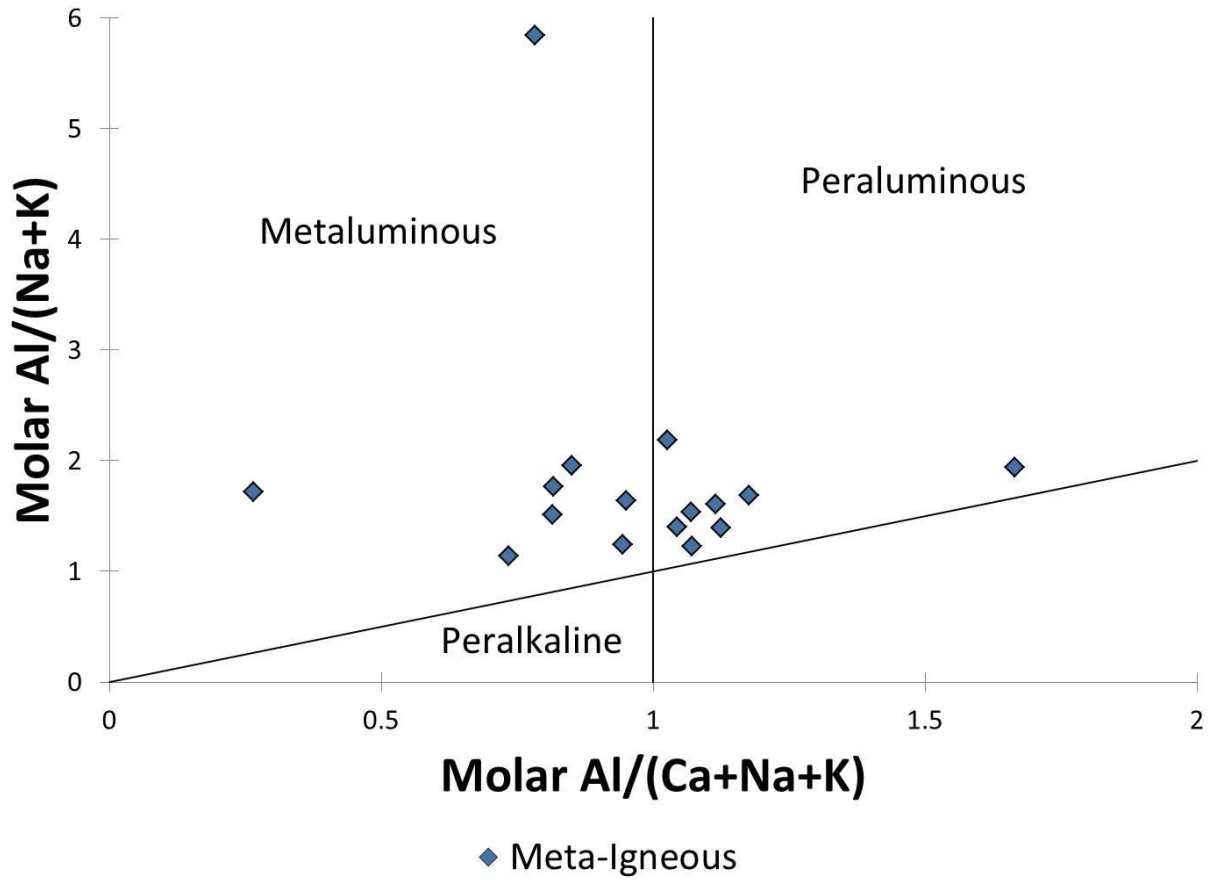


Figure 3-5. Xenolith samples plotted on an alumina saturation index (Shand, 1943; modified by Frost et al., 2001). Meta-igneous - blue diamonds.

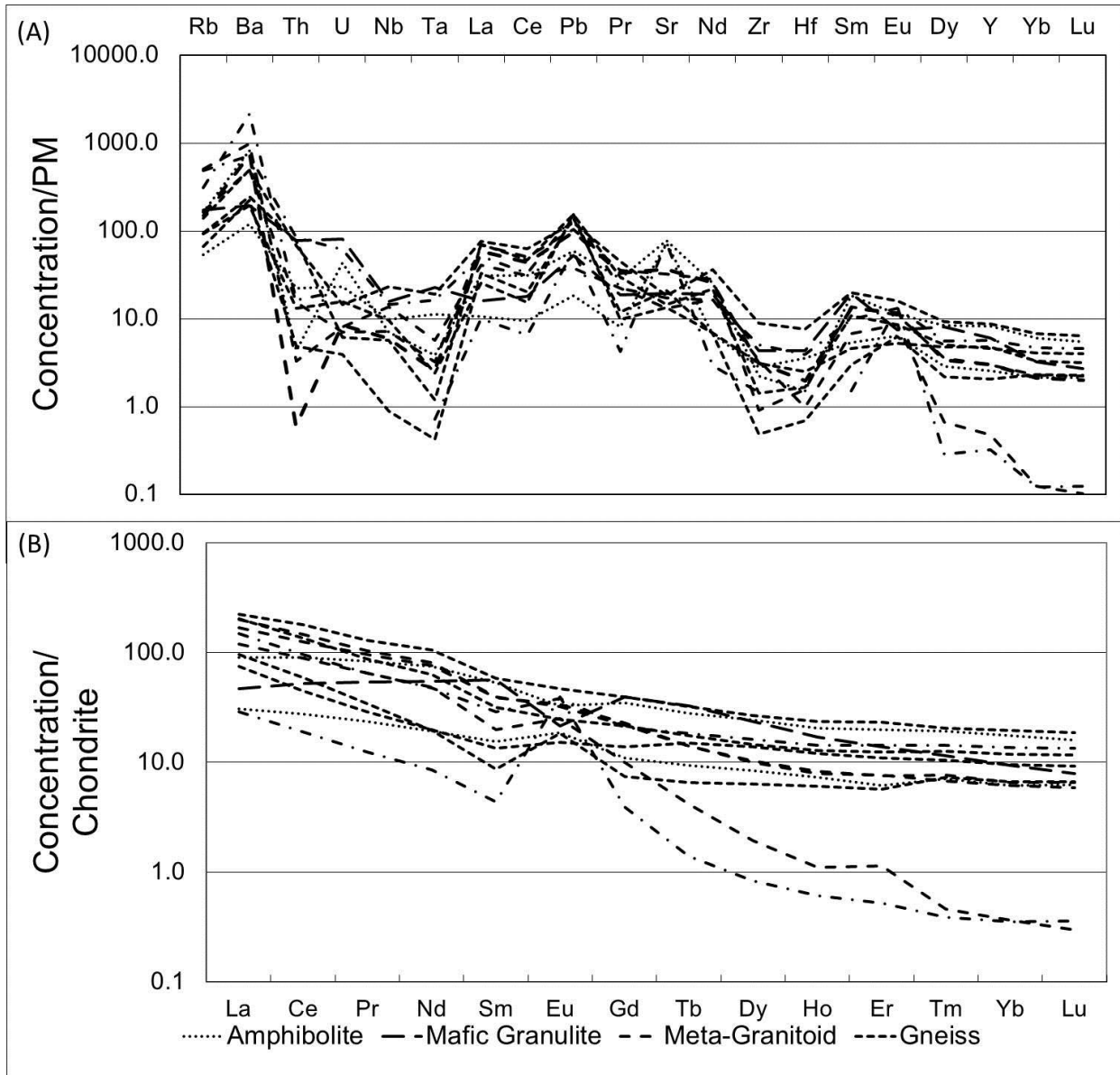


Figure 3-6. (A) Primitive-mantle normalized "spider" diagrams (McDonough and Sun, 1995) for meta-igneous samples. (B) Chondrite normalized REE diagram (McDonough and Sun, 1995) for meta-igneous samples using data in Table 3-1 and 3-2. Relative enrichment of LILEs to HFSE suggests formation in an arc environment.

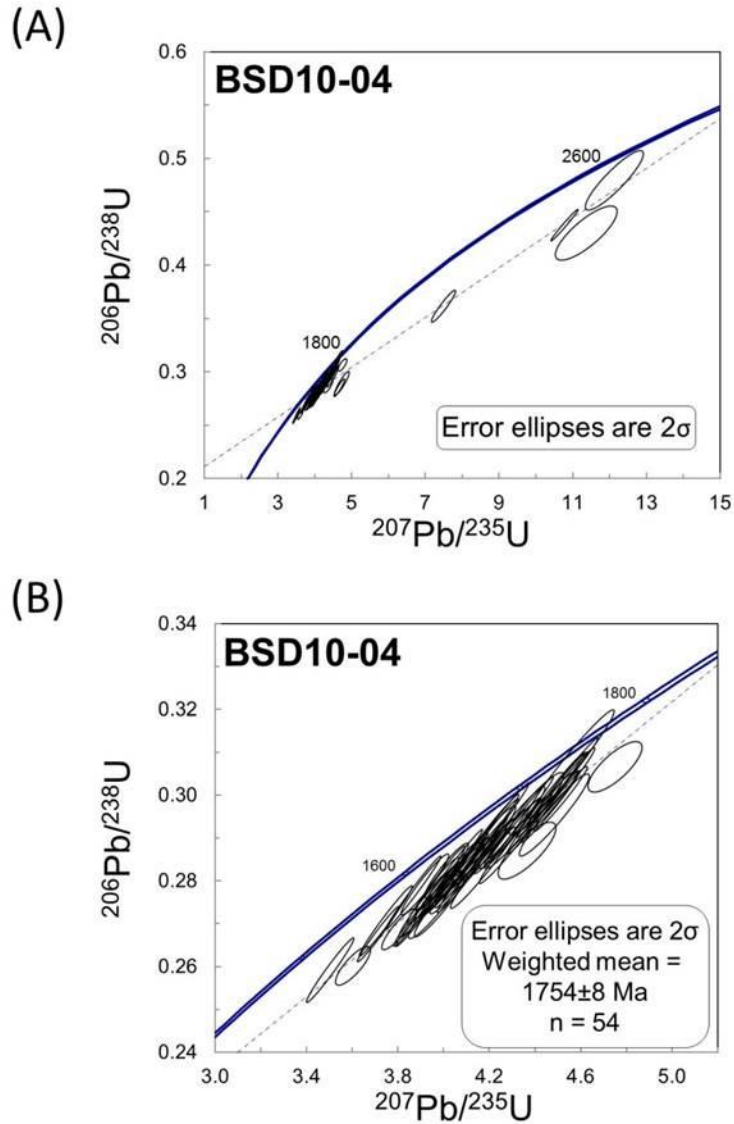


Figure 3-7. (A) Concordia diagram plotting composite U-Pb data for meta-granitoid sample BSD10-04. Each ellipse represents a single spot analysis and its 2σ error. (B) Expanded view of lower end of concordia showing spread of samples and weighted mean age.

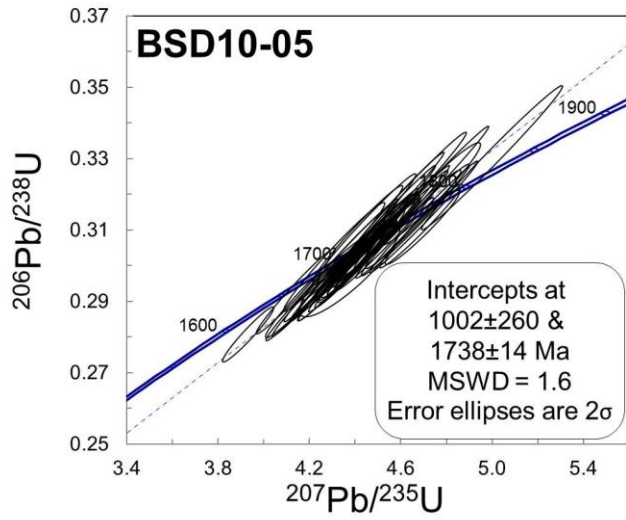


Figure 3-8. Concordia diagram plotting composite U-Pb data for mafic meta-granitoid sample BSD10-05. Each ellipse represents a single spot analysis and its 2σ error.

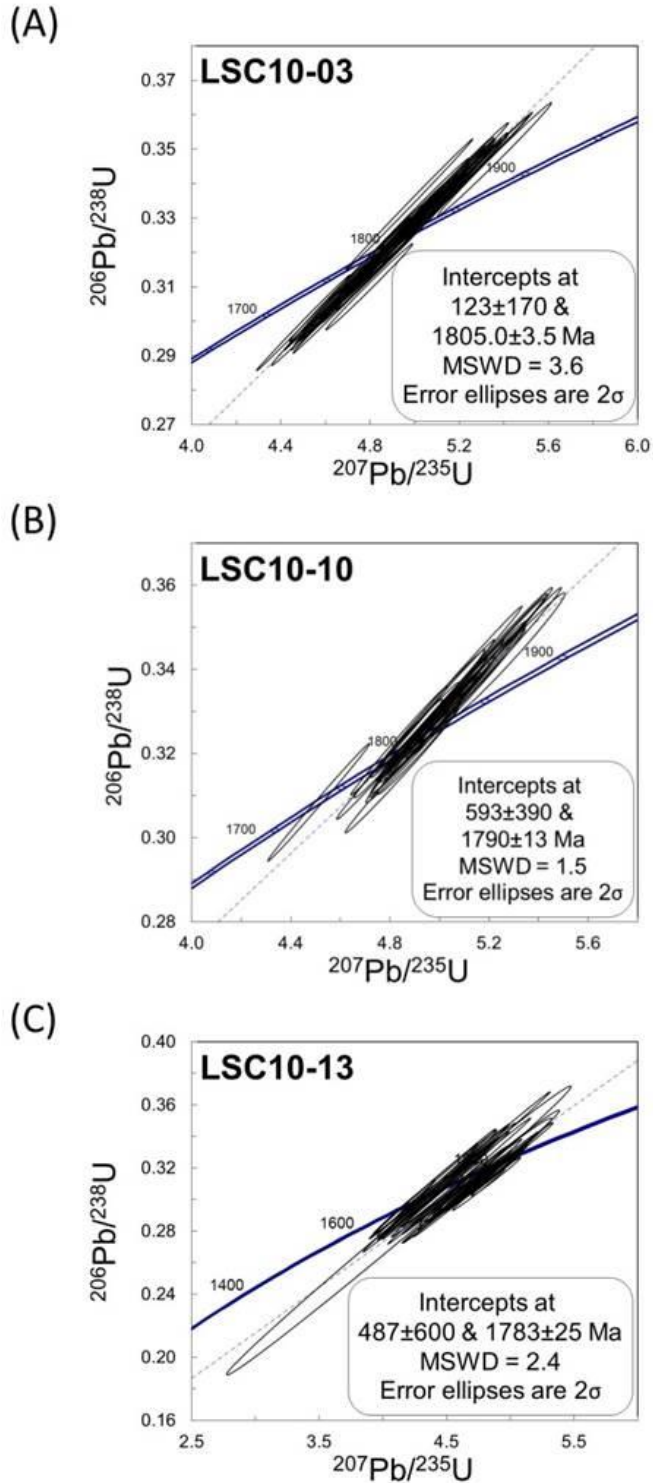


Figure 3-9. Concordia diagram showing U-Pb upper intercept regression for amphibolite samples LSC10-03 (A) and LSC10-10 (B) as well as mafic granulitic gneiss LSC10-13 (C). Each ellipse represents a single spot analysis and its 2σ error.

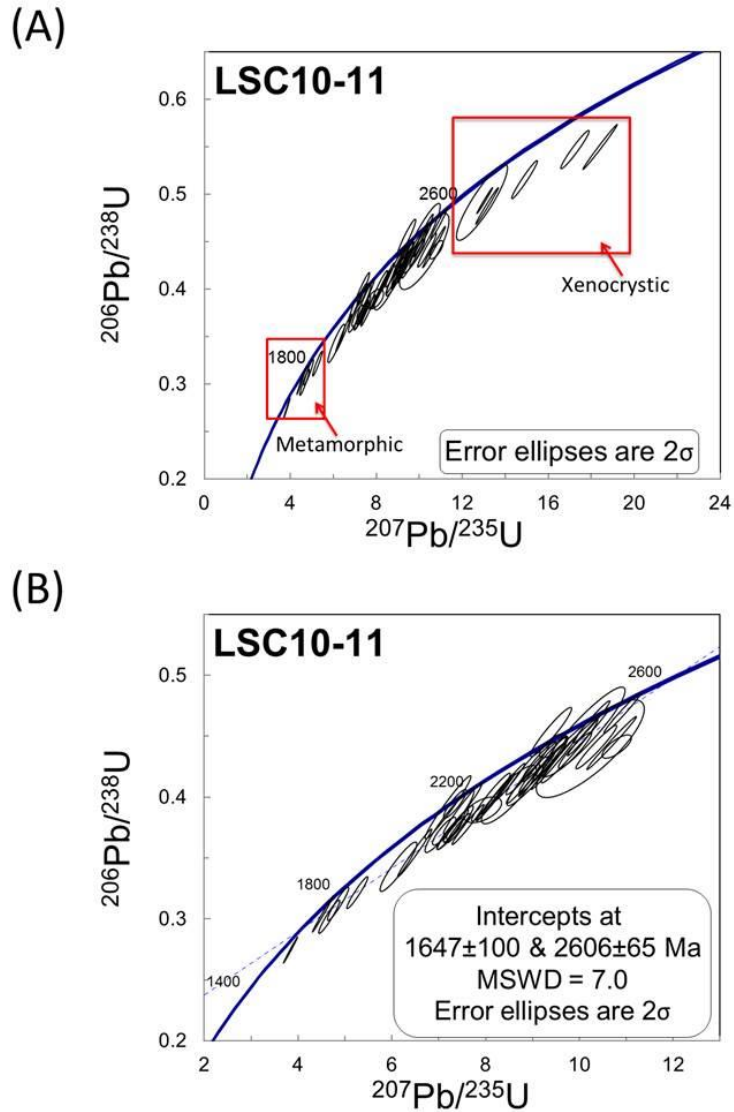
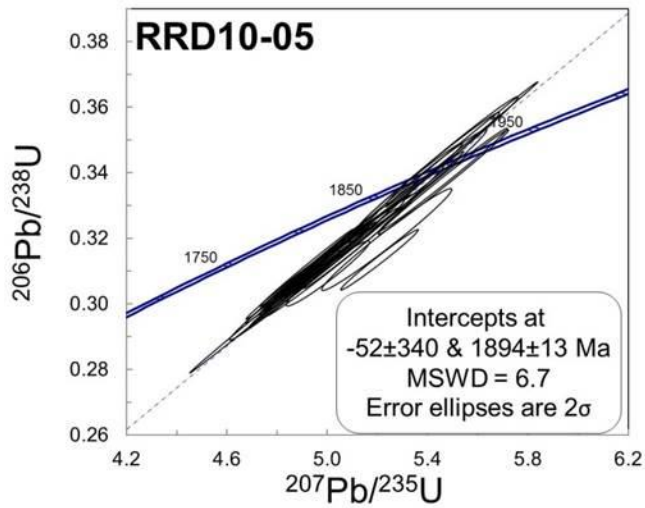


Figure 3-10. (A) Concordia diagram plotting discordance $\leq 10\%$ U-Pb data for mafic gneiss sample LSC10-11. Each ellipse represents a single spot analysis and its 2σ error. (B) Expanded view of concordia excluding xenocrystic zircons, showing spread of samples and the calculated upper intercept age.

(A)



(B)

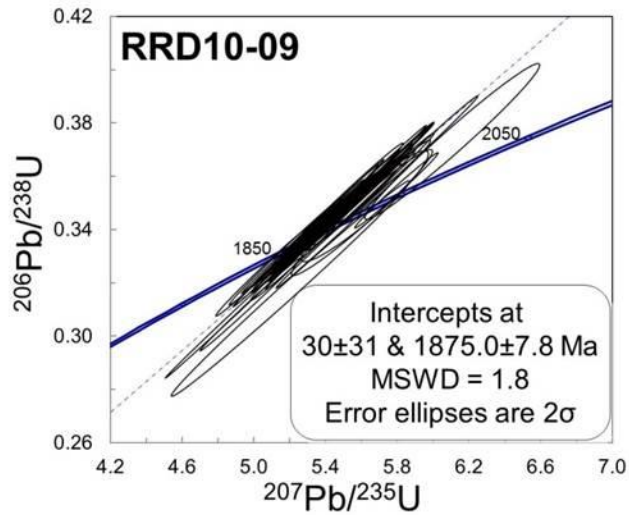


Figure 3-11. Concordia diagram showing U-Pb upper intercept regression for granitoid samples RRD10-05 (A) and RRD10-09 (B). Each ellipse represents a single spot analysis and its 2σ error.

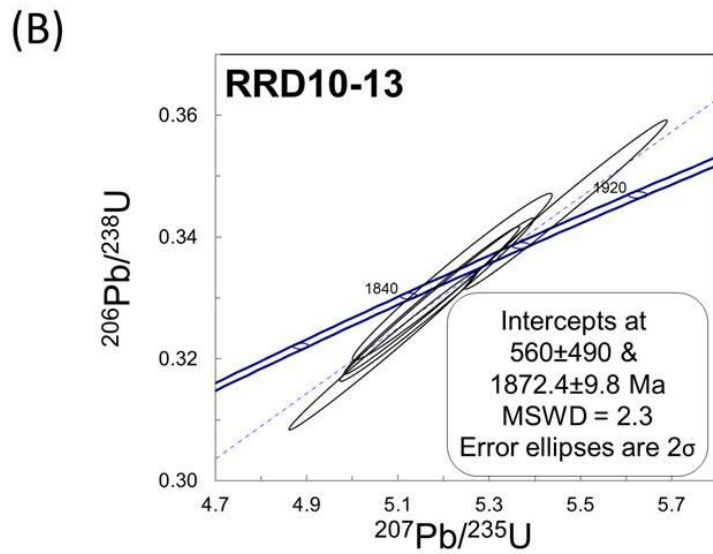
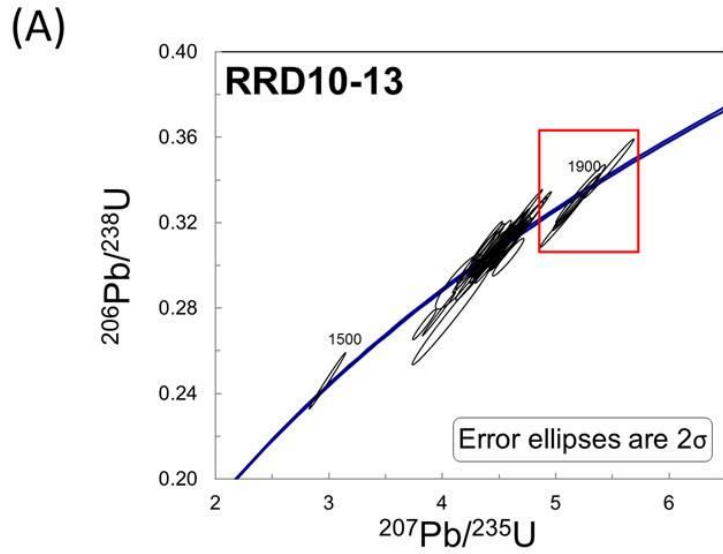


Figure 3-12. (A) Concordia diagram plotting composite U-Pb data for garnet granulite sample RRD10-13. Each ellipse represents a single spot analysis and its 2σ error. (B) Expanded view of upper end of concordia showing calculated upper intercept age.

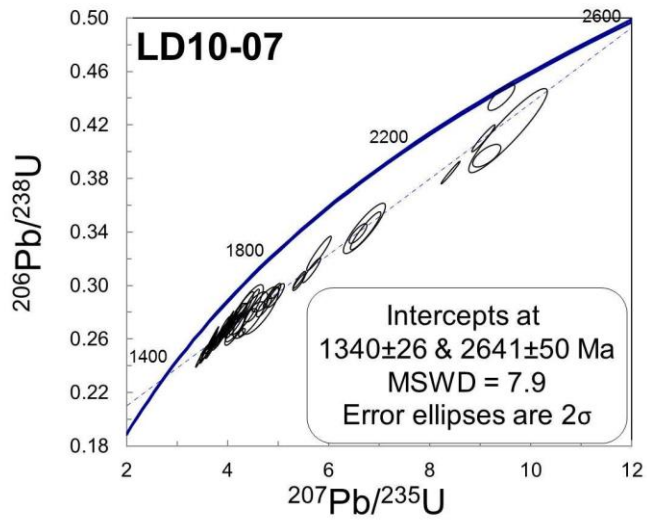


Figure 3-13. Concordia diagram plotting composite U-Pb discordia regression for orthogneiss sample LD10-07. Each ellipse represents a single spot analysis and its 2σ error.

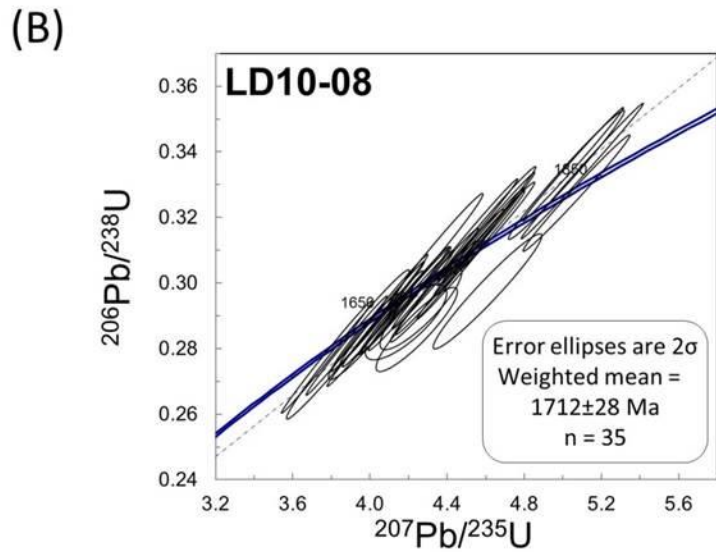
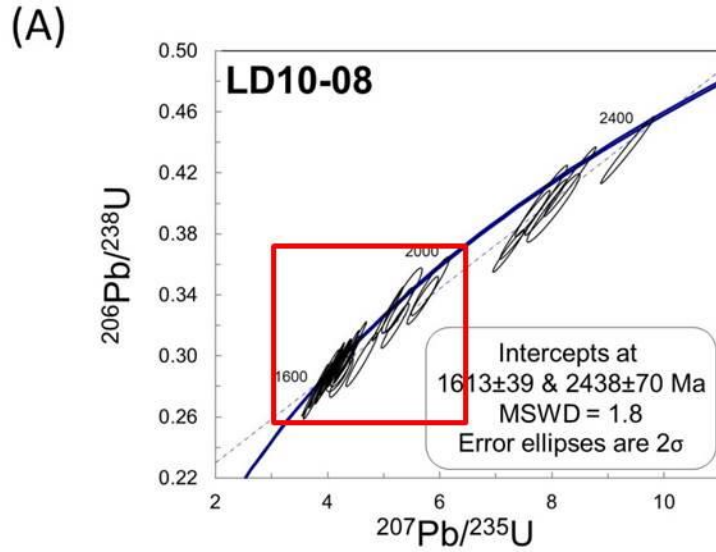
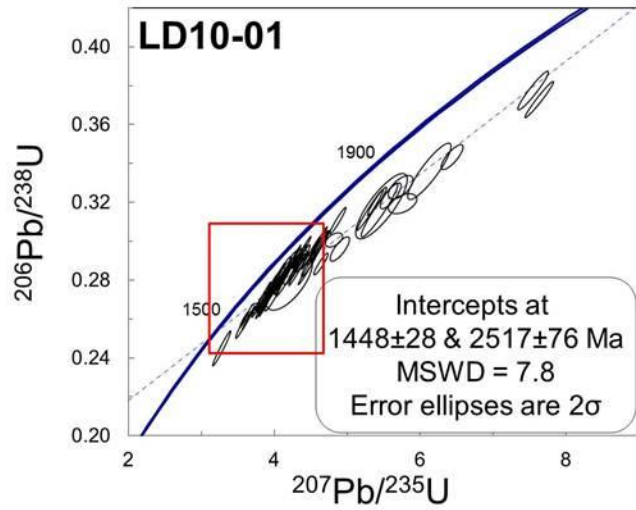


Figure 3-14. (A) Concordia diagram plotting composite U-Pb data for orthogneiss sample LD10-08. Each ellipse represents a single spot analysis and its 2σ error. (B) Expanded view of lower end of concordia showing spread of samples and weighted mean age.

(A)



(B)

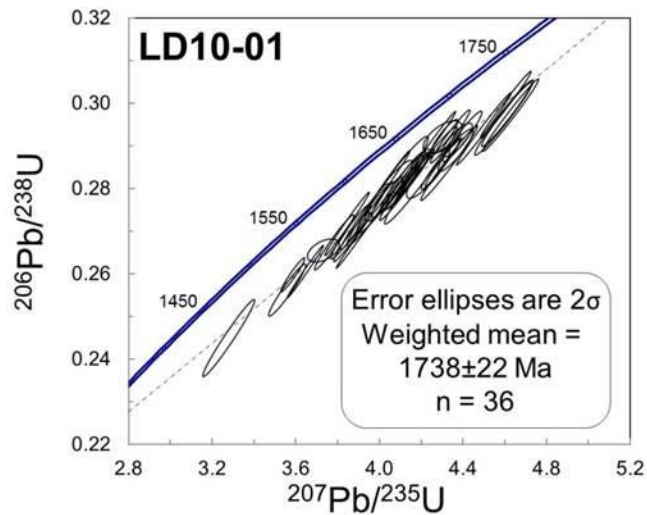


Figure 3-15. (A) Concordia diagram plotting composite U-Pb data for orthogneiss sample LD10-01. Each ellipse represents a single spot analysis and its 2σ error. (B) Expanded view of lower end of concordia showing spread of samples and weighted mean age.

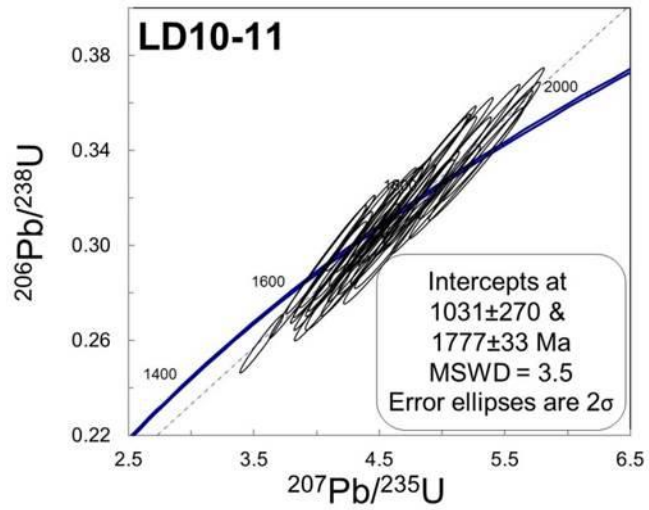


Figure 3-16. Concordia diagram showing U-Pb upper intercept regression for quartz pegmatite sample LD10-11. Each ellipse represents a single spot analysis and its 2σ error.

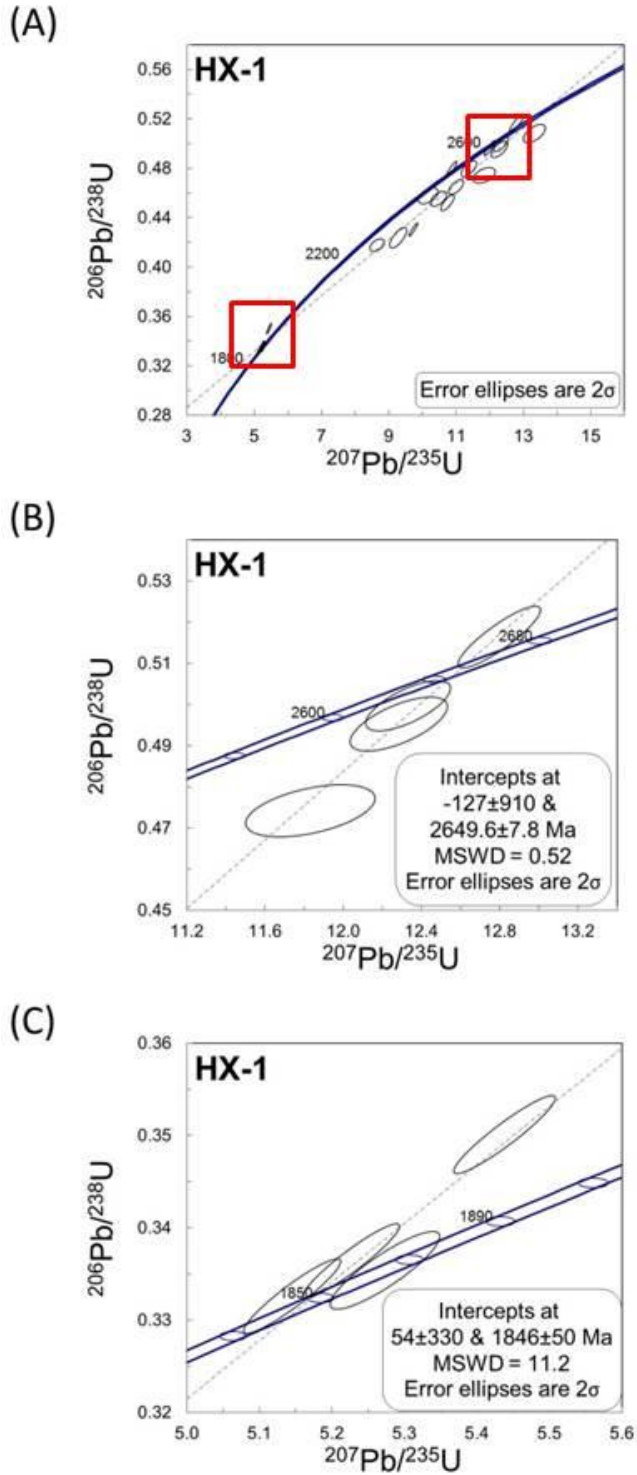


Figure 3-17. (A) Concordia diagrams plotting composite U-Pb data for orthogneiss sample HX-1. Each ellipse represents a single spot analysis and its 2σ error. (B) Expanded view of upper end of concordia showing samples selected for regression. (C) Expanded view of lower end of concordia showing samples selected for regression.

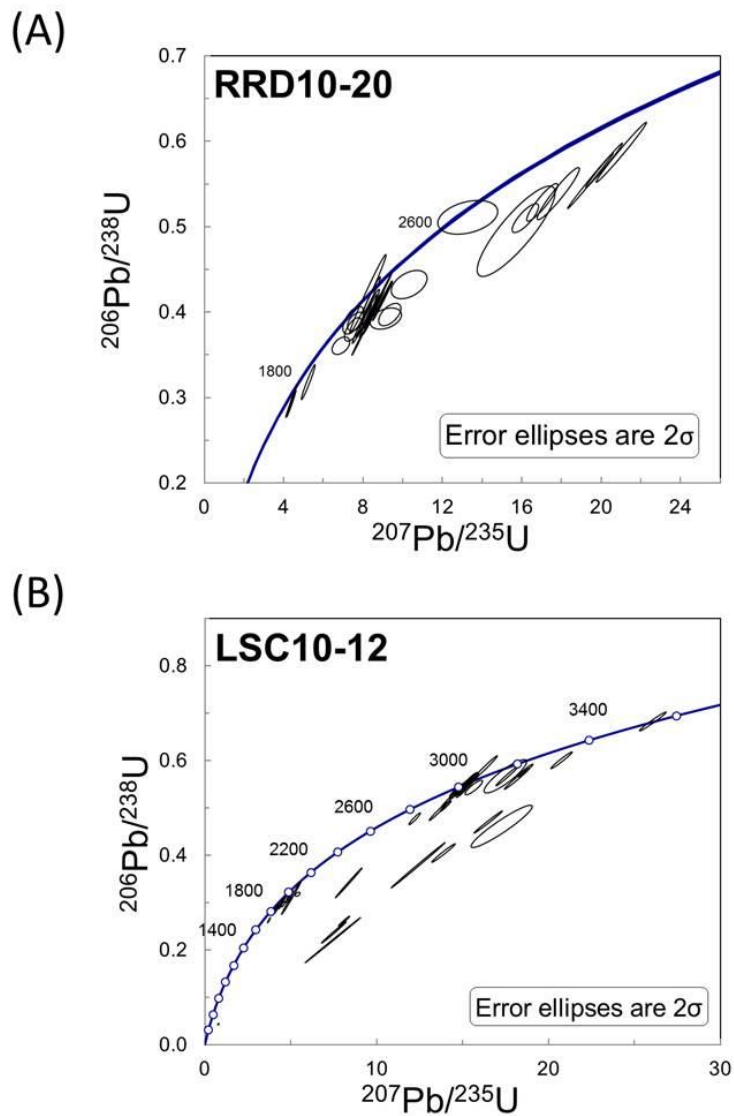


Figure 3-18. (A) Concordia diagram plotting composite U-Pb data for dioritic granulite sample RRD10-20. (B) Concordia diagram plotting composite U-Pb data for meta-granitoid sample LSC10-12. Each ellipse represents a single spot analysis and its 2σ error.

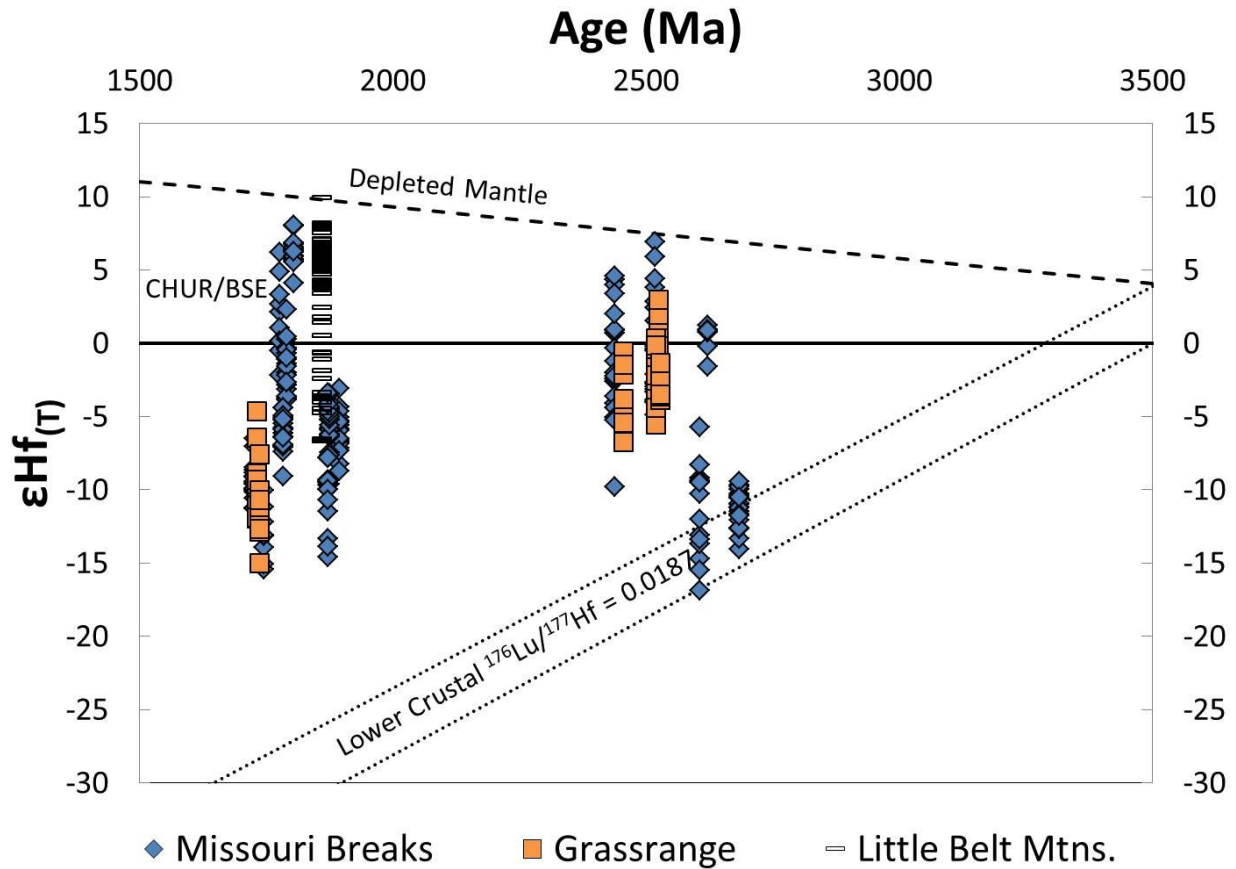


Figure 3-19. Hf evolution diagram showing the granitoid and meta-igneous samples (blue diamonds) against the granitoid samples from the Grassrange (Chapter 2) (orange squares) and data from the Little Belt Mountains (Weiss et al., 2009) (black bars). Lower Crustal – lower continental crust calculated using Rudnick and Gao (2003) (dotted line), CHUR – chondritic uniform reservoir, BSE – bulk silicate earth (Faure and Mensing, 2005) (solid line), DM – depleted mantle (Chauvel and Blichert-Toft, 2001) (dashed line).

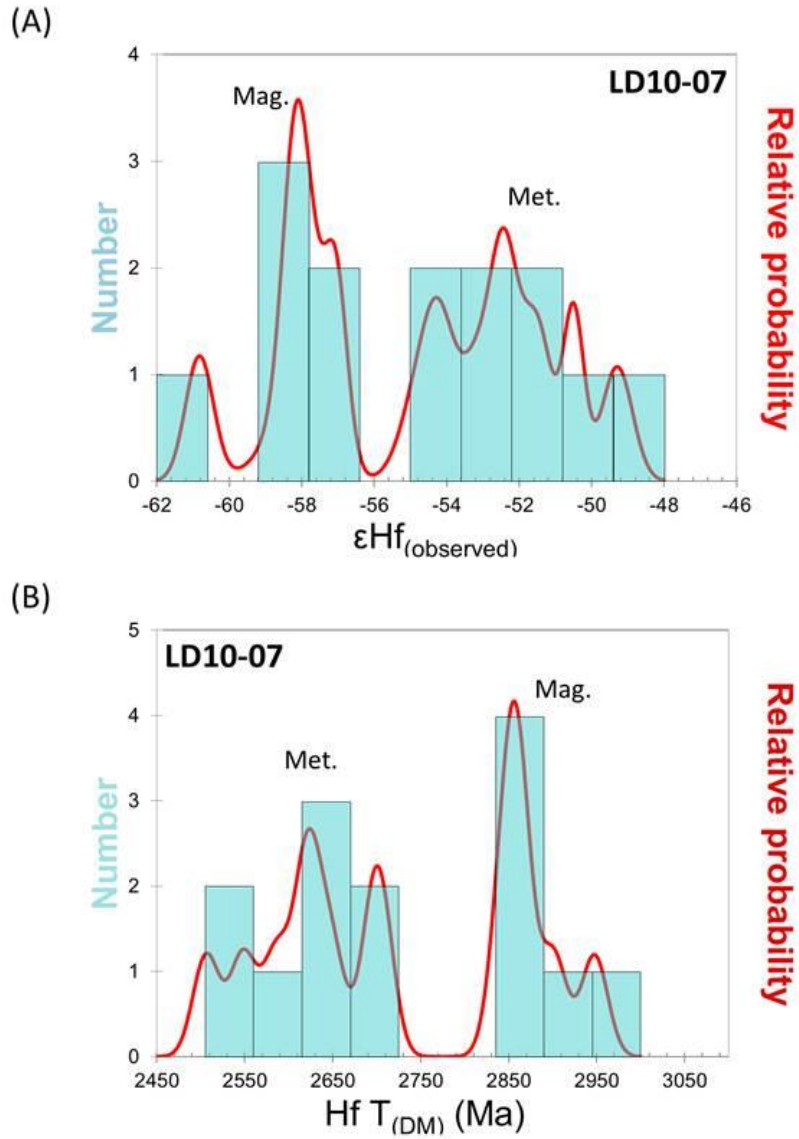


Figure 3-20. (A) Probability density plot showing initial ϵHf values for sample LD10-07. (B) Probability density plot showing Hf $T_{(DM)}$ values for sample LD10-07. Met. – metamorphic zircons; Mag. – magmatic zircons (see text for more details).

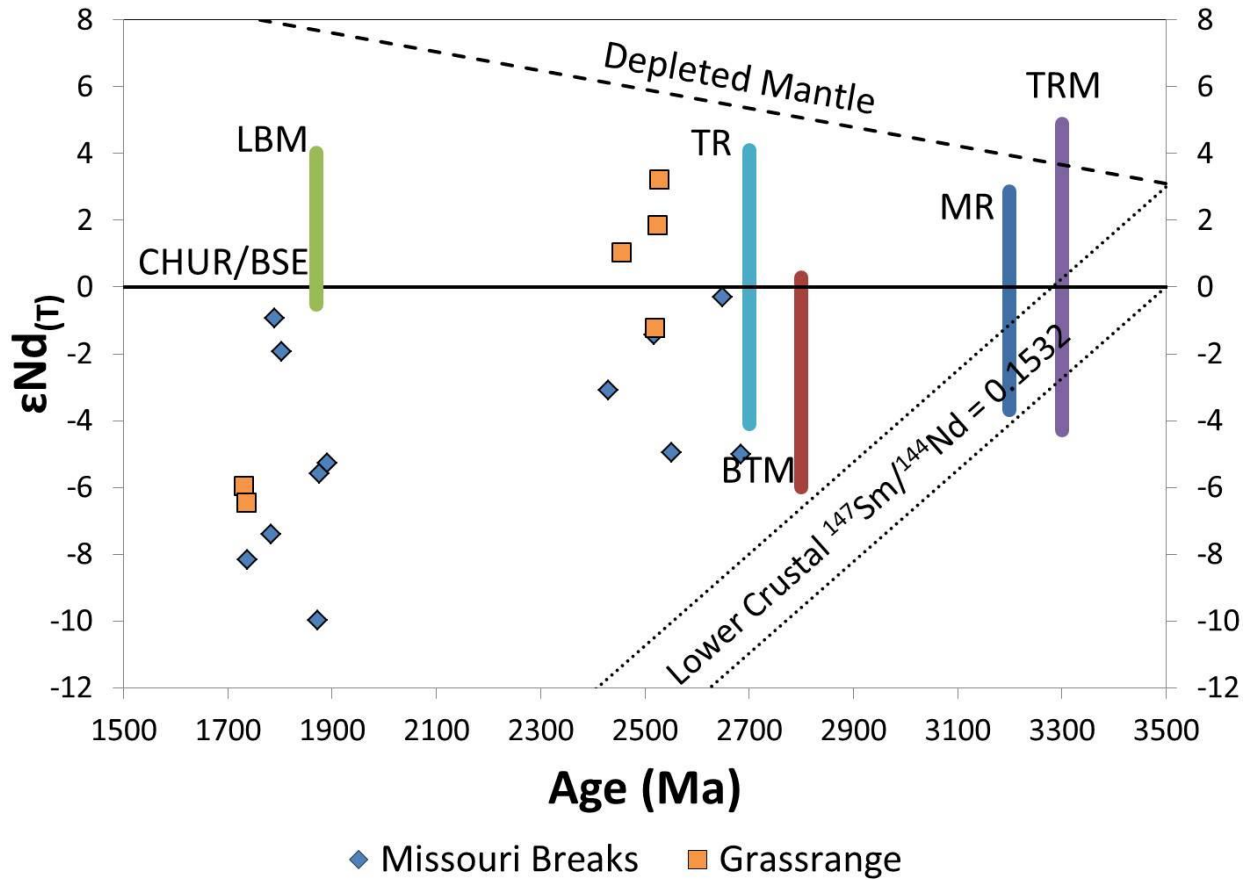


Figure 3-21. Sm-Nd evolution diagram showing the meta-igneous samples (blue diamonds), Little Belt Mountains (green bar), and four different northern Wyoming province crustal outcrops (all citations are in the text). The xenoliths from the Grassrange are shown for reference (orange squares). Lower Crustal – zone of lower continental crust calculated using Rudnick and Gao (2003) (dotted line), CHUR – chondritic uniform reservoir, BSE – bulk silicate earth (Faure and Mensing, 2005) (solid line), DM – depleted mantle (Chauvel and Blichert-Toft, 2001) (dashed line), LBM – Little Belt Mountains, TR – Teton Range, BTM – Beartooth Mountains, MR – Madison Range, TRM – Tobacco Root Mountains.

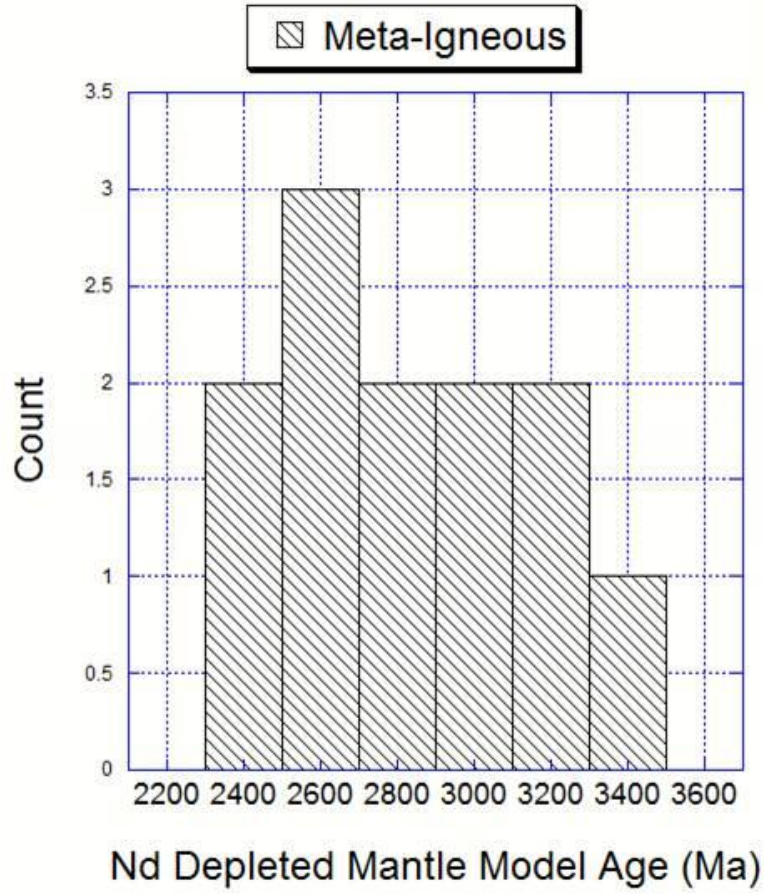


Figure 3-22. Histogram showing Sm-Nd depleted mantle model ages (Ga) of meta-igneous whole rocks. T_{DM} calculated using the model of DePaolo, 1981.

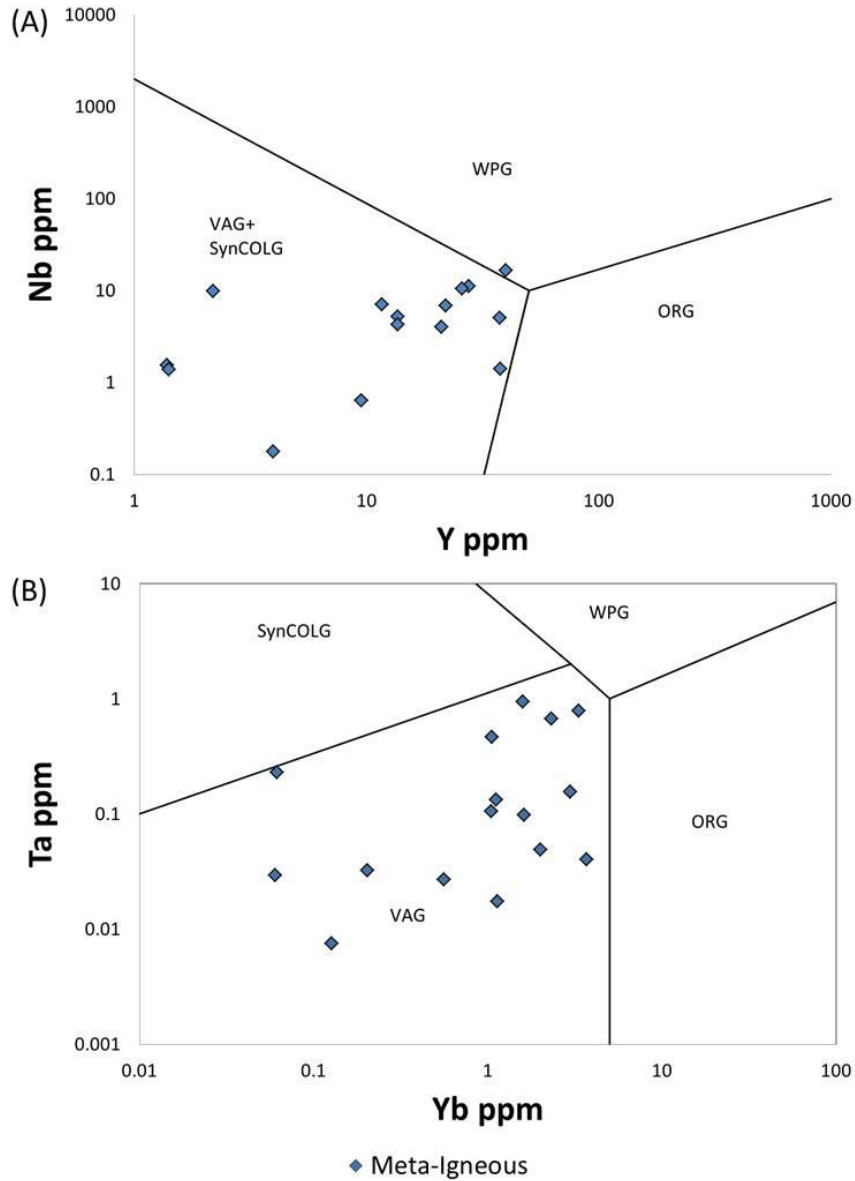


Figure 3-23. Trace element discrimination diagrams (after Pearce et al., 1984) for meta-igneous samples (blue diamonds): (A) Heavy rare earth element Y (ppm) vs. high field strength element Nb (ppm), (B) Heavy rare earth element Yb (ppm) vs. high field strength element Ta (ppm).

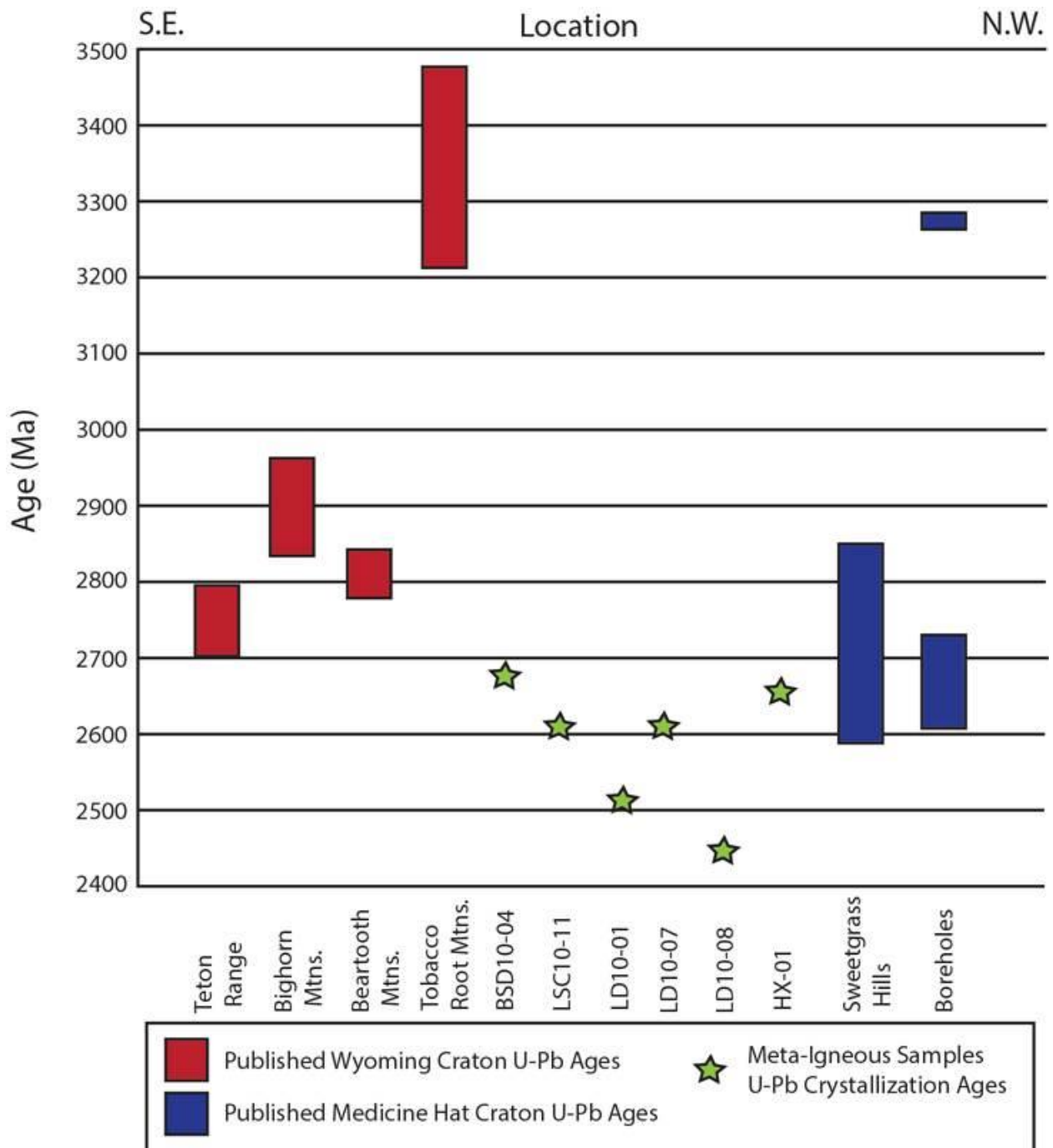


Figure 3-24. Published Archean to earliest Paleoproterozoic U-Pb ages of zircon from the northern Wyoming craton (red bars) compared to published ages for the MHB (blue bars) (all citations are in the text). OC – Owl Creek Mountains, BM - Bighorn Mountains, BT – Beartooth Mountains, TR – Tobacco Root Mountains, SG – Sweetgrass Hills, BH – borehole. Wyoming – light gray, Medicine Hat – dark gray. Crystallization ages of meta-igneous xenoliths from this study – green stars.

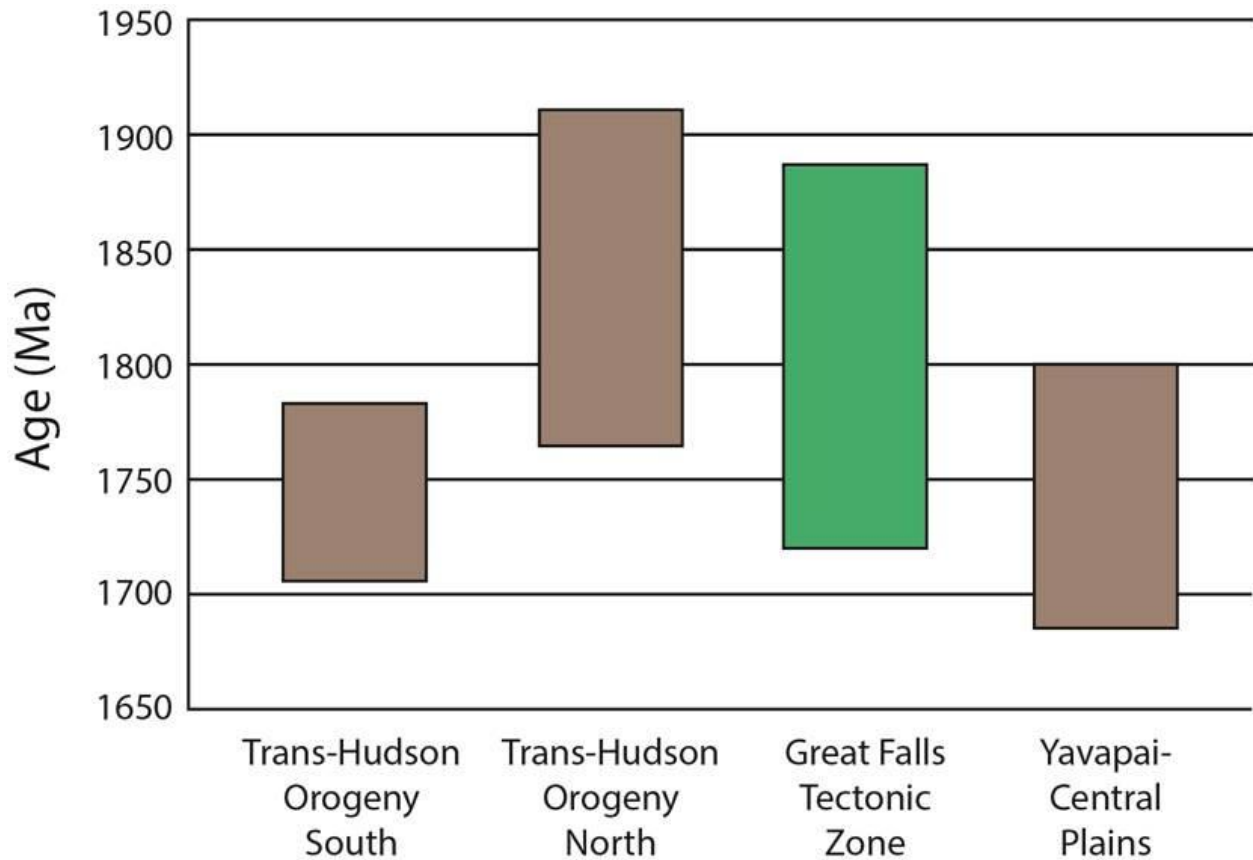


Figure 3-25. Comparison of published U-Pb ages from the southern Trans-Hudson Orogen (all citations are in the text) against the northern Trans Hudson Orogen, Great Falls tectonic zone (Chapter 2 and this study), and Yavapai-Central Plains.

CHAPTER 4 LITTLE ROCKY MOUNTAINS

Introduction

The Archean Medicine Hat block (MHB) lies within a 700 km wide zone of Archean and Paleoproterozoic tectonic elements that separate the Wyoming Craton from the Hearne Province. It is bracketed by the Paleoproterozoic suture Great Falls tectonic zone (GFTZ) to the south (O'Neill and Lopez, 1985; Mueller et al., 2002; Mueller et al., 2005; Foster et al., 2006), and the aeromagnetically defined Vulcan structure to the north (Thomas et al., 1987; Hoffman, 1988; Hoffman, 1990; Ross et al., 1991; Eaton et al., 1999) (Figure 4-1). This zone includes features identified from geophysical surveys (Lemieux et al., 2000), borehole data (Villeneuve et al., 1993), and limited xenoliths (Davis et al., 1995; Gorman et al., 2002). The Medicine Hat Block lies beneath the Phanerozoic sediments of the Western Canada Sedimentary Basin with no reported surface exposures. Because of this, the origin of the MHB and its tectonic relationships to the Hearne and Wyoming provinces are largely unknown.

The Little Rocky Mountains, Montana, contain excellent sections of Paleozoic and Mesozoic sedimentary rocks (Knetchel 1959) exposed in a domal uplift formed when Tertiary syenite porphyries intruded the section (Weed and Pirsson, 1898). Precambrian basement rocks are also exposed in the Little Rocky Mountains (LRM), but as blocks within and along the margins of the intrusions. These blocks provide one of only two outcrop accesses to otherwise buried basement in the central GFTZ. Southwest of the LRM, the Little Belt Mountains (LBM) provide the only other outcrop access to Precambrian crust within the central GFTZ. The Little Belt Mountains were determined by Mueller et al. (2002) via geochronologic and geochemical data from

gneisses to be a subduction-generated igneous arc formed during the time interval of 1.9 Ga to 1.8 Ga. Based on aeromagnetic data (Sims et al., 2004) and their geographic location within the GFTZ (Figure 4-2), the Little Rocky Mountains may comprise a segment of Medicine Hat Block crust, or may represent another opportunity, like the LBM, to gain greater insight into the formation of the GFTZ.

This paper presents the results of a geochemical and geochronologic study of the crystalline basement of the Little Rocky Mountains and compares it to the other basement exposure within the central GFTZ, the Little Belt Mountains. We then assess the relationship of the LRM to the Archean Medicine Hat block and Wyoming Province. Whole-rock major and trace element geochemistry, whole-rock Sm-Nd and Pb-isotopes, and zircon U-Pb geochronology and Hf-isotope studies were conducted on 12 orthogneiss, 9 amphibolite, 10 schist, and 3 paragneiss samples. Neoproterozoic ages from the LRM (this study) and the Priest River complex (Doughty et al., 1998) (Figure 4-1) are then combined with previously published ages from the MHB (Villeneuve et al., 1993; Davis et al., 1995; Gorman et al., 2002) to compare the MHB with both the Wyoming and Hearne Cratons.

Geologic Background

The Little Rocky Mountains, located in Philips and Blaine counties of north-central Montana, are a series of peaks and buttes exposing Precambrian through Cenozoic rocks (Figure 4-3). The core of the mountain range consists of Paleogene syenite intrusions surrounded by a structural dome of basement and cover rocks. Weed and Pirsson (1898) published the first detailed evaluation of the regional geology, observing how the uplift of the Little Rocky Mountains deformed the otherwise flat lying

sedimentary strata of the region, far from the main front of the Northern Rocky Mountains.

Stratigraphy

The central domain of the Little Rocky Mountains uplift is a series of porphyritic quartz syenite, hornblende syenite, and monzonite intrusions (Bailey, 1974; Russell, 1984). The syenite porphyry includes 2-20 mm diameter phenocrysts of orthoclase, often with albitic plagioclase inclusions, in a fine groundmass of feldspars and quartz (Wilson and Kyser, 1988). Biotite and amphibole occur as rare and generally altered mafic phases comprising $\leq 1\%$ of the typical rock. Older phases of syenite porphyry are silicified, and host gold and silver mineralization in the region (Peterman, 1980). K-Ar ages determined by Hearn et al. (1977) range between 58 and 66 Ma, interpreted as the age of the syenitic intrusion. Adjacent country rock lacks evidence of contact metamorphism, with contacts between the porphyry and country rock interpreted as faults (Wilson and Kyser, 1988).

Phanerozoic sedimentary strata are exposed in much of the uplift, including over 1000 m of Paleozoic and 1200 m of Mesozoic strata. The oldest unit in the LRM is the Cambrian Flathead Sandstone, deposited unconformably above pre-Belt Supergroup metamorphic units (Knetchel, 1959). The Flathead in turn is depositionally overlain by the mixed fine-grained clastics and carbonates of the Late Cambrian Emerson Formation (Knetchel, 1959). The late Ordovician Bighorn dolomite occurs disconformably above the Emerson Formation, and is a resistant, ridge forming unit locally rich in marine invertebrate fossils (Knetchel, 1959). Further up section, above another disconformity, lie Devonian sedimentary units, which are dominantly interbedded carbonate and shale (Knetchel 1959). Carbonates of the Madison group

dominate the Carboniferous section, and often form prominent ridges and buttes in the Little Rocky Mountains (Knetchel, 1959). The Mesozoic section includes both marine and non-marine sediments, and is dominated by fine grained clastics with subordinate limestone. These include carbonates of the Rierdron Formation, and marine to marine-terrestrial shale of the Swift and Morrison formations (Knetchel, 1959). Lower Cretaceous deposition is represented by the sandstone and shale of the Kootenai formation. This is overlain by the shale-rich Thermopolis, Mowry, and Warm Creek formations (Knetchel, 1959). The Montana group concludes the Cretaceous sequence, with both sandstone and shale formations. The Bearpaw Formation of the Montana Group is the youngest Mesozoic unit in the Little Rocky Mountains, consisting of marine shale with minor bentonite and cherty horizons (Knetchel, 1959).

Precambrian gneiss, schist, and amphibolite crop out in the Little Rocky Mountains in stream gorges and saddles between topographic highs (Weed and Pirsson 1896). Knetchel (1959) observed that many of the Archean metamorphic rocks are foliated meta-sedimentary rocks and meta-volcanic rocks, based on mineralogy and stratigraphic relationships between biotite rich gneiss and schist units, quartzites, and amphibolites. The metasedimentary rocks are dominantly quartzofeldspathic, with variable contents of garnet, chlorite, biotite and white mica, and amphibole (Knetchel, 1959). In the Ruby Gulch area, lithologies include fine grained amphibolite, finely banded white gneiss, sheared gneiss with elongate feldspars, a variety of micaceous, garnet-bearing, and amphibole schists, and thin beds of quartzite (Dyson, 1939). Peterman (1980) collected seven samples from road cuts near the Ruby Gulch mine site. These included several samples of fine grained biotite granitic gneiss, two samples

of biotite hornblende tonalitic-granodioritic gneiss, and one fine grained quartz amphibolite. Biotite in these samples is relatively fresh, and plagioclase grains display moderate sericitization (Peterman, 1980). The samples displayed strong fabrics, dominated by biotite foliation and (in some samples) quartz-feldspar augen (Peterman, 1980).

Previous Geochronology And Geochemistry

Limited age control exists for the Precambrian units of the Little Rocky Mountains. K-Ar dates published by Burwash et al. (1962) yielded ages of 1.71 Ga (hornblende) and 1.75 Ga (biotite), consistent with other cooling ages for the region (Giletti, 1966; Roberts et al., 2002). Rb-Sr isotopic analyses by Peterman (1980) yield a seven point isochron corresponding to an age of ~2.55 Ga, and an initial $^{87}\text{Sr}/^{86}\text{Sr}$ value of ~0.706.

Sample Descriptions

The samples collected for this study fall into several broad categories: Amphibolite, meta-supracrustal schist and gneiss, and orthogneiss. These are consistent with previous observations by Weed and Pirsson (1896) and Knetchal (1959). Sample mineralogy and characteristics are discussed below.

Amphibolite

Samples MLR-03 (Figure 4-4A, B), MLR-07 and MLR-14 are garnet amphibolites. They are dominated by fresh, anhedral to subhedral green amphibole grains up to 0.75 mm in length. The grain's preferred orientation defines a weak lineation. Anhedral plagioclase and quartz grains ≤ 0.4 mm in length are common. Garnet occurs as irregular fragmented masses with quartz, feldspar, and opaque inclusions. Trace volumes of opaque phases are present. MLR-10, MLR-11, and

LRMGM-2 (Figure 4-4C, D) are medium to fine grained garnet quartz amphibolites. Amphibole grain orientation and limited compositional variation between quartz poor and rich layers define a weak fabric in the samples. Amphibole is green to brownish-green, with anhedral grain shapes and embayed grain boundaries common. Grain size ranges between 0.1 to 0.5 mm in width. Plagioclase is the second most abundant phase, occurring as anhedral grains with lobate margins. Trace amounts of quartz grains are present and exhibit undulose extinction. Garnet occurs as subhedral grains up to 1 mm in width. The grains are fresh and contain abundant plagioclase and uncommon quartz inclusions. LRMGM-1, LRGM-6, and LRMPG-1 are medium to fine grained quartz amphibolites. Green to brown-green amphibole grains, generally between 0.1-0.5 mm wide and up to 1 mm long, dominate the samples. Amphibole grain orientation defines a lineation in the samples, and the grains are generally subhedral, with some embayed grain margins. Smaller anhedral plagioclase grains with generally lobate grain boundaries make up ~30-40% of each sample. The remainder is uncommon subhedral to anhedral quartz.

Quartzofeldspathic Schists

Sample LRMGM-3 and MLR-08 are medium grained, amphibole- biotite-bearing quartzofeldspathic schists. A foliation is defined by biotite, with compositional variation and amphibole orientation contributing to the overall fabric. Rounded plagioclase porphyroblasts up to 1 mm in diameter deflect the biotite foliation. Matrix plagioclase grains are smaller (only up to 0.5 mm in diameter), subhedral, and show some sericitic alteration. Uncommon microcline grains are similarly sized and typically less altered than plagioclase. Quartz is elongate, with grains up to 1 mm in length. Dynamic recrystallization of quartz is indicated by subgrain formation and undulose extinction.

Biotite grains are up to 0.5 mm in length, and are generally unaltered. Green to green-brown amphibole is subhedral, and shows evidence of alteration along cleavage planes. Samples LRMGM-4, LRMGM-5, and LRMPG-3 are similar to LRMGM-3, but include rare, euhedral titanite grains. MLR-16, MLR-18, MLR-18, LRMGM-7 (Figure 4-5E) and LRMPG-2 (Figure 4-5F) are fine grained biotite quartzofeldspathic schists. Biotite and a weak compositional variation define the layering within the samples. Biotite grains are euhedral to subhedral, and up to 0.2 mm in length. Quartz is the dominant mineral, with subhedral grains <0.2 mm in width making up over 50% of the samples. Plagioclase and K-feldspar are common, with unaltered subhedral grains similar in size to the quartz grains.

Gneisses

Sample LRMGM-8 (Figure 4-4E, F) is a biotite granitic gneiss with abundant rounded microcline and perthite grains up to 3 mm in diameter. Biotite defines a weak foliation in the sample. Quartz is abundant and shows extensive subgrain development and undulose extinction consistent with dynamic recrystallization. Samples MLR-04 (Figure 4-5C, D) and MLR-05 are garnet biotite quartzofeldspathic augen gneisses. Plagioclase grains core large porphyroclasts, often >2 mm in diameter. A biotite foliation and quartz ribbon lineation define a strong fabric in the sample. The quartz ribbons show extensive polygonal subgrain rotation recrystallization diagnostic of mid-temperature (~400-500°C) metamorphic dynamic recrystallization. Relatively unaltered, euhedral garnet porphyroblasts are present in the sample.

Sample MLR-13 (Figure 4-5A, B) is a staurolite chloritoid quartzofeldspathic gneiss, with cm-scale compositional variations defined by chloritoid rich and poor

domains. Chloritoid defines the foliation in the sample, and is scattered throughout the rock. Staurolites up to 2 mm in length are common. The grains commonly contain anhedral to subhedral quartz inclusions. Dynamically recrystallized, elongate quartz grains dominate the rock matrix, in association with uncommon k-feldspar. Uncommon euhedral titanite grains occur throughout the chloritoid and staurolite domains of the sample.

Samples MLR-06, MLR-09, and MLR-19 are biotite quartzofeldspathic gneisses. The samples contain biotite-rich and k-feldspar-rich bands, which are several mm thick. The sample fabric is defined by biotite foliation; recrystallized, elongate quartz grains and ribbons; and augen cored by feldspar. Gray gneiss samples MLR-15 and MLR-12 differ somewhat from MLR-06, MLR-09 and MLR-19, with a dominant granoblastic fabric and the presence of amphibole.

Other Samples

Sample MLR-01 is a garnet, two-mica, quartzofeldspathic mylonitic gneiss. Quartz dominates the sample, and occurs as dynamically recrystallized, elongate grains to ribbons. Microcline grains are up to 0.5 mm in length, blocky, with irregular grain boundaries. Large microcline porphyroclasts are common as well, and deflect quartz ribbons. Biotite and white mica grains define a weak foliation, and are scattered through the sample. Garnet occurs as euhedral, relatively fresh porphyroblasts with uncommon inclusions of quartz and fractures.

Samples LRM-1, LRM-3, LRM-5, LRM-6, and LRM-7 were received from Dr. Zell Peterman as vials of zircon separates having been previously prepared for Rb-Sr analyses (Peterman, 1981). Samples LRM-1, LRM-5, LRM-6 and LRM-7 were described by Peterman (1981) as "fine-grained biotite granite gneisses". LRM-3 was

described as “biotite-hornblende gneiss of tonalitic to granodioritic composition” (Peterman, 1981).

Results

U-Pb and Lu-Hf data from meta-plutonic and detrital zircons in addition to whole-rock geochemical and isotopic data from samples collected from the Little Rocky Mountains, Montana, are presented below. Sample locations are shown in Figure 4-3. Methods are described in Appendix A. Geochemical and isotopic data and the latitude and longitude of the sample locations are summarized in Tables B-7 through B-9 (Appendix B).

Whole-Rock Geochemistry

All of the samples from this study are metamorphic, and when examining the samples in thin-section, protolith determination is sometimes uncertain. Representative photomicrographs are shown in Figure 4-4 and 4-5. Based primarily on the diversity of ages of the zircon populations, 11 samples were determined to be meta-igneous (see below). The orthogneissic samples (Table 4-1) have silica contents ranging from 55.3 to 73.8 wt. %. Collectively, the orthogneiss samples cluster along the metaluminous – peraluminous boundary (Figure 4-6) when plotted according to the alumina saturation index of Shand (1943). Meta-igneous amphibolites (Table 4-2) yielded silica contents ranging from 46.5 to 53.1 wt. %.

Schist samples MLR-08, MLR-17, and MLR-18 yielded a diverse range of zircon ages that are compatible with a sedimentary protolith. Gneissic samples MLR-04, MLR-05, and MLR-13 also yielded a diverse range of zircon ages, compatible with a sedimentary protolith. The schists (Table 4-3) primarily fall within the metaluminous field, but with some samples extending into the peraluminous field of the alumina

saturation index of Shand (1943) (Figure 4-6). The paragneisses (Table 4-4), mostly fall within the peraluminous field of the alumina saturation index of Shand (1943) (Figure 4-6). The protolith(s) of these schists and paragneisses may be sedimentary, volcanoclastic, and/or volcanic based on major element compositions. Discrimination is determined by comparing wt. % values of MgO and CaO versus Al_2O_3 . Weathering processes leave behind residual Al_2O_3 , generally in clays, relative to MgO and CaO. MgO and CaO are carried away as a dissolved load when they are liberated by the breakdown of less stable igneous phases at surface conditions. Leyreloup et al. (1977) developed a ternary diagram, based on CaO-MgO- Al_2O_3 , for discrimination of igneous and sedimentary protoliths. Meta-sedimentary units are recognized by their abundance of Al, which is concentrated preferentially in sediments as plagioclase and mafic mineral weather. Abundances of Al_2O_3 are relatively low (12.8 to 18.9 wt. %), but alkali contents in some are sufficiently high that their normative mineralogy contains 0 - 7% corundum. Petrographic discrimination between sedimentary, volcanoclastic, and/or volcanic origins for the schists is difficult; however, variations of Ca, Mg, and Al concentrations provide some insight into their origins. Among the schistose samples, all plot in the meta-sedimentary field, with one lying on the border of meta-igneous, and all three of the paragneiss samples plot within the meta-sedimentary field. Although most of the schistose samples have compositional characteristics that indicate a sedimentary origin, these discriminants are not sufficiently accurate to exclude a volcanoclastic component.

Trace element compositions (Table 4-1 and 4-2) of the orthogneiss and amphibolite samples are summarized in Figure 4-8A, and plotted normalized to primitive mantle values of McDonough and Sun (1995). The plots show enrichments in fluid

mobile incompatible element concentrations, such as Rb, Ba, and Pb, up to 400 times the primitive mantle concentrations. This relative enrichment is paired with minimal enrichment in fluid immobile trace elements, including heavy REE (Figure 4-8A). The majority of the orthogneiss samples yielded low values of Eu and Sr relative to elements of similar compatibility, while the amphibolite samples yielded higher values of Eu and Sr relative to elements of similar compatibility (Figure 4-9). Nb and Ta are depleted relative to the observed values for neighboring elements in all of the orthogneiss and amphibolite samples when normalized to primitive mantle.

U-Pb Geochronology Of Zircon

Rock samples larger than ~20 cm in diameter were processed for zircon separates in addition to whole-rock geochemistry. The zircon concentrates were then analyzed for U-Pb ages and Hf isotopic composition to aid in characterizing the events recorded in the LRM. Zircon U/Pb age populations from meta-supracrustal samples were filtered for analyses $\leq 10\%$ discordant. This arbitrary cutoff is common in the U/Pb geochronology community, and served to filter out grossly disturbed grains from the sample set. Zircon failing this test typically represents disturbed grains, where Pb loss occurred during some past metamorphic or fluid flow event. Some analyses are rejected as “outliers” when the analysis and associated error do not overlap with the mean and standard deviation of the main age population. Grains passing through the filters typically define a discordia line, and are used to generate upper intercept ages. Crystallization ages for the meta-plutonic samples (orthogneisses and amphibolites) used analyses $\leq 10\%$ discordant, and yielded four different age populations (see discussions below). Apparent detrital zircon analyses $\leq 10\%$ discordant were used to generate age distributions for each meta-supracrustal sample.

U-Pb zircon ages from orthogneiss samples LRM-3, LRM-5, LRM-6, LRM-7, MLR-01, MLR-06, MLR-09, MLR-15, and MLR-19 yielded a wide spread of ages, from 1.87 Ga to 3.29 Ga, despite the relatively uniform bulk chemistries (Table 4-5). Zircons from 8 of the 9 samples reveal 2 distinct populations and a single sample of $^{207}\text{Pb}/^{206}\text{Pb}$ ages, and a third age is represented by a single sample. The first age-population includes samples MLR-01 and MLR-06. MLR-01 yielded 18 zircons $\leq 10\%$ discordant with a scatter of ages from ~ 2.39 to 2.44 Ga (Figure 4-10A). The scatter within the sample indicates that the isotopic system has likely been disturbed. The weighted mean $^{207}\text{Pb}/^{206}\text{Pb}$ age for the entire data set is 2.42 ± 0.01 Ga, which is interpreted as a minimum crystallization age. MLR-06 yielded 28 zircons with discordance $\leq 7\%$ with a scatter of ages from ~ 2.38 to 2.45 Ga (Figure 4-10B). Similar to MLR-01, the scatter indicates that the isotopic system was likely disturbed. The weighted mean $^{207}\text{Pb}/^{206}\text{Pb}$ age for the entire data set is 2.42 ± 0.01 Ga, which is interpreted as a minimum estimate of the crystallization age.

The second orthogneiss age-population includes samples MLR-15, MLR-19, LRM-3, LRM-5, LRM-6, and LRM-7, which yielded crystallization ages of ~ 2.8 Ga. MLR-15 and MLR-19 yielded ages of 2.78 ± 0.01 Ga, and 2.79 ± 0.01 Ga respectively, with no inheritance of older grains (Figure 4-11). MLR-15 yielded 43 grains ($\leq 10\%$ discordant), 16 of which were excluded from the crystallization calculation due to large measurement error ($>3\%$ Ma error), or due to anomalously young ages. These young ages reflect Pb-loss, causing grains to trend along a discordia line away from the main age population. One of the $\leq 10\%$ discordant grains from MLR-15 yielded an age of 1.87 ± 0.07 Ga, which is interpreted as a metamorphic age. MLR-19 yielded 56 grains

($\leq 10\%$ discordant), 6 of which have much younger ages that are attributed to Pb-loss causing grains to trend along a discordia line away from the main population. With these 6 grains excluded, 50 grains went into the crystallization calculation. LRM-3 yielded 23 zircons, 13 of which appear to fall along a discordia line (Figure 4-12A). The oldest 6 grains yielded an upper intercept age of 2.80 ± 0.09 Ga (Figure 4-12B). LRM-5 yielded 55 zircons, only 8 of which had discordance $\leq 10\%$. Of those 8, 4 grains had younger ages and higher discordance between 7-10% and 4 had older ages and discordance $\leq 3\%$. The younger ages in the higher discordance grains are attributed to Pb-loss, and these grains were excluded from the crystallization calculation. The four grains with discordance $\leq 3\%$ yielded an upper intercept age of 2.83 ± 0.04 Ga (Figure 4-13). LRM-6 yielded 6 zircons total, with only 2 meeting the concordance criteria ($\leq 10\%$ discordant). LRM-6 did not yield a crystallization age as any calculation with so few analyses is of dubious reliability. LRM-7 yielded 59 zircons; 12 were $\leq 10\%$ discordant. Six grains went into the upper intercept age calculation of 2.77 ± 0.04 Ga (Figure 4-14). Two grains were excluded because of high measurement errors, and 4 were excluded for being outliers.

Orthogneiss sample MLR-09 is the only orthogneiss sample that yielded a Paleoproterozoic age. The sample yielded 24 grains with $\leq 10\%$ discordance, 4 of which were excluded for being outliers. When all of the grains are plotted on concordia (Figure 4-15A) analyses scatter between ~ 3.2 and ~ 2.8 Ga indicating that metamorphism at c. 2.8 Ga likely disturbed the isotopic system. Ten analyses were rejected due to possible Pb-loss shifting their ages younger. The remaining 10 grains

yielded a weighted average $^{207}\text{Pb}/^{206}\text{Pb}$ age of 3.20 ± 0.01 Ga (Figure 4-15B) which is interpreted as a minimum crystallization age.

Amphibolites MLR-03 and MLR-10 were large enough for zircon separation. MLR-03 yielded 58 grains, only 32 of which had $\leq 10\%$ discordance. When all of the zircons are plotted on concordia (Figure 4-16A) analyses scatter between ~ 3.0 and ~ 2.8 Ga indicating that metamorphism likely disturbed the isotopic system similar to MLR-09. 20 analyses were rejected due to significant Pb-loss. The remaining 12 grains yielded a weighted average $^{207}\text{Pb}/^{206}\text{Pb}$ age of 3.01 ± 0.01 Ga (Figure 4-16) which is interpreted as a minimum crystallization age. Sample MLR-10 yielded 60 zircons total, with only 5 low discordance ($\leq 10\%$) grains recording individual $^{207}\text{Pb}/^{206}\text{Pb}$ ages between 3.10 Ga and 3.17 Ga. This hindered the calculation of a concordia intercept age, and indicates that the sample likely records multiple Pb-loss events.

The schist and paragneiss samples yielded 132 detrital zircon grains. The three schist samples (MLR-08, MLR-17, and MLR-18) yielded zircons ranging from sub-rounded to well-rounded. In aggregate, $^{207}\text{Pb}/^{206}\text{Pb}$ ages from 99 zircons $\leq 10\%$ discordant range from ~ 2.57 Ga to ~ 3.32 Ga (Table 4-6). On a probability density plot there are prominent age peaks at ~ 2.79 Ga (65% of the grains, from 2.74 – 2.81 Ga) and ~ 3.19 Ga (5% of the grains, from 3.13 – 3.20 Ga) (Figure 4-17). The three paragneiss samples (MLR-04, MLR-05, and MLR-13) yielded zircons ranging from subhedral to well-rounded. $^{207}\text{Pb}/^{206}\text{Pb}$ ages from 34 zircons ($\leq 10\%$ discordant) range from ~ 1.78 Ga to ~ 3.20 Ga (Table 4-6). The data have a prominent peak at ~ 2.79 Ga (41% of the grains, from 2.76 – 2.80 Ga) (Figure 4-17). Figure 4-17 shows a probability

distribution function comparing detrital zircon age spectra from the schists and paragneisses; data from the orthogneiss samples are provided for comparison.

Hf Isotopes In Zircon

Zircons were chosen for Lu-Hf analysis based on a number of different factors. Samples were arranged by age to better select a representative population of ages for Hf analysis. Zircons were preferentially chosen for low discordance (as discussed above) to have a more accurate U-Pb age with which to reduce the Hf isotope data. Zircons were further chosen for zonation patterns and grain size. If a zircon showed zonation and a U-Pb analysis was undertaken in a particular zone, ideally, the Hf spot would also be analyzed within the same zonation. The Hf spot-size is 40 μ m and the zircon (or zonation) needed to be large enough to fit the spot. ϵ Hf_(initial) calculations used rock-crystallization ages for meta-plutonic samples, and $^{207}\text{Pb}/^{206}\text{Pb}$ ages of individual detrital grains. For mantle separation ages, Hf T_{DM} represents minima because Lu/Hf in zircon is invariably lower than in whole-rocks (e.g., Griffin et al., 2002). Calculation of 2-stage or crustal residence ages, however, requires knowledge of the Lu/Hf of source(s) and were not calculated because the isotopic compositions are likely to result from a mixing of crustal and mantle sources. For those meta-plutonic samples (orthogneisses and amphibolite) that had an estimated time of protolith crystallization, ϵ Hf was calculated in two different ways. The first was based on the individual age (IA) of each analyzed grain within each sample regardless of discordance or Pb-loss. This range of ϵ Hf values is recorded in Table 4-5 labeled as “ ϵ Hf_(IA) Highest” and “ ϵ Hf_(IA) Lowest”. Next, ϵ Hf was calculated at the estimated time of protolith crystallization (i.e. ~2.4, ~2.8, ~3.0, or ~3.2 Ga) for each sample. This range of values was also recorded in Table 4-5 labeled as “ ϵ Hf_(T) Highest” and “ ϵ Hf_(T) Lowest”. These values were averaged and a

standard deviation used to characterize the spread of values (Table 4-5). ϵHf values are plotted on Figure 4-18A vs. $^{207}\text{Pb}/^{206}\text{Pb}$ age (Ma).

The youngest group of orthogneiss samples (MLR-01 and MLR-06) yielded U-Pb ages of ~ 2.42 Ga. Zircon $\epsilon\text{Hf}_{(2.4\text{ Ga})}$ for these samples ranges from -2.2 to -11.6 (Table 4-5). $\epsilon\text{Hf}_{(\text{IA})}$ values for the same samples ranged from -2.7 to -16.1 (Table 4-5). These differences likely reflect variable input of juvenile mantle-derived versus evolved crustal materials in the genesis of the parental magma over the course of zircon crystallization. The more coherent Hf isotopic compositions calculated at ~ 2.4 Ga suggest that the younger ages reflect Pb-loss and that the Lu-Hf system remained largely closed during a younger metamorphic event. These samples give a limited range of average depleted mantle model ages (T_{DM}) from 2.97 Ga to 3.00 Ga with standard deviations of 0.04 and 0.10 (Table 4-5). $\epsilon\text{Hf}_{(2.8)}$ values for orthogneiss samples MLR-15, MLR-19, LRM-3, LRM-5, and LRM-7 were also calculated (Table 4-5). The $\epsilon\text{Hf}_{(2.8\text{ Ga})}$ for $\leq 10\%$ discordant zircons from the samples range from -6.6 to -14.5, averages of -9.4 to -12.9, and standard deviations of 0.8 to 1.9 (Table 4-5). Because LRM-6 did not yield a crystallization age, $\epsilon\text{Hf}_{(\text{T})}$ values were not calculated. Average Hf $T_{(\text{DM})}$ for the ~ 2.8 Ga orthogneiss samples range from 3.31 Ga to 3.53 Ga with standard deviations from 0.03 to 0.07 (Table 4-5). The oldest orthogneiss sample (MLR-09) yielded a U-Pb crystallization age of 3.19 Ga, which was used for initial ϵHf calculations. The $\epsilon\text{Hf}_{(3.2\text{ Ga})}$ for $\leq 10\%$ discordant zircons from MLR-09 range from 3.8 to -2.2 with an average of 0.1 and a standard deviation of 1.7. As with the younger samples, calculating the initial Hf compositions using the upper intercept ages ($\epsilon\text{Hf}_{(\text{T})}$) yields more coherent estimates of initial Hf compositions than using the $^{207}\text{Pb}/^{206}\text{Pb}$ age of each zircon ($\epsilon\text{Hf}_{(\text{IA})}$), i.e., the

discordant ages represent Pb-loss rather than extraneous grains. Open system behavior, however, cannot be excluded.

The amphibolite samples (MLR-03 and MLR-10) yielded some zircons large enough for Hf isotopes to be analyzed. In sample MLR-03, the measured Hf isotopic compositions for all zircons were recalculated to the U-Pb crystallization age of 3.01 Ga. The $\epsilon_{\text{Hf}(3.0 \text{ Ga})}$ for $\leq 10\%$ discordant zircons from the sample range from 4.4 to -6.1 with an average of -1.0 and a standard deviation of 2.4. When the initial ϵ_{Hf} is calculated for the individual age (IA) of each analyzed grain (~ 2.7 to ~ 3.0 Ga) within MLR-03, the initial ϵ_{Hf} values ranged from 3.6 to -9.8 (Table 4-5). The average Hf $T_{(\text{DM})}$ for sample MLR-03 was calculated to be 3.28 Ga with a standard deviation of 0.09. MLR-10 did not yield a crystallization age, but for those zircons with discordance $\leq 10\%$, when initial ϵ_{Hf} is calculated for the individual age (IA) of each analyzed grain (~ 3.1 to ~ 3.2 Ga) within MLR-10, the initial ϵ_{Hf} values ranged from 2.4 to -4.4 (Table 4-5). The average Hf $T_{(\text{DM})}$ for sample MLR-10 was calculated to be 3.40 Ga with a standard deviation of 0.08.

All three schist samples yielded zircons large enough for paired U-Pb and Lu-Hf isotopic analysis. Initial Hf isotopic compositions were calculated using the $^{207}\text{Pb}/^{206}\text{Pb}$ age of each individual zircon. MLR-08 has initial ϵ_{Hf} values that range from 5.6 at 3.32 Ga to -15.7 at 2.48 Ga, and Hf $T_{(\text{DM})}$ ranging from 3.27 Ga to 3.44 Ga (Table 4-6). MLR-17 has initial ϵ_{Hf} values for the $\leq 10\%$ discordant grains that range from -6.9 at 2.82 Ga to -18.5 at 2.57 Ga, and Hf $T_{(\text{DM})}$ ranging from 3.32 Ga to 3.69 Ga (Table 4-6). MLR-18 has initial ϵ_{Hf} values for the $\leq 10\%$ discordant grains that range from -8.5 at 2.80 Ga to -16.0 at 2.78 Ga, and Hf $T_{(\text{DM})}$ ranging from 3.44 Ga to 3.63 Ga (Table 4-6).

All three paragneiss samples yielded zircons large enough for U-Pb and Hf isotopic analysis. Initial Hf isotopic compositions were calculated using the $^{207}\text{Pb}/^{206}\text{Pb}$ age of each individual zircon. MLR-04 has initial ϵHf values that range from 8.0 at 2.60 Ga to -16.0 at 1.78 Ga, and Hf $T_{(\text{DM})}$ model ages ranging from 2.57 Ga to 3.01 Ga (Table 4-6). MLR-05 has initial ϵHf values for the $\leq 10\%$ discordant grains that range from -1.1 at 3.20 Ga to -7.1 at 2.37 Ga, and Hf $T_{(\text{DM})}$ model ages ranging from 2.75 Ga to 3.44 Ga (Table 4-6). MLR-13 yields initial ϵHf values for the $\leq 10\%$ discordant grains that range from -7.7 at 2.78 Ga to -13.3 at 2.64 Ga, and Hf $T_{(\text{DM})}$ model ages ranging from 3.32 Ga to 3.53 Ga (Table 4-6).

Sm-Nd Whole-Rock Isotopes

As a group, the orthogneiss samples (including those without U-Pb ages) show a range in whole-rock $\epsilon\text{Nd}_{(0)}$ from -20.2 to -50.2. Initial ratios were calculated for samples MLR-01 and MLR-06 using the best estimates of the individual crystallization ages shown in Figure 4-10 ($^{207}\text{Pb}/^{206}\text{Pb}$ age of 2.42 Ga), which yielded $\epsilon\text{Nd}_{(2.4)}$ of -5.7 and -7.3 (Table 4-7, Figure 4-18B). Values for samples MLR-15, MLR-19, LRM-3, LRM-5, and LRM-7 were calculated using the $^{207}\text{Pb}/^{206}\text{Pb}$ ages shown in Figure 4-11 to Figure 4-14 (i.e., ~ 2.8 Ga), which yielded $\epsilon\text{Nd}_{(2.8)}$ of -6.5 to -10.5 (Table 4-7, Figure 4-18B). Initial ϵNd for sample MLR-09 was calculated using the crystallization age of 3.19 Ga (Figure 4-15). This calculation yielded $\epsilon\text{Nd}_{(3.2 \text{ Ga})}$ of -0.9 (Table 4-7, Figure 3-18B). Sm-Nd depleted mantle model ages were calculated for each sample using the model of DePaolo (1981). Orthogneiss samples MLR-01 and MLR-06 yielded Sm-Nd $T_{(\text{DM})}$ calculated to be 3.55 Ga and 3.15 Ga respectively (Figure 4-10). Samples MLR-15, MLR-19, LRM-3, LRM-5, and LRM-7 yielded a range of Sm-Nd $T_{(\text{DM})}$ model ages from 3.28 to 3.80 Ga (Table 4-7). Sample MLR-09 yielded a Sm-Nd $T_{(\text{DM})}$ of 3.42 Ga (Table

4-7). The amphibolite samples (including those without U-Pb ages) show a range in $\epsilon\text{Nd}_{(0)}$ values from 3.8 to -21.0. Initial ratios were calculated for sample MLR-03 using the best estimate of crystallization age ($^{207}\text{Pb}/^{206}\text{Pb}$ age 3.01 Ga) shown in Figure 4-16. This yielded $\epsilon\text{Nd}_{(3.0)}$ of -2.0 (Table 4-7, Figure 4-18B). The schist samples show a range in $\epsilon\text{Nd}_{(0)}$ values from -30.1 to -50.7, and Sm-Nd $T_{(\text{DM})}$ ranging from 2.99 Ga to 3.72 Ga (Table 4-7).

Discussion

Geochemical Insight Into Sample Origins

Geochemical evidence suggests that the orthogneiss samples either formed in a subduction zone environment, or represent remobilization of rocks that have an arc-signature. Most of the meta-plutonic are metaluminous, and one is peraluminous (Figure 4-6), which is not particularly diagnostic, but is consistent with observed granitoid suites from continental arc and continental collision settings (e.g., Mainar and Piccoli, 1989; Rogers and Hawkesworth, 1989; Chappell and White, 2001; Villaseca et al., 2012). Trace element patterns observed in the orthogneiss samples are also consistent with patterns in rocks from modern continental arcs (Figure 4-8A; e.g., Pearce, 1983; Thompson et al., 1984). Similarities include negative Eu and Sr anomalies indicative of fractional crystallization or residual plagioclase in the source, negative Nb and Ta anomalies, and elevated concentrations of some fluid-mobile elements such as Ba and Pb. Chondrite-normalized REE plots reveal elevated concentrations of light versus heavy rare earth elements, with non-enrichment to depletion in heavy REE suggestive of residual garnet and/or amphibole-pyroxene in the source region (La/Yb values between 150 and 1.5; Figure 4-9).

The meta-supracrustal samples are difficult to characterize in terms of protolith. Trace element patterns (Fig 4-8B) broadly mirror those of the meta-plutonic sample suite (Fig 4-8A), and again are consistent with a convergent margin provenance (Pearce, 1984; Rogers and Hawkesworth, 1989; Taylor and McLennan, 1995; Chappell and White, 2001). When the samples are plotted on a ternary diagram of the CaO-MgO-Al₂O₃ system (Figure 4-7) (Leyreloup et al., 1977), most of the schist samples lie within the “meta-sedimentary” field, with one falling into the “meta-igneous” field.

Little Rocky Mountains as Exposed Medicine Hat Block Crust

Correlation of igneous ages

Due to the lack of exposure of Medicine Hat Block crust, it remains poorly characterized. Data presented in this study link the Little Rocky Mountains to the Medicine Hat Block, and provide a valuable opportunity to characterize materials otherwise known mostly from geophysical evidence. Xenoliths from the Sweetgrass Hills yield zircon U-Pb ages of 2.60 to 2.84 Ga (Davis et al., 1995; Gorman et al., 2002). Similarly, Villeneuve et al. (1993) analyzed basement samples from core penetrating the MHB crust, revealing U-Pb zircon crystallization ages of 2.62 to 2.72 Ga, and one crystallization age of 3.28 Ga. Orthogneiss samples from this study reveal three distinct crystallization age ranges in the LRM: 2.42 Ga for two of the nine orthogneisses, 2.77 Ga to 2.81 Ga for five of the nine samples, and finally one sample at 3.19 Ga (Figure 4-19). The ninth orthogneiss sample did not yield a crystallization age. These ages overlap with the documented MHB ages noted above, suggesting a geochronologic link between the blocks. The abundance of Neoproterozoic crystallization ages in the LRM suggests that they share a closer affinity with the MHB than the Wyoming craton, which preserves an extensive Mesoproterozoic igneous history. Mueller et al. (1988; 1993; 2010)

report extensive c. 2.8 Ga magmatism in the Beartooth and Madison ranges. In contrast to the current MHB data, however, the Wyoming Craton also contains abundant Paleoproterozoic ages (Figure 4-19). Mogk et al. (1990) and Mueller et al. (1993) report abundant TTG gneiss units in the Madison Range with c. 3.1 to 3.3 Ga crystallization ages. Data from the Tobacco Root Mountains reveals this older age component as well, Krogh et al. (2011) dating tonalitic gneiss and amphibolite samples at c. 3.33 Ga and c. 3.34 Ga respectively. While age-matching is by no means conclusive, the lack of igneous ages >3.2 Ga in the Little Rocky Mountains (Figure 4-19) suggests a closer tie to the MHB than the Wyoming Craton.

Whole-rock Sm-Nd and zircon Hf isotopic data can also be used in evaluating the crustal affinities of the LRM, relative to the Wyoming Craton in light of the absence of MHB isotopic data. Three of the orthogneiss samples (c. 2.4 Ga and c. 3.2 Ga) and the amphibolite sample (c. 3.0 Ga) do not have a direct age correlation with the northern Wyoming craton (Figure 4-18A). The c. 2.8 Ga orthogneiss samples are of a similar age to the Beartooth Mountains. The Beartooth Mountain $\epsilon\text{Nd}_{(2.8)}$ values range from 0.3 to -6.0, while the LRM orthogneiss samples have much lower $\epsilon\text{Nd}_{(2.8)}$ values, between -6.5 to -10.5. This indicates that formation of the LRM ~2.8 Ga orthogneiss involved a larger percentage of evolved (crustal) material than rocks of the same age from the Beartooth Mountains in the Wyoming craton.

Insights into meta-sediment provenance

Detrital zircons extracted from presumed meta-supracrustal units of the LRM reveal a dominance of Neoproterozoic ages, in line with published Medicine Hat Block magmatic events (Figure 4-17). Zircon $^{207}\text{Pb}/^{206}\text{Pb}$ ages from the schist samples (discordance $\leq 10\%$) reveal a wide range of ~2.57 to ~3.32 Ga. Maximum depositional

ages based on the youngest zircons within each sample are variable, ranging from 2.57 to 2.78 Ga. Two of the 3 samples (MLR-17, MLR-18) show a prominent age peak at ~2.8 Ga, and the final sample (MLR-08) contains a small population of zircons of that age. This age overlaps with the crystallization ages of 6 of the orthogneiss samples from the LRM, as discussed above. The ~2.8 Ga detrital grains from the schist samples (Figure 4-18A) show initial ϵ_{Hf} values ranging from -6.9 to -16.6, indicating derivation from an evolved source region (Table 4-6). These $\epsilon_{\text{Hf}}(c. 2.8 \text{ Ga})$ values overlap with initial ϵ_{Hf} data from the ~2.8 Ga orthogneiss samples previously discussed, which range from -6.6 to -14.5, and suggest that the protolith sediments may be locally derived. However, there is a large amount of ~2.8 Ga in the Beartooth Mountains from the Wyoming craton which could have contributed. The range of $\epsilon_{\text{Nd}}(0)$ for the schist samples is relatively large, from -36.3 to -50.7, and the Nd depleted mantle model ages range from 3.47 Ga to 3.72 Ga (Table 4-7). The model ages for these meta-sediments suggest that they received detritus from older crust, possibly reflecting a contribution from the older material documented in the MHB. The Sm-Nd isotopic data corroborate the zircon Hf data, indicating significant contributions from evolved materials into the protolith sediments.

Paragneiss MLR-13 yielded a similar age-range to the schist samples discussed above, from ~2.64 Ga to ~2.82 Ga with a prominent age peak of ~2.80 Ga (Figure 4-17). The ~2.8 Ga detrital grains from MLR-13 (Figure 4-18A) show initial ϵ_{Hf} values ranging from -7.7 to -12.9 (Table 4-6). The initial ϵ_{Hf} values for the ~2.8 Ga detrital grains overlap with initial ϵ_{Hf} data from the ~2.8 Ga LRM orthogneisses, which range from -6.6 to -14.5. Again, initial ϵ_{Hf} values suggest that an evolved (crust like) source

contributed to the petrogenesis of their source. In contrast to MLR-13, samples MLR-04 and MLR-05 yielded few low discordance zircons and are dominated by younger Neoproterozoic ages (Figure 4-17). MLR-04 only yielded 4 grains with discordance $\leq 10\%$, but they range from 1.78 Ga (one grain) to the other 3 between ~ 2.55 Ga and ~ 2.59 Ga. Given the tectonic and magmatic activity in the GFTZ during the Paleoproterozoic (see Chapters 2 and 3), the single zircon grain from MLR-04, which yielded the 1.78 Ga age, is likely to be metamorphic. MLR-05 yielded only 7 grains with discordance $\leq 10\%$, which range from ~ 2.29 Ga to ~ 2.61 Ga. A single Paleoproterozoic grain yields a $^{207}\text{Pb}/^{206}\text{Pb}$ age of 3.20 Ga. While a single detrital zircon age is of limited significance, this age does correlate with data from Villeneuve et al. (1993) documenting c. 3.2 Ga material in the MHB.

The $\epsilon\text{Nd}_{(0)}$ values for the paragneiss samples are -30.1, -31.2, and -43.6 for MLR-04, MLR-05, and MLR-13, respectively (Table 4-7). The Sm-Nd depleted mantle model ages are 2.99 Ga, 3.04 Ga, and 3.69 Ga respectively (Table 4-7). Both the Hf in zircon and Sm-Nd in whole-rock systematics indicate a mixture of sources in the provenance of these samples. Sm-Nd data from MLR-13 support the Hf in zircon data of a greater evolved crustal contribution, whereas the MLR-04 and MLR-05 seem to have a somewhat greater juvenile component.

Both age-data and Hf isotopic data are consistent with a MHB provenance for the meta-supracrustal samples. Meta-supracrustal units deposited on the northern margin of the Wyoming Craton (representing the Beartooth, Ruby, and Tobacco Root mountains) between 2.7 Ga and 3.2 Ga would likely yield age spectra far richer in 3.2 Ga – 3.4 Ga zircons (Mueller et al., 1998). Source areas for these ages are particularly

well represented in the Madison and Tobacco Root mountains, where extensive TTG magmatism occurred between 3.1 Ga to 3.5 Ga (Mogk et al. 1990; Mueller et al., 1993; Krogh et al., 2011). Although data from unequivocal MHB is limited, the oldest age occurs at c. 3.27 Ga, and is documented from a single drill core sample (Ross et al., 1991). Taken in conjunction with the younger igneous age ranges observed from the LRM samples, the detrital zircon data favor a MHB affinity over a Wyoming Craton provenance for the meta-supracrustal rocks.

Other regional considerations

The Little Rocky Mountains and the Little Belt Mountains to the southwest represent the most extensive basement exposures in the GFTZ; however, they differ greatly in character. The Little Belt Mountains (LBM) are composed of predominantly dioritic to granitic gneisses and migmatites (Pirsson, 1900; Weed, 1900; Schafer, 1935; Vogl et al., 2003). Zircons analyzed from three of the dioritic rocks, as well as trace elements and Nd isotopes led Mueller et al. (2002) to the conclusion that the rocks exposed in the LBM developed at ~1.86 Ga in response to subduction between the MHB and the Wyoming craton. Similar to the LBM, trace elements from the Little Rocky Mountains also are similar to those of modern convergent margins with classic depletions in high field strength elements (HFSE) relative to the large ion lithophile elements (LIL) (e.g., Thompson et al., 1984). However, unlike the Paleoproterozoic Little Belt Mountains, the Little Rocky Mountains appear to be primarily Archean in age, with geochronologic results that are quite varied. Orthogneiss and amphibolite samples range from ~2.4 Ga up to ~3.2 Ga, and detrital grains from the meta-supracrustal schists and paragneisses ranging from ~1.8 Ga up to ~3.3 Ga. The whole-rock Nd (Mueller et al., 2002) and zircon Hf (Weiss et al., 2006) isotopic data from the LBM both

suggest extensive involvement of the depleted mantle in the petrogenesis of the samples (Mueller et al., 2002; Chapter 2 and 3). The ~3.2 Ga orthogneiss and ~3.0 Ga amphibolite from the LRM show similar patterns, but the ~2.8 Ga orthogneisses from the LRM have Hf and Nd data that lie below CHUR/BSE and within or just above zones with slopes indicative of lower crustal values (Figure 4-18). The Little Belt Mountains appear to have formed as part of the GFTZ in an ocean-subduction convergent-margin environment, and the Little Rocky Mountains represent older earliest Paleoproterozoic to Archean continental crust.

Doughty et al. (1998) was the first to date the Archean basement of the Priest River complex (Figure 4-1), and documented an age of 2.65 Ga from U-Pb analyses of zircon. This was suggested to indicate that the Priest River Complex is either a western extension of the Rae-Hearne craton, or that it is a unique block separated from North American Archean crust by a domain of Early Proterozoic crust. Similarly, the Clearwater metamorphic core complex, located south of the Priest River complex and west of the MHB, also yields an Archean basement age (~2.67 Ga) from gneiss (Brewer et al., 2008; Jansen et al., 2011). Guevera et al. (2012) and Jansen et al. (2011) also report 1.87 Ga ages from orthogneiss samples within the Clearwater complex. These ages are similar to those found in orthogneiss samples from the LBM along the southern margin of the Archean MHB. Foster et al. (2006) suggested that, based on the Archean ages (Doughty et al., 1998) and inferred by isotopic tracer data and xenocrystic zircons from Eocene plutons (Whitehouse et al., 1992), the Archean basement in the Priest River and Clearwater complexes are instead an extension of the Medicine Hat block.

Crystallization ages from the Rae-Hearne craton range from ~2.54 to ~2.73 Ga, with major plutonic events occurring between 2.58 and 2.57 Ga (Ray and Wanless, 1980; Bickford et al., 1987; Annesley et al., 1992; Bickford et al., 2001). The oldest known components of the Peter Lake domain, which represents the southeastern component of the Hearne craton, are tonalitic to granodioritic gneisses >2.58 Ga (Rayner et al., 2005). Within the age span of ~2.54 to ~2.73, Hearne ages correlate well with MHB and LRM ages. However, Hearne is lacking in ages approximating the ~2.8 Ga ages that are seen in the MHB and LRM.

Conclusions

Igneous crystallization and detrital zircon age correlation are consistent with the Little Rocky Mountains sharing a strong tie to the Medicine Hat Block, rather than with the generally older Wyoming province. As such, the Archean basement of the Little Rocky Mountains likely represents the only surface exposure of Medicine Hat block crust. U-Pb data for meta-plutonic samples taken from the LRM range from 2.42 to 3.19 Ga, documenting numerous crustal-building episodes in the LRM. Detrital zircon ages range from 1.78 to 3.32 Ga and are particularly abundant at c. 2.8 Ga, recording what is likely the period of most active crustal growth in the LRM. Geochemical data from the Little Rocky Mountains show HFSE depletions and LIL enrichments characteristic of subduction zone magmatism. The limited enrichment of HREE relative to primitive mantle values reflects the source mineralogy, likely lower crustal materials where garnet is residual after melt extraction. This pattern suggests partial melting deep enough for garnet to remain stable, again supporting a subduction zone origin for the LRM meta-igneous samples.

Regional correlations between Archean tectonic elements are possible, using the LRM data set to expand on previous geochronology and geochemistry extant for the MHB. Both the Little Belt Mountains and Little Rocky Mountains are surface exposures of basement rock within the GFTZ; however, they are geologically very different. The Little Belt Mountains appear to have developed in response to subduction between the MHB and the Wyoming craton at ~1.86 Ga, the Little Rocky Mountains appear to represent earliest Paleoproterozoic to Archean continental crust. The combined LRM-MHB dataset also yields more c. 2.4 and 2.8 Ga igneous activity in the MHB, strengthening interpretations of the MHB as an independent entity relative to both the northerly Hearne craton, and the Wyoming craton to the south. These published data, in addition to the LRM dataset generated by this study, allows a greater understanding and definition of the MHB.

Table 4-1. Major, trace and rare earth element data of orthogneiss samples from the Little Rocky Mountains. Major elements in wt. %, trace and rare earth elements in ppm.

Sample wt.%	MLR-01* Orthogneisses	MLR-06*	MLR-09*	MLR-12	MLR-15*	MLR-19*	LRM-1	LRM-3	LRM-5	LRM-6	LRM-7	LRMGM-08*
SiO ₂	73	74	61	68	61	56	74	63	74	69	72	55
TiO ₂	0.04	0.08	0.59	0.59	1.1	1.3	0.21	0.9	0.24	0.47	0.36	1.1
Al ₂ O ₃	13	14	15	14	14	14	13	15	13	14	13	18
Fe ₂ O ₃	0.82	0.17	5.2	4.1	6.7	9.0	1.9	6.5	2.1	3.9	3.2	7.4
MnO	0.03	0.01	0.09	0.05	0.09	0.20	0.03	0.09	0.04	0.06	0.04	0.09
MgO	0.23	0.49	3.6	1.3	3.4	4.6	0.38	2.2	0.63	1.3	0.93	4.6
CaO	0.92	1.4	6.1	3.1	4.9	6.4	1.6	4.2	1.6	2.8	1.9	2.5
Na ₂ O	3.5	5.1	6.9	3.0	4.0	4.1	3.1	3.5	3.0	3.5	2.9	4.4
K ₂ O	7.6	4.9	1.2	4.4	4.6	4.0	4.8	3.5	4.9	3.7	4.9	5.9
P ₂ O ₅	0.10	0.07	0.21	0.18	0.42	0.53	0.05	0.33	0.05	0.14	0.11	0.33
LOI	0.46	0.47	0.56	1.1	1.7	1.7	0.52	0.89	0.56	0.71	0.09	0.92
Total	100.46	100.47	100.56	100.13	101.68	101.67	99.11	99.94	100.21	99.64	99.77	100.92
ppm												
Li	N/A	N/A	N/A	11	6.6	14	4.7	18	6.3	8.1	9.1	11
Sc	N/A	N/A	N/A	7.4	8.7	13	0.03	11	0.12	4.0	4.3	11
Ti	N/A	N/A	N/A	4900	4112	5302	1739	8232	1973	3886	3002	3048
V	N/A	N/A	N/A	54	68	81	20	87	22	50	35	54
Cr	N/A	N/A	N/A	37	49	50	23	60	24	34	37	36
Co	N/A	N/A	N/A	16	11	13	3.2	15	3.5	7.8	6.0	9.3
Ni	N/A	N/A	N/A	19	25	28	8.4	30	8.8	14	15	20
Cu	N/A	N/A	N/A	11	26	29	8.5	32	8.6	9.9	16	13
Zn	N/A	N/A	N/A	49	53	77	30	73	32	48	35	50
Ga	N/A	N/A	N/A	17	16	19	14	20	14	17	17	16
Rb	N/A	N/A	N/A	129	107	112	125	116	128	108	107	98
Sr	N/A	N/A	N/A	212	281	252	218	278	233	243	181	179
Y	N/A	N/A	N/A	28	31	50	4.3	39	4.7	13	8.3	24
Zr	N/A	N/A	N/A	24	111	126	41	55	32	65	33	154
Nb	N/A	N/A	N/A	14	16	32	7.0	22	7.8	11	8.3	11
Cs	N/A	N/A	N/A	2.4	2.9	2.7	1.4	1.7	1.1	2.6	2.1	0.80
Ba	N/A	N/A	N/A	1194	1608	868	1735	1449	1901	1369	692	869

Table 4-1. Continued.

Sample ppm	MLR-01 Orthogneisses	MLR-06	MLR-09	MLR-12	MLR-15	MLR-19	LRM-1	LRM-3	LRM-5	LRM-6	LRM-7	LRMGM-08
La	N/A	N/A	N/A	173	109	99	44	114	61	50	59	44
Ce	N/A	N/A	N/A	286	183	202	60	210	86	82	94	86
Pr	N/A	N/A	N/A	26	18	22	4.8	22	6.7	7.8	8.2	9.7
Nd	N/A	N/A	N/A	73	57	74	13	74	18	26	25	36
Sm	N/A	N/A	N/A	9.8	9.5	13	1.4	11	1.9	3.9	3.0	7.0
Eu	N/A	N/A	N/A	1.2	1.5	1.7	1.2	1.8	1.5	1.3	0.83	0.98
Gd	N/A	N/A	N/A	7.6	8.0	11	1.3	9.5	1.7	3.3	2.7	6.1
Tb	N/A	N/A	N/A	0.98	1.0	1.5	0.15	1.3	0.19	0.44	0.32	0.85
Dy	N/A	N/A	N/A	5.0	5.6	8.3	0.66	6.9	0.83	2.3	1.5	4.5
Ho	N/A	N/A	N/A	0.95	1.0	1.6	0.14	1.3	0.17	0.44	0.29	0.82
Er	N/A	N/A	N/A	2.7	2.8	4.5	0.51	3.9	0.59	1.3	0.89	2.2
Tm	N/A	N/A	N/A	0.36	0.40	0.65	0.06	0.55	0.06	0.18	0.11	0.30
Yb	N/A	N/A	N/A	2.1	2.3	4.0	0.42	3.4	0.47	1.1	0.73	1.6
Lu	N/A	N/A	N/A	0.31	0.32	0.56	0.06	0.48	0.07	0.17	0.11	0.23
Hf	N/A	N/A	N/A	0.75	2.8	3.3	1.3	1.6	1.1	1.9	1.0	3.9
Ta	N/A	N/A	N/A	0.85	0.60	1.3	0.31	0.93	0.34	0.43	0.38	0.44
Pb	N/A	N/A	N/A	23	18	19	34	18	37	16	16	15
Th	N/A	N/A	N/A	72	12	15	88	34	127	21	11	4.39
U	N/A	N/A	N/A	0.99	0.73	0.99	0.82	0.85	0.99	0.57	0.55	0.65

*Major elements were analyzed with an incorrect calibration, thus values may be off by 10%.

Table 4-2. Major, trace and rare earth element data of amphibolite samples from the Little Rocky Mountains. Major elements in wt. %, trace and rare earth elements in ppm.

Sample wt. %	MLR-03* Amphibolites	MLR-07*	MLR-10	MLR-11*	MLR-14*	LRMPG-01*	LRMGM-01*	LRMGM-02*	LRMGM-06*
SiO ₂	49	51	53	49	47	50	47	48	50
TiO ₂	8.6	8.2	0.90	9.4	7.7	0.97	1.8	1.7	1.2
Al ₂ O ₃	17	13	12	13	22	11	9.2	8.9	11
Fe ₂ O ₃	7.2	6.9	12	7.9	7.7	14	17	16	14
MnO	8.5	9.3	0.24	8.4	5.8	0.20	0.24	0.23	0.20
MgO	6.9	6.1	6.8	7.2	6.2	8.1	6.0	6.4	7.9
CaO	1.2	2.0	9.9	1.7	1.2	12	9.0	9.6	11
Na ₂ O	0.27	0.42	2.6	0.69	0.63	1.7	1.2	1.6	1.6
K ₂ O	0.81	1.0	0.72	0.72	1.7	0.24	0.98	0.32	0.62
P ₂ O ₅	0.05	0.07	0.08	0.05	0.12	0.10	0.22	0.21	0.16
LOI	0.72	1.4	1.6	2.3	0.87	1.1	0.99	0.69	1.0
Total	99.96	99.86	100.15	100.11	100.03	98.97	93.92	93.83	97.98
ppm									
Li	2.9	5.4	3.4	5.7	13.6	N/A	7.6	4.3	4.8
Sc	43	30	30	34	43	N/A	42	40	40
Ti	4934	5323	7564	3956	10089	N/A	10715	9523	7017
V	279	222	215	228	421	N/A	422	372	276
Cr	169	172	158	69	69	N/A	62	65	66
Co	49	38	50	39	50	N/A	50	46	47
Ni	70	91	103	70	53	N/A	46	51	45
Cu	125	9	12	50	104	N/A	98	117	65
Zn	99	68	93	98	114	N/A	125	117	96
Ga	15	14	16	14	18	N/A	19	15	17
Rb	15	16	18	29	21	N/A	22	13	18
Sr	96	279	203	177	110	N/A	90	98	164
Y	23	16	18	21	43	N/A	44	39	27
Zr	13	18	9.7	12	26	N/A	22	23	40
Nb	2.5	4.8	4.1	3.5	3.9	N/A	4.2	3.5	6.9
Cs	1.2	2.1	1.5	2.9	1.4	N/A	3.3	1.4	0.92
Ba	95	51	100	103	158	N/A	110	69	178

Table 4-2. Continued.

Sample ppm	MLR-03 Amphibolites	MLR-07	MLR-10	MLR-11	MLR-14	LRMPG-01	LRMGM-01	LRMGM-02	LRMGM-06
La	4.8	11	9.2	6.3	7.1	N/A	8.3	5.8	12
Ce	10	21	18	14	17	N/A	20	14	26
Pr	1.4	2.4	2.3	1.9	2.5	N/A	2.9	2.1	3.3
Nd	6.9	9.8	9.5	8.2	12	N/A	14	11	14
Sm	2.2	2.5	2.5	2.5	4.4	N/A	4.4	3.7	3.7
Eu	0.70	0.83	0.80	0.68	1.3	N/A	1.3	1.2	1.1
Gd	2.8	2.6	2.9	2.8	5.5	N/A	5.8	5.0	4.1
Tb	0.52	0.44	0.50	0.51	1.0	N/A	1.1	0.94	0.71
Dy	3.6	2.8	3.0	3.5	7.2	N/A	7.1	6.2	4.4
Ho	0.76	0.56	0.61	0.70	1.5	N/A	1.5	1.3	0.88
Er	2.2	1.5	1.7	2.0	4.4	N/A	4.4	3.9	2.5
Tm	0.36	0.24	0.25	0.32	0.68	N/A	0.67	0.60	0.39
Yb	2.3	1.4	1.6	2.0	4.4	N/A	4.4	3.9	2.3
Lu	0.35	0.21	0.24	0.28	0.63	N/A	0.65	0.58	0.34
Hf	0.75	0.89	0.72	0.69	1.3	N/A	1.2	1.2	1.3
Ta	0.17	0.35	0.27	0.27	0.27	N/A	0.30	0.25	0.46
Pb	3.0	4.6	4.0	4.4	6.7	N/A	4.4	2.8	6.1
Th	0.77	3.0	2.6	0.75	1.3	N/A	1.4	1.1	2.6
U	0.15	0.70	0.46	0.75	0.42	N/A	0.46	0.34	0.59

*Major elements were analyzed with an incorrect calibration, thus values may be off by 10%.

Table 4-3. Major, trace and rare earth element data of schist samples from the Little Rocky Mountains. Major elements in wt. %, trace and rare earth elements in ppm.

Sample wt. %	MLR-08* Schists	MLR-16	MLR-17	MLR-18	LRMPG-2*	LRMPG-3*	LRMGM-3*	LRMGM-4*	LRMGM-5*	LRMGM-7*
SiO ₂	69	63	61	68	69	66	52	56	56	54
TiO ₂	0.28	0.94	1.0	0.63	0.39	0.56	1.6	1.8	1.3	1.2
Al ₂ O ₃	14	15	15	14	14	15	14	16	14	19
Fe ₂ O ₃	2.0	6.2	7.3	4.3	1.7	3.3	11	10.0	9.0	7.5
MnO	0.03	0.1	0.1	0.05	0.02	0.05	0.18	0.13	0.12	0.08
MgO	1.2	2.0	2.3	1.4	2.0	2.1	6.3	5.7	5.4	4.1
CaO	3.7	4.0	4.7	2.9	3.8	3.3	7.5	2.3	5.0	4.8
Na ₂ O	8.2	3.5	3.5	3.3	7.2	5.3	2.7	3.0	2.9	4.9
K ₂ O	0.81	3.5	3.0	4.2	1.5	4.3	4.5	5.3	5.8	4.7
P ₂ O ₅	0.06	0.35	0.41	0.21	0.11	0.13	0.55	0.54	0.43	0.31
LOI	0.53	0.67	2.2	0.93	0.23	0.52	3.2	2.4	1.1	1.1
Total	100.52	98.85	100.18	99.99	100.23	100.52	103.18	102.39	101.05	101.15
ppm										
Li	2.4	18	21	14	6.8	N/A	17	16	17	7.5
Sc	2.1	11	14	6.4	2.9	N/A	14	13	11	6.6
Ti	778	8302	9331	4965	1042	N/A	5751	5609	4754	3181
V	19	87	100	57	21	N/A	102	90	79	49
Cr	7.9	47	61	36	8.1	N/A	57	49	50	17
Co	3.3	30	39	11	4.1	N/A	15	15	12	9.9
Ni	5.0	28	33	18	7.0	N/A	32	29	25	15
Cu	5.1	24	46	16	17	N/A	43	28	22	31
Zn	22	77	88	49	18	N/A	86	64	70	45
Ga	17	20	21	18	16	N/A	19	21	19	17
Rb	11	111	116	124	15	N/A	110	112	131	56
Sr	663	270	288	233	501	N/A	302	292	244	295
Y	2.4	44	54	23	5.2	N/A	50	41	41	9.0
Zr	17	48	48	28	57	N/A	60	20	120	75
Nb	1.2	26	25	12	2.2	N/A	24	23	18	6.9
Cs	0.79	1.5	5.2	1.4	0.45	N/A	3.5	3.84	1.91	1.2
Ba	186	1553	1123	1537	263	N/A	1002	1314	1385	848

Table 4-3. Continued.

Sample ppm	MLR-08 Schists	MLR-16	MLR-17	MLR-18	LRMPG-2	LRMPG-3	LRMGM-3	LRMGM-4	LRMGM-5	LRMGM-7
La	7.7	97	344	86	39	N/A	89	137	126	46
Ce	13	202	558	152	62	N/A	181	247	220	76
Pr	1.4	21	50	15	5.8	N/A	20	25	24	7.1
Nd	5.1	70	140	48	18	N/A	72	82	77	23
Sm	0.96	12	19	7.2	2.8	N/A	13	13	12	3.4
Eu	0.55	1.7	2.0	1.4	0.81	N/A	1.6	1.7	1.7	1.0
Gd	0.58	9.6	15	5.8	1.9	N/A	11	11	10	2.9
Tb	0.08	1.4	1.9	0.77	0.20	N/A	1.6	1.4	1.3	0.35
Dy	0.41	7.4	9.5	4.0	0.91	N/A	8.3	7.4	7.0	1.8
Ho	0.07	1.4	1.8	0.77	0.15	N/A	1.6	1.4	1.3	0.33
Er	0.19	4.1	5.0	2.2	0.42	N/A	4.7	4.0	3.7	0.77
Tm	0.02	0.60	0.69	0.30	0.05	N/A	0.65	0.54	0.51	0.13
Yb	0.14	3.7	4.2	1.8	0.28	N/A	3.9	3.3	3.0	0.67
Lu	0.02	0.53	0.59	0.26	0.04	N/A	0.53	0.46	0.42	0.11
Hf	0.54	1.4	1.4	0.78	1.5	N/A	1.7	0.72	3.1	2.0
Ta	0.02	1.6	1.7	0.40	0.08	N/A	0.94	0.86	0.66	0.24
Pb	10	27	36	18	12	N/A	22	18	29	18
Th	1.6	68	125	19	10	N/A	14	53	35	3.8
U	0.11	0.73	0.83	0.46	0.69	N/A	0.64	0.53	0.86	0.26

*Major elements were analyzed with an incorrect calibration, thus values may be off by 10%.

Table 4-4. Major, trace and rare earth element data of paragneiss samples from the Little Rocky Mountains. Major elements in wt. %, trace and rare earth elements in ppm.

Sample wt. %	MLR-04* Paragneisses	MLR-05	MLR-13
SiO ₂	62	68	69
TiO ₂	1.1	0.64	0.58
Al ₂ O ₃	13	14	14
Fe ₂ O ₃	9.1	8.2	4.1
MnO	0.09	0.1	0.05
MgO	7.2	3.0	1.3
CaO	1.8	1.2	2.6
Na ₂ O	1.7	1.5	3.3
K ₂ O	3.7	2.5	4.3
P ₂ O ₅	0.16	0.05	0.19
LOI	1.1	0.63	0.80
Total	101.10	100.33	100.48
ppm			
Li	22	11	10
Sc	14	14	7.1
Ti	3944	3565	4135
V	121	107	61
Cr	134	125	35
Co	20	19	9.8
Ni	61	50	20
Cu	38	40	20
Zn	81	83	51
Ga	17	16	17
Rb	83	82	130
Sr	115	108	220
Y	21	25	34
Zr	94	80	176
Nb	9.8	8.7	17
Cs	5.1	1.3	1.5
Ba	435	639	1274
La	38	60	102
Ce	74	113	186
Pr	7.9	12	19
Nd	28	43	63
Sm	5.2	7.9	11
Eu	1.1	1.5	2.0
Gd	4.3	6.6	8.8
Tb	0.60	0.81	1.2
Dy	3.4	4.4	6.3
Ho	0.66	0.84	1.2
Er	1.9	2.5	3.2
Tm	0.30	0.36	0.44
Yb	1.9	2.4	2.7

Table 4-4. Continued.

Sample ppm	MLR-04* Paragneisses	MLR-05	MLR-13
Lu	0.28	0.35	0.38
Hf	2.7	2.3	4.7
Ta	0.67	0.48	0.62
Pb	15	19	19
Th	13	20	24
U	2.3	2.5	0.96

*Major elements were analyzed with an incorrect calibration, thus values may be off by 10%.

Table 4-5. Orthogneiss and amphibolite samples, Little Rocky Mountains, zircon LA-ICP-MS U-Pb data $^{207}\text{Pb}/^{206}\text{Pb}$ ages and Hf-isotope data reported (Ma).

Sample Number	Number of Grains Discordance $\leq 10\%$	$^{207}\text{Pb}/^{206}\text{Pb}$ Age	Error 2σ	$\epsilon\text{Hf}_{(\text{IA})}$ Highest	$\epsilon\text{Hf}_{(\text{IA})}$ Lowest	$\epsilon\text{Hf}_{(\text{T})}^*$ Highest	$\epsilon\text{Hf}_{(\text{T})}^*$ Lowest	$\epsilon\text{Hf}_{(\text{T})}^*$ Average	Std. Dev.	Hf Model Age (DM) ^a *	Std. Dev.
Orthogneisses											
MLR-01	20	2420	12	-2.7	-16.1	-2.2	-11.6	-7.4	2.5	2973	95
MLR-06	31	2416	9	-5.5	-10.5	-5.9	-10.0	-7.8	1.2	3002	42
MLR-15	43	2776	9	-7.7	-14.6	-7.9	-14.5	-10.5	1.8	3415	64
MLR-19	56	2793	5	-8.7	-14.3	-8.3	-14.4	-10.7	1.9	3439	71
LRM-3	13	2800	91	-12.1	-18.4	-11.4	-14.2	-12.9	0.8	3526	30
LRM-5	8	2827	39	-6.7	-12.5	-6.6	-11.7	-9.4	1.4	3416	57
LRM-6	2	N/A	N/A	-5.8	-9.1	N/A	N/A	N/A	N/A	3313	70
LRM-7	12	2769	37	-9.2	-15.6	-8.4	-14.0	-11.1	1.4	3436	58
MLR-09	24	3199	8	5.2	-11.5	3.7	-2.3	0.0	1.7	3392	65
Amphibolites											
MLR-03	32	3006	7	3.6	-9.8	4.2	-6.3	-1.2	2.35	3279	94
MLR-10	5	N/A	N/A	2.4	-4.4	N/A	N/A	N/A	N/A	3402	82

(IA) Zircons reduced to individual U-Pb age.

*zircons reduced to calculated $^{207}\text{Pb}-^{206}\text{Pb}$ crystallization age.

^aDM model ages were calculated using the model of Mueller et al. (2008).

Table 4-6. Schist and paragneiss samples, Little Rocky Mountains, zircon LA-ICP-MS U-Pb data $^{207}\text{Pb}/^{206}\text{Pb}$ ages and Hf-isotope data reported (Ma).

Sample Number	Number of Grains Discordance $\leq 10\%$	Age Range	Age Population	Age Population	$\epsilon\text{Hf}_{(IA)}$ [*] Highest	$\epsilon\text{Hf}_{(IA)}$ [*] Lowest	Hf $T_{(DM)}$ ^a Highest	Hf $T_{(DM)}$ ^a Lowest
Schists								
MLR-08	18	2614 - 3315	3188	N/A	5.6	-15.7	3441	3274
MLR-17	52	2569 - 2835	2794	2806	-6.9	-18.5	3685	3318
MLR-18	28	2702 - 2799	2776	N/A	-8.5	-16.0	3625	3437
Paragneisses								
MLR-13	23	2644 - 2825	2798	2755	-7.7	-13.3	3531	3315
MLR-04	4	1782 - 2594	N/A	N/A	8.0	-16.0	3005	2565
MLR-05	7	2286 - 3203	2580	3204	-1.1	-7.1	3437	2749

^(IA)Zircons reduced to individual U-Pb age.

^{*}zircons reduced to calculated ^{207}Pb - ^{206}Pb crystallization age.

^aDM model ages were calculated using the model of Mueller et al. (2008).

Table 4-7. Whole rock LA-ICP-MS Nd isotope data reported (Ma), Little Rocky Mountains.

Sample Number	Sm (ppm)	Nd (ppm)	$^{143}\text{Nd}/^{144}\text{Nd}$	$\epsilon\text{Nd}_{(0)}$	$\epsilon\text{Nd}_{(T)}$ *	Nd Model Age (DM) ^a
Orthogneisses						
MLR-01	2.31	9.34	0.511596	-20.2	-5.7	3.551
MLR-06	1.72	10.28	0.510748	-36.7	-7.3	3.151
MLR-09	2.92	15.89	0.510789	-35.9	-0.9	3.418
MLR-12	9.77	73.44	0.510065	-50.2	N/A	3.458
MLR-15	9.52	57.23	0.510372	-44.0	-10.0	3.676
MLR-19	13.33	74.44	0.510478	-42.0	-10.5	3.801
LRM-1	1.36	13.20	0.509820	-54.8	N/A	3.279
LRM-3	11.38	74.01	0.510360	-44.3	-7.2	3.443
LRM-5	1.86	18.39	0.509797	-55.3	-6.5	3.281
LRM-6	3.88	26.24	0.510292	-45.6	N/A	3.430
LRM-7	3.00	24.54	0.510053	-50.3	-6.8	3.300
LRMPG-03	2.01	11.87	0.510440	-42.7	N/A	3.643
LRMGM-05	12.07	77.19	0.510341	-44.7	N/A	3.519
LRMGM-08	7.01	35.89	0.510788	-35.9	N/A	3.690
Amphibolites						
MLR-03	2.18	6.91	0.512424	-4.0	-2.0	N/A
MLR-07	2.50	9.83	0.511552	-21.0	N/A	3.993
MLR-10	2.49	9.48	0.511716	-18.0	N/A	3.861
MLR-11	2.53	8.24	0.512031	-11.7	N/A	N/A
MLR-14	4.36	12.14	0.512783	3.0	N/A	N/A
LRMPG-01	2.47	7.76	0.512448	-3.6	N/A	N/A
LRMGM-01	4.43	13.89	0.512526	-2.0	N/A	N/A
LRMGM-02	3.74	10.72	0.512825	3.8	N/A	N/A
LRMGM-06	3.66	13.78	0.512002	-12.3	N/A	3.061
Schist						
MLR-08	0.96	5.06	0.510768	-36.3	N/A	3.604
MLR-16	11.83	69.55	0.510424	-43.2	N/A	3.679
MLR-17	18.52	140.44	0.510041	-50.7	N/A	3.467
MLR-18	7.25	48.21	0.510266	-46.3	N/A	3.507
LRMPG-02	2.79	18.49	0.510235	-46.7	N/A	3.557
LRMGM-03	12.91	71.80	0.510540	-40.8	N/A	3.720
LRMGM-04	12.96	81.83	0.510341	-44.7	N/A	3.558
LRMGM-07	3.38	22.81	0.510262	-46.2	N/A	3.475
Paragneiss						
MLR-04	5.22	28.02	0.511089	-30.1	N/A	2.985
MLR-05	7.95	43.07	0.511030	-31.2	N/A	3.040
MLR-13	10.68	63.47	0.510393	-43.6	N/A	3.690

*Orthogneiss and amphibolite samples reduced to ^{207}Pb - ^{206}Pb age (Table 4-5).

^aDM model ages were calculated using the model of DePaolo (1981).

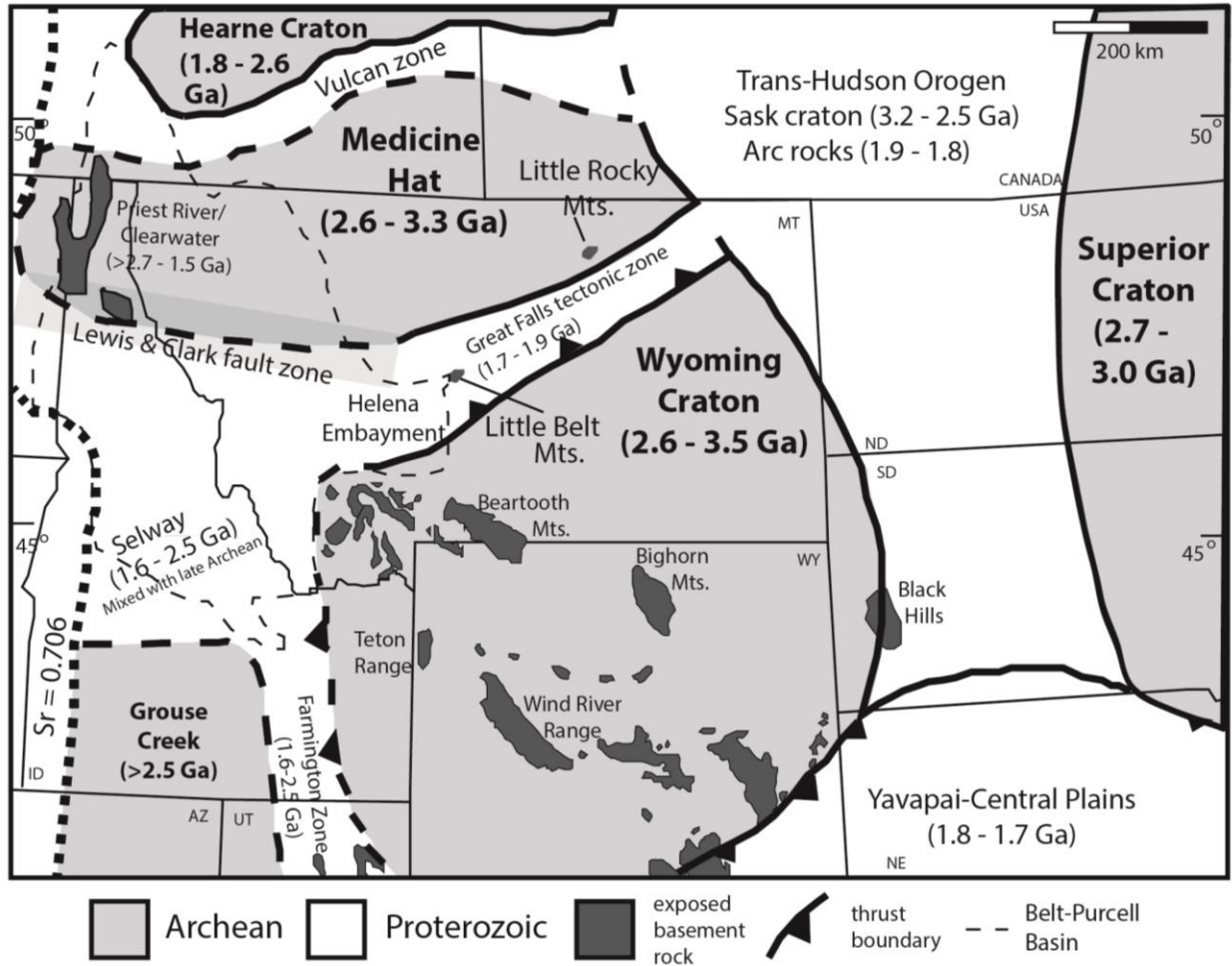


Figure 4-1. Generalized map of Precambrian basement provinces of southwestern Laurentia (after Ross et al., 1991; Condie, 1992; Doughty et al., 1998; Vogl et al., 2004; Foster et al., 2006, 2012). Exposures of basement in Laramide-style uplifts are shown in the dark grey shaded areas.

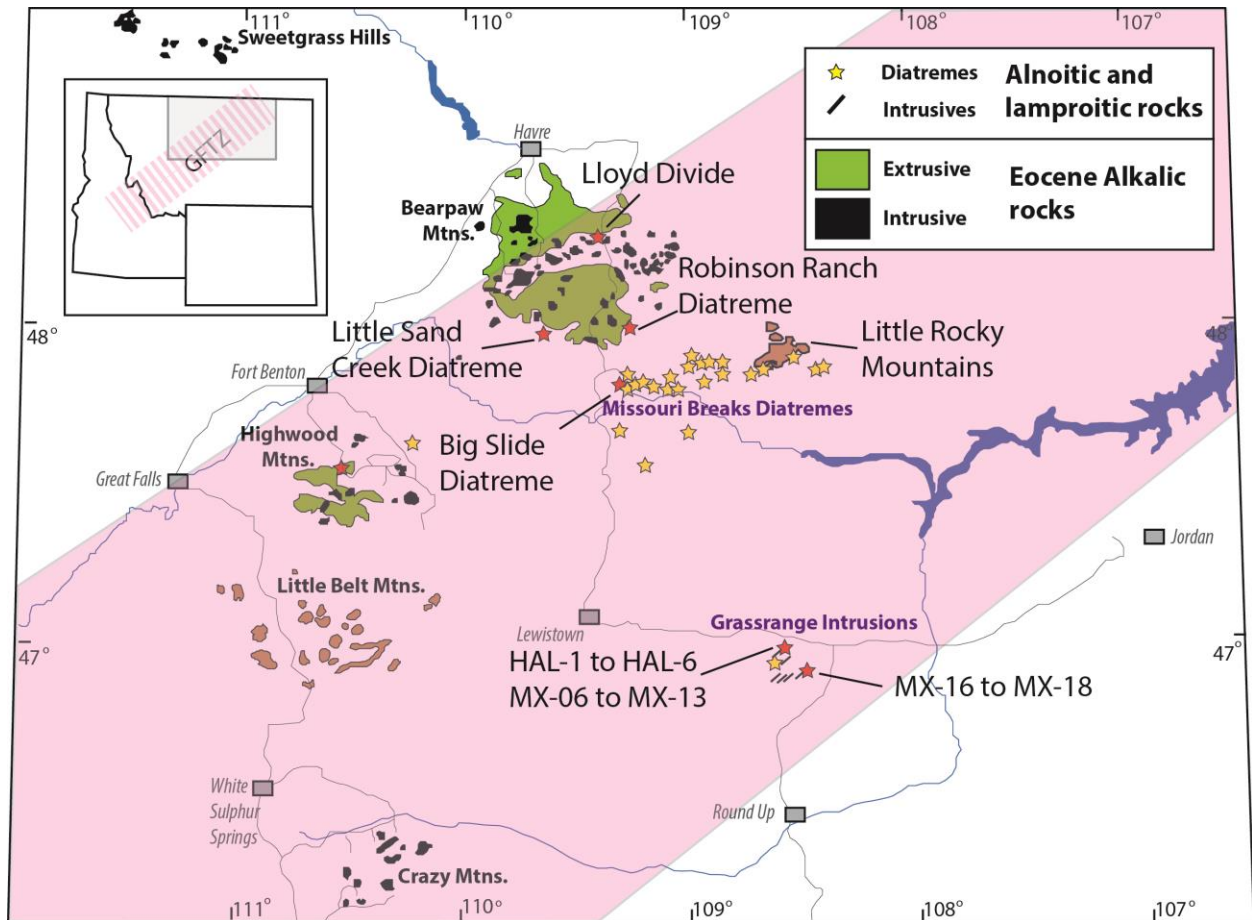


Figure 4-2. Location of the Little Rocky Mountains relative to a generalized depiction of Cenozoic alkaline rock occurrences in the Montana alkali province (after Hearn et al., 1989). The limits of the Great Falls tectonic zone (shown in pink) are not well defined and are based on aeromagnetic data from Sims et al. (2004).

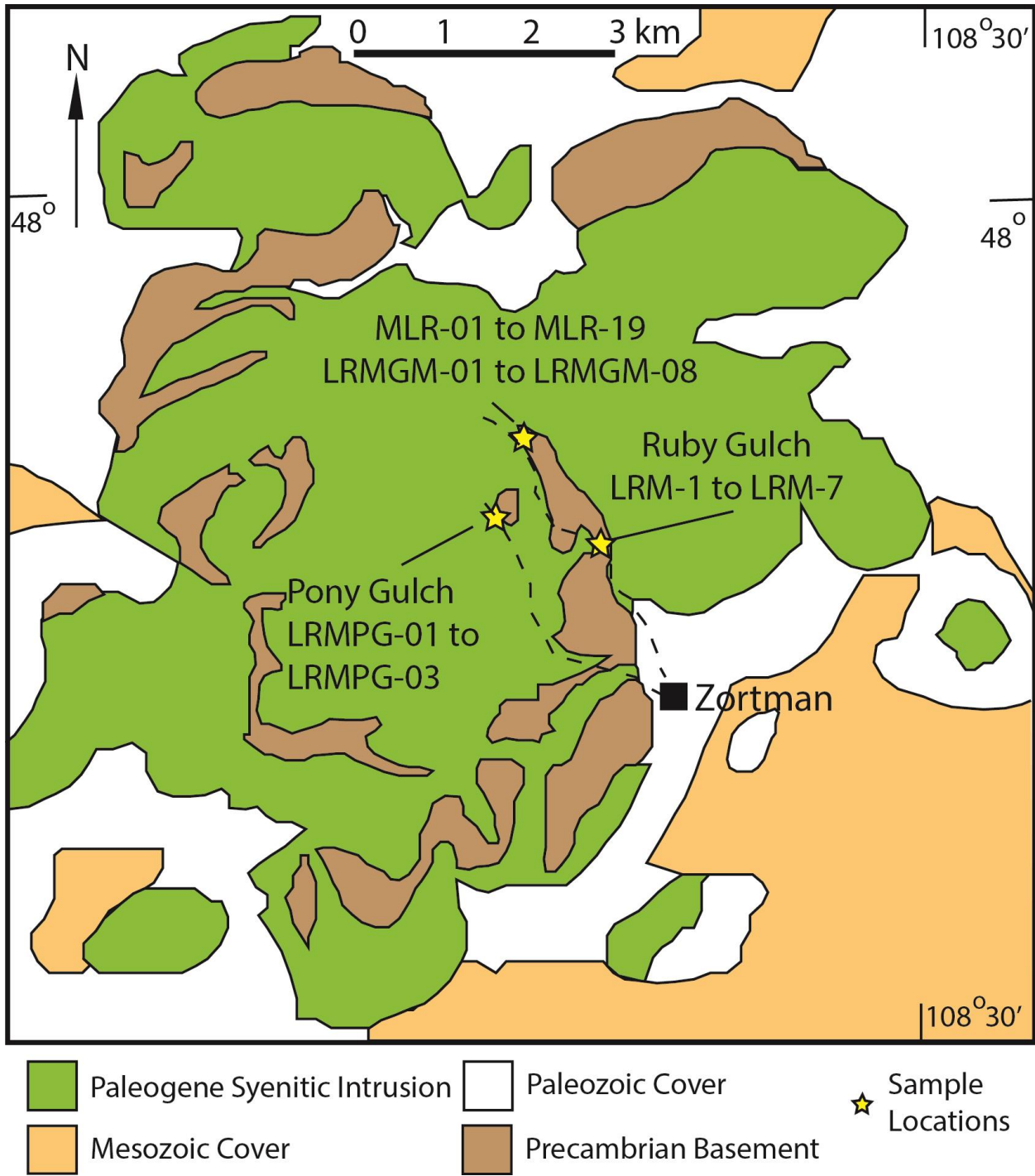


Figure 4-3. Map of the Little Rocky Mountains (after Hearn et al., 1989). Sample locations are shown as yellow stars.

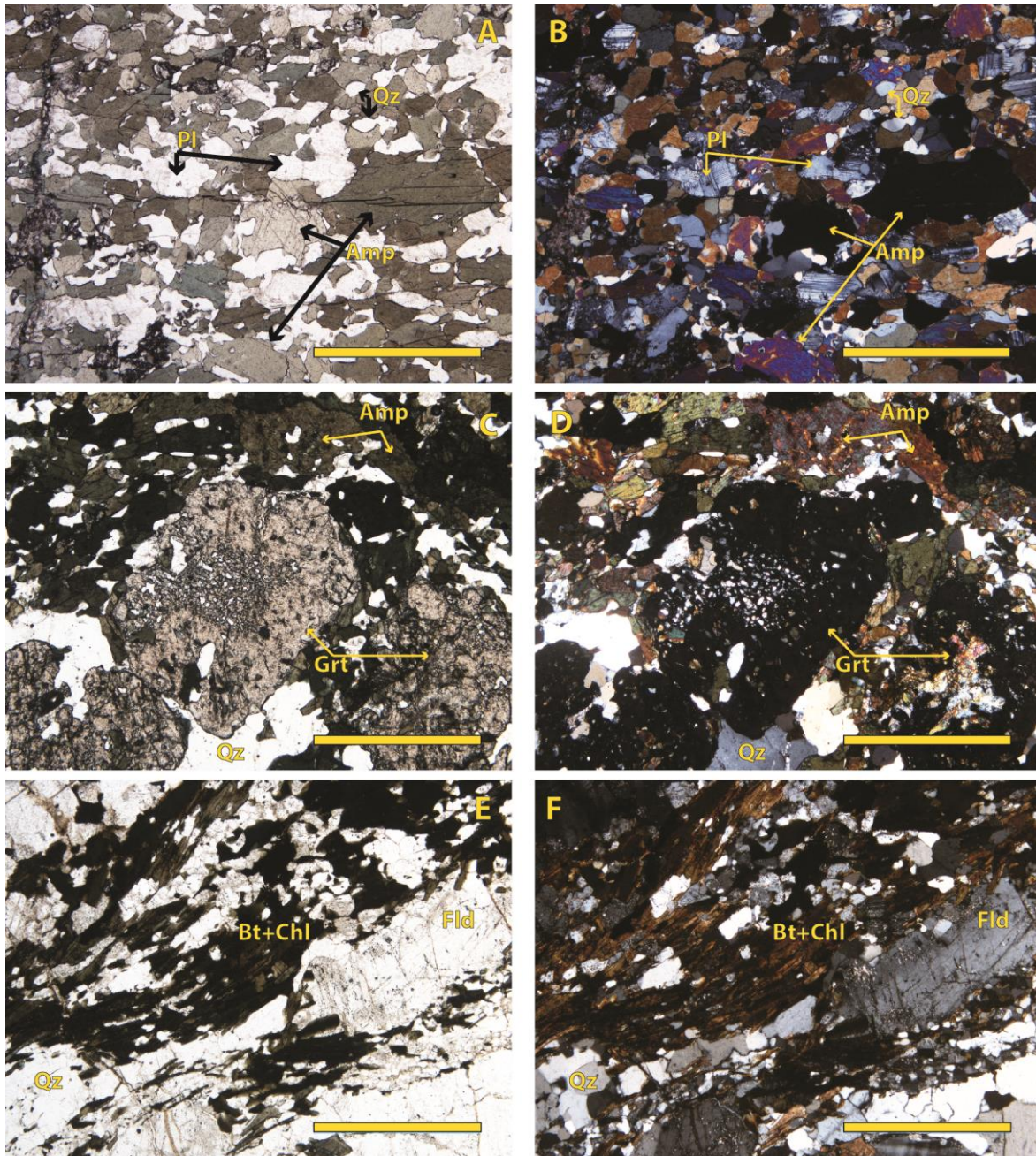


Figure 4-4. Photomicrographs of selected meta-plutonic samples from the Little Rocky Mountains. Mineral abbreviations are after Whitney and Evans (2010). Plane light (PPL) micrographs are on the left, and Cross-Polarized light (XPL) micrographs are on the right. Sample MLR-03 (A & B) is an amphibolite, and contains abundant subhedral amphibole grains, anhedral plagioclase, and anhedral, lobate quartz. Sample LRMGM-02 (C & D) is similar, but with abundant ≥ 1 mm euhedral garnet grains. Garnet is rich in quartz and feldspar inclusions. Sample LRMGM-08 (E & F) is a biotite granitic orthogneiss, showing biotite with some chlorite alteration, recrystallized quartz, and somewhat altered feldspar. Scale bars represent 1 mm.

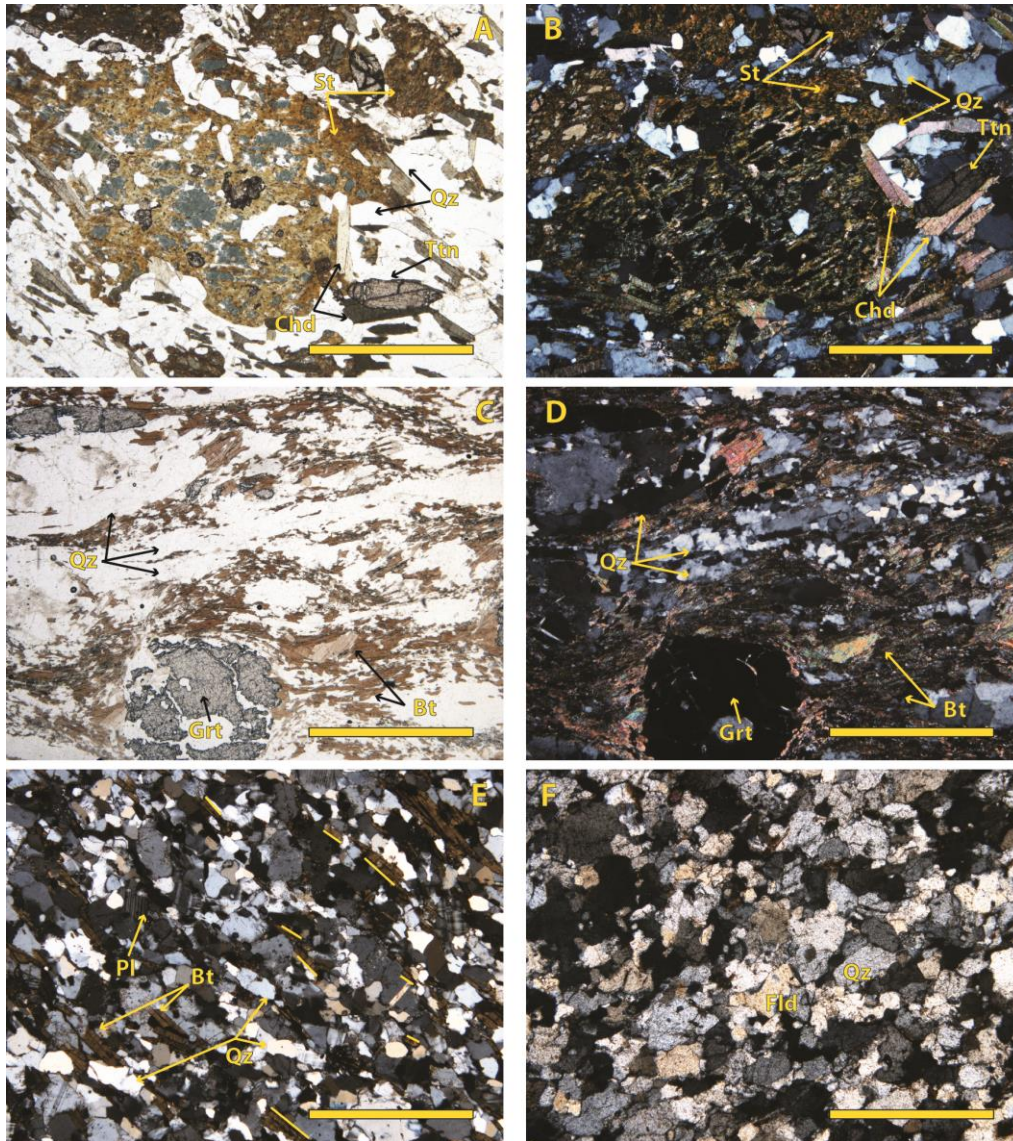


Figure 4-5. Photomicrographs of selected meta-supracrustal samples from the Little Rocky Mountains. Mineral abbreviations are after Whitney and Evans (2010). PPL micrographs are on the left, and XPL micrographs are on the right for the first two samples. Sample MLR-13 (A & B) is a staurolite chloritoid quartzofeldspathic paragneiss. Staurolite is poikiloblastic, containing numerous inclusions of amphibole, feldspar, and quartz. Chloritoid defines a foliation in the sample, as well as compositional banding between chloritoid rich and poor layers. Titanite occurs as an accessory phase, commonly near staurolite. Sample MLR-04 (C & D) is a garnet biotite quartzofeldspathic augen gneiss. Biotite defines as strong foliation, supported by ribbons of recrystallized quartz. Garnet occurs as subhedral grains up to 1mm in diameter, with numerous quartz inclusions. Sample LRMGM-07 (E; XPL) and sample LRMPG-02 (F; XPL) are fine grained biotite quartzofeldspathic schist. Biotite and a weak compositional variation define banding. The yellow lines in (E) show the biotite defined foliation. Scale bars represent 1 mm.

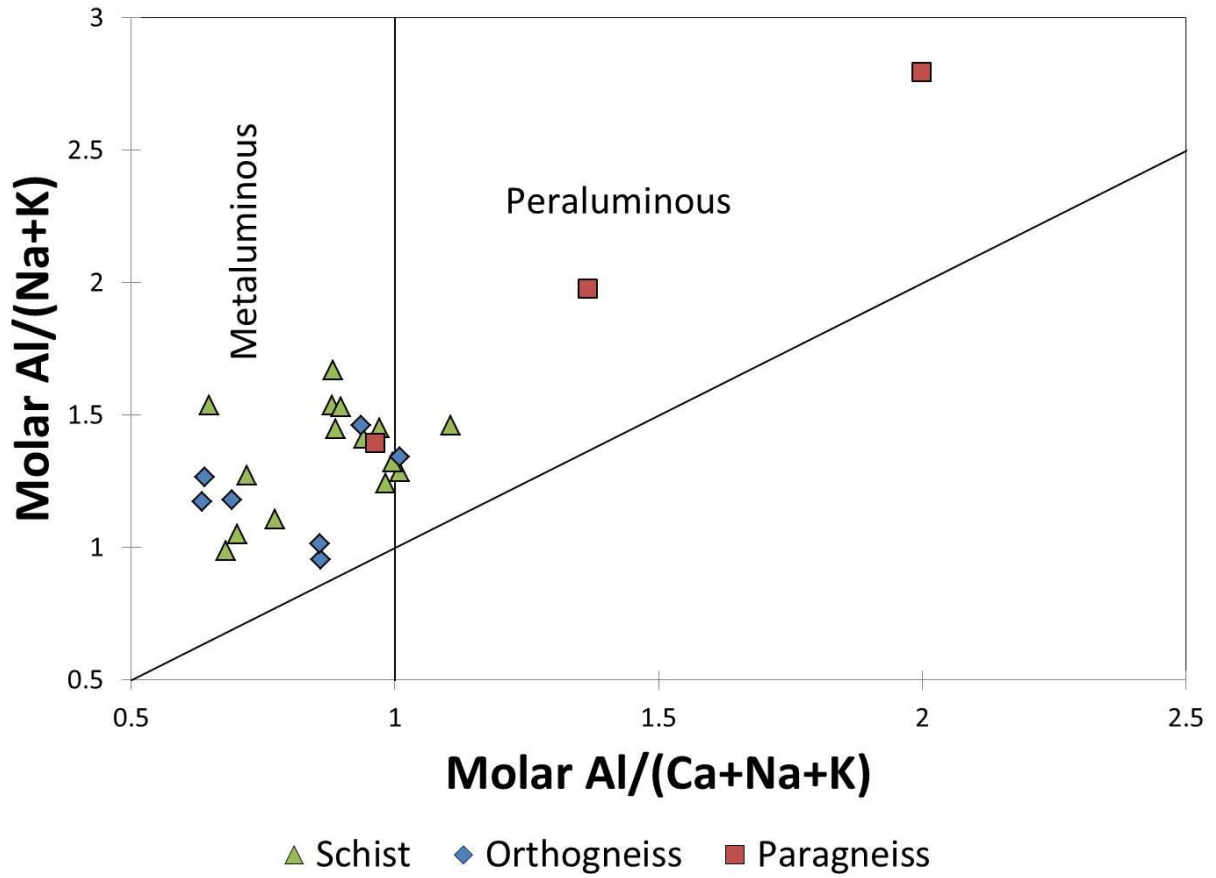


Figure 4-6. Schist, orthogneiss and paragneiss samples plotted on an alumina saturation index (Shand, 1943; modified by Frost et al., 2001). Schists (green triangles), orthogneisses (blue diamonds), and paragneisses (red squares).

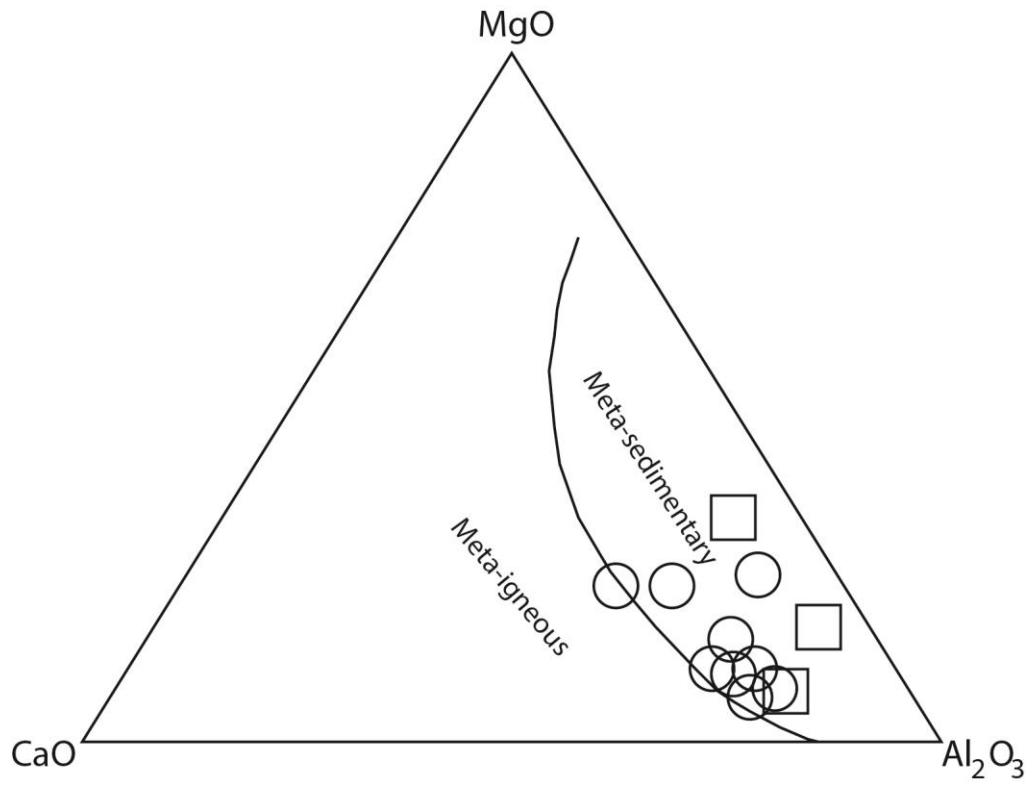


Figure 4-7. Ternary CaO-MgO-Al₂O₃ variation diagram showing the expected fields of meta-igneous and meta-sedimentary rocks for all schists (circles) and paragneisses (squares) (after Leyreloup et al., 1977).

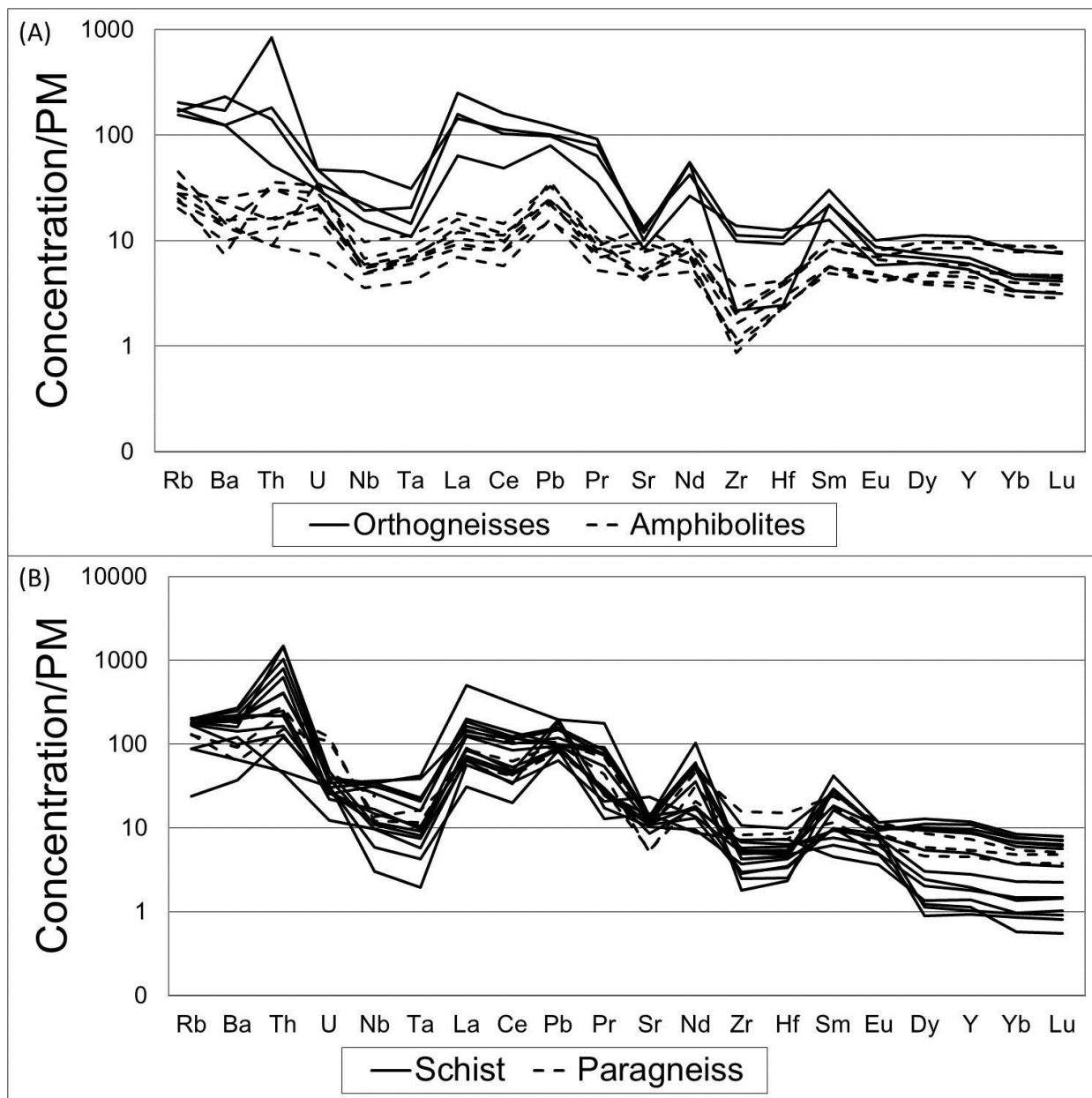


Figure 4-8. Primitive-mantle normalized “spider” diagrams (McDonough and Sun, 1995) for (A) orthogneiss and amphibolite samples and (B) detrital schistose and paragneiss samples. Relative enrichment of large ion lithophile elements (LILE) to high field strength elements (HFSE) suggests formation in an arc environment.

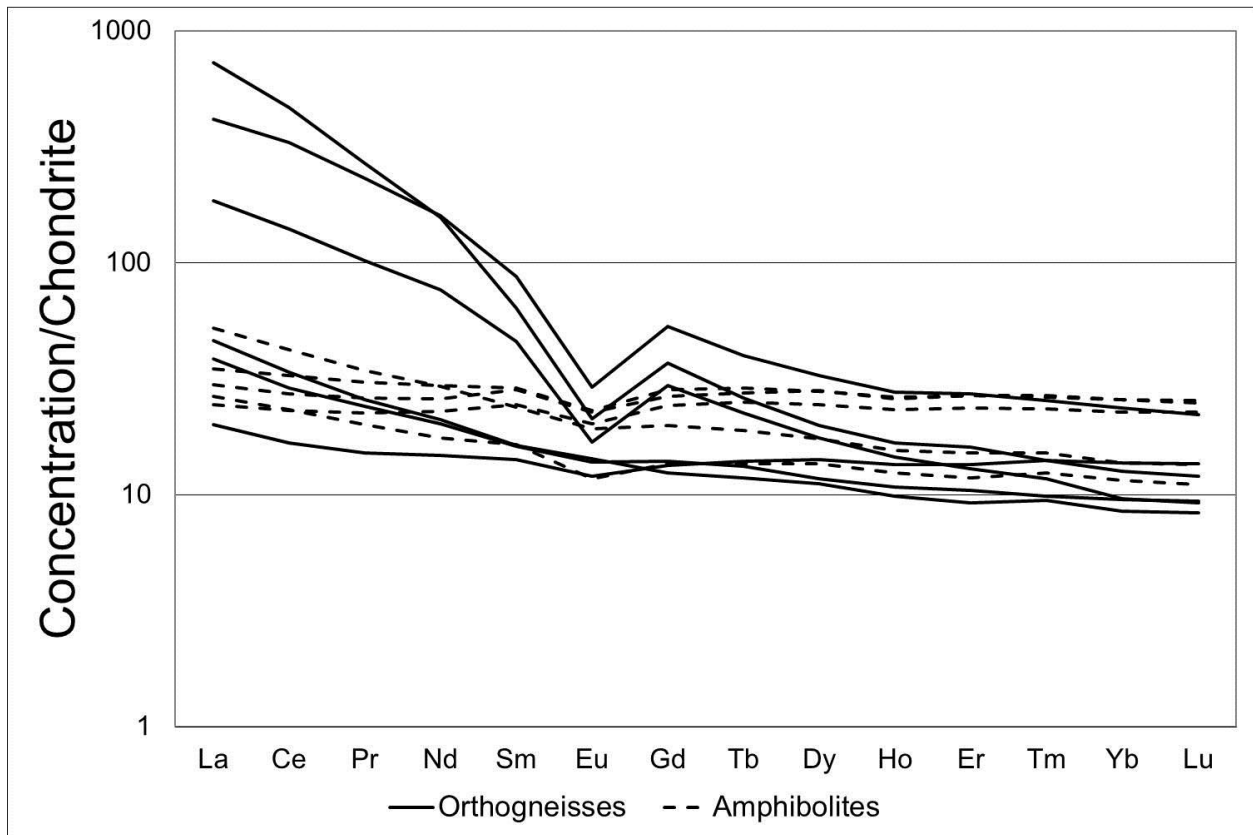


Figure 4-9. Chondrite normalized diagram (McDonough and Sun, 1995) for orthogneiss and amphibolite samples using data from Tables 4-1 and 4-2. Orthogneiss samples show elevated concentrations of light versus heavy rare earth elements.

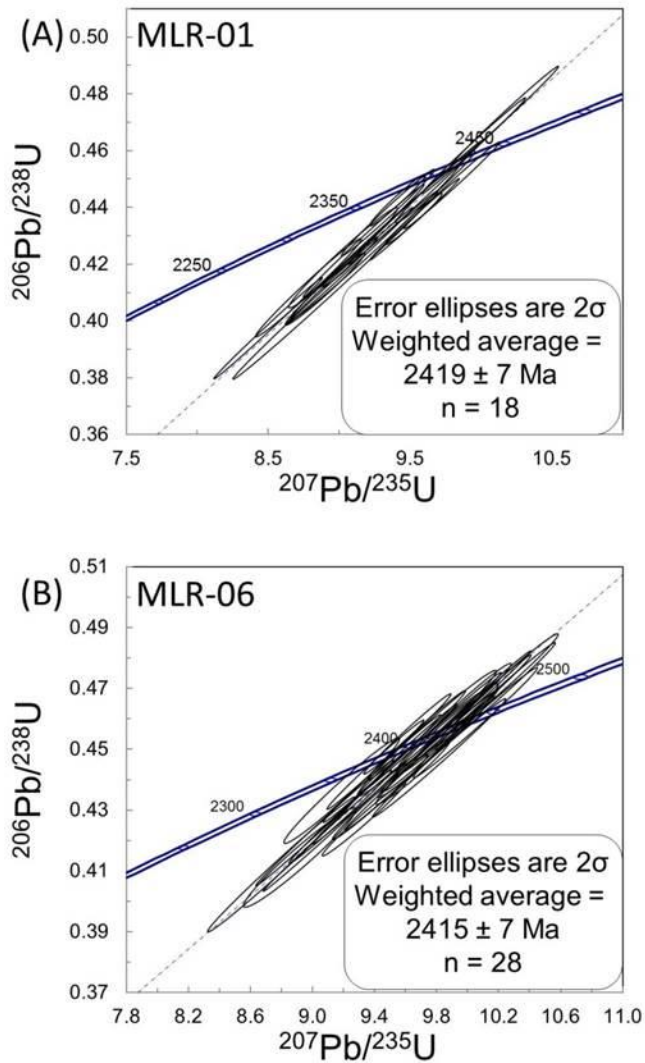


Figure 4-10. Concordia diagrams showing U-Pb data showing spread of zircons and weighted mean age for orthogneiss samples MLR-01 (A) and MLR-06 (B). Each ellipse represents a single spot analysis and its 2σ error.

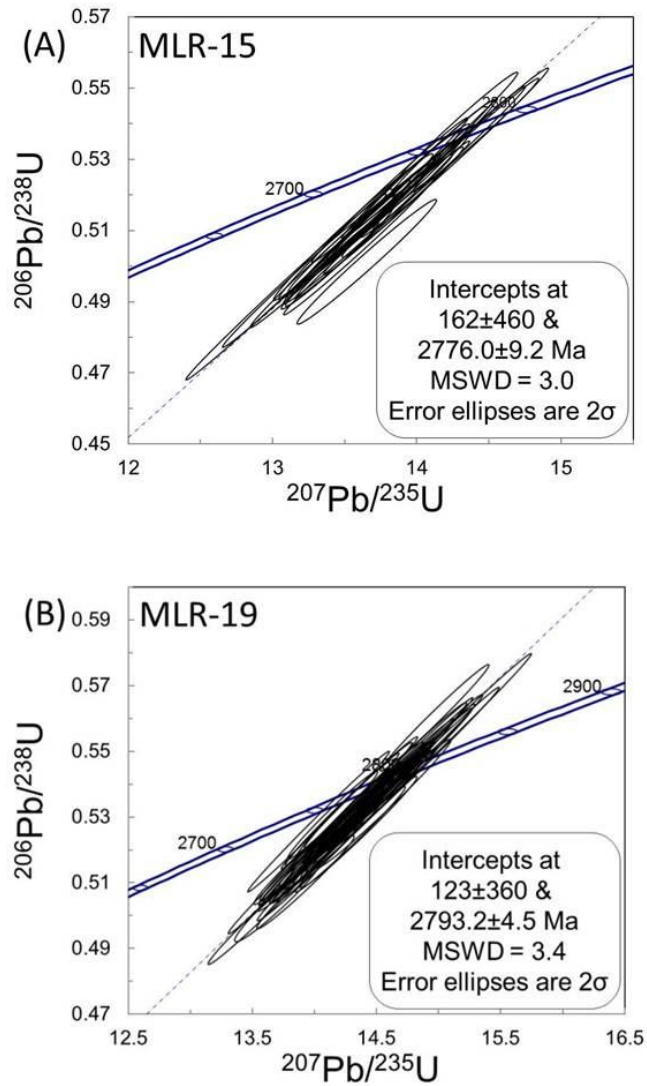


Figure 4-11. Concordia diagrams showing U-Pb data for orthogneiss samples MLR-15 (A) and MLR-19 (B). Each ellipse represents a single spot analysis and its 2σ error.

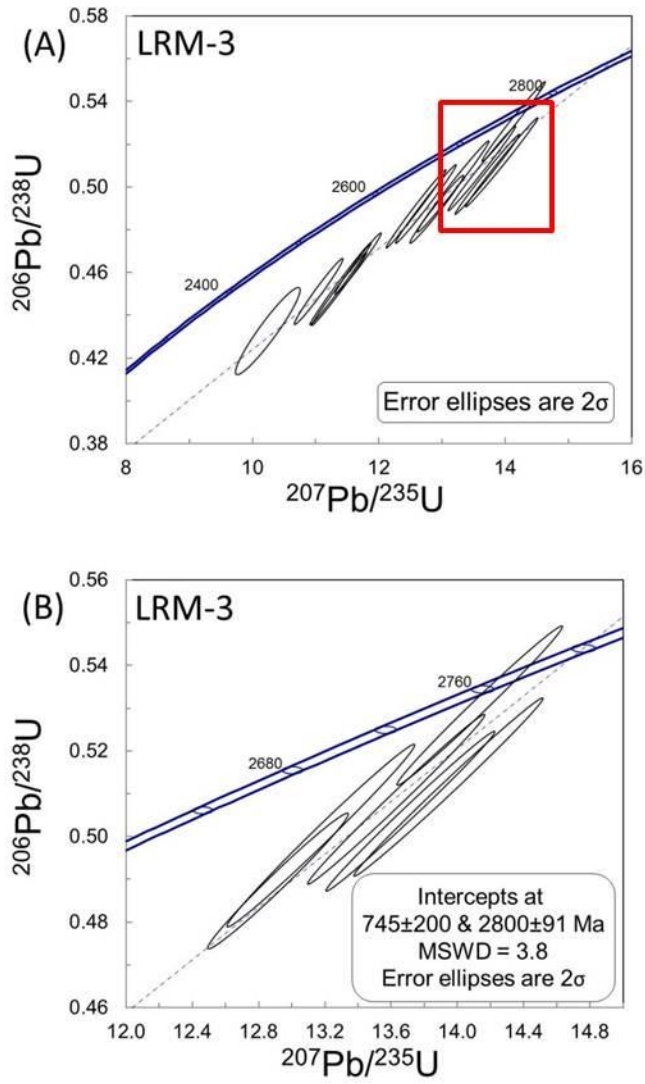


Figure 4-12. (A) Concordia diagrams plotting composite U-Pb data for orthogneiss sample LRM-3. Each ellipse represents a single spot analysis and its 2σ error. (B) Expanded view of upper end of concordia showing the oldest, most concordant zircons selected for regression.

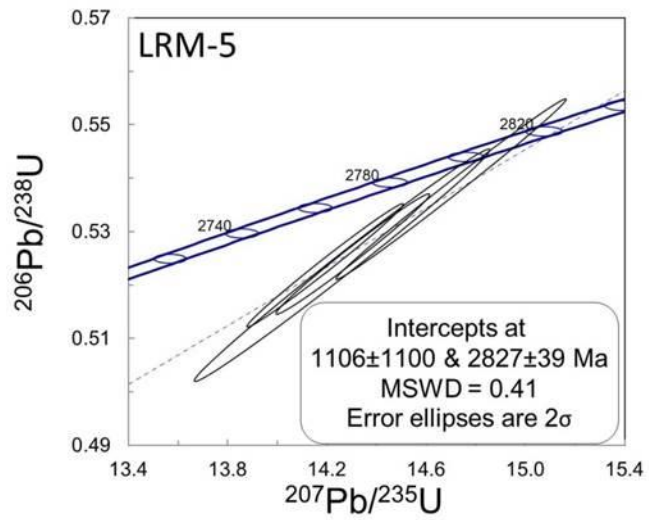


Figure 4-13. Concordia diagram showing U-Pb data for orthogneiss sample LRM-5. Each ellipse represents a single spot analysis and its 2σ error.

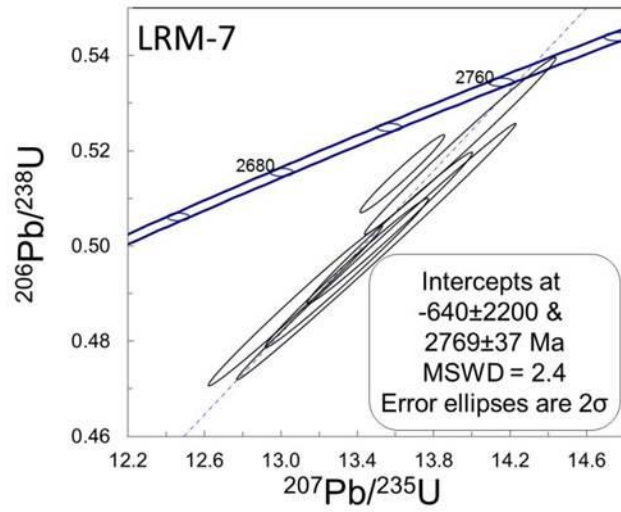


Figure 4-14. Concordia diagram showing U-Pb data for orthogneiss sample LRM-7. Each ellipse represents a single spot analysis and its 2σ error.

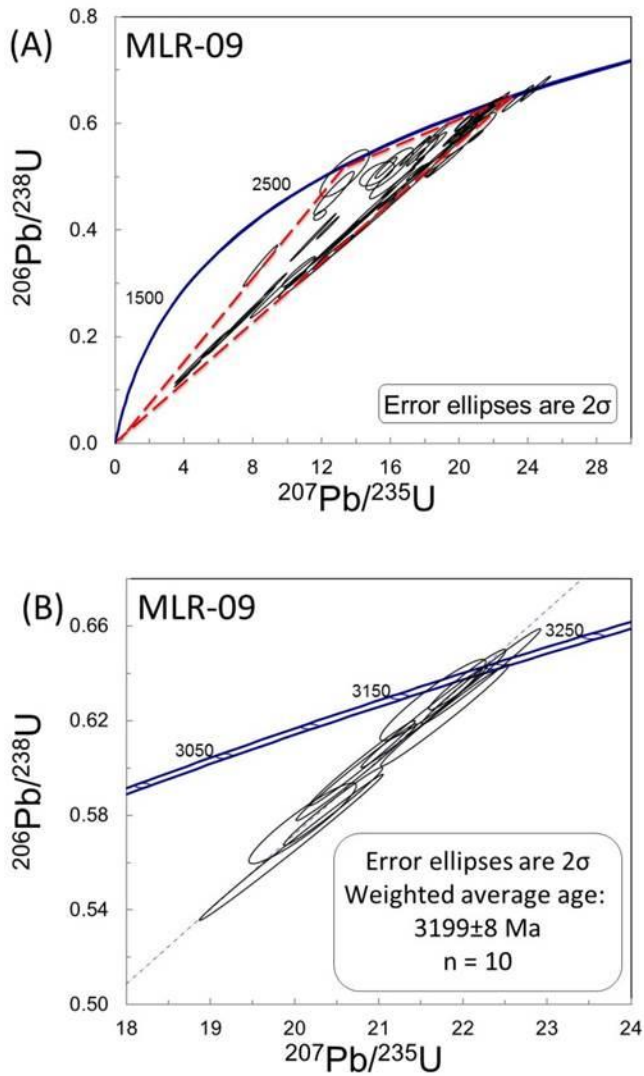


Figure 4-15. (A) Concordia diagrams plotting composite U-Pb data for orthogneiss sample MLR-09. Red dashed lines indicate trends within the analyses. (B) Expanded view of upper end of concordia showing the oldest, most concordant zircons selected for weighted average. Each ellipse represents a single spot analysis and its 2σ error.

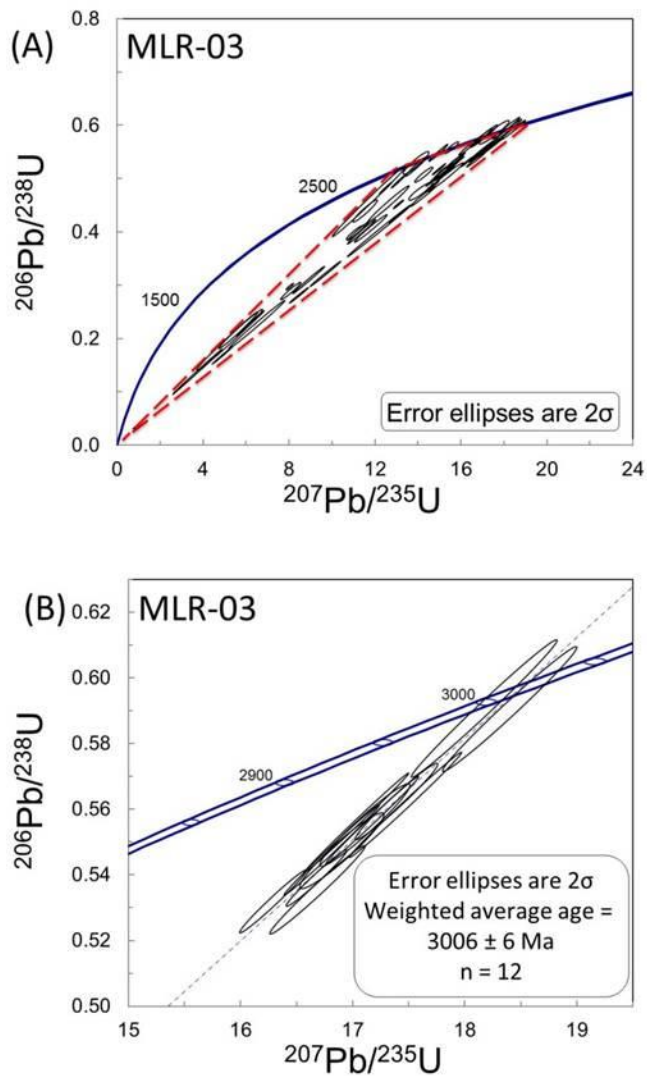


Figure 4-16. (A) Concordia diagrams plotting composite U-Pb data for amphibolite sample MLR-03. Red dashed lines indicate trends within the analyses. (B) Expanded view of upper end of concordia showing the oldest, most concordant zircons selected for weighted average. Each ellipse represents a single spot analysis and its 2σ error.

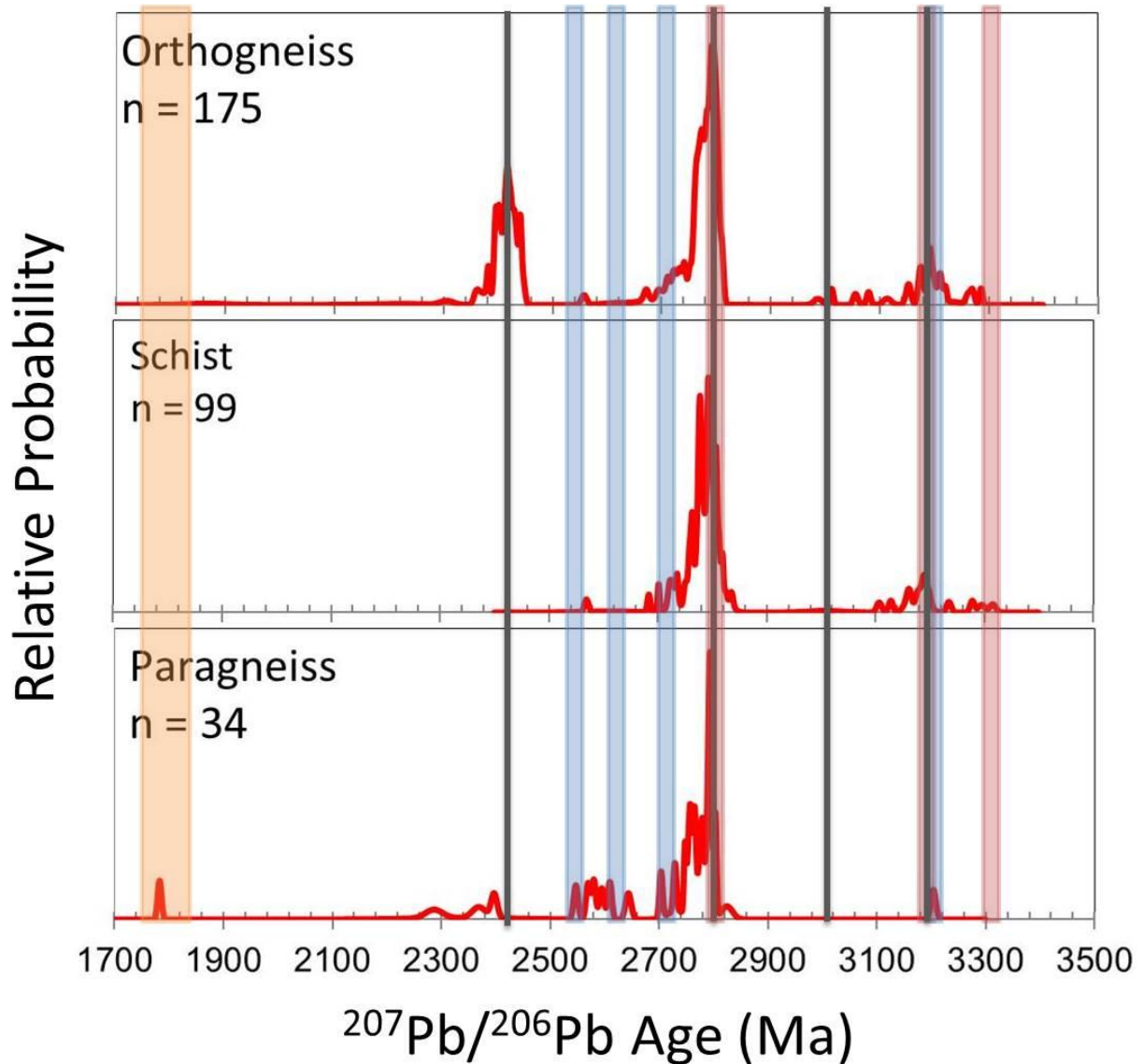


Figure 4-17. Probability density plots comparing the $\leq 10\%$ discordant detrital zircon analyses of the schist and paragneiss samples. Orthogneiss ages are included for comparison. The orange vertical bar represents a time frame when there was both regional metamorphism and igneous crystallization occurring in the GFTZ (Chapters 2 and 3). Blue vertical bars represent crystallization ages from the MHB and GFTZ (Chapters 2 and 3). Red vertical bars represent crystallization ages from the Wyoming craton. Gray vertical lines represent orthogneiss and amphibolite samples from the LRM.

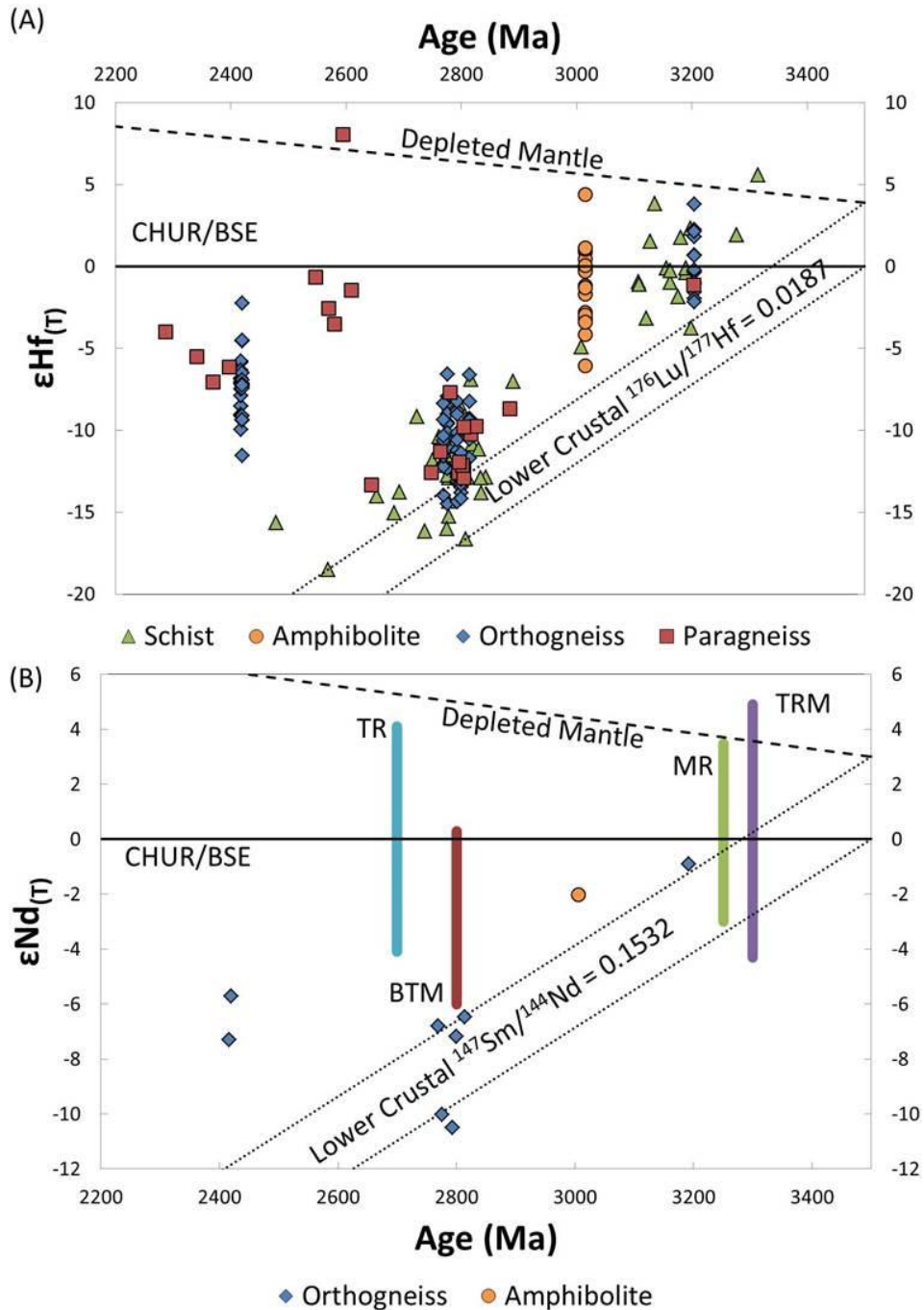


Figure 4-18. (A) Lu-Hf evolution diagram showing the range for the orthogneiss (blue diamond), amphibolites (orange circle), schistose (green triangle), and paragneisses (red square). (B) Sm-Nd evolution diagram showing ϵNd values for the orthogneiss (blue diamond) and the amphibolite (orange circle), and the range of ϵNd values of northern Wyoming province crust. TR – Teton Range, BTM – Beartooth Mountains, MR – Madison Range, TRM – Tobacco Root Mountains (citations can be found in the text). Zone of lower crustal ratios calculated using Rudnick and Gao (2003) (dotted lines).

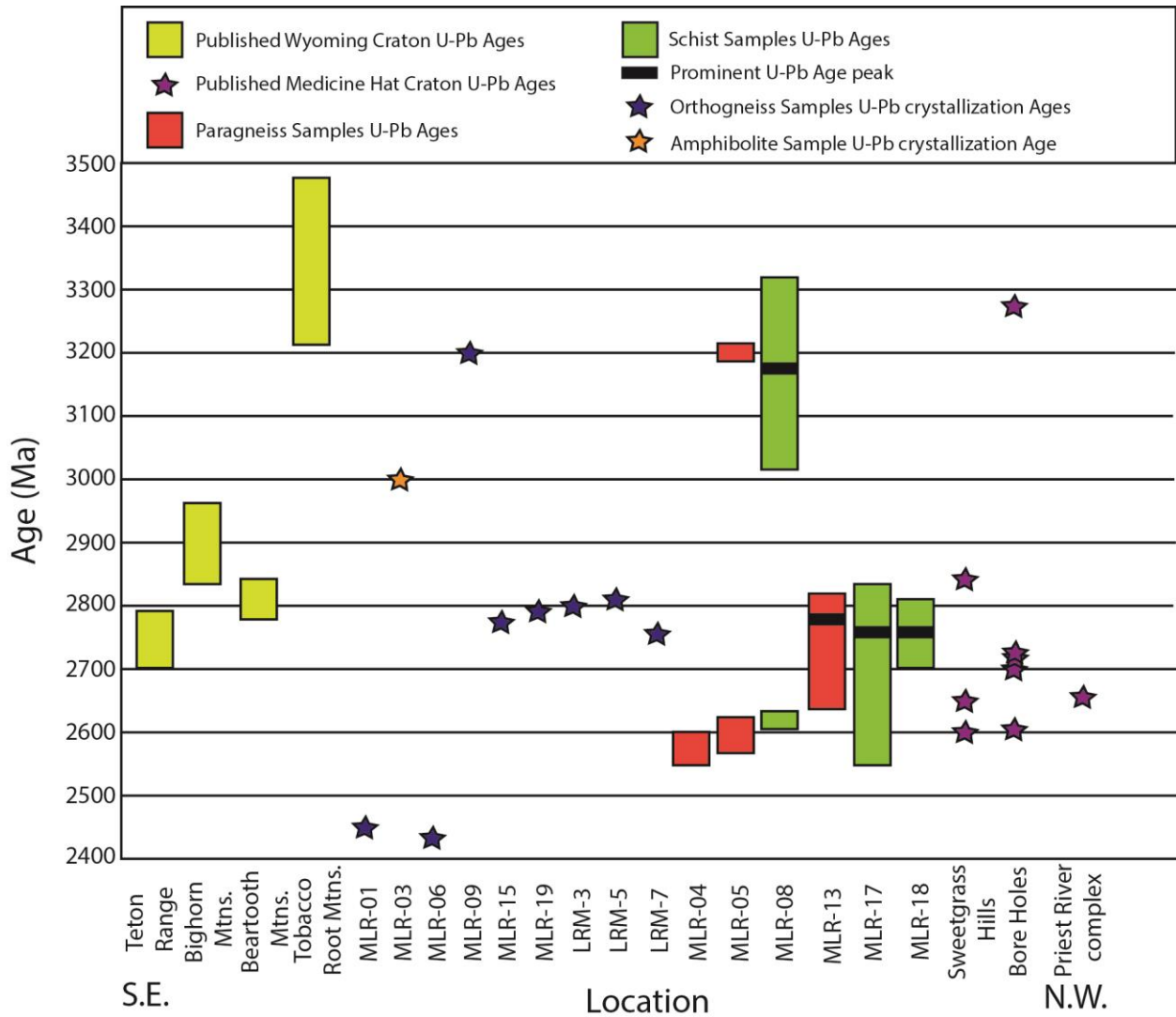


Figure 4-19. Published Archean to earliest Proterozoic U-Pb ages of zircon from the northern Wyoming craton (citations in the text) compared to published, ages for the MHB (citations in text). Wyoming – yellow bars, Medicine Hat – purple stars. Crystallization ages of orthogneiss from this study – blue stars, from amphibolite – orange star, from paragneiss (detrital) – pink bars, from schists (detrital) – green bars. Prominent age peaks from Table 4-6 – black bars.

CHAPTER 5 SUMMARY/CONCLUSIONS

Geochronology and geochemistry of crustal xenoliths and samples from the Little Rocky Mountains (LRM) within the Great Falls tectonic zone (GFTZ) provide new insight into the complex history and heterogeneity of the generally buried Precambrian crust in this region. Xenoliths were entrained in magma by Cenozoic volcanics in the Montana Alkali Province and recovered from two Grassrange diatremes, which yielded granitoid, schist, and quartzite/sandstone xenoliths; from within the Missouri Breaks Diatremes (Big Slide, Little Sand Creek, and Robinson Ranch localities); from the Bearpaw Mountains at Lloyd Divide, and from the Highwood Mountains. These samples included meta-granitoids, orthogneisses, amphibolites, one granulite, one mafic granulite, schistose, and paragneiss xenoliths. In addition, samples of Archean basement rocks exposed within the Little Rocky Mountains were also collected (meta-plutonic orthogneisses and amphibolites as well as meta-supracrustal rocks as schists and gneisses).

All of the granitoid and meta-igneous xenoliths show relative high field strength element (HFSE) depletions and large ion lithophile (LIL) element enrichments characteristic of subduction zone magmatism. The limited enrichment of heavy rare earth elements (HREE) relative to primitive mantle values reflects the source mineralogy, likely lower crustal materials where garnet is residual after melt extraction. Zircons from the orthogneiss samples from the Grassrange (Chapter 2) fall into two age populations. The first population is represented by magmatic zircons that yield minimum crystallization ages of ~2.5 Ga. The second age-population within the meta-plutonic xenoliths is represented by metamorphic zircon growth yielding minimum

metamorphic ages that range between ~1.77 and 1.84 Ga. Two granitoid samples from the Grassrange yield minimum igneous crystallization ages of ~1.73 and 1.74 Ga. Zircon Hf and whole-rock Sm-Nd isotopic data for the Archean meta-plutonic xenoliths indicate that juvenile and reworked crustal material mixed to varying degrees during crustal formation at ~2.5 Ga. The Hf and Nd isotopic data for the ~1.7 Ga granitoid samples indicate a mixture of older crust (e.g., the ~2.5 Ga crust in the older xenoliths) and a more juvenile source. This is in contrast to exposures of 1.8-1.9 Ga igneous material in the Little Belt Mountains, which involve far higher proportions of juvenile material, hypothesized to represent the arc formed during closure of the Little Belt ocean (Mueller et al., 2002).

Similar to data from the Grassrange, granitoid and meta-plutonic xenoliths from the Missouri Breaks yield two categories of xenoliths. The first category includes meta-plutonic samples with two age populations. The first age population is represented by magmatic zircons that yield minimum igneous crystallization ages that range between ~2.43 and 2.65 Ga, extending the range of Archean ages from within the GFTZ. The second age population is represented by metamorphic zircon growth yielding minimum metamorphic ages that range from 1.72 to 1.75 Ga. The second category of xenoliths include samples that yield a single age population, represented by magmatic zircons with calculated minimum igneous crystallization ages of ~1.73 Ga to ~1.89 Ga. Similar to the Grassrange, zircon Hf and whole-rock Sm-Nd isotopic data for the Archean meta-plutonic xenoliths indicate that juvenile and reworked crustal material mixed to varying degrees during crustal formation between ~2.4 and 2.7 Ga. The only exception to this is a single sample at 2.68 Ga, which seems to primarily be a crustal melt. Unlike the

xenoliths from the Grassrange, the Hf and Nd isotopic data for the Paleoproterozoic xenoliths from the Missouri Breaks, Bearpaw, and Highwood Mountains are generally similar to Hf and Sm-Nd values from the LBM. The data reveal xenoliths which, similar to the LBM, involve far higher proportions of juvenile material and might represent further arc material formed during closure of the Little Belt ocean (e.g., Mueller et al., 2002).

The range of earliest Paleoproterozoic to Archean igneous crystallization ages from the two xenolith suites are coincident with documented crystallization ages in the Medicine Hat Block (MHB), suggesting that the buried crust sampled by the xenoliths may represent reworked MHB material. The metamorphic ages of the Archean xenoliths and the igneous crystallization ages of the Paleoproterozoic xenoliths correlate with ~1.86 Ga ages from the Little Belt Mountains (LBM) and the tectonic event associated with the collision of the MHB with the Wyoming craton to form the GFTZ. The range of ages in detrital zircons from meta-supracrustal xenoliths (schists, paragneisses, etc.) likewise record crustal growth at the times documented in the meta-plutonic suites. These data, along with initial Hf isotopic ratios for Archean detrital zircons, provide no evidence for crust as old as that which characterizes the northern Wyoming Province (2.8-3.5 Ga). The crustal xenoliths from this study support the hypothesis that the GFTZ formed due to oceanic plate subduction and arc magmatism that initialized prior to ~1.9 Ga, and continued to 1.78 Ga. The boundary then evolved into a more transpressional continent-continent collision by 1.77 Ga as Wyoming moved east towards final collision with the Superior and Hearne provinces as well as the MHB (Dahl et al., 1999; Mueller et al., 2000; Mueller et al., 2002; Mueller et al., 2005). There

was likely a period of crustal thickening and metamorphism related to terminal collision followed by crustally derived granitoid magmatism, recorded by the ~1.73 Ga granitoid xenoliths from the Grassrange (Chapter 2).

Samples from the Little Rocky Mountains (LRM) reinforce the heterogeneous nature of the GFTZ, as well as the presence of reworked MHB material within it. Magmatic ages from meta-plutonic rock collected from the LRM are dominantly Neoproterozoic (~2.8 Ga) in age, with two early Paleoproterozoic (~2.4 Ga) and two Paleoproterozoic (~3.0 and 3.2 Ga) ages determined. LRM geochemical data reveal relative HFSE depletions and LIL enrichments characteristic of subduction zone melts, common to continental crustal material. The HREE show limited enrichment relative to primitive mantle values. This reflects the source mineralogy, which is likely lower crustal where garnet is residual after melt extraction. Detrital zircon age spectra from meta-supracrustal units in the LRM strongly record the c. 2.8 Ga crustal growth event, but lack the older detritus observed in Wyoming Craton detrital zircon suites (e.g. Mueller et al., 1998). The paucity of >3.0 Ga detrital zircon is consistent with a MHB affinity for the LRM sample suite.

Evidence of a thermal event that affected the LRM is indicated by the previously determined K-Ar and Ar-Ar ages at c. 1.7 Ga (Burwash et al., 1962). This age coincides with metamorphism in the northwestern Wyoming craton (Giletti, 1966; Roberts et al., 2002; Brady et al., 2004). These metamorphic ages record the final continental collision between MHB and WY craton, and link the LRM into the larger sample suite studied in this work. Data from this study indicate that the LRM is the only exposed region of MHB crust. These data provide evidence for a tectonic model in which the MHB at least

partially overrode the Wyoming craton. This significantly improves age control and the isotopic fingerprint on the otherwise concealed MHB, and allows for more robust comparisons to other Archean elements of the region.

Based on data from the xenolith suites and from the LRM, it is possible to extend and refine existing tectonic models for the evolution of the GFTZ. Between 1.89 and 1.79 Ga subduction was ongoing between the MHB and the Wyoming craton with subduction beneath MHB (Figure 5-1A and B). Arc magmatism was active and granitoid and meta-plutonic protoliths to the xenoliths were crystallizing. By 1.78 to 1.77 Ga, the terminal phase of subduction between the MHB and Wyoming province was occurring, leading to crustal thickening, deformation, and wide-scale metamorphism as the MHB partially overrode the Wyoming craton (Figure 5-1C). Evidence can be seen in the Tobacco Root Mountains, southwestern Montana, of Wyoming province material being buried to depths great enough for anatectic melts to have been created at 1.77 Ga (Mueller et al., 2004; 2005). Similarly, based on the MHB affinity of the Archean meta-plutonic samples from this study, the Paleoproterozoic magmatic arc was likely built on MHB crust. Further support is provided by a Deep Probe velocity model (Gorman et al., 2002), which cited an upper mantle floating reflector, interpreted to be a subducted slab, dipping beneath the MHB. This subduction would have led to the arc magmatism exposed in the LBM (Mueller et al., 2002). However, the model does not work across the entire GFTZ. If the Medicine Hat Block overrode the Wyoming craton in the central GFTZ, then the ~1.7 Ga granitoids from the Grassrange (Chapter 2) might be expected to have similarities with the anatectic melts from the southwestern GFTZ, which are melts of Wyoming province material. If the ~1.7 Ga Grassrange granitoids

were melts from Wyoming crust, the ϵNd values should be more negative than they are ($\epsilon\text{Nd} = -6$ to -10.0). This is evidence that portions of the MHB had to have been at depth as well as Wyoming, leading to partial melting of MHB crustal material as well as Wyoming material (Figure 5-1D; Mueller et al., 1996). When the oceanic subduction stopped driving crustal thickening, it is likely that post-orogenic collapse and extension began to take place (Figure 5-1E). This would have led to upwelling of mantle and crustal heating and partially melting lower crustal material, possibly leading to the ~ 1.73 and 1.74 Ga ages seen in xenoliths from the Grassrange (Chapter 2). It is possible that the upwelling mantle could have added mafic magmas to the base of the crust (i.e. high velocity layer; Gorman et al., 2002; Barnhart et al., 2012). Continental collision in the GFTZ ended by ~ 1.73 Ga, but metamorphic ages within xenolith as young as 1.72 Ga, and xenolith crystallization ages as young as 1.70 (Davis et al., 1995) indicates that there was post-collision extensional collapse, and related magmatism and metamorphism within the GFTZ. This could be explained by intraplate orogenesis from the accretion of the Yavapai and Mazatzal terrane which occurred between 1.80 to 1.70 Ga, reactivating tectonic structures within the GFTZ, and leading to further metamorphism and partial melting within the area.

The formation of the GFTZ appears to have concluded by 1.73 Ga with suturing of the Medicine Hat Block with the Wyoming Province. However, it is important to note that the collision of MHB and Wyoming coincided with other circum-Wyoming province collisions (Mueller et al., 2011). For example, the Cheyenne belt is proposed to be a Proterozoic suture between the Wyoming province and the Yavapai province. This was believed to have occurred during the Paleoproterozoic Medicine Bow orogeny between

1.66 and 1.80 Ga (Bickford and Boardman, 1984; Sims and Peterman, 1986; Karlstrom and Bowring, 1988; Premo and Van Schmus, 1989; Van Schmus et al., 1993; Chamberlain, 1998; Selverstone et al., 2000; Hill and Bickford, 2001; Hill, 2004), clearly overlapping in time with the development of the GFTZ. Further, the Trans-Hudson orogen suturing the Wyoming and Superior provinces occurred between 1.71 and 1.77 Ga (Karlstrom and Houston, 1984; Nelson et al., 1993; Resor et al., 1996; Dahl et al., 1999). Collision between the MHB, Wyoming Craton, and Superior Province occurred broadly contemporaneously. This is problematic from a geodynamic perspective, as the high angles of intersection between these convergence zones indicate that they were inherently unstable. The data presented here support the suggestion of Mueller et al. (2005) that the amalgamation of the Wyoming craton to the Superior craton and the Medicine Hat Craton was in part simultaneous, which places significant limits on plate tectonic relations during this very rapid period of continental growth (e.g., Hoffman, 1988; Mueller et al., 2005).

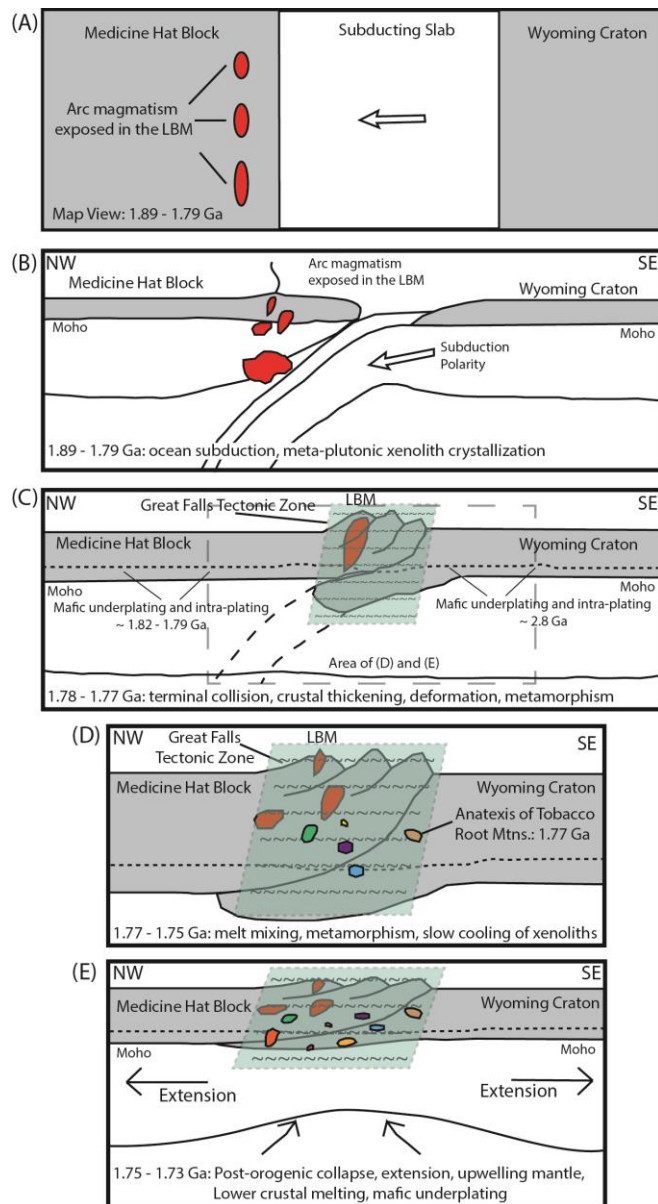


Figure 5-1. Schematic evolution of the Great Falls tectonic zone based on geologic constraints and chronology. (A) map-view: ocean subduction between the Wyoming province (WP) and the Medicine Hat Block (MHB). Each subsequent panel is a cross-section, from modern NW to SE, across the MHB to the WP. (B) 1.89 – 1.79 Ga, ocean subduction between the WP and the MHB, arc magmatism in the LBM and xenolith crystallization. (C) 1.78 – 1.77 Ga, terminal collision, deformation and metamorphism. (D) 1.77 – 1.75 Ga, crustal thickening as MHB overrides WP crust. Anatexis of WP crust in SW GFTZ (Mueller et al., 2004, 2005), melt mixing and xenolith crystallization, contact metamorphism of MHB crust. (E) 1.75 – 1.73 Ga, post-orogenic collapse and extension, upwelling mantle, mafic underplating, partially melting lower crustal rocks, magma crystallization. LBM – Little Belt Mtns.; TRM – Tobacco Root Mtns.

APPENDIX A METHODS

U-Pb And Hf Isotopic Analysis Of Zircon

Samples were crushed and pulverized using a jaw crusher and disk mill, then washed over a Gemini water table to obtain a heavy mineral fraction. The heavy mineral fraction was subjected to magnetic separation using a Franz electromagnetic separator and then concentrated by density in methylene iodide. Zircon grains were selected for analysis using an optical microscope and mounted in a 1-inch epoxy round mount with natural zircon standard (FC-1). The mounts were polished and cathodoluminescence (CL) images obtained in order to guide U-Pb and Lu-Hf analyses. U/Pb analyses were conducted at the University of Florida utilizing a New Wave 213 nm laser to ablate material, which was then analyzed using a Nu Plasma multi-collector inductively coupled plasma mass spectrometer (MC-ICP-MS) following methods summarized by Mueller et al. (2008a). Each U/Pb analysis consists of a 20-second background measurement, 30 seconds of measurement during ablation, and a one-minute purging period between analyses. Fractionation corrections are calibrated against the FC-1 natural zircon standard (1098 Ma; Mattinson, 2010). Lu-Hf analyses were also conducted with the MC-ICP-MS with each analysis consisting of a 20-second background measurement, one minute of measurement during ablation, and a one-minute purging period between analyses. The samples were calibrated against the FC-1 natural zircon standard (Black et al., 2003; Woodhead et al., 2004). Initial Hf isotopic compositions are calculated based on the $^{207}\text{Pb}/^{206}\text{Pb}$ age of the grain and the measured Lu/Hf ratio, unless otherwise stated.

Whole-Rock Geochemistry

A fraction of each sample was coarsely crushed for whole-rock geochemistry. Fragments with fresh surfaces were selected and then powdered in a puck mill. Five grams of this aliquot were separated for loss-on-ignition analysis and then fused for major element analysis by XRF (Geoscience Laboratories). For trace elements, approximately 50 mg of powdered material was dissolved in a 6:1 ratio of concentrated hydrofluoric to nitric acid (trace metal grade). After dissolution, the samples were dried and re-dissolved in *optima* (Fisher Scientific) hydrochloric acid. After a second dissolution and drying, the samples were re-dissolved in 5% Re-Rh spiked nitric acid and analyzed on an ICP-MS (Element 2, Thermo Scientific) for trace element abundances. Samples were run against USGS standards AGV-1 and G-2 (Table A-1). All standard values lie within error (3-7%) of accepted values when calibrated against AGV-1. After trace elements were measured, a portion of the solution was used to extract Nd for isotopic analysis. Rare earth elements (REE) were separated using cation exchange resin AG50W-X12, 200-400 mesh, and Nd was separated from the other REE with *Ln Resin* (Eichrom) prior to isotopic analysis. Sm-Nd systematics were evaluated using the Sm/Nd ratios from the trace element analyses, which are accurate to $\pm 3\%$ (2σ).

Table A-1. Trace Element data for USGS standards AGV-1 and G-2.

Sample	AGV-1	AGV-1	AGV-1	G-2	G-2	G-2
ppm	Average n = 7	Standard Deviation	% Error	Average n = 4	Standard Deviation	% Error
Li	11	1.5	12.7	31	2.1	6.7
Sc	12	0.31	2.6	3.2	0.56	17.5
Ti	7565	1836	24.3	3036	361	11.9
V	120	1.5	1.3	37	2.3	6.3
Cr	11	0.46	4.3	8.5	0.87	10.1
Co	15	0.14	0.9	4.2	0.22	5.1
Ni	16	0.33	2.1	3.9	0.17	4.3
Cu	57	1.8	3.1	11	1.6	14.2
Zn	87	1.9	2.1	81	3.8	4.7
Ga	20	0.22	1.1	23	0.66	2.9
Rb	68	0.79	1.2	165	3.3	2.0
Sr	662	6.0	0.9	463	7.5	1.6
Y	20	0.15	0.8	9.7	0.56	5.7
Zr	227	1.3	0.6	148	32	21.9
Nb	15	0.12	0.8	12	0.30	2.4
Cs	1.2	0.02	1.4	1.3	0.05	3.6
Ba	1196	63	5.3	2020	90	4.5
La	38	1.1	2.7	84	3.9	4.6
Ce	69	1.1	1.6	153	9.5	6.2
Pr	8.2	0.15	1.8	16	0.56	3.6
Nd	31	0.92	3.0	50	1.5	3.1
Sm	5.8	0.12	2.1	6.9	0.17	2.4
Eu	1.6	0.03	1.5	1.4	0.07	5.0
Gd	4.8	0.10	2.1	4.7	0.30	6.5
Tb	0.68	0.01	1.6	0.49	0.02	4.4
Dy	3.6	0.06	1.7	2.1	0.08	4.0
Ho	0.67	0.01	1.0	0.35	0.02	5.1
Er	1.9	0.04	2.0	0.95	0.06	6.1
Tm	0.27	0.01	3.1	0.11	0.00	4.0
Yb	1.7	0.02	1.5	0.66	0.02	3.7
Lu	0.25	0.00	1.7	0.09	0.00	5.1
Hf	5.1	0.08	1.6	3.6	0.71	20.0
Ta	0.89	0.03	3.1	0.79	0.04	4.5
Pb	37	0.38	1.0	33	1.1	3.3
Th	6.3	0.09	1.4	25	0.77	3.1
U	1.9	0.07	3.6	1.9	0.08	4.4

APPENDIX B
SUPPLEMENTARY DATA TABLES

Object B-1. External supplemental data tables.

LIST OF REFERENCES

- Annesley, I.R., Madore, C., Krogh, T.E., Anonymous, 1992, U-Pb geochronology of mylonitic gneiss and foliated granite from the boundary zone of the Wollaston and Peter Lake domains, Saskatchewan: Program with Abstracts - Geological Association of Canada; Mineralogical Association of Canada: Joint Annual Meeting, v. 17, p. 3-4.
- Bailey, R.L., 1974, Geology and ore deposits of the Alder Gulch area, Little Rocky Mountains, Montana: Unpublished Masters of Science Thesis, Montana State Univ., Bozeman, 81 p.
- Baird, D.J., Nelson, K.D., Knapp, J.H., Walters, J.J., Brown, L.D., 1996, Crustal structure and evolution of the Trans-Hudson orogen: Results from seismic reflection profiling: *Tectonics*, v. 15, n. 2, p. 416-426.
- Barnhart, K.R., Mahan, K.H., Blackburn, T.J., Bowring, S.A., Dudas, F.O., 2012, Deep crustal xenoliths from central Montana, USA: Implications for the timing and mechanisms of high-velocity lower crust formation: *Geosphere*, v. 8, n. 6, p. 1408-1428.
- Bickford, M.E., and Boardman, S.J., 1984, A Proterozoic volcanic-plutonic terrane, Gunnison and Salida areas, Colorado: *Journal of Geology*, v. 92, p. 657-666.
- Bickford, M.E., Van Schmus, W.R., Collerson, K.D., Macdonald, R., 1987, U-Pb zircon geochronology project: New results and interpretation, in Summary of investigations, 1987: Saskatchewan Geological Survey Miscellaneous Report 87-4, p. 76-79.
- Bickford, M.E., 1988, The formation of continental crust; Part 1, A review of principles; Part 2, An application to the Proterozoic evolution of southern North America: *Geological Society of America Bulletin*, v. 100, p. 1375-1391.
- Bickford, M.E., Collerson, K.D., Lewry, J.F., Van Schmus, W.R., Chiarenzelli, J.R., 1990, Proterozoic collisional tectonism in the Trans-Hudson Orogen, Saskatchewan: *Geology*, v. 18, p. 14-18.
- Bickford, M.E., Hamilton, G.L., Wortman, G.L., Hill, B.M., 2001, Archean rocks in the southern Rottenstone Domain: significance for the evolution of the Trans-Hudson Orogen: *Canadian Journal of Earth Sciences*, v. 38, p. 1017-1025.
- Black, L.P., Kumo, S.L., Williams, I.S., Mundil, R., Davis, D.W., Korsh, R.J., Foudoulis, C., 2003, The application of SHRIMP to Phanerozoic geochronology; a critical appraisal of four zircon standards: *Chemical Geology*, v. 200, p. 171-188.
- Blackburn, T.J., Bowring, S., Burdick, S., van der Hilst, R., Mahan, K., Dudas, F., 2010, U-Pb thermochronology: 4-dimensional imaging of the North American lithosphere: *inSights: The EarthScope Newsletter*, spring 2010, 2 p.

- Blackburn, T.J., Bowring, S.A., Schoene, B., Mahan, K., Dudas, F., 2011, U-Pb thermochronology: Creating a temporal record of lithosphere thermal evolution: *Contributions to Mineralogy and Petrology*, v. 162, p. 479-500.
- Boerner, D.E., Craven, J.A., Kurtz, R.D., Ross, G.M., Jones, F.W., 1998, The Great Falls Tectonic Zone: Suture or intracontinental shear zone?: *Canadian Journal of Earth Sciences*, v. 35, n. 2, p. 175-183.
- Bolhar, R., Kamber, B., Collerson, K., 2007, U-Th-Pb fractionation in Archaean lower continental crust: Implications for terrestrial Pb isotope systematics: *Earth and Planetary Science Letters*, v. 254, p. 127-145.
- Brewer, R.A., Vervoort, J., Lewis, R.S., Gaschnig, R.M., Hart, G., 2008, New constraints on the extent of Paleoproterozoic and Archean basement in the Northwest U.S. cordillera, *Eos Trans. AGU*, 89(53), Fall Meet. Suppl., Abstract T23C-2066.
- Buhlmann, A.L., Cavell, P., Burwash, R.A., Creaser, R.A., Luth, R.W., 2000, Minette bodies and cognate mica-clinopyroxenite xenoliths from the Milk River area, southern Alberta: records of a complex history of the northernmost part of the Archean Wyoming craton: *Canadian Journal of Earth Sciences*, v. 37, p. 1629-1650.
- Burwash, R.A., Baadsgaard, H., Peterman, Z.E., 1962, Precambrian K-Ar dates from the western Canada sedimentary basin: *Journal of Geophysical Research*, v. 67, n. 4, p. 1617-1625.
- Carlson, R.W. and Irving, A., 1994, Depletion and enrichment history of subcontinental lithospheric mantle: An Os, Sr, Nd and Pb isotopic study of ultramafic xenoliths from the northwestern Wyoming Craton: *Earth and Planetary Science Letters*, v. 126, p. 457-472.
- Chamberlain, K.R., 1998, Medicine Bow Orogeny; timing of deformation and model of crustal structure produced during continent-arc collision, ca. 1.78 Ga, southeastern Wyoming: *Rocky Mountain Geology* v. 33, n. 2 p. 259-277.
- Chappell, B.W. and White, J.R., 2001, Two contrasting granite types: 25 years later: *Australian Journal of Earth Science*, v. 48, p. 489-499.
- Chauvel, C. and Blichert-Toft, J., 2001, A hafnium isotope and trace element perspective on mentoring of the depleted mantle: *Earth and Planetary Science Letters*, v. 190, p. 137-151.
- Collerson, K., Hearn, B.C., MacDonald, R.A., Upton, B.G.J., Harmon, R.S., 1989, Composition and evolution of lower continental crust: Evidence from xenoliths in Eocene lavas from the Bearpaw Mountains, Montana, *in* *Continental magmatism: Abstracts of the IAVCEI: New Mexico Bureau of Mines and Resources Bulletin* 131, p. 57.

- Condie, K.C., 1992, Proterozoic terranes and continental accretion in southwestern North America: *In* Condie, K. C., ed. Proterozoic crustal evolution. Amsterdam, Elsevier, chap. 12, p. 447-480.
- Cox, D., Frost, C., Chamberlain, K., 2000, 2.01-Ga Kennedy dike swarm, southeastern Wyoming: Record of a rifted margin along the southern Wyoming Province: *Rocky Mountain Geology*, v. 35, n. 1, p. 7-30.
- Dahl, P.S., Holm, D.K, Gardner, E.T., Hubacher, F.A., Foland, K.A., 1999, New constraints on the timing of Early Proterozoic tectonism in the Black Hills (South Dakota), with implications for docking of the Wyoming province with Laurentia: *GSA Bulletin*, v. 111, n. 9, p. 1335-1349.
- Dahl, P.S., Hamilton, M.A., Stern, R.A., Frei, R., Berg, R.B., 2000, In situ SHRIMP investigation of an early Proterozoic metapelite, with implications for Pb-Pb step-leach dating of garnet and staurolite: *Abstracts with Programs - Geological Society of America*, v. 32, n. 7, p. 297.
- Davidson, A., 2008, Late Paleoproterozoic to mid-Neoproterozoic history of northern Laurentia; an overview of central Rodinia: *Precambrian Research*, v. 160, p. 5-22.
- Davis, W.J., Berman, R., Kyarsgaard, B., 1995, U-Pb geochronology and isotopic studies of crustal xenoliths from the Archean Medicine Hat block, northern Montana and southern Alberta: Paleoproterozoic reworking of Archean crust. *In* 1995 Alberta Basement Transects Workshop. *Edited by* G.M. Ross. Lithoprobe secretariat, The University of British Columbia, Lithoprobe Report 47, p. 330-335.
- Deer, W.A., Howe, R.A., Zussman, J., 1992, *The rock forming minerals*, second edition. Pearson Education, Ltd, Essex. 696 p.
- DePaolo, D.J., 1981, Trace element and isotopic effects of combined wallrock assimilation and fractional crystallization: *Earth and Planetary Science Letters*, v. 53, p. 189-202.
- Dhuime, B., Hawkesworth, C., Cawood, P., 2011, When continents formed: *Science*, v. 331, p. 154-155.
- Doughty, P.T., Price, R.A., Parrish, R.R., 1998, Geology of Archean basement and Proterozoic cover in the Priest River complex, northwestern United States, and their implications for Cordilleran structure and Precambrian continent reconstructions: *Canadian Journal of Earth Sciences*, v. 35, p. 39-54.
- Downes, H., MacDonald, R., Upton, B., Cox, K., Bodinier, J., Mason, P., James, D., Hill, P., Hearn, B.C., 2004, Ultramafic xenoliths from the Bearpaw Mountains, Montana, USA: Evidence for multiple metasomatic events in the lithospheric mantle beneath the Wyoming craton: *Journal of Petrology*, v. 45, p. 1631-1662.

- Dyson, J.L., 1939, Ruby Gulch mining district, Little Rocky Mountains, Montana. *Economic Geology*, v. 34, p. 201-213.
- Eaton, D.W., Ross, G.M., Clowes, R.M., 1999, Seismic-reflection and potential-field studies of the Vulcan structure, Western Canada; a Paleoproterozoic Pyrenees?: *Journal of Geophysical Research*, v. 104, p. 23,255-23,269.
- Facer, J., Downes, H., Beard, A., 2009, In situ serpentinization and hydrous fluid metasomatism in spinel dunite xenoliths from the Bearpaw Mountains, Montana, USA: *Journal of Petrology*, v. 50, p. 1443-1475.
- Faure, G. and Mensing, T.M., 2005, *Isotopes Principles and Applications*, Third edition. John Wiley & Sons, Inc. Hoboken.
- Foster, D.A., Mueller, P.A., Mogk, D.W., Wooden, J.L., Vogl, J.J., 2006, Proterozoic evolution of the western margin of the Wyoming craton: implications for the tectonic and magmatic evolution of the northern Rocky Mountains: *Canadian Journal of Earth Sciences*, v. 43, n, p. 1601-1619.
- Foster, D.A., Mueller, P.A., Heatherington, A. Kalakay, T.J., 2012, Lu–Hf systematics of magmatic zircons reveal a Proterozoic crustal boundary under the Cretaceous Pioneer batholith, Montana: *Lithos*, v. 142-143, p. 216-225.
- Frost, C.D., 1993, Nd isotopic evidence for the antiquity of the Wyoming province: *Geology*, v. 21, p. 351-354.
- Frost, C.D., Frost, B.R., Chamberlain, K.R., Hulsebosch, T.P., 1998, The Late Archean history of the Wyoming province as recorded by granitic magmatism in the Wind River Range, Wyoming: *Precambrian Research*, v. 89, p. 145-173.
- Frost, B.R., Barnes, C.G., Collins, W.J., Arculus, R.J., Ellis, D.J., Frost, C.D., 2001, A geochemical classification for granitic rocks: *Journal of Petrology*, v. 42, p. 2033-2048.
- Frost, C.D. and Fanning, C.M., 2006a, Archean geochronological framework of the Bighorn Mountains, Wyoming: *Canadian Journal of Earth Sciences*, v. 43, n. 10, p. 1399-1418.
- Frost, C.D., Frost, B.R., Kirkwood, R., Chamberlain, K., 2006b, The tonalite-trondhjemite-granodiorite (TTG) to granodiorite-granite (GG) transition in the late Archean plutonic rocks of the central Wyoming Province: *Canadian Journal of Earth Sciences*, v. 43, p. 1419-1444.
- Giletti, B., 1966, Isotopic ages from southwestern Montana: *Journal of Geophysical Research*, v. 71, 4029-4036.

- Gordon, T.M., Hunt, P.A., Bailes, A.H., Syme, E.C., 1990, U-Pb ages from the Flin Flon and Kisseynew belts, Manitoba; chronology of crust formation at an early Proterozoic accretionary margin: Special Paper, Geological Association of Canada, v. 37, p. 177-199.
- Gorman, A, Clowes, R, Ellis, R., Henstock, T., Spence, G., Keller, G., 2002, Deep Probe: imaging the roots of western North America: Canadian Journal of Earth Sciences, v. 39, n. 3, p. 375-398.
- Griffin, W.L., Wang, X., Jackson, S.E., Pearson, N.J., O'Reilly, S.Y., Xu, X., Zhou, X., 2002, Zircon chemistry and magma mixing, SE China: In-situ analysis of Hf isotopes, Tonglu and Pingtan igneous complexes: Lithos, v. 61, p. 237-269.
- Guevara, V.E., Baldwin, J.A., Foster, D.A., Lewis, R.S., 2012, From peak metamorphism to orogenic collapse: insights into the exhumation history of the Clearwater metamorphic core complex: Mineralogical Magazine, v. 76, p. 1788.
- Harms, T., Brady, J., Burger, H., Cheney, J., 2004, Advances in the geology of the Tobacco Root Mountains, Montana, and their implications for the history of the northern Wyoming Province, *in* Brady, J.B., et al., eds., Precambrian geology of the Tobacco Root Mountains, Montana: Geological Society of America Special Paper 377, p. 227-243.
- Hearn, B.C., Jr., Marvin, R.F., Zartman, R.E., Naeser, C.W., 1977, Geochronology of igneous activity in the north-central alkalic province. Geological Society of America Abstracts with Programs, v. 9, p. 732.
- Hearn, B.C., Jr., Dudas, F.O., Eggler, D.H., Hyndman, D.W., O'Brien, H.E., 1989, Volcanism and plutonism of western North America; Volume 2, Montana high-potassium igneous province, Washington, DC, United States (USA): American Geophysical Union.
- Heimlich, R.A. and Banks, P.O., 1968, Radiometric age determinations, Bighorn Mountains, Wyoming: American Journal of Science, v.266, n. 3, p. 180-192.
- Henstock, T.J., Levander, A., Snelson, C.M., Keller, G.R., Miller, K.C., Harder, S.H., Gorman, A.R., Clowes, R.M., Burianyk, M.J.A., Humphreys, E.D., 1998, Probing the Archean and Proterozoic Lithosphere of Western North America: GSA Today, v. 8, n. 7, p. 1-5.
- Hill, B.M., and Bickford, M.E., 2001, Paleo Proterozoic rocks of central Colorado: Accreted arcs or extended older crust?: Geology, v. 29, p. 1015-1018,
- Hill, B.M., 2004, Paleoproterozoic of central Colorado: Island arcs or rifted older crust? [Ph.D. thesis]: Syracuse, New York, Syracuse University, 145 p.

- Holm, D. and Schneider, D., 2002, $^{40}\text{Ar}/^{39}\text{Ar}$ evidence for ca. 1800 Ma tectothermal activity along the Great Falls tectonic zone, central Montana: *Canadian Journal of Earth Sciences*, v. 39, p. 1719-1728.
- Hoffman, P.F., 1988, United plates of America, the birth of a craton: Early Proterozoic assembly and growth of Laurentia: *Annual Review of Earth and Planetary Sciences*, v. 16, p. 543-603.
- Hoffman, P.F., 1989, Speculations on Laurentia's first gigayear (2.0 to 1.0 Ga): *Geology*, v. 17, p. 135-138.
- Hoffman, P., 1990, Archean continental plates; old and young mantle roots: *Nature*, v. 347, p. 19-20.
- Jansen, A.C., Vervoort, J.D., Reed, S., Anonymous, 2011, Precambrian basement rocks of the Clearwater metamorphic complex: a new piercing point along the western margin of Laurentia: *Abstracts with Programs - Geological Society of America*, v. 43, p. 491.
- Joswiak, D., 1992, Composition and evolution of the lower crust, central Montana; evidence for granulite xenoliths [M.S. thesis]: Seattle, University of Washington, 154 p.
- Karlstrom, K.E. and Houston, R.S., 1984, The Cheyenne Belt: Analysis of a Proterozoic suture in southern Wyoming: *Precambrian Research*, v. 25, p. 415-446.
- Karlstrom, K.E. and Bowring, S.A., 1988, Early Proterozoic orogeny assembly of tectonostratigraphic terranes in southwestern North America: *Journal of Geology*, v. 96, p. 561-576.
- Kirkwood, R., 2000, Geology, geochronology and economic potential of the Archean rocks in the western Owl Creek Mountains, Wyoming: Dissertation at University of Wyoming, Laramie, WY, United States.
- Kleinkopf, M.D., Witkind, I.J., Keefer, W.R., 1972, Aeromagnetic, Bouguer gravity, and generalized geologic maps of the central part of the Little Belt Mountains, Montana: *Geophysical Investigations Map: 4*. U. S. Geological Survey.
- Knechtel, M., 1959, Stratigraphy of the Little Rocky Mountains and encircling foothills, Montana. *U.S. Geological Survey Bulletin 1072-N*, p. 723-752.
- Krogh, T., Kamo, S.L., Hanley, T.B., Hess, D.F., Dahl, P.S., et al., 2011, Geochronology and geochemistry of Precambrian gneisses, metabasites, and pegmatite from the Tobacco Root Mountains, northwestern Wyoming craton, Montana: *Canadian Journal of Earth Sciences*, v. 48. n. 2, p. 161-185.

- Lemieux, S., Ross, G.M., Cook, F.A., 2000, Crustal geometry and tectonic evolution of the Archean crystalline basement beneath the southern Alberta Plains, from new seismic reflection and potential-field studies: *Canadian Journal of Earth Sciences*, v. 37, n. 11, p. 1473-1491.
- Lewry, J.F., Thomas, D.J., MacDonald, R., Chiarenzelli, J., 1987, Structural relations in accreted terranes of the Trans-Hudson Orogen, Saskatchewan: telescoping in a collisional regime?: Geological Association of Canada meeting, Abstracts, v.12, p. 67.
- Lewry, J.F., Hajnal, Z., Green, A., Lucas, S.B., White, D., Stauffer, M., Ashton, K., Weber, W., Clowes, R., 1994, Structure of the Paleoproterozoic continent–continent collision zone: a LITHOPROBE seismic reflection profile across the Trans-Hudson Orogen, Canada: *In Proceedings of the 5th International conference on seismic reflection probing of continents and their margins. Edited by R.M. Clowes and A.G. Green. Tectonophysics*, v. 232, p. 143-160.
- Leyreloup, A., Dupuy, C., Andriambololona, R., 1977, Catazonal xenoliths in French Neogene volcanic rocks: Constitution of the lower crust: *Contributions to Mineralogy and Petrology*, v. 62, p. 283-300.
- Lucas, S.B., Stern, R.A., Syme, E.C., Reilly, B.A., Thomas, D.J., 1996, Intraoceanic tectonics and development of continental crust: 1.92–1.84 Ga evolution of the Flin Flon Belt, Canada: *Geological Society of America Bulletin*, v. 108, p. 602-629.
- MacDonald, R., Upton, B., Collerson, K., Hearn, B.C., James, D., 1992, Potassic mafic lavas of the Bearpaw Mountains, Montana: Mineralogy, chemistry, and origin: *Journal of Petrology*, v. 33, p. 305-346.
- Machado, N., 1990, Timing of collisional events in the Trans-Hudson Orogen: Evidence from U–Pb geochronology for New Quebec Orogen, the Thompson Belt, and the Reindeer Zone Manitoba and Saskatchewan: *In The Early Proterozoic Trans-Hudson Orogen of North America Edited by J.F. Lewry and M.R. Stauffer. Geological Association of Canada, Special Paper*, v. 37, p. 433-441.
- Machado, N., Zwanzig, H., Parent, M., 1999, U-Pb ages of plutonism, sedimentation, and metamorphism of the Paleoproterozoic Kiseynew metasedimentary belt, Trans-Hudson Orogen (Manitoba, Canada): *Canadian Journal of Earth Science*, v. 36, p. 1829-1842.
- Maniar, P.D. and Piccoli, P.M., 1989, Tectonic discrimination of granitoids: *Geological Society of America Bulletin*, v. 101, p. 635-643.
- Marvin, R.F., Witkind, I.J., Keefer, W.R., Mehnert, H.H., 1973, Radiometric ages of intrusive rocks in the Little Belt Mountains, Montana: *GSA Bulletin*, v. 84, n. 6, p. 1977-1986.

- Marvin, R.F., Hearn, B.C., Mehnert, H.H., Naeser, C.W., Zartman, R.E., Lindsey, D.A., 1980, Late Cretaceous-Paleocene-Eocene igneous activity in north-central Montana: *Isochron-West*, v. 29, n. 3, p. 5-25.
- Mattingon, J., 2010, Analysis of the relative decay constants of ^{235}U and ^{238}U by multi-step CA-TIMS measurements of closed system natural zircon samples: *Chemical Geology* v. 275, p. 186-198.
- McDonough, W.F. and Sun, S., 1995, The composition of the Earth: *Chemical Geology*, v. 120, p. 223-253.
- Miller, S.H., Hildebrandt, P.K., Erlsev, E.A., Reed, J.C., Jr., 1986, Metamorphic and deformation history of the gneiss complex in the northern Teton Range, Wyoming. *In* *Geology of the Beartooth uplift and adjacent ranges, Montana Geologic Society and Yellowstone-Beartooth Research Association Joint Field Conference and Symposium, Red Lodge, Mont., 31 August - 1 September 1986*, p. 91-110.
- Mirnejad., H. and Bell, K., 2006, Origin and source evolution of the Leucite Hills lamproites: evidence from Sr-Nd-Pb-O isotopic compositions: *Journal of Petrology*, v. 47, p. 2,463 – 2,489.
- Mirnejad., H. and Bell, K., 2008, Geochemistry of crustal xenoliths from the Hatcher Mesa lamproite, Wyoming, USA: Insights into the composition of the deep crust and upper mantle beneath the Wyoming craton. *Can. Mineral.*, v. 46, p. 583 - 596.
- Mogk, D.W., Mueller, P.A., Weyand, E., Heatherington, A.L., 1990, Middle Archean gneisses of the northern Madison Range, SW Montana: Crustal genesis in a magmatic arc?: *Eos (American Geophysical Union Transactions)*, v. 17, p. 655.
- Mogk, D.W., Mueller, P.A., Wooden, J.L., 2004, Tectonic implications of late Archean-early Proterozoic supracrustal rocks in the Gravelly Range, SW Montana: *Abstracts with Programs, Geological Society of America*, v. 36, p. 507.
- Mueller, P.A. and Wooden, J.L., 1988, Evidence for Archean subduction and crustal recycling, Wyoming province: *Geology*, v. 16, p. 871-874.
- Mueller, P.A., Shuster, R., Wooden, J., Erslev, E., Bowes, D., 1993, Age and composition of Archean crystalline rocks from the southern Madison Range: Implications for crustal evolution in the Wyoming craton: *Geological Society of America Bulletin*, v. 105, p. 437-446.
- Mueller, P.M., Heatherington, A., Weyand, E., Wooden, J., Mogk, D.A., 1995, Geochemical evolution of Archean crust in the northern Madison Range, Montana, evidence from U-Pb and Sm-Nd systematics: *Abstracts with Programs - Geological Society of America*, v. 27, n. 4, p. 49.

- Mueller, P.A., Wooden, J.L., Mogk, D.W., Nutman, A.P., Williams, I.S., 1996, Extended history of a 3.5 Ga trondhjemitic gneiss, Wyoming Province, USA: Evidence from U-Pb systematics in zircon: *Precambrian Research*, v. 78, p. 41-52.
- Mueller, P.A., Heatherington, A., Kelly, D., Wooden, J.L., Mogk, D., 2000, The Great Falls tectonic zone and its role in the Paleoproterozoic assembly of southern Laurentia: *Abstracts with Programs - Geological Society of America* v. 32, n. 7, p. 318.
- Mueller, P.A., Heatherington, A.L., Kelly, D.M., Wooden, J.L., Mogk, D.W., 2002, Paleoproterozoic crust within the Great Falls tectonic zone: Implications for the assembly of southern Laurentia: *Geology*, v. 30, n. 2, p. 127-130.
- Mueller, P.A., Burger, H., Wooden, J.L., Heatherington, A., Mogk, D.W., D'Arcy, K., 2004, Age and evolution of the Precambrian crust of the Tobacco Root Mountains, Montana, *in* Brady, J.B., et al., eds., *Precambrian geology of the Tobacco Root Mountains, Montana: Geological Society of America Special Paper 377*, p. 181-202.
- Mueller, P., Burger, H., Wooden, J., Brady, J., Cheney, J., Harms, T., Heatherington, A., and Mogk, D., 2005, Paleoproterozoic metamorphism in the northern Wyoming Province: Implications for the assembly of Laurentia: *Journal of Geology*, v. 113, p. 169-179.
- Mueller, P.A. and Frost, C.D., 2006, The Wyoming province: a distinctive Archean craton in Laurentian North America: *Canadian Journal of Earth Sciences*, v. 43, p. 1391-1397.
- Mueller, P.A., Kamenov, G.D., Heatherington, A.L., Richards, J., 2008a, Crustal evolution in the Southern Appalachian orogen: Evidence from Hf isotopes in detrital zircons: *Journal of Geology*, v. 116, n. 4, p. 414-422.
- Mueller, P.A., Foster, D.A., Gifford, J.N., Wooden, J., Mogk, D.W., 2008b, Tectonic and stratigraphic implications of detrital zircon suites in Cambrian and Precambrian sandstones from the Eastern margin of the belt basin: *Northwest Geology*, v. 37, p. 61-68.
- Mueller, P., Wooden, J.L., Mogk, D., Henry, D., Bowes, D.R., 2010, Rapid growth of an Archean continent by arc magmatism: *Precambrian Research*, v. 183, p. 70-88.
- Mueller, P.A., Foster, D.A., Gifford, J.N., Vogl, J.J., Wooden, J., Mogk, D.W., 2011, Closure of a Paleoproterozoic ocean recorded by Hf isotopes in zircons: *Geological Society of America Abstracts with Programs* v. 43, n. 5, p. 323.
- Mueller, P.A. and Wooden, J.L., 2012, Trace element and Lu-Hf systematics in Hadean-Archean detrital zircons: Implications for crustal evolution: *The Journal of Geology*, v. 120, n. 1, p. 15-29.

- Nelson, K.D., Baird, D.J., Walters, J.J., Hauck, M., Brown, L.D., Oliver, J.E., Ahern, J.L., Hajnal, Z., Jones, A.G., Sloss, L.L., 1993, Trans-Hudson orogen and Williston basin in Montana and North Dakota: New COCORP deep-profiling results: *Geology*, v. 21, p. 447-450.
- O'Neill, J. and Lopez, D., 1985, Character and regional significance of Great Falls tectonic zone, East-Central Idaho and West-Central Montana: *American Association of Petroleum Geologists Bulletin*. v.69, p. 437-447.
- Pearce, J.A., 1983. The role of the sub-continental lithosphere in magma genesis at destructive plate boundaries: In Thorpe, R.S. (ed.) *Continental Basalts and Mantle Xenoliths*, Shiva, Nantwich, p. 230-249.
- Pearce, J.A., Harris, N.B.W., Tindle, A.G., 1984, Trace element discrimination diagrams for the tectonic interpretation of granitic rocks: *Journal of Petrology*. v. 25, p. 956-983.
- Peterman, Z.E., 1981, Archean Gneisses in the Little Rocky Mountains, Montana. *Geological Survey Professional Paper 1199-A*, p. 1-47.
- Pilkington, M., Grieve, R.A.F., Rupert, J.D., Halpenny, J.F., 1992, Gravity anomaly map with shaded relief of gradient of North America. *Geologic Survey of Canada, Map 1807A*, scale 1:10,000,000.
- Pirsson, L., 1900, Petrography of the igneous rocks on the Little Belt Mountains: *U.S. Geological Survey, 20th Annual report, Part III*, p. 116-134.
- Premo, W. R. and Van Schmus, W.R., 1989, Zircon geochronology of Precambrian rocks in southeastern Wyoming and northern Colorado: Proterozoic geology of the southern Rocky Mountains: *Geological Society of America Special Paper*, v. 235, p. 13-32.
- Ray, G.E. and Wanless, R.K., 1980, The age and geological history of the Wollaston, Peter Lake, and Rottenstone domains in northern Saskatchewan: *Canadian Journal of Earth Sciences*, v. 17, p. 333-347.
- Rayner, N.M., Stern, R.A., Bickford, M.E., 2005, Tectonic implications of new SHRIMP and TIMS U-Pb geochronology of rocks from the Sask Craton, Peter Lake Domain, and Hearne margin, Trans-Hudson Orogen, Saskatchewan: *Canadian Journal of Earth Sciences*, v. 42, p. 635-657.
- Resor, P.G., Snoke, A.W., Chamberlain, K.R., 1996, Development of a shear-zone bounded block uplift within the middle crust of the Archean Wyoming Province during Proterozoic accretion, Laramie Mts., WY: *Abstracts with Programs, Geological Society of America*, v. 28, p. 496.

- Roberts, H., Dahl, P., Kelley, S., and Frei, R., 2002, New ^{207}Pb - ^{206}Pb and ^{40}Ar - ^{39}Ar ages from SW Montana, USA: Constraints on the Proterozoic and Archean tectonic and depositional history of the Wyoming Province: *Precambrian Research*, v. 117, p. 119-143.
- Rogers, G.R. and Hawkesworth, C.J., 1989, A geochemical traverse across the north Chilean Andes: evidence for crust generation from the mantle wedge: *Earth and Planetary Science Letters*, v. 91, p. 271-285.
- Ross, G.M., 1991, Precambrian basement in the Canadian Cordillera: an introduction: *Canadian Journal of Earth Sciences*, v. 28, p. 1133-1139.
- Ross, G.M., 2002, Evolution of Precambrian continental lithosphere in Western Canada: Results from Lithoprobe studies in Alberta and beyond: *Canadian Journal of Earth Sciences*, v. 39, p. 413-437.
- Rubatto D., 2002, Zircon trace element geochemistry: partitioning with garnet and the link between U-Pb ages and metamorphism: *Chemical Geology*, v. 184, p. 123-138.
- Rudnick, R.L. and Gao, S., 2003, Composition of the continental crust: *Treatise on geochemistry*, v. 3, p. 1-64.
- Russell, C.W., 1984, Geology of the central portion of the Little Rocky Mountains, Phillips County, Montana: Unpublished Masters of Science Thesis, Univ. Idaho, Moscow, 92 p.
- Schafer, P.A., 1935, Geology and ore deposits of the Neihart mining district, Cascade County, Montana: *Memoir - State of Montana, Bureau of Mines and Geology*, v. 62.
- Sears, J.W. and Link, P.K., 2007, A field guide to the quartzite of Argenta; Neihart Quartzite equivalent?: *Northwest Geology*, v. 36, p. 221-230.
- Selverstone, J., Condie, K.C., Van Schmus, W.R., 2000, The crust of the Colorado Plateau; evidence from the xenolithic record: *Abstracts with Programs, Geological Society of America*, v. 32, p. 386.
- Shand, S.J., 1943, *The Eruptive Rocks*, 2nd edition: New York, John Wiley, 444 p.
- Shaw, D.M., 1972, *Geochemistry in Canada: Earth-Science Reviews*. v. 8, p. 129-131.
- Sims, P.K. and Peterman, Z.E., 1986, Early Proterozoic Central Plains orogen: a major buried structure in the north-central United States: *Geology*, v. 14, p. 488-491.
- Sims, P.K., O'Neill, J.M., Bankey, V., Anderson, E.D., 2004, Precambrian basement geologic map of Montana; an interpretation of aeromagnetic anomalies. *Scientific Investigations Map, United States Geologic Survey*.

- Taylor, S.R. and McLennan, S.M., 1995, The geochemical evolution of the continental crust: *Reviews of Geophysics*, v. 33, n. 2, p. 241-265.
- Thomas, M.D., Sharpton, V.L., Grieve, R.A.F., 1987, Gravity patterns and Precambrian structure in the North American Central Plains: *Geology*, v. 15, p. 489-492.
- Thompson, R.N., Morrison, M., Hendry, G., Parry, S., 1984, An assessment of the relative roles of crust and mantle in magma genesis: an elemental approach. *Philosophical Transactions of the Royal Society of London*. v. A310, p. 549-590.
- Van Schmus, W.R., Bickford, M.E., Condie, K.C., 1993, Early Proterozoic transcontinental orogenic belts in the United States: Abstracts with Programs, *Geological Society of America*, v. 25, p. 44.
- Villaseca, C., Orejana, D., Belousova, E.A., 2012, Recycled metagneous crustal sources for S- and I-type Variscan granitoids from the Spanish Central System batholith: Constraints from Hf isotope zircon composition: *Lithos*, v. 153, p. 84-93.
- Villeneuve, M.E., Ross, G.M., Parrish, R.R., Theriault, R.J., Miles, W., Broome, J., 1993, Geophysical subdivision, U-Pb geochronology and Sm-Nd isotope geochemistry of the crystalline basement of the Western Canada sedimentary basin, Alberta and northeastern British Columbia: *Geological Survey of Canada Bulletin* 447, 86 p.
- Vogl, J.J., Mueller, P.A., Foster, D.A., Wooden, J.L., 2003, Paleoproterozoic history of the Great Falls tectonic zone; results from an integrated study of basement exposures in the Little Belt Mountains, Montana: Abstracts with Programs - *Geological Society of America*, v. 35, n. 6, p. 595-596.
- Vogl, J., Foster, D., Mueller, P., Wooden, J., Mogk, D., 2004, Lithology and age of pre-Belt Precambrian basement in the Little Belt Mountains, Montana: Implications for the role of the Great Falls tectonic zone in the Paleoproterozoic assembly of North America: *Northwest Geology*, v. 33, p. 15-32.
- Weed, W.H., 1900, *Geology of the Little Belt Mountains, Montana: Twentieth Annual Report of the United States Geological Survey. Part III. Precious-Metal Mining Districts*. Government Printing Office, Washington, D. C.
- Weed, W.H. and Pirsson, L.V., 1896, *The Geology of the Little Rocky Mountains, Montana*. *Journal of Geology*, p. 399-428.
- Weiss, R., Vogl, J., Mueller, P., Foster, D., Wooden, J., 2009, Lu-Hf analyses of zircons in the Little Belt Mountains suggest Paleoproterozoic subduction in the Great Falls tectonic zone: AGU Fall Meeting, V43E-2321.

- Werner, C. D., 1987, Saxonian granulites: a contribution to the geochemical diagnosis of original rocks in high-metamorphic complexes: *Gerlands Beitrage zur Geophysik*, v. 96, p. 271-290.
- Whitehouse, M.J., Stacey, J.S., Miller, F.K., 1992, Age and nature of the basement in northeastern Washington and northern Idaho: isotopic evidence from Mesozoic and Cenozoic granitoids. *Journal of Geology*, v. 100, p. 691-701.
- Wilson, M.R. and Kyser, T.K., 1988, Geochemistry of porphyty-hosted Au-Ag deposits in the Little Rocky Mountains, Montana. *Economic Geology*, v. 83, p. 1329-1346.
- Wooden, J.L., and Mueller, P.A., 1988, Pb, Sr, and Nd isotopic compositions of a suite of Late Archean, igneous rocks, eastern Beartooth Mountains: Implications for crust-mantle evolution: *Earth and Planetary Science Letters*, v. 87, p. 59-72.
- Woodhead, J., Hergt, J., Shelley, M., Eggins, S., Kemp, R., 2004, Zircon Hf-isotope analysis with an excimer laser, depth profiling, ablation of complex geometries, and concomitant age estimation: *Chemical Geology* v. 209, n. 1-2, p. 121-135.

BIOGRAPHICAL SKETCH

Jennifer was born in Hartford, Connecticut, in 1983 to Michael and Terry Gifford. She is the youngest of three sisters. She graduated from Regional Hebron Andover Marlborough (RHAM) high school (Hebron, Connecticut) in 2001. She received a Bachelor of Science degree in geology from Syracuse University (Syracuse, New York) in 2005. While attending graduate school at the University of Florida (Gainesville, Florida), Jennifer served as a teaching assistant for several courses in the Department of Geological Sciences and as a research assistant for Dr. David A. Foster and Dr. Paul A. Mueller. She received a master's degree in geology from the University of Florida in May of 2008. She received a doctoral degree in geology from the University of Florida in May of 2013.